



TECHNISCHE
UNIVERSITÄT
WIEN

Dissertation

Applications of Nanoscale Chemical Imaging in the Life and Polymer Sciences

A thesis submitted for the degree of
Doctor of Natural Sciences (Dr. rer. nat)

at

Technische Universität Wien

Faculty of Technical Chemistry

Institute of Chemical Technologies and Analytics

under supervision of

Dr. Georg Ramer

&

Univ. Prof. Dr. Bernhard Lendl

defended by

Ana Catarina Vieira Dias dos Santos

Mat.Nr. 11936020

Vienna, June 2023



*“Recomeça...
Se puderes,
Sem angústia e sem pressa.”*

*“Start again...
If you can,
Without anguish and without haste.”*

Miguel Torga

Abstract

Atomic Force Microscopy – Infrared Spectroscopy (AFM-IR) is a scanning probe-based nanoscale IR technique that combines the resolution of an AFM with the chemical information provided by IR spectroscopy. AFM-IR benefits from bulk IR spectroscopy's long established spectra-structure correlations to extract valuable information at a maximum resolution of 10 nm. Despite its potential to obtain nanoscale chemical characterization of a broad range of samples, AFM-IR is still not widely used to solve applied problems, particularly those involving interdisciplinary research. In this thesis, AFM-IR was applied to the life and polymer sciences through a series of collaborative works with both other research groups within TU Wien, as well as external companies. Additionally, a perspective article was written on the application of AFM-IR to the life sciences, with the aim of incentivizing future interdisciplinary collaboration between the two fields.

T. Reesei is a filamentous fungi used in industrial enzyme production due to its exceptional production and secretion of cellulases, xylanases and endoglucanases. In this work, the intracellular distribution of β -sheet containing cellulases and xylanases was mapped by combining contact mode AFM-IR with fluorescence microscopy and chemometric analysis. This was possible through the use of a fluorescent label (enhanced yellow fluorescent protein) which is produced in small amounts under the same condition as the cellulases and is collocated with them. The resulting fluorescence signal was used to calibrate a partial least squares model which is capable of predicting the distribution of cellulases and xylanases intracellularly.

When applied to polymer science, the first step was the development of a reliable protocol for the nanoscale characterization of polymer samples using AFM-IR. Particular emphasis was placed on the sample preparation, which requires microtome sectioning at a temperature lower than the glass-transition temperature of the material to prevent smearing, and subsequent artifacts and increased measurement difficulty. The protocol was then followed for the analysis of four different commercially available polymer samples, allowing the identification and mapping of not only the major components of the blends, but also of their mineral fillers.

Finally, a commercially available post-consumer polyolefin recyclate blend was thoroughly characterized at the nanoscale using tapping mode AFM-IR. The presence of an interface between the polyethylene (PE) and polypropylene (PP) phases was detected using a gaussian mixture model and identified as being ethylene propylene rubber, which potentially acts as a compatibilizer to the polyolefin blend. Additionally, the presence of small PP droplets inside the PE phase was detected, as well as the widespread distribution of non-polyolefin polymer contaminants. These results showcase the usefulness of AFM-IR in the analysis of complex recyclate samples, where the traditional nanoscale characterization methods (electron microscopies and AFM) do not offer direct chemical information without the use of staining protocols.

Keywords: Infrared Spectroscopy • Atomic Force Microscopy • Photothermal Infrared Spectroscopy • Polymer analysis • Recyclates • Intracellular protein distribution • Fungi analysis • AFM-IR

Kurzfassung

Rasterkraftmikroskopie - Infrarotspektroskopie (AFM-IR) ist eine auf Rastersonden basierende IR-Technik, die die Ortsauflösung eines AFM mit den chemischen Informationen der IR-Spektroskopie kombiniert. AFM-IR profitiert von den seit langem etablierten Spektren-Struktur-Korrelationen der Bulk-IR-Spektroskopie und kann chemische Bilder mit einer Ortsauflösung von 10 nm detektieren. Trotz des Potenzials zur chemischen Charakterisierung eines breiten Spektrums von organischen Materialien im Nanomaßstab wird AFM-IR noch nicht in großem Umfang in der angewandten Forschung eingesetzt, insbesondere nicht in interdisziplinären Forschungsgebieten. In dieser Arbeit wurde AFM-IR in den Bio- und Polymerwissenschaften durch eine Reihe von Kooperationen sowohl mit anderen Forschungsgruppen innerhalb der TU Wien als auch mit Unternehmenspartnern angewandt. Zusätzlich wurde ein perspektivischer Artikel über die Anwendung von AFM-IR in den Biowissenschaften verfasst, mit dem Ziel, die zukünftige interdisziplinäre Zusammenarbeit mit dieser Disziplin zu fördern.

T. Reesei ist ein filamentöser Pilz, der aufgrund seiner außergewöhnlichen Produktion und Sekretion von Cellulasen, Xylanasen und Endoglucanasen in der industriellen Enzymproduktion eingesetzt wird. In dieser Arbeit wurde die intrazelluläre Verteilung von β -Faltblatt-haltigen Cellulasen und Xylanasen durch die Kombination von Kontaktmodus-AFM-IR mit Fluoreszenzmikroskopie und chemometrischer Analyse kartiert. Dies war durch die Verwendung eines fluoreszierenden Markers (verstärkt gelb fluoreszierendes Protein) möglich, der in kleinen Mengen unter den gleichen Bedingungen wie die Cellulasen produziert und mit ihnen zusammengebracht wird. Das daraus resultierende Fluoreszenzsignal wurde zur Kalibrierung eines Regressionsmodells der partiellen kleinsten Quadrate (PLS) verwendet, das in der Lage ist, die intrazelluläre Verteilung von Cellulasen und Xylanasen vorherzusagen.

Bei der Anwendung auf die Polymerwissenschaft war der erste Schritt die Entwicklung eines zuverlässigen Protokolls für die nanoskalige Charakterisierung von Polymerproben mit AFM-IR. Besonderes Augenmerk wurde auf die Probenvorbereitung gelegt. Diese erfordert einen Mikrotomschnitt bei einer Temperatur, die unter der Glasübergangstemperatur des Polymers liegt, um ein Verschmieren und damit verbundene Artefakte und somit erhöhte Messschwierigkeiten zu vermeiden. Das Protokoll wurde dann für die Analyse von vier verschiedenen handelsüblichen Polymerproben angewandt, was die Identifizierung und Kartierung nicht nur der Hauptbestandteile der Mischungen, sondern auch ihrer mineralischen Füllstoffe ermöglichte.

Schließlich wurde ein handelsübliches Recycling-Polyolefin-Gemisch mit Hilfe von AFM-IR im Tastmodus auf der Nanoskala gründlich charakterisiert. Das Vorhandensein einer Grenzfläche zwischen der Polyethylen (PE)- und der Polypropylen (PP)-Phase wurde mithilfe eines Gaußschen Mischungsmodells nachgewiesen und als Ethylen-Propylen-Kautschuk identifiziert, der möglicherweise als Kompatibilisierungsmittel für die Polyolefinmischung dient. Darüber hinaus wurde das Vorhandensein kleiner PP-Tropfen in der PE-Phase sowie die weite Verbreitung von Verunreinigungen aus Nicht-Polyolefin-Polymeren festgestellt. Diese Ergebnisse zeigen die Nützlichkeit der AFM-IR-Methode bei der Analyse komplexer Rezyklatproben, bei denen die herkömmlichen Methoden zur Charakterisierung im Nanobereich (Elektronenmikroskopie und AFM) ohne die Verwendung von Färbeprotokollen keine direkten chemischen Informationen liefern.

Schlagworte: Infrarotspektroskopie • Rasterkraftmikroskopie • Photothermische Infrarotspektroskopie • Polymeranalyse • Rezyklate • Intrazelluläre Proteinverteilung • Pilzanalyse • AFM-IR

Acknowledgements

The last nearly four years have been quite a journey, and I am grateful to have had so many great people beside me who supported me even during such challenging times as a global pandemic. Therefore, I would like to thank:

My supervisors *Georg Ramer* and *Bernhard Lendl*. *Georg*, thank you for introducing me and supervising my way through the world of AFM-IR, and for always being ready to lend a helping hand. I learned a lot from you, and I will miss not only our scientific discussions, but also the more informal talks and meme exchanges. *Bernhard*, thank you for giving me the opportunity to do a PhD in your group back when I had just arrived in Vienna and knew no one. Thank you for making sure that whatever was necessary was available, for the freedom to pursue various projects throughout my PhD, and for the opportunity to attend several international conferences.

All members of the research group during my time there for the nice working environment, social activities, and (second) lunch time conversations. Especially *Alicja*, my German course partner, *Andreas*, for your kindness and readiness to help, *Daniel*, *Elizabeth*, and *Felix* for the interesting conversations and great company, *Davide* and *Giovanna*, the Italians, for the jokes and good humor during challenging pandemic times, *Pily*, for being always ready to help whenever necessary and for your contagious good mood, *Shilpa*, for your friendship, all the great memories and for being the best typo-hunter, *Vicky*, for all the interesting and fun talks and for the ham, and finally, as is tradition, I want to thank *Ufuk*.

Rosa Heydenreich and *Davide Tranchida* for the great collaborations, as well as all the companies that agreed to send me samples to analyze with AFM-IR.

The COMET Centre CHASE funded by Austrian federal and regional governments and managed by the FFG, for providing the financial support that made this work possible.

My friends in Vienna, particularly the board game night and pub quiz crew *Viola*, *Öli*, *Shilpa*, *Michael*, *Miri*, *Matthias*, *Daniel*, and *Connie*. Thank you for making me feel at home in Vienna.

My friends in Portugal and Sweden for all the good times, dinners, and holidays, in particular *Tiago*, for the “therapy” gaming sessions, *Fábio*, for the python tips, and *Tita* cause Gé.

My family back at home, especially my parents, *José Joaquim* and *Adelaide* for always believing in me and supporting me even when that meant being far away from each other during times that included a pandemic. Thank you, mom, for all the packages filled with Portuguese goods, which made home feel closer when I most needed it to be.

My *Alex*, without whom none of this would have been possible. You have been with me through thick and thin, and knowing that you would be there at the end of the day was all I needed. Thank you for your support and encouragement throughout these years. I am so grateful our paths crossed and that you are such an important part of my life.

Content

<i>Abstract</i>	v
<i>Kurzfassung</i>	vi
<i>Acknowledgements</i>	vii
<i>Content</i>	viii
<i>Abbreviations</i>	ix
<i>Symbols</i>	xi
Chapter 1 Theoretical Introduction	1
1.1 <i>Mid-Infrared Spectroscopy</i>	1
1.1.1 Principles	1
1.1.2 Direct and Indirect Techniques	3
1.1.3 Mid-IR Microscopy	4
1.2 <i>Atomic Force Microscopy</i>	6
1.2.1 Instrumentation	6
1.2.2 General Measurement Principles.....	7
1.2.3 Contact Mode.....	10
1.2.4 Tapping Mode	11
1.3 <i>Atomic Force Microscopy – Infrared Spectroscopy (AFM-IR)</i>	14
1.3.1 AFM-IR Signal	14
1.3.2 Illumination Geometries	15
1.3.3 Contact Mode AFM-IR.....	17
1.3.4 Tapping mode AFM-IR.....	20
1.4 <i>Fluorescence Microscopy</i>	23
1.4.1 Epifluorescence Microscopes.....	25
1.5 <i>Chemometric Models and Data Processing</i>	27
1.5.1 Hierarchical Cluster Analysis (HCA)	27
1.5.2 Principal Component Analysis (PCA)	28
1.5.3 Partial Least Squares (PLS)	29
1.5.4 Gaussian Mixture	30
1.5.5 Savitzky-Golay Filter	31
Chapter 2 Results and Introduction to the publications	34
2.1 <i>AFM-IR in life sciences (Publications I and IV)</i>	34
2.1.1 AFM-IR for the localization of intracellular protein distribution (Publication I)	34
2.2 <i>AFM-IR in polymer science (Publications II and III)</i>	42
2.2.1 Analysis of polymers using tapping mode AFM-IR (Publication II).....	43
2.2.2 Analysis of post-consumer polyolefin recyclates using tapping mode AFM-IR (Publication III) 47	
Chapter 3 Conclusion and Outlook	53
Bibliography 55	
Appendix 70	
A. <i>Scientific publications</i>	70
Publication I.....	71
Publication II.....	79
Publication III.....	87
Publication IV	95
B. <i>Curriculum Vitae</i>	110

Abbreviations

acrylonitrile-butadiene-styrene	ABS
attenuated total reflection	ATR
atomic force microscopy	AFM
atomic force microscopy – infrared spectroscopy	AFM-IR
cellobiohydrolase I	CBHI
cryogenic electron microscopy	cryo-EM
endoglucanase I	EGL1
enhanced green fluorescent protein	EGFP
enhanced yellow fluorescent protein	EYFP
error sum of squared values	ESS
ethylene-propylene block copolymer	EbP
ethylene-propylene rubber	EPR
external cavity quantum cascade laser	EC-QCL
focal plane array	FPA
frequency modulated atomic force microscopy	FM-AFM
Fourier transform infrared	FTIR
green fluorescent protein	GFP
high density polyethylene	HDPE
hierarchical cluster analysis	HCA
highest occupied molecular orbital	HOMO
impact polypropylene copolymer	IPC
infrared	IR
intermittent contact atomic force microscopy	IC-AFM
isotactic polypropylene	iPP
linear array	LA
linear discriminant analysis	LDA
linear low-density polyethylene	LLDPE
low-density polyethylene	LDPE
lowest unoccupied molecular orbital	LUMO
mercury-cadmium-telluride	MCT
mixed polyolefin waste fraction	MPO
non-contact atomic force microscopy	NC-AFM
nuclear magnetic resonance	NMR
numerical aperture	NA
optical parametric oscillator	OPO
partial least squares	PLS
phase locked loop	PLL
photo-activated localization microscopy	PALM
photothermal-induced resonance	PTIR
polyethylene	PE
polypropylene	PP
polystyrene	PS
polyurethane	PU
principal component analysis	PCA
principal component regression	PCR
proportional-integral-derivative	PID

quantum cascade laser	QCL
reactor thermoplastic polyolefin	rTPO
root mean squared error	RMSE
Savitzky-Golay	SG
scanning electron microscopy	SEM
selectivity ratio	SR
signal-to-noise ratio	SNR
single point detector	SPD
stimulated emission depletion microscopy	STED
stochastic optional reconstruction microscopy	STORM
structured illumination microscopy	SIM
support vector machine	SVM
transmission electron microscopy	TEM
xylanase II	XYNII

Symbols

absorbance	A
absorption coefficient	α
amplitude, predictor variable (context)	X
anharmonicity constant	x_i
complex refractive index	\hat{n}
concentration	c
critical angle	$\theta_{critical}$
damping ratio	ζ
data matrix	D
depth of penetration, penetration depth	d_p
derivative gain in a proportional-integral-derivative controller	D
dipole moment, Gaussian mean (context)	μ
distance	d, z
electronic level 0, 1, 2	S_0, S_1, S_2
error (residual) matrix	E, F
error signal in a proportional-integral-derivative controller	Z_{err}
force	F
frequency	ν, f
fundamental frequency of the i -th energy level	ν_i
half-angle of the cone of light accepted by an objective	θ
index of absorption	k
index of refraction, refractive index	n
intensity, integral gain in a proportional-integral-derivative controller (context)	I
inverse variance	τ
loadings matrix	L, P, Q
mass	m
mass of individual atoms	m_1, m_2
minimum distance between two objects at which they can still be resolved	Δ_x
molar decadic absorption coefficient	ε
non-linear material elasticity	χ_s
pathlength	d
phase angle	ψ
phase shift	$\Delta\psi$
photon energy	E_p
Planck's constant	\hbar
potential energy	V
probability density function	x
proportional gain in a in a proportional-integral-derivative controller	P
quality factor	Q
quantum yield	φ
refractive index	n
response variable	Y
scores matrix	T, U
signal output in a proportional-integral-derivative controller	Z_v
speed of light in vacuum	c
spring constant of the cantilever	k_c

spring constant of the tip-sample interaction	k^*
standard deviation	σ
time	t
vibrational quantum number	ν_i
wavelength	λ
wavenumber	$\bar{\nu}$

Chapter 1 Theoretical Introduction

The work presented in this thesis is at the interface of several techniques which are introduced in this chapter consisting of five main subjects: Mid-Infrared Spectroscopy (**Section 1.1**), Atomic Force Microscopy (**Section 1.1**), Atomic Force Microscopy-Infrared Spectroscopy (**Section 1.1**), Fluorescence Microscopy (**Section 1.1**), and Chemometric Models and Data Processing methods required to analyze the obtained AFM-IR data (**Section 1.1**).

1.1 Mid-Infrared Spectroscopy

1.1.1 Principles

The following sub-chapter is based on the works by Peter J. Larkin¹, Peter R. Griffiths,² and James M. Thompson.³ For a more detailed description of vibrational spectroscopies, the reader is advised to consult these publications.

Mid-infrared spectroscopy, like all spectroscopies, takes advantage of the interaction between electromagnetic radiation and matter to obtain information about the latter. Within the electromagnetic radiation spectrum, mid-IR corresponds to the range between 2.5 μm and 25 μm (4000 cm^{-1} – 400 cm^{-1}). The energy of the photons in this range corresponds to that of molecular vibrations, and is thus insufficient to break chemical bonds. This means that mid-IR spectroscopy is part of the larger group of vibrational spectroscopies (together with near- and far- IR spectroscopy, and Raman spectroscopy), and is non-destructive. According to quantum theory, the energy of a photon (E_p) is directly proportional to its frequency (ν) times the Planck's constant (h):

$$E_p = h\nu \quad (1.1)$$

The photon frequency is related to the wavenumber ($\bar{\nu}$), and to the wavelength (λ) by the following expression:

$$\bar{\nu} = \frac{\nu}{(c/n)} = \frac{1}{\lambda} \quad (1.2)$$

with c being the speed of light in vacuum and n the refractive index of the medium. When the energy of an infrared photon precisely matches the difference in energy between two molecular vibration energy levels and it leads to a change in the dipole moment (μ), absorption occurs.

To understand what influences the frequency of molecular vibrations, a model based on classical mechanics is commonly used. In this model, a molecule is constituted of two atoms with point masses m_1 and m_2 in grams that are connected by a spring (chemical bond) with a force constant

K in newtons-cm⁻¹ (corresponding to the bond strength). The frequency in wavenumber units ($\bar{\nu}$) at which the stretching oscillation occurs is given by:

$$\bar{\nu} = \frac{1}{2\pi c} \sqrt{K \left(\frac{1}{m_1} + \frac{1}{m_2} \right)} \quad (1.3)$$

Eq. 1.3 shows that the frequency of a molecular vibration is a function of:

- The force constant K , which represents the bond strength. For example, the higher the bond order, the higher the frequency of the corresponding molecular vibration. In addition to bond order, K is also affected by intra- and intermolecular effects. These include electron withdrawing or donating neighboring functional groups, hydrogen bonds and other intermolecular forces, and changes in bond angles, for example, due to steric constraints.
- The atomic masses m_1 and m_2 of the bonded atoms. A bond consisting of lighter atoms will vibrate at higher frequencies than if it was composed of heavier ones.

Molecules have several possible fundamental molecular vibrations, in which the atoms have approximately harmonic displacements from their equilibrium positions at a characteristic frequency.⁴ A molecule constituted by n atoms has $3n$ degrees of motional freedom, as these can move in the x , y , and z directions. However, three of these motional degrees of freedom correspond to rotations around one of the axes for non-linear molecules (only two in the case of linear molecules), and three others correspond to translational movements. This results in linear molecules having $3n-5$ fundamental vibrations, whereas non-linear molecules have $3n-6$ fundamental vibrations. Whether or not all molecular vibrations allowed by this rule can be observed depends on there being a temporary change in the dipole moment (μ) of the whole molecule during vibration (no change means no molecular vibration occurs), on whether or not all the vibrations have unique energy values (are not degenerate), and on the sensitivity and range of the instrument used. The intensity of IR bands is proportional to the square of the variation in the dipole moment.

There are two main types of fundamental vibrations: stretching and bending. Stretching vibrations occur when there is a change in the bond length and can be symmetric or asymmetric. Bending vibrations correspond to changes in the bond angle both in-plane (rocking and scissoring) as well as out-of-plane (twisting and wagging).³ Stretching vibrations typically require the absorption of higher energy photons than bending vibrations, and thus, assuming the same type of bond, stretching vibrations will be present at higher wavenumbers in the IR spectrum.

The potential energy V_{iv} of the possible vibrational states of a molecule can be described using a harmonic oscillator model:

$$V_{iv} = hv_i \left(v_i + \frac{1}{2} \right) \quad v_i = 0, 1, 2, \dots \quad (1.4)$$

where h is Planck's constant, ν_i the fundamental frequency of the oscillator, and v_i is the vibrational quantum number. In this model (Figure 1.1, red lines), only transitions of ± 1 of v_i are permitted, which correspond to fundamental vibrations. A more complete model can be achieved when using an anharmonic potential function (Morse-type), which offers a better description at high vibrational quantum numbers and is depicted in Eq. 1.5 where x_i is the anharmonicity constant:

$$V_{iv} = hv_i \left(v_i + \frac{1}{2} \right) + hv_i x_i \left(v_i + \frac{1}{2} \right)^2 \quad (1.5)$$

In this model (Figure 1.1, blue lines), transitions with a $\Delta v_i > 1$ can also happen. These transitions are called overtones, and they are a type of non-fundamental vibration. Other non-fundamental vibrations include combination and difference bands occurring at positions near the sum or subtraction of fundamental vibrations, respectively.³ Non-fundamental vibrations produce generally weaker absorption bands and are less common in the mid-IR range than fundamental vibrations.

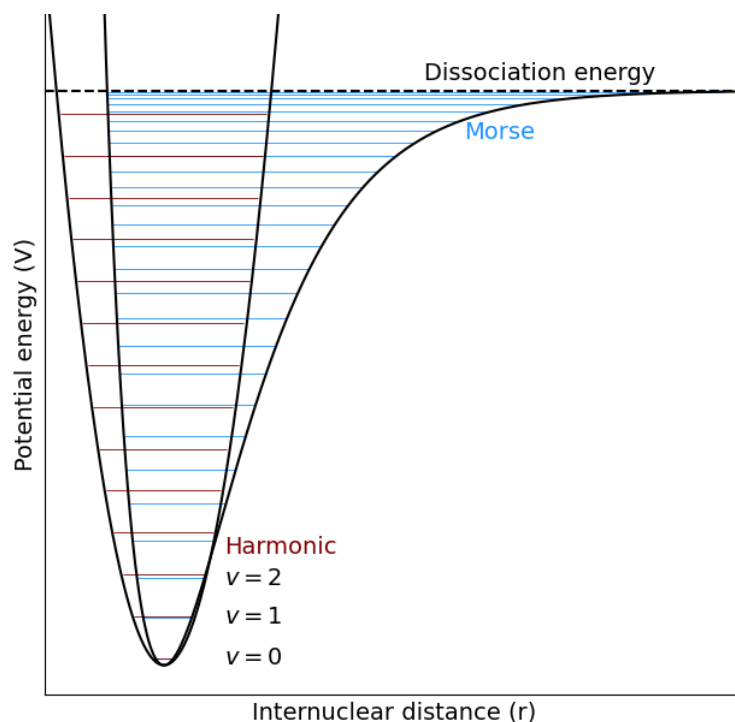


Figure 1.1: Potential energy diagram of a harmonic and Morse (anharmonic) type oscillator model for a diatomic molecule.

1.1.2 Direct and Indirect Techniques

The interaction of mid-IR radiation with matter can be measured either by its direct effects on the properties of light such as intensity and phase (direct spectroscopy), or by the effects that this interaction causes in the sample or surrounding medium (indirect spectroscopy). The most widespread bulk mid-IR spectroscopy technique is absorption spectroscopy based on transmission measurements. In such setups, the wavelength-dependent intensity loss of the mid-IR is measured, and can be used to obtain quantitative information about the sample through the Beer-Lambert law, expressed as:

$$A(\bar{\nu}) = -\log_{10} \left(\frac{I_s(\bar{\nu})}{I_0(\bar{\nu})} \right) = \varepsilon(\bar{\nu})cd \quad (1.6)$$

where A is the absorbance, ε the molar (decadic) absorption coefficient, d is the pathlength, I_0 the intensity of light before passing through the sample, and I_s the intensity of light after passing through the sample.⁵ Attenuated total reflection (ATR) is another common absorption spectroscopy configuration, and is further discussed in section 1.3.2. in the context of AFM-IR. Other types of direct mid-IR spectroscopy include dispersion spectroscopy, which measures the phase shift of

coherent light after interacting with matter,⁶ and vibrational circular dichroism, which measures the different absorption of left and right polarized light by chiral molecules.⁷

Changes in the surrounding medium's temperature and refractive index are measured by photothermal spectroscopy,^{8,9} whereas changes in pressure are in the realm of photoacoustic spectroscopy.¹⁰ These two methods represent bulk indirect spectroscopic techniques.

1.1.3 Mid-IR Microscopy

In a standard Fourier transform infrared spectrometer (FTIR), the spectrum collected corresponds to an average of the infrared spectra in the area irradiated by the IR beam. By contrast, infrared microscopy yields spatially resolved infrared spectroscopic information which is of particular use in heterogeneous samples. The spatial resolution can be achieved through three different types of detectors: single point detectors (SPD), linear arrays (LA) or focal plane arrays (FPA):

- SPD: this method uses a single MCT detector to capture light from a location in the sample with the help of an aperture and a motorized stage capable of making precise movements from one measurement spot to the next. The process is repeated, until all the defined locations have been measured, making this mode very time consuming in the case of measurements with high spatial resolution (many points).¹¹ The aperture can be placed either before the sample (to confine the illumination beam to a smaller area), or before the detector in a confocal setup and typically ranges in diameter from 100 to 20 μm , with the lower limit being defined by the λ of the light being used.¹² The smaller the aperture, the higher the spatial resolution, but lower the signal-to-noise ratio (SNR). Apertures of the same size or smaller than the λ of the IR light in use result in significant loss of signal intensity due to diffraction.¹³ To overcome the limitation caused by the aperture on the signal intensity, this setup is sometimes combined with high intensity IR light sources such as synchrotrons,¹² or external cavity quantum cascade lasers (EC-QCLs).¹⁴ This type of technique can also be called FTIR microspectroscopy.¹²
- LA: in this method, an LA detector consisting of individual mercury cadmium telluride (MCT) detectors in a row is typically employed. The image is collected one row/column at a time, at which point the next one follows (raster scan in the second dimension). Compared to SPD, using an LA results in a lower measurement time by a factor corresponding to the number of individual detectors in the array.¹⁵ LAs are slower at acquiring images than FPAs, and despite having an SNR advantage, this may not be significant if several co-scans are averaged in the FPA system.¹⁵
- FPA: FPA detectors have MCT as the detector material and are composed of a grid of pixels, with sizes from 64x64 to 128x128 being commonly available in commercial instruments. FPA FTIR spectrometers collect a full-length spectrum at each of the points (pixels) in the chosen area simultaneously, and thus, have a major time advantage when compared to both SPD and LA instruments. On the other hand, the detector sensitivity of each FPA pixel is lower than that of a single point MCT, and as the number of pixels increases, a smaller number of incoming photons reaches each FPA pixel,¹⁶ in practice leading to a 40x worse SNR.¹³ In most cases this can be partially mitigated by increasing the acquisition time and/or the number of averages.¹⁵ The spatial resolution of an FPA increases with the number of pixels of the array until the diffraction limit (explained below) is reached, at which point further increase in pixel number has no

effect.¹⁵

Mid-infrared microscopy finds broad use in a number of fields due to its non-destructive and label-free nature. An example is the analysis of tissue sections, where infrared microscopy is often combined with multivariate analysis with the ultimate goal of identifying pathological markers.^{17–21} Other applications include, but are not limited to the analysis of polymers,^{22–24} artworks (conservation),^{16,25,26} and bacteria (detection of antibiotic resistance).^{27,28} Mid-infrared microscopy, like other microscopies that rely on optical systems for the detection of the signal in the far-field (distance from radiating source $> 2\lambda$), is diffraction-limited. For microscopes, the Rayleigh criterion (Figure 1.2) defines the minimum distance between two objects at which they can still be resolved as two separate objects, Δ_x , as dependent on the wavelength, λ and the numerical aperture of the lens, NA :

$$\Delta_x = \frac{0.61\lambda}{NA} = \frac{0.61\lambda}{n \sin \theta} \quad (1.7)$$

with n being the refractive index and θ the half-angle of the cone of light that is accepted by the objective. In infrared microscopy, the typical values for the NA of the objective in air are ≈ 0.6 ,¹² which means that the best possible spatial resolution is approximately the wavelength of the radiation being used.² In the mid-infrared region, the limit of resolution is thus approximately from 2.5 μm to 25 μm . This limit can be improved by the use of materials with a higher refractive index than air and operating the microscope in the ATR. This allows for a maximum 4-fold improvement of the achievable resolution when using germanium as the ATR crystal material, which nonetheless leaves the resolution limit in the micrometer range (2–4 μm).²⁹ Despite the improvement, the analysis of samples such as intracellular structures within individual bacteria remains beyond reach, and requires the use of other techniques.

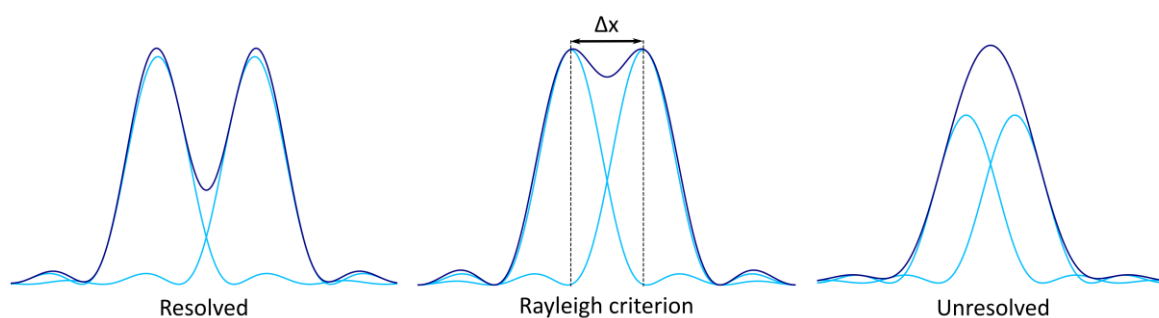


Figure 1.2: The minimum distance at which two separate objects can be resolved (Rayleigh criterion), occurs when the central maximum of light intensity from one object corresponds to the first minimum of the second.³⁰

1.2 Atomic Force Microscopy

The following sub-chapter and sub-sections are based on the book by P. Eaton and P. West.³¹ For a more detailed description of AFM and its applications, the reader is advised to read this publication. Atomic Force Microscopy, abbreviated as AFM, is a scanning probe technique that was first described in 1986 by Binnig, Quate, and Gerber.³² Scanning probe microscopes do not rely on the focusing of photons or electrons on a surface to generate an image, like conventional optical and electron microscopes do. Instead, a probe moving over the surface in a raster pattern is used to obtain information about the sample's surface. AFM produces topographic images of the sample's surface by mapping the height at each pixel, but it can also be used to measure mechanical, electrical, magnetic, and thermal properties of the samples analysed. It should be noted that for some of these imaging modes, specialized scanning probe tips are required. AFM topographic maps can achieve resolutions of 1-5 nm in the x-y axis (lateral resolution), and up to $\approx 1 \text{ \AA}$ in the z axis (vertical resolution).³³ This places AFM at the same level as transmission electron microscopy (TEM) and above scanning electron microscopy (SEM) in terms of resolution.³¹ A further advantage of AFM over these techniques is the much simpler sample preparation: no fixation, staining or sputtering is necessary, the only requirement being a relatively flat surface. AFM also does not require operation under vacuum, and can be measured at ambient conditions.³⁴ Some disadvantages of AFM include a poor depth of field when compared to SEM, and a longer measurement time than both TEM and SEM.

1.2.1 Instrumentation

A typical AFM setup (depicted in Figure 1.3) consists of a cantilever held by a support at one end and with a tip (the probe) at the other. The support can contain a piezoelectric element, which will be responsible for oscillating the cantilever during tapping mode measurements. The sample is placed on a sample stage that can be moved in the x, y and z directions. In a sample-scanning configuration, an x-y-z scanner, typically a piezoelectric material, is responsible for smaller and very precise movements required for raster scanning. The changes in position of the cantilever (deflection) are measured by an optical lever sensor that detects changes in position of a laser beam reflected off the back of the cantilever (force transducer). In AFM this is often achieved by having a laser beam reflected off the upper side of the cantilever, which is detected by a four-quadrant photodiode detector. This configuration is highly sensitive to any changes in the cantilever's deflection angle due to the large distance between the detector and the cantilever. Other components include a proportional-integral-derivative controller (PID) that works as a feedback control circuit by regulating the position of the sample stage during the measurement, and an integrated optical microscope to aid in finding the desired measurement location. The PID is governed by equation 1.8,³⁵ where Z_{err} is the error signal (the difference between the current tip-sample interaction force measured by the cantilever deflection, and a defined set-point), and P , I , and D are terms manually set by the AFM user, with the goal of reducing Z_{err} as much as possible.

$$Z_v = PZ_{err} + I \times \int Z_{err} dt + D \frac{dZ_{err}}{dt} \quad (1.8)$$

Z_v represents the signal output by the controller (in V), P stands for proportional gain, and its value affects the tracking of smaller details on the surface, whereas the integral (I) gain affects the tracking of the overall sample surface. In AFM, only the P and I elements of the PID are taken into consideration, the derivative gain (D) is not used.

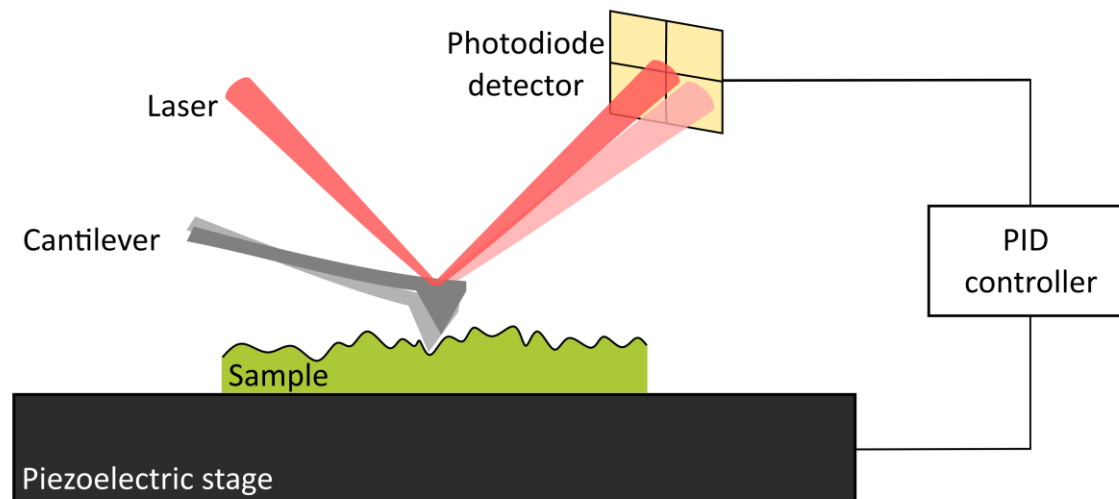


Figure 1.3: Simplified schematic diagram of the main components of an AFM setup and of how changes in the cantilever's deflection angle are picked up by the photodiode detector.

1.2.2 General Measurement Principles

Briefly, during operation in contact mode, the sample and probe are brought into contact with a set force (usually in the order of 10^{-9} N or less).³¹ As the probe is moved across the sample's surface, changes in the force between sample and probe are detected by the cantilever, which acts as a force transducer. These values are fed to the PID controller that determines if changes in the z position of the stage (controlled by changing the voltage applied to the piezoelectric element) are necessary to keep the force at the defined value. In the end of the raster scan, a topographic map of the selected region is generated (typically called a height map). In addition to height maps, AFM can also provide information on the sample's mechanical (e.g. Young's modulus, viscoelasticity), magnetic, and electrical properties. AFMs can be operated in several modes, and one possible classification is according to whether or not there is an oscillation of the cantilever during the measurement (if yes, it is an oscillating mode, if not it is contact mode). The majority of the experiments in this thesis were carried out in either contact mode or tapping mode (a type of oscillating mode, where the cantilever is in intermittent contact with the surface).³⁶ Further examples of oscillating modes include frequency modulation (FM-AFM) and non-contact mode (NC-AFM).

1.2.2.1 AFM Cantilever

The cantilever is the central element of an AFM and usually consists of a beam attached on one end to a chip (in turn attached to the instrument) with a tip on the underside of the other end. The following paragraphs will focus on rectangular beam-shaped cantilevers, as these were the type used in this work, however, AFM cantilevers are not limited to this geometry.

A cantilever can be modeled as an elastic beam made of a single material and with a uniform cross-section.³⁷ Cantilevers have several vibration modes that occur at characteristic frequencies, the natural (resonance) frequencies, without any external drive. These natural frequencies can be calculated from the elastic beam model by applying different boundary conditions such as:

- The beam is clamped at one end with the remaining end free (mimicking an AFM cantilever not in contact with the surface, Figure 1.4, (a));
- The beam is clamped at one end and the remaining end is coupled to a spring with a spring

constant k^* (mimicking an AFM cantilever affected by the tip-sample interaction forces (further explained in section 1.2.3) that are present during measurement, Figure 1.4, (b) and (c)).

The effect of having one end coupled to a spring in the resonance frequencies of a cantilever is described by:³⁷

$$f_{res} = \sqrt{\frac{k_c + k^*}{k_c}} f_0 \quad (1.9)$$

where f_{res} is the resonance frequency of the spring coupled clamped cantilever, k_c is the spring constant of the cantilever, k^* is the spring constant of the tip-sample interaction, and f_0 is the resonance frequency of the clamped-free cantilever. k^* varies with the sample's mechanical properties and the strength of the tip-sample interactions, the latter is subject to variations throughout the measurement and results in shifts in the f_{res} . Figure 1.4 shows the effect of increasing k^* in the vibration amplitude of the cantilever in the first three modes. As the tip-sample interactions become stronger, the cantilever oscillations resemble more and more those expected for a clamped cantilever with the other end fixed (Figure 1.4, (d)). In a real-life situation, an increase in k^* can be expected as the tip-sample distance is reduced during the approach (section 1.2.3), making the system move from a clamped-free state to a spring-coupled state.

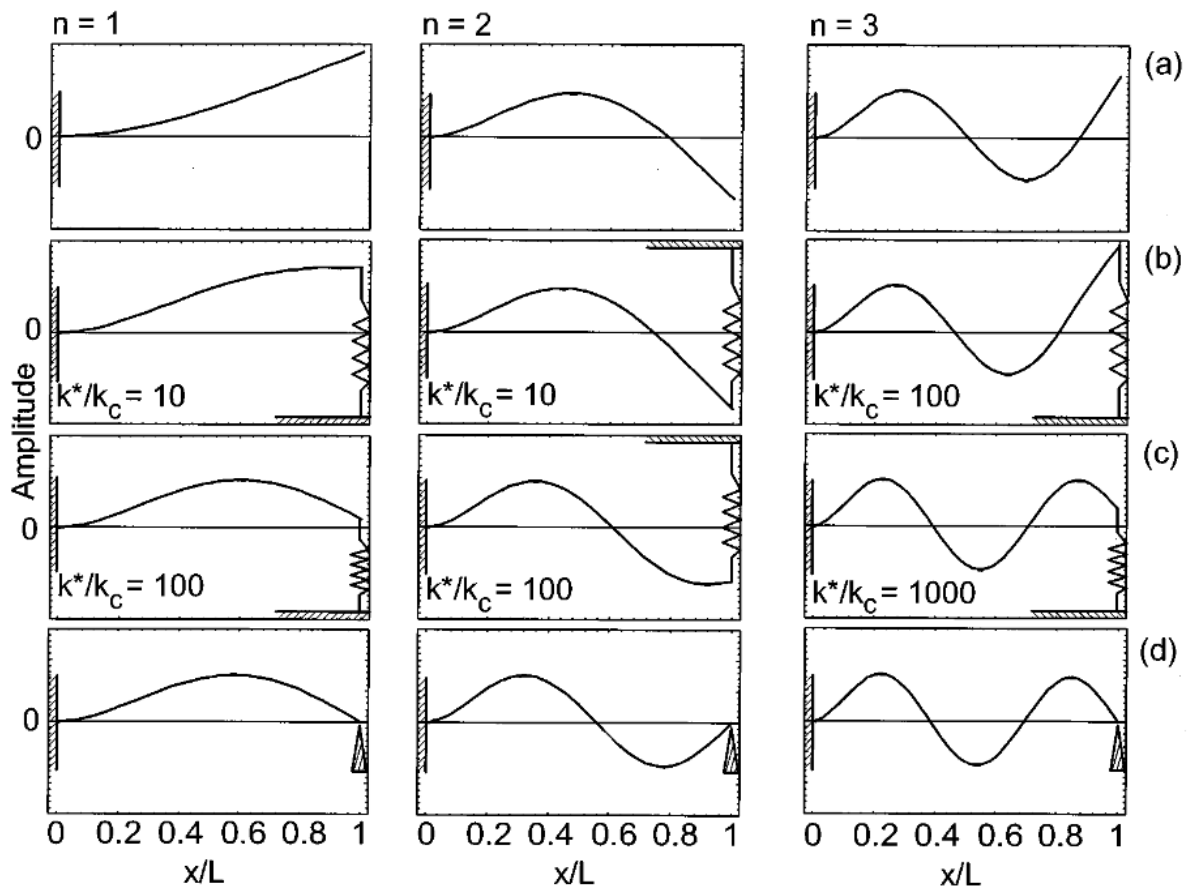


Figure 1.4: Effect of increasing tip-sample interactions (represented by an increase in k^* , the spring constant) in the local vibration amplitudes of the first three resonance modes ($n=1,2,3$). (a) local vibration amplitudes for a clamped-free cantilever; (b, c) local vibration amplitudes for a spring-coupled cantilever with increasing tip-sample interactions; (d) local vibration amplitudes for a clamped cantilever with the other end pinned to the surface. Reproduced with permission from Rev. Sci. Instrum. 67, 9 (1996). Copyright 1996, American Institute of Physics.³⁷

The above explanation using the elastic beam model is a representation of what happens during a contact mode AFM measurement, however, in oscillating modes, such as the tapping mode or some contact mode AFM-IR measurements, the cantilever is driven at one of its resonant frequencies (section 1.2.4). The dynamic behaviour of the cantilever in oscillating modes is also covered by the elastic beam model, however, the corresponding equations are fairly complex. Hence, to understand this case, the simpler approximation of the system to a mass-spring oscillator can be used.

When a periodic force (driving force), $F(t)$ is applied to a system that makes it oscillate (forced vibration), the amplitude of the resulting oscillation will be greatly amplified at its resonant frequencies, owing to vibrational energy storage.³⁸ The mass-spring model assumes that the cantilever can be modelled as a point mass, m attached to a linear spring with spring constant k , subject to a forced oscillation caused by a driving force at frequency f . In the absence of damping, the amplitude of the forced oscillation of the system when f is equal to the resonance frequency f_{res} increases to infinity. Under normal circumstances however, an AFM cantilever is subject to damping, which dissipates the oscillation energy and reduces the amplitude over time. The response of the cantilever is then described by:³⁸

$$x(t) = X \sin(2\pi ft - \psi) \quad (1.10)$$

where X is the amplitude and ψ is the phase angle. X is given by:

$$X = \frac{X_s}{\sqrt{(1 - r^2)^2 + 4r^2\zeta^2}} \quad (1.11)$$

where X_s is the static displacement of the mass if it was caused by a static force (F_0) $X_s = F_0/k$, r is the ratio between f and f_{res} , and ζ is the damping ratio. The phase shift ψ is defined as:

$$\psi = \tan^{-1} \left(\frac{2\zeta r}{1 - r^2} \right) \quad (1.12)$$

The damping factor can be approximated in cases where the damping is small ($\zeta \ll 1$) by the quality factor Q , which is expressed as:

$$Q = \frac{1}{2\zeta} = \frac{1}{r_2 - r_1} \quad (1.13)$$

where r_1 and r_2 are the frequency ratios corresponding to $X = X_{max}/\sqrt{2}$. The quality factor can be easily determined from empirical measurements. A high Q factor means the cantilever loses energy at a slow rate, whereas a low Q factor means that the oscillation will quickly be dampened. Figure 1.5 shows the amplitude and phase angle response of a cantilever with a resonance frequency of 265 kHz (similar to the tapping mode cantilevers used in this work) and a Q factor of 50 to a forced oscillation. The phase angle and corresponding phase shift calculated during AFM-IR measurements are used in the implementation of a phase locked loop (PLL), which is essential during resonance enhanced contact mode AFM-IR measurements (explained later in section 1.3.3.1).

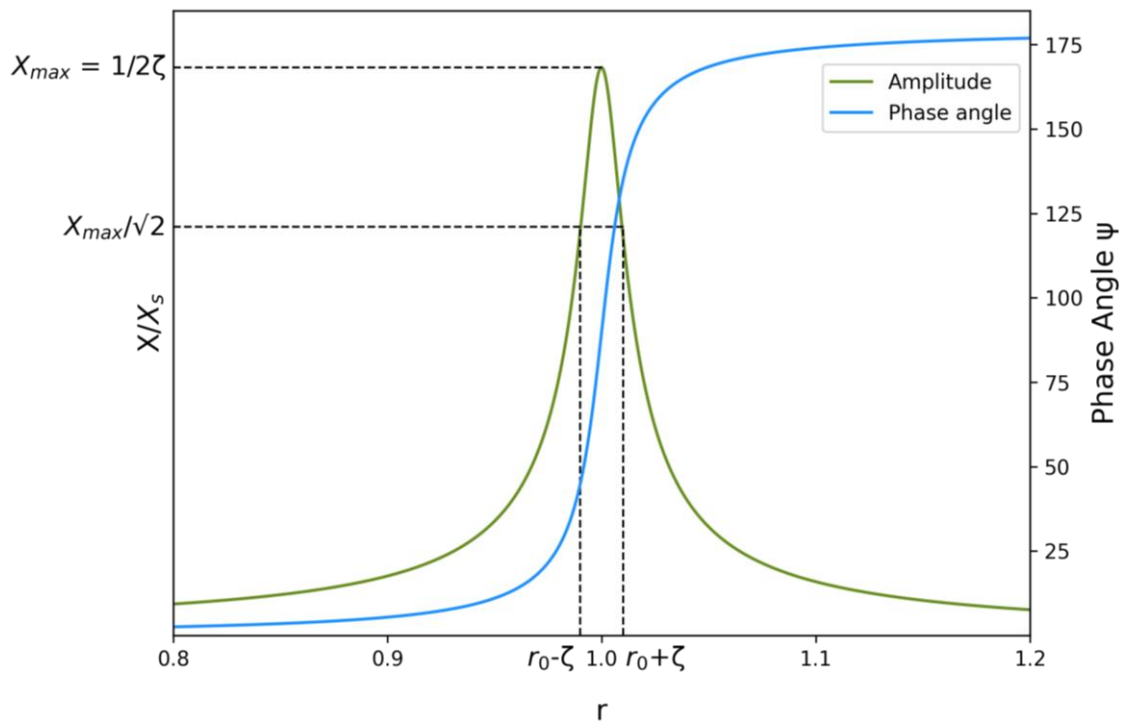


Figure 1.5: Amplitude and phase angle of a forced oscillation with damping. $r_0=1$ and represents the resonant frequency of the oscillator (cantilever). The Q factor and respective damping ratio, ζ can be calculated from experimental values, as depicted here.

1.2.3 Contact Mode

As the name indicates, in contact mode the cantilever and the sample are in contact, “touching” each other during the whole measurement. Contact mode is the oldest and most straightforward AFM mode.

At the beginning of a measurement, the tip of the cantilever (probe) and the sample are at a distance where there is no interaction between them. As the tip approaches the sample, it enters the “attractive regime”, where attractive van der Waals forces pull the tip towards the sample surface and cause a bending of the cantilever which is picked up by the deflection signal.³⁶ As the distance decreases, the cantilever eventually snaps towards the surface and the two are now in contact. Further decreases in the tip-sample distance lead to a “repulsive regime” where the tip and sample apply opposite forces to each other which increase with decreasing distance (Figure 1.6). Once again there is cantilever deformation, this time in the opposite direction, which is monitored by the deflection signal. Recording this information in addition to the reverse movement (withdrawing the tip), leads to a force-distance curve which can be used for obtaining information about interaction forces between the tip and the sample.³⁶

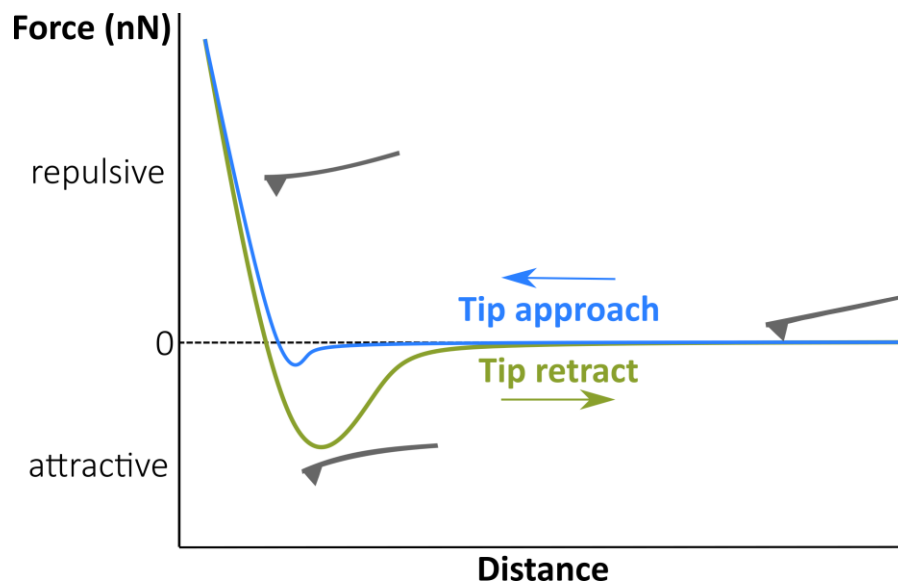


Figure 1.6: Force-distance curves for contact mode AFM. In blue the curve corresponding to the tip approach, and in green the curve corresponding to the tip retraction.

For topographic imaging however, the tip is kept in contact with the sample in the repulsive regime throughout the raster scan. In constant-force contact-mode AFM, the cantilever deflection is fixed by the user at a value called the set-point, and the PID controller makes the necessary height adjustments through the piezo element to ensure constant force.³⁶ A lower set point corresponds to lower tip-sample force in most AFMs, and a higher set point to a higher tip-sample force. As explained before, the P and I values are adjusted by the user and affect how fast the feedback loop reacts to changes in the sample's height. Higher values lead to quicker reaction times, but may lead to "ringing". Settings that are adequate for samples with higher roughness, might already show ringing in flatter samples. Hence, feedback needs to be adjusted for each sample. The height map corresponds to the cantilever height adjustments made by the piezo element plotted versus distance.

Due to the tip and sample being in contact throughout the whole measurement in the repulsive regime, certain samples, especially softer ones, may be damaged by both the normal force as well as the lateral forces that occur as the tip moves across the sample. The same applies to the tip, which is also vulnerable to sustaining damage that could alter its shape and affect the measurement.³⁶ For example, a blunted tip will lead to a lower resolution, whereas if a particle sticks to the tip it will often lead to artifacts in the images obtained. In addition to lateral forces, capillary forces are also present when measuring in air due to the thin layer of water present between the tip and the surface,³⁹ which adds to the force defined by the set-point.

All in all, contact mode is a powerful technique which combines high resolution with ease of use. However, care is needed when imaging soft samples to ensure that no damage is being incurred by it. Nonetheless, imaging of soft samples such as microorganisms is possible.^{40–42} Perhaps the greatest limitation of contact mode is the imaging of typically loosely adhered samples, such as liposomes or bacterial spores. In these situations, the sample may simply be pushed around by the tip, and no measurement can be performed.

1.2.4 Tapping Mode

Tapping mode, also called intermittent contact AFM (IC-AFM), is the most common type of oscillating mode. In tapping mode, the cantilever is oscillated at one of its resonant frequencies

with a constant amplitude. As the tip approaches the sample and begins to interact with it, changes to the amplitude are monitored by the deflection beam. During each oscillation cycle, the cantilever goes through the zero-attraction regime, then to the attractive and then repulsive, before returning to the attractive and zero-attraction regime and repeating the cycle.³⁶ When the attractive forces (van der Waals forces) dominate, the resonance curve shifts to lower frequencies (Figure 1.7).⁴³ As the repulsive forces (Pauli and ionic repulsion) begin to increase as the tip-sample distance decreases, the resonance frequency shifts to higher frequencies.⁴³ The transition between the attractive and repulsive regimes can lead to discontinuous or smooth transitions between the two, which can in turn lead to signal instability during imaging.^{44,45}

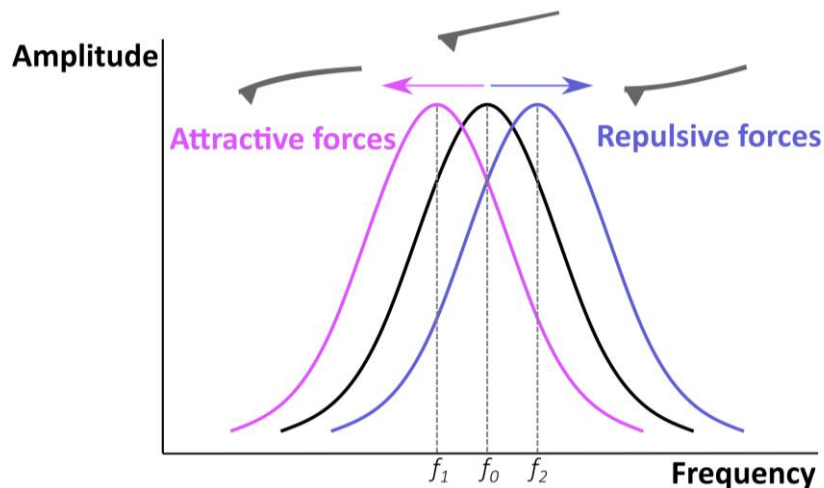


Figure 1.7 Effect of attractive and repulsive forces on the resonance frequency of the cantilever. Compared to the free resonance frequency (f_0) attractive forces (pink) lower the resonance frequency (f_1) whereas repulsive forces (purple) drive it to higher numbers (f_2).

During the times in the oscillation cycle when the cantilever is in contact with the sample surface there is a reduction in the oscillation amplitude compared to the free amplitude (Figure 1.8). These changes caused by topographic features are detected by the force transducer and fed to a feedback loop similar to the one used in contact mode, that makes the necessary adjustments to the z piezo to ensure a constant amplitude throughout the measurement.³⁶ As in contact mode, the height map corresponds to the cantilever height adjustments made by the piezo element plotted at each pixel. The phase-shift of the oscillation is often recorded and used to distinguish between different materials due to its sensitivity to several sample properties such as hardness, viscoelasticity, and stiffness.^{46–48} Tapping mode measurements can also be conducted at higher order resonance modes than the fundamental one, which can sometimes lead to increased image contrast.⁴⁹

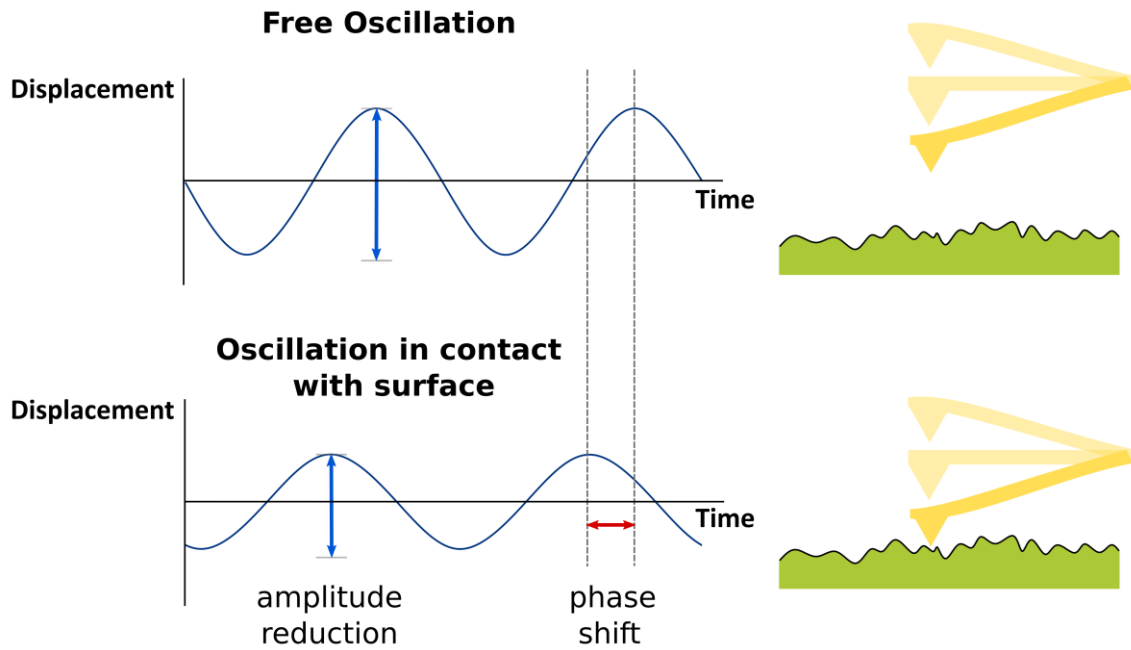


Figure 1.8: Changes in the cantilever oscillation due to contact with the surface in tapping mode AFM. Surface contact reduces the oscillation amplitude and leads to a phase shift.

The greatest advantage of tapping mode when compared to contact mode is the near absence of lateral forces during the measurement, which makes tapping mode more indicated for delicate and/or soft samples, or samples that are loosely adhered to the substrate.⁵⁰⁻⁵²

1.3 Atomic Force Microscopy – Infrared Spectroscopy (AFM-IR)

The technique that came to be known as AFM-IR was first published in 2005 by researchers of the University of Paris-Sud.⁵³ Despite the many instrumental improvements it has been the subject of since then, the basic principles remain the same. The most recent reviews of the field by Schwartz *et al.*⁵⁴ and Mathurin *et al.*⁵⁵ offer a comprehensive description of the method, its principles and some recent applications, which the interested reader can consult.

A general AFM-IR, also called photothermal induced resonance (PTIR), setup is similar to an AFM setup, with the addition of a pulsed tunable IR laser source. This pulsed IR laser is commonly either an optical parametric oscillator (OPO), or a quantum cascade laser (QCL), the latter being the type used in the experiments further described in this thesis. When comparing the two types of laser, the main advantages of OPOs are their high output power and broad tuning range.⁵⁶ On the other hand, QCLs offer tunable repetition rates and pulse lengths, as well as a faster wavelength tuning ($>100 \text{ cm}^{-1}\text{s}^{-1}$ compared to approximately $3 \text{ cm}^{-1}\text{s}^{-1}$ for external cavity OPOs). Regardless of the IR laser source used, the beam is focused on to the area of the sample underneath the AFM tip. During a measurement for a full spectrum at a certain location, the IR laser operates in pulse mode and sweeps across its wavelength range, but it is also possible to scan a whole area for absorption at a designated wavenumber and obtain an image. When the conditions for IR radiation absorption described in section 1.1.1 are met (energy of an infrared photon matches the difference in energy between two molecular vibration energy levels and there is a change in μ), some of the laser light is absorbed and the molecules move to an excited vibrational state. As the absorbed photons return to their ground vibrational state, some of the energy is dissipated in the lattice through heat transfer. This increase in temperature is in turn dissipated as mechanical expansion.^{57,58} The sample quickly expands during the laser pulse, which is followed by a slower exponential relaxation during the off phase of the laser cycle.⁵⁹ Most cantilevers cannot directly detect these phenomena, because their response time is too slow compared to that of the sample's expansion and contraction. Nonetheless, the fast changes in the sample kick the cantilever into oscillation, which can be detected in the deflection signal.⁶⁰ AFM-IR is thus a type of indirect spectroscopy, since it detects the expansion as a consequence of thermal changes in the medium caused by the optical absorption of radiation, and not the changes to the radiation itself (such as absorption or dispersion) as in direct spectroscopy.⁶ Regardless of the spot size of the IR laser, only the portion of the sample directly below the tip contributes to the AFM-IR signal,⁶¹ thus enabling lateral resolutions as small as 10 nm.⁶² The expansion detected during AFM-IR measurements is in the nanometer scale and the sample quickly relaxes back to its original state in a matter of nanoseconds (dependent on sample properties such as thickness and thermal conductivity) during the time in between laser pulses.⁵⁹ Like in classical IR transmission spectroscopy, the signal obtained in AFM-IR is proportional to the wavelength-dependent absorption coefficient, allowing for direct comparison of the spectra obtained from both techniques, and access to the long established spectra-structure correlations and databases available for FTIR spectroscopy.⁵⁷

1.3.1 AFM-IR Signal

A theoretical description of the AFM-IR signal has been developed by Dazzi *et al.*⁵⁷ which will be presented here in the notation of Ramer *et al.*⁶³ For a more thorough understanding of the theory behind AFM-IR signal transduction, the reader is advised to consult these publications.

The intensity of the AFM-IR signal, S_{AFM-IR} is proportional to the contributions of the different steps in the transduction chain multiplied by each other:

$$S_{AFM-IR} \propto H_{AFM} H_m H_{th} H_{opt}(\lambda) I_{inc}(\lambda) \quad (1.14)$$

Of the five factors, two are wavelength dependent ($H_{opt}(\lambda)$ and $I_{inc}(\lambda)$), whereas the remaining three are wavelength independent (H_{AFM} , H_m , H_{th}). Of the wavelength independent factors, H_{AFM} is the contribution of the cantilever and is proportional to its properties such as resonance frequencies, shape, modal stiffness, tip-sample interactions and deflection sensitivity. H_m is the mechanical contribution and accounts for the influence of the sample's thermal expansion coefficient, sample thickness, and tip-sample contact stiffness. H_{th} is the thermal contribution and is proportional to the sample's temperature during the measurement, as determined by the laser pulse length and thermal properties of the sample. The wavelength dependent factors include the laser incident power, $I_{inc}(\lambda)$ at the wavelength λ , which is measured in the separately acquired background spectrum. Finally, the optical contribution, $H_{opt}(\lambda)$ is defined as its absorptance (the fraction of incident light absorbed by the sample),⁵ which is the only term to include the complex refractive index of the sample, $\hat{n}(\lambda)$ (Eq. 1.15), the refractive index of the substrate, as well as the polarization and angle of the incident IR laser beam. The complex refractive index of a material $\hat{n}(\lambda)$ describes the interaction of light and an absorbing medium, and is defined as:

$$\hat{n}(\lambda) = n(\lambda) + ik(\lambda) \quad (1.15)$$

where $k(\lambda)$ is the index of absorption (imaginary part) and $n(\lambda)$, the real part, is the index of refraction. $k(\lambda)$ is proportional to the attenuation of light, and consequently, to the absorption coefficient, $\alpha(\lambda)$ through the following relation:

$$\alpha(\lambda) = \frac{4\pi k(\lambda)}{\lambda} \quad (1.16)$$

The contribution of the real part of the complex refractive index, $n(\lambda)$ is negligible for sample thicknesses up to 500 nm, meaning that in these cases, the AFM-IR signal is directly proportional to the index of absorption $k(\lambda)$.⁶³ In the case of thicker samples (> 500 nm) and/or samples with a high absorption coefficient, increasing peak shifts akin to those present in ATR spectroscopy are present, demonstrating the effect of anomalous dispersion.⁶³ Thus, the AFM-IR signal is directly proportional to the absorbance through the absorption coefficient,⁶³ and comparable to standard absorption spectroscopies.

Therefore, the term $H_{opt}(\lambda)$ alone is responsible for the form of the AFM-IR spectra, with the remaining wavelength-independent terms contributing solely as scaling factors. Due to the dependence of the $H_{AFM}H_mH_{th}$ on the mechanical and thermal properties of the sample and on the cantilever used, the quantitative analysis of samples, particularly heterogeneous samples, is challenging. This can be partly circumvented by the use of band ratios, which cancel out the contribution of the scaling factors.^{64,65}

1.3.2 Illumination Geometries

AFM-IR instruments can have two types of optical configurations: top or bottom illumination. This refers to the placement of the IR laser relative to the sample and cantilever. Bottom illumination configurations take advantage of attenuated total reflection (ATR) to measure the sample, which is placed on top of a prism made of an IR-transparent material (most commonly ZnSe), or on top of a thin slide of an IR transparent material, which is in turn placed on top of the IR prism (Figure 1.9). The IR laser is then focused on to the IR prism, so that total internal reflection occurs at the face of

the prism where the sample is placed. For total internal reflection of a light beam at the interface between a material with high refractive index n_1 (the IR prism) and a material with low refractive index n_2 (air or sample) to occur, the angle of incidence has to be larger than the critical angle, $\theta_{critical}$ which is defined as:

$$\theta_{critical} = \arcsin\left(\frac{n_2}{n_1}\right) \quad (1.17)$$

In this case, only an evanescent wave passes the interface into the lower refractive index material, whose intensity decays exponentially as the distance to the interface increases. The distance at which the intensity of the evanescent wave is $1/e$ of its intensity at the interface is called the depth of penetration, d_p .

$$d_p = \frac{\lambda}{2\pi n_1 \sqrt{\sin^2 \theta - \left(\frac{n_2}{n_1}\right)^2}} \quad (1.18)$$

The d_p corresponds to the distance over which the evanescent wave is considered to be capable of effectively interacting with the lower refractive index material,² and it is usually of the order of magnitude of the wavelength of the radiation being used (wavelength dependent). For radiation in the mid-IR this would mean the d_p is on the order of several micrometres, however, due to the loss of linearity of the AFM-IR signal for samples thicknesses above 500 nm,⁶³ samples are usually kept below this threshold. This short depth of penetration of the evanescent wave allows for the use of a large range of cantilevers with mid-IR absorbing materials (such as silicon and silicon nitride), and also for measurements in liquid, due to the reduced background contribution of the environment (e.g. water) to the AFM-IR signal.⁶⁶

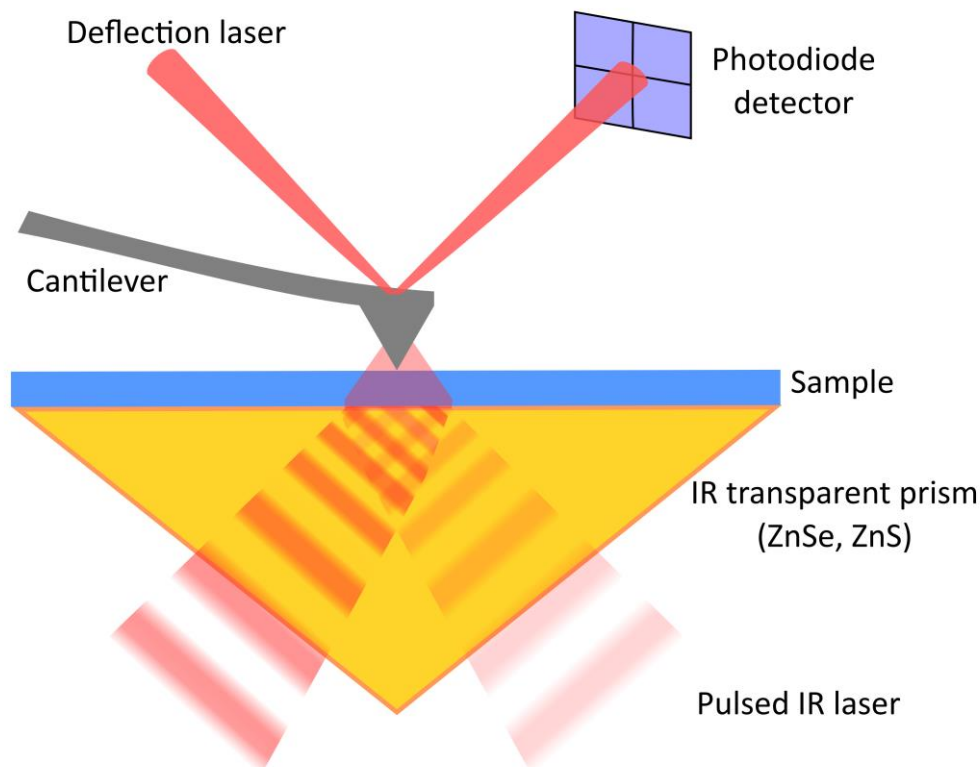


Figure 1.9: Schematic representation of an AFM-IR setup with a bottom illumination configuration. Sourced under the terms of CC BY 4.0 license from ref.⁶⁷ (Publication IV).

Alternatively, measurements can also be conducted using top illumination (Figure 1.10), where the pulsed IR laser beam comes from above the sample. In this configuration there is no need for an internal reflection element (the IR-transparent prism), which allows for more flexibility in the choice of substrates and thus of sample preparation protocols. In addition to mid IR-transparent materials such as ZnSe, ZnS, and CaF₂, other substrates such as silicon and gold-coated substrates (silicon, mica) can also be used.⁶⁸ Moreover, there is no limitation on the depth of penetration of the IR laser beam, which is no longer an evanescent wave when in contact with the sample. Since the cantilever is now directly in the path of the IR beam, it must be coated in metal (typically gold) to avoid interference with the AFM-IR signal from the sample due to absorption of light by the cantilever. The use of gold-coated cantilevers or substrates separately, or in combination allows for near field electromagnetic enhancements of the optical field intensity (“lightning rod” effect) to take place, which lead to AFM-IR signal enhancements of up to 8-fold.^{61,69} However, the signal enhancement obtained when using a reflective gold-coated substrate is wavelength-dependent, and can thus lead to artifacts due to optical interference between the incident and reflected light, which become more pronounced with increased sample thickness in the range between 90 nm and 3000 nm.⁷⁰

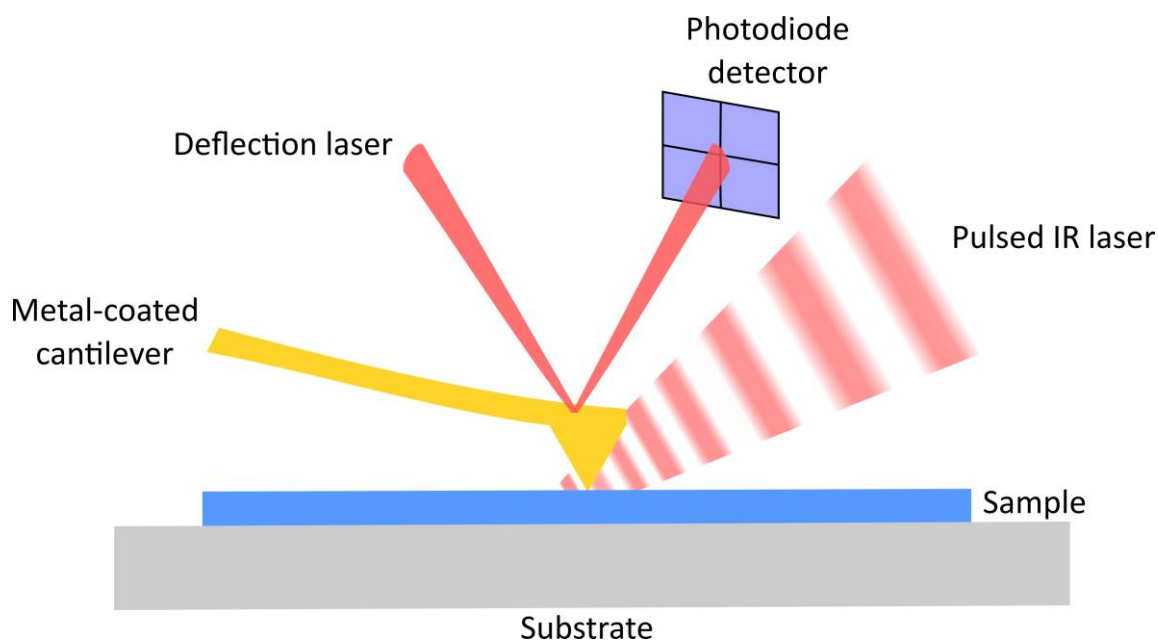


Figure 1.10: Schematic representation of an AFM-IR setup with a top illumination configuration. The substrate can now be either IR-transparent (ZnSe, ZnS, CaF₂) or IR-opaque (gold-coated substrates, silicon). Sourced under the terms of CC BY 4.0 license from ref.⁶⁷ (Publication IV).

1.3.3 Contact Mode AFM-IR

The first implementation of AFM-IR was in contact mode, with bottom illumination and signal detection through the cantilever ringdown.⁵³ In this type of measurement, laser pulse durations can be anywhere from 0.1 ns to 500 ns, although the most common laser type used are OPOs, with characteristically short pulse lengths of < 10 ns.⁷¹ Several of the cantilever modes are excited, and the amplitudes of the cantilever oscillation induced by the expansion is directly proportional to the wavelength-dependent absorption coefficient of the sample,⁵⁷ which allows for the direct obtention of infrared spectra at the nanoscale. Despite the mechanical expansion quickly relaxing back in a matter of nanoseconds, the oscillation of the cantilever takes longer to subside

(> 500 μs),⁵⁹ and the amplitude decrease over time produces the “ringdown” pattern that gives the name to this type of AFM-IR measurement (Figure 1.11). Ringdown measurements have reached lateral resolutions down to $\approx 20\text{ nm}$ ⁷¹ and $>1\ \mu\text{m}$ of probe depth.⁷²

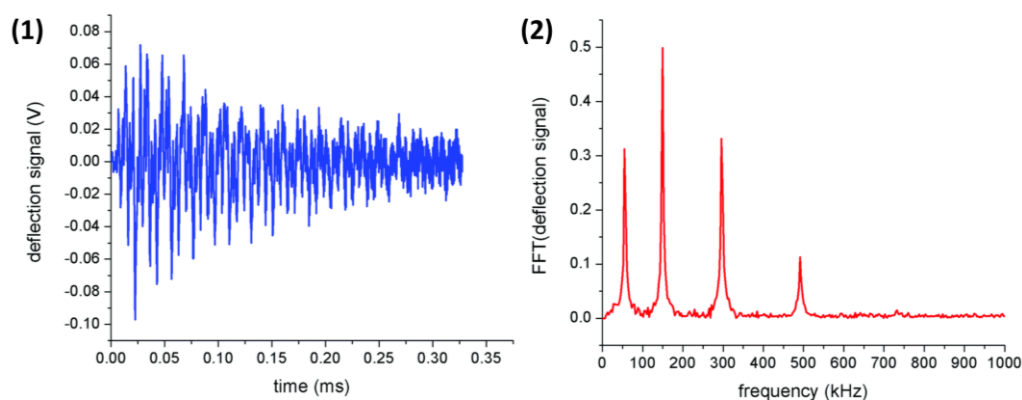


Figure 1.11: Time domain (1) and frequency domain (2) of a typical AFM-IR ringdown measurement, showing the characteristic ringdown pattern (1) and the simultaneous excitation of all the cantilever’s mechanical resonance modes (2). Adapted from Kurouski, D.; Dazzi, A.; Zenobi, R.; Centrone, A. Infrared and Raman Chemical Imaging and Spectroscopy at the Nanoscale. *Chem. Soc. Rev.* **2020**, *49* (11), 3315–3347 with permission from the Royal Society of Chemistry.⁷³

1.3.3.1 Resonance-enhanced contact mode AFM-IR

In 2011, Lu and Belkin reported a new type of contact mode measurement that has since been called resonance-enhanced contact mode AFM-IR.⁷⁴ This mode offers superior SNR and spatial resolution, and lower acquisition times when compared to ringdown measurements. In resonance-enhanced AFM-IR, the pulse rate of the IR laser is tuned to match one of the cantilever’s free resonance frequencies. This is possible through the use of QCLs as the laser source, which can reach the high laser repetition rates required (a typical contact mode cantilever such as the ContGB-G model from Budget Sensors will have several contact resonance frequencies around for example 60 kHz, 200 kHz, 300 kHz, 500 kHz, 800 kHz, and even further). When the thermal expansion due to absorbance of the IR laser occurs at a mechanical resonance of the cantilever, the kinetic energy transferred by the expanding sample will be stored exclusively in the corresponding mechanical resonance mode (Figure 1.12), instead of resulting in the simultaneous excitation of all the resonance modes (ringdown measurements). The continuous excitation of the cantilever at its resonance frequency leads to a storage of the oscillation energy between pulses, keeping the cantilever in a continuous wave oscillation while in contact mode. This amplifies the deflection amplitude proportional to the Q -factor of the resonance mode being excited, which for commercially available cantilevers corresponds to up to a 100-fold increase of the deflection amplitude.⁶¹ The AFM-IR signal itself is amplified by a factor of $Q/2\pi$.⁵⁵ It is possible to use any of the cantilever’s resonance modes for the signal enhancement: the higher the frequency of the chosen mode, the higher the achievable spatial resolution.⁷⁵

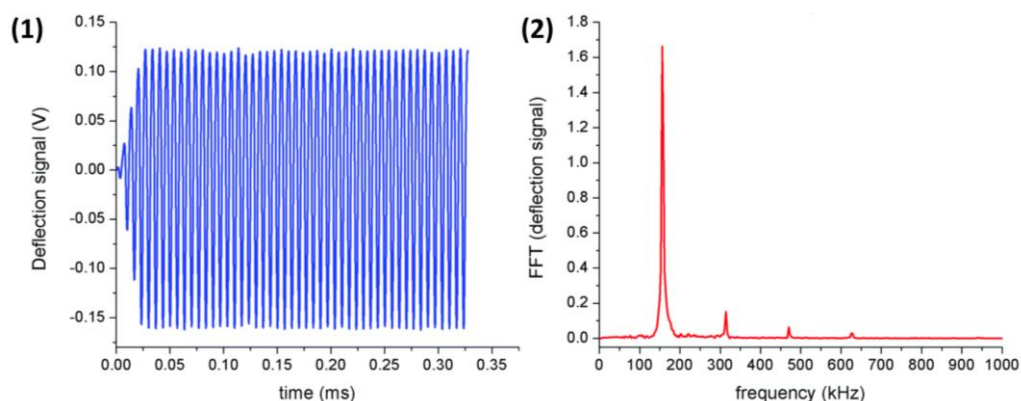


Figure 1.12: Time domain (1) and frequency domain (2) of a typical resonance-enhanced AFM-IR measurement, showing the preferential excitation of only one of the cantilever's mechanical resonance modes (2). Adapted from Kuroski, D.; Dazzi, A.; Zenobi, R.; Centrone, A. Infrared and Raman Chemical Imaging and Spectroscopy at the Nanoscale. *Chem. Soc. Rev.* **2020**, *49* (11), 3315–3347 with permission from the Royal Society of Chemistry.⁷³

Resonance-enhanced measurements require additional care to ensure that the pulse rate matches the cantilever's resonance frequency throughout the measurement: if this does not happen, then there will be a signal decrease due to the mismatch, and not due to a reduction in the thermal expansion. As the contact resonance frequencies are influenced by the mechanical properties of the sample, heterogeneous samples will easily lead to significant resonance peak shifts, particularly during imaging. In general, softer materials will lead to a resonance peak shift to lower values, whereas harder materials will lead to shifts to higher frequencies.⁷⁶ This problem can be tackled in three different ways:

- By measuring off resonance, which negates the resonance-enhancement.⁷⁷
- By chirping the laser pulse repetition rate within an estimated range around the resonance peak and picking the frequency with the maximum amplitude (resonance frequency),⁷⁶ which sacrifices some of the improved sensitivity.
- By implementing a phase locked loop (PLL), which tracks the changes in phase angle instead of the amplitude (Figure 1.13). In the beginning of each measurement, the user defines a setpoint corresponding to the phase angle at the contact resonance in that location and a frequency range in which the variation is expected to occur. The PLL will then use a PID to track the changes to the phase angle and make the necessary adjustments to the laser pulse rate to ensure constant resonant excitation.

Resonance-enhanced AFM-IR can reach down to ≈ 20 nm of lateral resolution,⁶¹ at least >430 nm of probe depth,⁷⁸ and monolayer sensitivity when using gold coated cantilevers and substrates.⁶¹ Some examples of areas of application include the life sciences,^{79–82} polymer science,^{83–85} material science,^{86,87} and geology,^{88,89} to name a few.

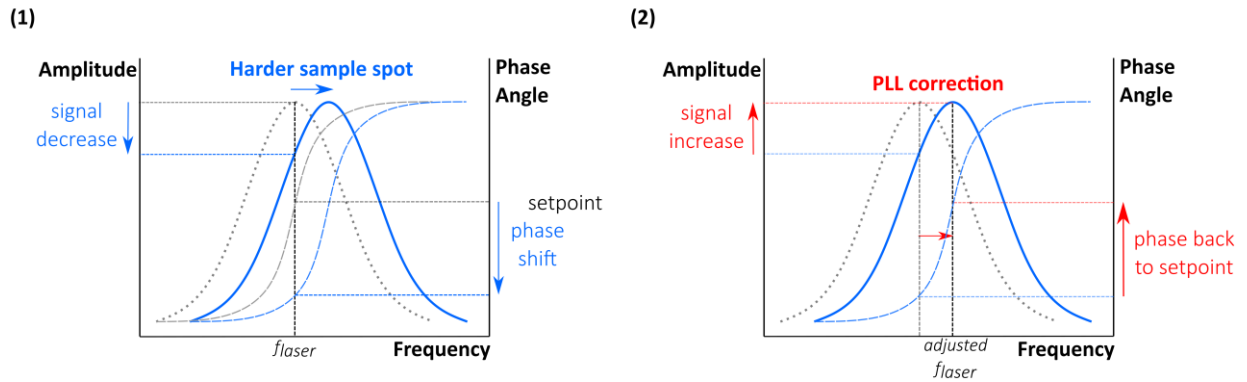


Figure 1.13: (1) Effect of scanning a harder spot of a heterogeneous sample on the contact resonance frequency of the cantilever. At the beginning of the measurement the laser frequency was set to f_{laser} , but due to the shift of the resonance frequency to higher numbers, part of the signal enhancement is lost, leading to imaging artifacts. (2) The PLL tracks the changes in the resonance frequency in real-time and makes the necessary adjustments to ensure the laser pulse rate matches the cantilever resonance frequency.

1.3.4 Tapping mode AFM-IR

Tapping mode AFM-IR (Figure 1.14) was first described in 2018 by Tuteja *et al.*⁹⁰ In this measurement mode, as in tapping mode AFM, the cantilever is oscillating at one of its mechanical resonance frequencies, and is in contact with the sample intermittently (see section 1.2.2). The AFM-IR signal is detected through a heterodyne detection scheme where the cantilever is oscillated at e.g., its first resonance frequency, f_1 and the signal is demodulated at the second resonance frequency, f_2 through the use of a lock-in amplifier. A lock-in amplifier takes the measured signal (input), which consists of several frequency components, and outputs only the signal at the desired frequency. It achieves this by multiplying the input signal by a reference sine wave at a reference frequency (in this case, this frequency is provided by the laser trigger) and applying a low pass filter to the result.⁹¹ The lock-in amplifier can also provide the amplitude of the signal at the reference frequency and the phase of the signal relative to the phase of the reference signal, which can be used for the implementation of PLLs. The cantilever can also be driven at the second resonance frequency, with the signal detection taking place at the first resonance frequency, which produces higher quality spectra,⁹² but can be prone to signal instability. The laser repetition rate, f_L is set to $f_2 - f_1$, so that the sum of the laser repetition rate and the oscillation rate of the cantilever correspond to another of the cantilever's mechanical resonance frequencies. Depending on the cantilever used the f_L will usually be between 250 kHz and 1500 kHz,^{62,64} thus requiring the use of a laser type with tunable repetition rate, in addition to wavelength tunability, such as QCL. Tapping mode AFM-IR takes advantage of the non-linear interactions that occur during a measurement when there is IR radiation absorption: the oscillation corresponding to the cantilever tapping (e.g. first mode) and the oscillation provoked by the thermal expansion mix and generate amplitude signal changes at a frequency that also corresponds to a resonance mode (e.g second mode), which results in signal amplification.⁹³ This effect can be seen by first considering the position of the tip, z as it varies in time during a tapping mode AFM-IR measurement, which is described by:

$$z(t) = X_{tip} \cos(2\pi f_{tap} t) + X_{IR} \cos(2\pi f_{IR} t) \quad (1.19)$$

where X is the amplitude due to either the tapping drive or the IR absorption, f_{tap} is the frequency at which the cantilever is tapping, and f_{IR} is the frequency of the IR laser pulse. The force between the tip and the sample during the oscillation cycle can be approximated using a Taylor expansion:

$$F_{ts}(z) = a_0 + a_1\Delta z + a_2\Delta z^2 + \dots \quad (1.20)$$

where a_i are Taylor coefficients $\frac{F_{ts}^{(i)}(z_0)}{i!}$, z_0 the tip-sample distance around which the tapping tip moves, and $\Delta z = z - z_0$, which corresponds to:

$$\Delta z = X_{tip} \cos(2\pi f_{tap}t) + X_{IR} \cos(2\pi f_{IR}t) \quad (1.21)$$

The term $a_2\Delta z^2$ in Eq. 1.20 is the lowest order term that permits mixing and hence, only this term will be considered. By inserting Eq. 1.21 into this term the following is obtained:

$$a_2 [X_{tip} \cos(2\pi f_{tap}t) + X_{IR} \cos(2\pi f_{IR}t)]^2 \quad (1.22)$$

which in turn can be expanded to:

$$a_2 [X_{tip}^2 [\cos(2\pi f_{tap}t)]^2 + 2X_{tip}X_{IR} \cos(2\pi f_{tap}t) \cos(2\pi f_{IR}t) + X_{IR}^2 [\cos(2\pi f_{IR}t)]^2] \quad (1.23)$$

and using $\cos(\alpha) \cos(\beta) = \frac{1}{2} (\cos(\alpha - \beta) + \cos(\alpha + \beta))$ the term highlighted in orange can be rewritten as:

$$X_{tip}X_{IR} [\cos(2\pi f_{tap}t + 2\pi f_{IR}t) + \cos(2\pi f_{tap}t - 2\pi f_{IR}t)] \quad (1.24)$$

leading to additional oscillations at the sum and difference frequencies $f_{tap} + f_{IR}$ and $f_{tap} - f_{IR}$, i.e. mixing the two frequencies. To detect either of these additional oscillations in the tip-sample force in tapping mode AFM-IR the laser pulse frequency is chosen so that $f_{tap} + f_{IR}$ or $f_{tap} - f_{IR}$ coincides with a mechanical resonance frequency of the cantilever, thus resulting in signal enhancement (Figure 1.14).

The demodulated cantilever oscillation amplitude, Z detected at the second mode contains information on the sample's thermal expansion due to the IR radiation absorption. This relation is presented in the expression below, which was developed by Mathurin *et al.*,⁹³ and is presented here as an adaptation of the simplified form of Schwartz *et al.*:⁵⁴

$$Z \propto \chi_s \frac{f_{demod} - f_{tap}}{f_{demod}^2} f_{tap} Q_{demod} H_{opt}(\lambda) I_{inc}(\lambda) \quad (1.25)$$

where χ_s is the non-linear material elasticity, and f_{demod} is the frequency at which the signal is detected. Q_{demod} is the Q -factor of the mode at which the signal is detected, and most importantly, $H_{opt}(\lambda)$ is the IR absorptance, and $I_{inc}(\lambda)$ is the laser incident power, at the wavelength λ . Thus, harder cantilevers with higher resonance frequencies will produce higher tapping mode AFM-IR signals.

Tapping mode AFM-IR can reach down to ≈ 10 nm of lateral resolution⁶² (due to the reduced interaction time between the tip and the sample),⁵⁴ and 50 nm of probe depth (an effect of the superficiality of the non-linear mixing interactions).⁵⁵ This mode inherits all the advantages of tapping mode AFM when it comes to the measurement of soft, easily damageable, rough, or loosely adhered samples and allows for the extension of the possible applications of AFM-IR. It has been applied to the analysis of drug-loaded nanoparticles,^{62,94} oil paint,^{92,95} bitumen,⁹⁶ as well as to polymer samples,^{64,97} which will be discussed further along in this thesis. Furthermore, since the resonance frequency of the cantilever has a lower susceptibility to changes in the sample's

mechanical properties,⁹³ tapping mode AFM-IR does not require frequency tracking as is the case for resonance-enhanced AFM-IR, although it can benefit from it in extreme cases. The reduced tip-sample interaction and subsequent benefits do come at the cost of requiring a higher IR laser power, which must be handled carefully, so as not to cause thermal damage to the sample.

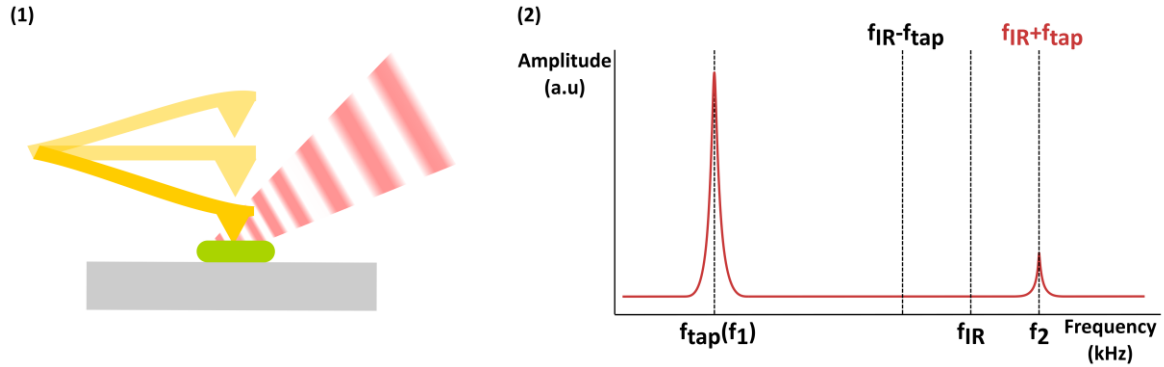


Figure 1.14: (1) Schematic representation of tapping mode AFM-IR with a top illumination configuration. (2) Frequency domain of a tapping mode AFM-IR heterodyne detection. In the case depicted the cantilever is driven at its first resonance frequency, $f_1 = f_{\text{tap}}$ and signal detection takes place at the second resonance frequency, f_2 . The f_{IR} is calculated as the difference between f_2 and f_1 .

1.4 Fluorescence Microscopy

Fluorescence microscopy is a type of optical microscopy technique characterized by the use of fluorophores to obtain high contrast (in most cases only the fluorophore is responsible for the signal, everything else is part of the background) and sensitivity. The wide range of fluorophores available with varying absorption and emission spectra, as well as possibility of selective targeting within cells, make this technique one of the most widely used microscopy techniques in cell and molecular biology. As a type of optical microscopy, fluorescence microscopy is diffraction-limited to a resolution dependent on the wavelengths used, which is typically around 200 nm.⁹⁸ However, several techniques have been developed that make use of fluorophores and are capable of obtaining better resolutions, such as confocal microscopy. More recent techniques, called super-resolution fluorescence microscopies, are based on fluorescence microscopy but circumvent the diffraction limit, such as stimulated emission depletion microscopy (STED), structured illumination microscopy (SIM), stochastic optical reconstruction microscopy (STORM), among others. These techniques will not be described in this thesis, however, the following review on the subject is suggested to the interested reader.⁹⁹

The following paragraph is based on a publication by Lichtman and Conchello,¹⁰⁰ as well as book chapter by Dobrucki and Kubitscheck.¹⁰¹ To understand the phenomenon of fluorescence one must first look at the energy levels electrons can occupy in a molecule, commonly depicted in a Jablonski diagram. There are three types of energy: electronic, vibrational, and rotation levels. Each electronic level has multiple vibrational levels, which in turn have multiple rotational levels, as depicted in Figure 1.15. Fluorophores are molecules that after absorbing a photon of a certain frequency emit a photon of a lower frequency than the one absorbed (red-shift). For absorption to occur the incoming photon must have an energy which at least the energy difference between the ground state and the first excited electronic level. In cases where the photon energy is above this required level, the photon will still be absorbed, and the electron in question will transition to one of the higher vibrational levels of the S_1 , or to one of the higher electronic levels. The range of wavelengths that can lead to excitation of a fluorophore is called the excitation spectra. Excitation spectra have a sharp cutoff on its lower end, corresponding to the minimum energy required to transition from S_0 to S_1 , but a gentler slope on the lower wavelengths. Once a photon with appropriate energy is absorbed, an electron transitions to an excited state. As stated above, this is often a transition not only to a higher electronic state, but also to a higher vibrational state. The absorption of a photon with these characteristics thus leads to molecular vibrations with changes in internuclear distances. The vibrational energy is lost rapidly in collisions with solvent molecules, or with other molecules, resulting in vibrational relaxation, a non-radiative process that brings the energy of the electron to the lowest vibrational state of the excited electronic state in which it is found. In fluorescence, the excited electron will return to the ground state through the emission of a photon with energy that corresponds to the difference between S_1 and S_0 . This photon has less energy than the corresponding absorbed photon, which is key of fluorescence microscopy's sensitivity. The whole cycle described above of excitation, non-radiative relaxation and photon emission takes places in a nanosecond time range.

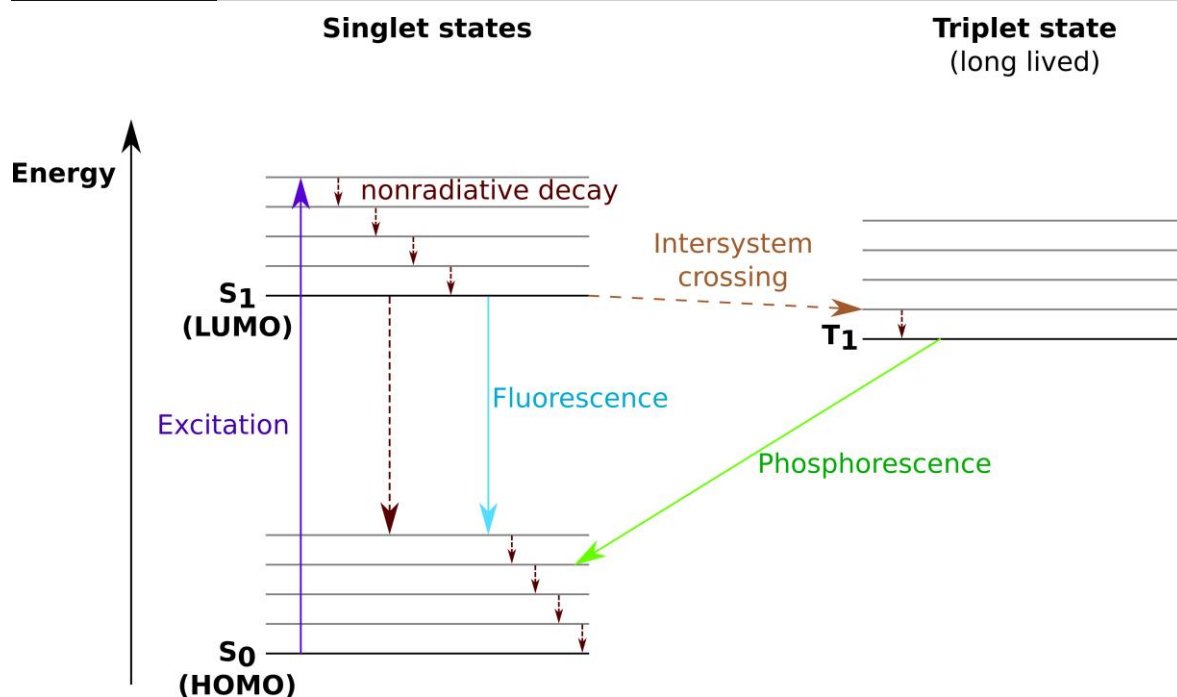


Figure 1.15: Jablonski diagram of the fluorescence process. Electronic levels (singlet and triplet) are displayed as black horizontal lines, vibrational levels as grey horizontal lines. Non-radiative processes are shown as dashed arrows and radiative processes as full arrows. In both fluorescence and phosphorescence, a photon of lower energy than the excitation photon is emitted, the difference between the two being the amount of time spent in the excited state (S_1 or T_1). HOMO stands for highest occupied molecular orbital and LUMO for lowest unoccupied molecular orbital.

The emission spectrum of a fluorophore is, however, not limited to one single wavelength. The shape of an emission spectrum has a sharper cutoff at lower wavelengths (corresponding to the drop from the lowest vibrational state of S_1 to S_0 , see Figure 1.16), and a smoother drop at higher wavelengths (corresponding, for example, to transitions from higher vibrational states to the ground state, or even from higher electronic states S_2 or higher, see Figure 1.16). The gap between the peak of the excitation and emission spectra is called the Stokes shift. A larger Stokes shift has the advantage of allowing for a better separation between incoming (excitation) and outgoing (emission) photons by the microscope's filters. Fluorescence is not the only process through which an excited electron can return to the ground state, but it should be the preferred one in fluorophores. Other relaxation paths are intersystem crossing and non-radiate decay. In intersystem crossing, the excited electron changes its spin during the excitation, and is thus found in a triplet state, with a lower energy than the excited state, S_1 . Returning to the ground state means once again changing the spin. Since both these transitions are spin-forbidden, the probability of two of them happening to the same electron is rather low, and triplet states are long lived (microsecond range), contributing to a smaller population of fluorophore molecules in the ground state. Additionally, triplet states can be more chemically reactive, contributing to bleaching and potential cell toxicity. Triplet states can relax back to the ground state via phosphorescence, a phenomenon similar to fluorescence, but that occurs over a much longer time scale, or through non-radiative decay.

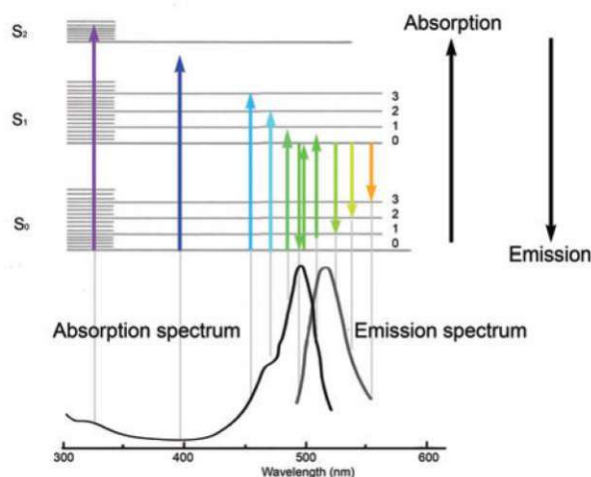


Figure 1.16: Absorption and emission spectra of FITC (fluorescein-5-isothiocyanate) with the corresponding electronic transitions responsible for them. Arrow colour gradient corresponds to the energy of the photon involved. Adapted with permission from Springer Nature, Nature Publishing group, Nature methods, Fluorescence Microscopy, Lichtman, J. W.; Conchello, J.-A. ©Nature Publishing Group (2005).

Fluorophores can be relatively small organic molecules, such as fluorescein, but also larger biomolecules, such as proteins. The latter one has the huge advantage when studying cellular systems of allowing for studies where target genes can be tagged with the sequence belonging to a fluorescent protein, thus allowing for highly specific monitoring of protein expression and location within the cell.¹⁰² The most prominent example of such protein is the green fluorescent protein (GFP), whose discovery and development was the subject of the 2008 Nobel Prize in Chemistry. Since then, many other fluorescent proteins have been discovered and optimized through protein-engineering,¹⁰³ such as in the case of the enhanced green fluorescent protein (EGFP).¹⁰⁴ Fluorophores typically have conjugated π systems (double or triple bonds) that absorb in the UV or visible area due to the relatively small energy gap between the π (ground state, the HOMO orbital) and the π^* (LUMO) orbitals characteristic of such systems.¹⁰⁵

An important indicator of fluorophore performance is the quantum yield, ϕ defined as the ratio between the number of photons emitted and the number of photons absorbed.¹⁰⁶ A high quantum yield means that fluorescence is the dominant relaxation process, whereas a low quantum yield can be indicative of the predominance of non-radiative processes. When using lasers or other high intensity light sources, the quantum yield alone can be used to measure the maximum intensity that a fluorophore can achieve.¹⁰⁰ However, for non-laser excitation light sources, the molar decadic absorption coefficient ϵ , a measure of how efficiently a sample absorbs light at a given wavenumber, also plays an important role in the maximum intensity that a fluorophore can achieve.¹⁰⁰

1.4.1 Epifluorescence Microscopes

A fluorescence microscope has all the components of a conventional optical microscope with the addition of an excitation source, emission and excitation filters, and often a dichroic mirror. The arrangement of the components has historically evolved,¹⁰⁷ and nowadays the most common one is the epifluorescence microscope. In an epifluorescence microscope (Figure 1.17), the exciting light and the emitted light travel through the same optical path. This type of arrangement reduces the amount of excitation light reaching the emission filter, because only the excitation photons that are reflected by the sample (a small fraction of the total amount) travel in the same direction (inside of

the microscope) as the emitted fluorescence photons (emitted in every direction).¹⁰⁰ The key element of an epifluorescence microscope is the dichroic mirror, which reflects certain wavelengths (excitation light) and transmits others (emitted light). Additionally, an excitation filter that selects only the part of the light coming from the excitation source which corresponds to the fluorophore's excitation spectra, and an emission filter which only lets through wavelengths corresponding to the fluorophore's emission spectra.¹⁰⁸ These three elements are often combined in a filter cube, which is a replaceable part of the microscope optimized for a particular fluorophore.

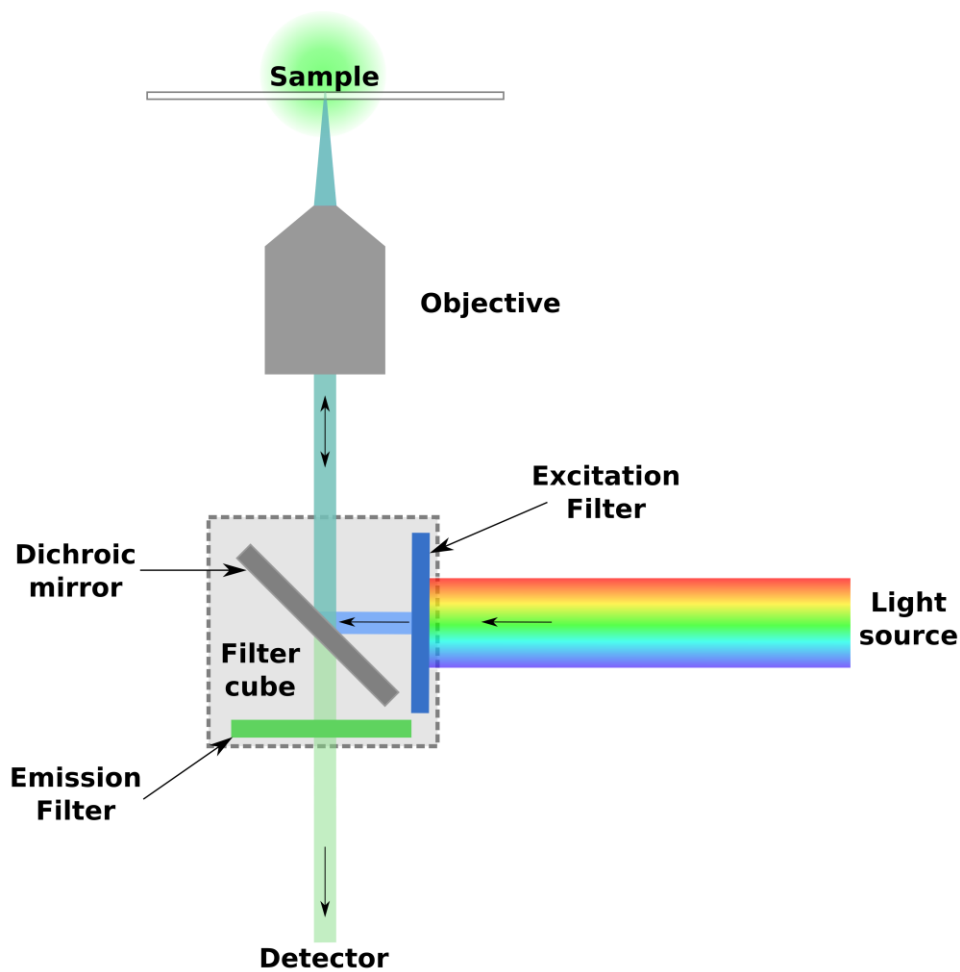


Figure 1.17: Light path in an epifluorescence microscope. Light emitted by the light source passes through the excitation filter which selects the correct wavelength for fluorophore excitation. Exciting light is then reflected by the dichroic mirror towards the sample. Emitted light by the sample then travels in the opposite direction and is transmitted by the same dichroic mirror, finally passing through the emission filter and reaching the detector.

1.5 Chemometric Models and Data Processing

Chemometrics is defined by the journal *Chemometrics and Intelligent Laboratory Systems* (Elsevier) as “the chemical discipline that uses mathematical and statistical methods to design or select optimal procedures and experiments, and to provide maximum chemical information by analyzing chemical data”. Chemometrics is often used to facilitate the extraction of information from large datasets, where it can help to reveal trends otherwise hidden to the “human eye”. For instance, a single AFM-IR spectrum contains around 1000 wavenumbers, as well as the signal intensity for each of them. Additionally, spectra can be collected in different locations, which adds to the complexity of the dataset. In the case of chemical images collected at a resolution of, for example, 200 x 200 points at a several wavenumbers, the total number of data points can easily reach hundreds of thousands. In such cases, the field of chemometrics known as multivariate analysis is particularly useful, almost mandatory. Virtually all the multivariate analysis relies on computers using machine learning to build models that fit the data. There are two important classes of machine learning methods: unsupervised and supervised. Unsupervised machine learning uses unlabeled (without extra input by the user) raw data to generate a model whose goal is to find patterns or structures in the dataset, which can then be interpreted by the user. Some examples of unsupervised machine learning methods include clustering (hierarchical cluster analysis, k-means clusters, among others), and dimensionality reduction algorithms (principal component analysis, factor analysis, independent component analysis).¹⁰⁹ Supervised machine learning on the other hand, requires the input of labels in addition to the raw data, which can have discrete or continuous values. The models that result from this type of machine learning have a predictive value, that is, they can be applied to data previously unseen by the model, which will make a prediction about which class each new point belongs to (in the case of discrete variables). Examples of supervised machine learning methods include k-nearest neighbor, linear discriminant analysis (LDA), and support vector machines (SVM).¹⁰⁹

1.5.1 Hierarchical Cluster Analysis (HCA)

HCA is a type of cluster analysis, which in turn is a type of unsupervised machine learning. In any type of cluster analysis, the algorithm, divides the dataset into a number of classes (defined by the user) which contain objects judged to be similar. Hierarchical means that once a point has been assigned to a cluster it will not be reassigned in further iterations.¹¹⁰ Similarity is measured by the distance between each data point in an n -dimensional space (n being the number of dimensions), with short distances meaning higher similarity. Distance can be measured in several ways such as Euclidean, Manhattan, Hamming, and Mahalanobis distance. The most commonly used distance measure is the Euclidean distance, which is defined as:

$$d = \sqrt{(a_1 - b_1)^2 + (a_2 - b_2)^2 + \dots + (a_n - b_n)^2} \quad (1.26)$$

where d is the distance between two points, a and b , in an n -dimensional space with coordinates (x_1, x_2, \dots, x_n) , $x = a, b$. Euclidean distance (as well as Manhattan and Hamming) is strongly affected by data scaling, and thus requires corrective data scaling (e.g. normalization) before application.^{111,112} Furthermore, correlations between the variables can also lead to distortions of the calculated distances and consequently of the obtained final clusters.¹¹² In datasets where this is an issue, the Mahalanobis distance can be used instead, which accounts for these characteristics. For data that has been properly corrected for outliers and correlation, both distances will give the

same result.¹¹²

In addition to the distance measure, the linkage method is another adjustable parameter of HCA, which defines the criterion according to which the datapoints, and later on the different clusters, will be joined into larger clusters (until the number of clusters defined by the user has been reached). Examples of linkage methods include single linkage, centroid linkage, average linkage, and Ward's method.¹¹⁰ In the beginning of the clustering process, all datapoints are considered to be an individual cluster. Once the distance is calculated, two clusters will then be merged according to the linkage method and be considered as one in the next iteration. This is called an agglomerative approach, as opposed to the divisive approach which begins with one single cluster containing all the data points and then breaks it down.¹¹⁰ In single linkage, clusters are joined according to the closest minimum distance. Ward's method, also called the minimum variance method, merges clusters with the lowest error sum of square values (ESS), which is the sum of the squared deviations of each object in a cluster to the cluster centroid. The resulting new cluster is that which leads to the smallest possible increment of variance within itself.¹¹³ The distances between the objects and corresponding clusters can be visualized in a dendrogram (Figure 1.18).

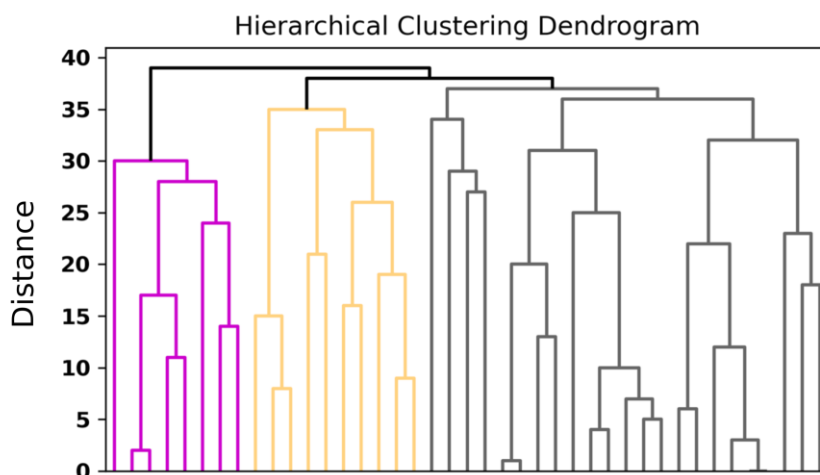


Figure 1.18: Dendrogram obtained in a hierarchical cluster analysis of AFM-IR spectra taken in grid format. The y axis represents the calculated distance between two points and the horizontal lines the distance at which the two were joined into the same cluster.

1.5.2 Principal Component Analysis (PCA)

PCA is a type of unsupervised algorithm where the data matrix, D is decomposed into two matrices of a lower dimensionality: the loadings matrix and the scores matrix, according to

$$D = TL^T + E \quad (1.27)$$

where T is the scores matrix, L is the loadings matrix, and E is the error matrix (Figure 1.19). PCA can be understood as establishing a new coordinate system, where the dimensions are chosen according to the amount of variance within the dataset. Often the most important information contained in a high dimensional dataset can be visualized using only the few directions where the variance is highest (the principal components).¹¹⁰ The scores matrix contains the coordinates of the data in the new coordinate system, whereas the loadings matrix contains the weights of each variable to each principal component.¹⁰⁹ A large weight indicates that a certain variable has a large contribution to the latent variable in question, which can be positive or negative.

Thus, PCA reduces a high-dimensional dataset to a few major components, which simplifies the finding and interpretation of data structures. The number of principle components is fewer than or equal to the original n dimensions of the dataset. However, for interpretation, only the first few components are used, so that we can benefit from the dimensionality reduction. Ideally the data which is excluded (error matrix, E) has low variability, and corresponds to the noise in the dataset. PCA is particularly useful in datasets where the predictor variables have correlations among themselves, as it allows the explanation of a larger portion of the dataset's variance using a smaller number of PCs. Additionally, the new variables (components) generated are uncorrelated to each other (orthogonal to each other in the new space).¹¹⁰ This makes PCA a useful pre-treatment of the data before a regression (often affected negatively by collinearities between variables) is applied. For example, in principal component regression (PCR) the independent variables are subject to a PCA, creating a new, reduced dataset which will then be the basis of a regression model.^{109,112} However, the PCA does not take into account any relationship with the target variable, only the directions of maximum variance within the predictors (which may not be the ones explaining the variations in the target variable).¹¹⁰

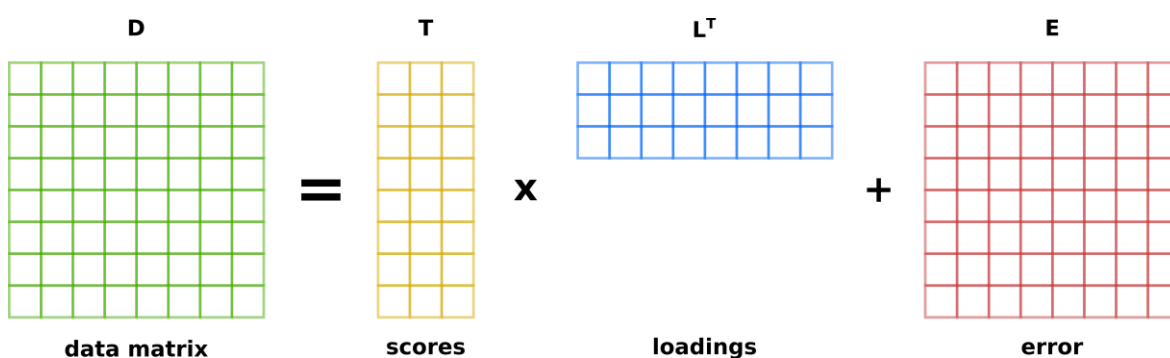


Figure 1.19: Original data matrix D and the three resulting matrices, T , L^T and E from the PCA according to the relation presented in equation 1.27.

1.5.3 Partial Least Squares (PLS)

PLS is a supervised machine learning algorithm which is based on two steps: first, the dimensionality of the data is reduced and second, a regression on the reduced dataset is calculated. The decomposition of the data matrix is applied to both the predictor (X) and the response (Y) variables, creating a new, reduced dataset, which will then be the basis of a regression model. What sets PLS apart from PCR, is that the decomposition of the predictor dataset takes into account response data, so that the obtained latent variables (similar to the principal components in PCA) are chosen to maximize covariance between the resulting X loadings matrix and the Y matrix vector.¹¹⁴ This is in contrast with the simpler PCR, where only the independent variables are subject to decomposition. In addition to a scores and loadings matrix, a third matrix called the error (or residual) matrix, E or F is also generated:

$$\begin{aligned} X &= TP^T + E \\ Y &= UQ^T + F \end{aligned} \quad (1.28)$$

where T and U are the scores matrices of X and Y respectively, and P and Q are respective the loadings matrices.¹¹⁴

The most important parameter in a PLS is how many latent variables will be used in the establishing of the regression model. This is usually determined by cross validation, where the dataset used to

train the model is split into two datasets, one larger and one smaller. The model is then trained on the larger dataset and tested on the smaller dataset, and the result is recorded. The process is repeated with a different split of the data until all the data has been used as the test group. The process is repeated for each number of components defined and the model with the best result is chosen.

The performance of the model is measured by the root mean squared error (RMSE), which is a measure how different the predicted value the model outputted (on the test set) is from the actual value observed. It is defined as:

$$RMSE = \sqrt{\frac{\sum_{i=1}^n (a_i - b_i)^2}{n}} \quad (1.29)$$

where n is the number of objects in the test set, a is the predicted value, and b is the actual value. PLS is particularly indicated for datasets where there is large number of collinearities among the predictor values, such as is the case in spectral data.

Understanding which variables contributed the most to a PLS model can provide useful information about the dataset being analysed. The selectivity ratio (SR) provides such information and is calculated as the ratio between the explained and unexplained variance for each variable.¹¹⁵ A high SR value means that the variable in question has a high contribution to the model and is correlated to the target variable. To set a cut-off between statistically relevant and irrelevant variables, an F -test can be performed with the null hypothesis being that the explained and residual variances of a variable are the same. If the SR is higher than the calculated F value at a set confidence level (usually 90 or 95%), then the null hypothesis is rejected, and the variable in question has a high discriminatory ability.¹¹⁶

1.5.4 Gaussian Mixture

Gaussian mixtures are a type of unsupervised machine learning, that can be used to divide a larger population of data points into subpopulations based on their similarity (similar to cluster analysis). The dataset is assumed to be composed of a mixture (weighted sum) of n Gaussian probability densities, each corresponding to a subpopulation (Figure 1.20). The probability density function of the data, x is defined as:

$$p(x|\mu, \tau, \pi) = \sum_{j=1}^n \pi_j G(\mu_j, \tau_j^{-1}) \quad (1.30)$$

where μ is the mean of the Gaussian, τ is the inverse variance, and π is the influence of the Gaussian on the mixture.¹¹⁷

In a fully unlabeled dataset, the algorithm does not have any starting point for which subpopulation each observation should belong to. This can be addressed using an expectation-maximization algorithm, which makes random assumptions for an initial subpopulation distribution and calculates the likelihood of each observation belonging to the subpopulation it has been randomly assigned to. Using these values, it will make adjustments to the subpopulation's parameters to improve the results. It will then repeat these steps in an iterative fashion until a local maximum has been reached.¹¹⁸

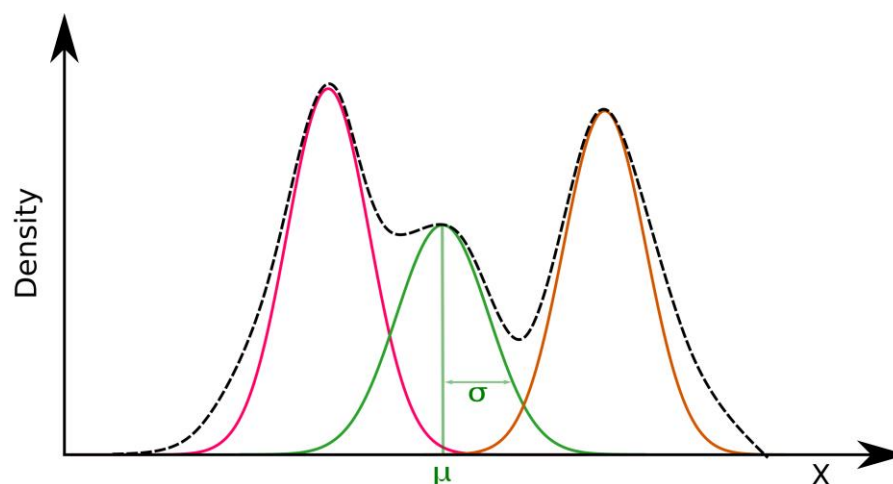


Figure 1.20: Representation of a Gaussian mixture applied to a one-dimensional variable, X . The observed values are represented by the dashed line, which is decomposed as several sub-populations with normal distributions.

Gaussian mixture models have been applied in multiple fields,^{119–121} but of particular interest is their use for the classification of pixel distribution in (hyperspectral) images.^{122–124}

1.5.5 Savitzky-Golay Filter

The Savitzky-Golay (SG) filter, first proposed in 1964,¹²⁵ is a smoothing algorithm that works by fitting a polynomial function to the dataset within a small window which is then moved along the dataset until all new points have been found. The partial least squares method is used to compute the polynomial fit, and the two adjustable parameters are the polynomial degree and the window size. An SG filter acts not only as a smoothing algorithm, but also as a low-pass filter by removing the contribution of higher frequencies, which often correspond to the noise in the dataset. Additionally, when the parameters are chosen appropriately, it preserves the band features such as relative maxima, minima, as well as width and height.¹²⁶ The window size chosen should be smaller than the width of the bands in the spectrum but larger than the noise, and the polynomial degree should be chosen according to the characteristics one is interested in: smooth features such as bands are better preserved by a lower order polynomial, whereas high frequency features will benefit from higher order polynomials.

The SG filter is routinely applied to infrared spectra, where due the characteristics of the bands, which are the feature spectroscopists are interested in, increasing the window size or decreasing the degree of the polynomial leads to a smoother spectrum (Figure 1.21). These parameters need to be adjusted carefully to achieve a balance between noise reduction and preservation of important spectral features: too high window values lead to distortions such as band height reduction, particularly in narrower bands (Figure 1.21, (2) compared to (4)).

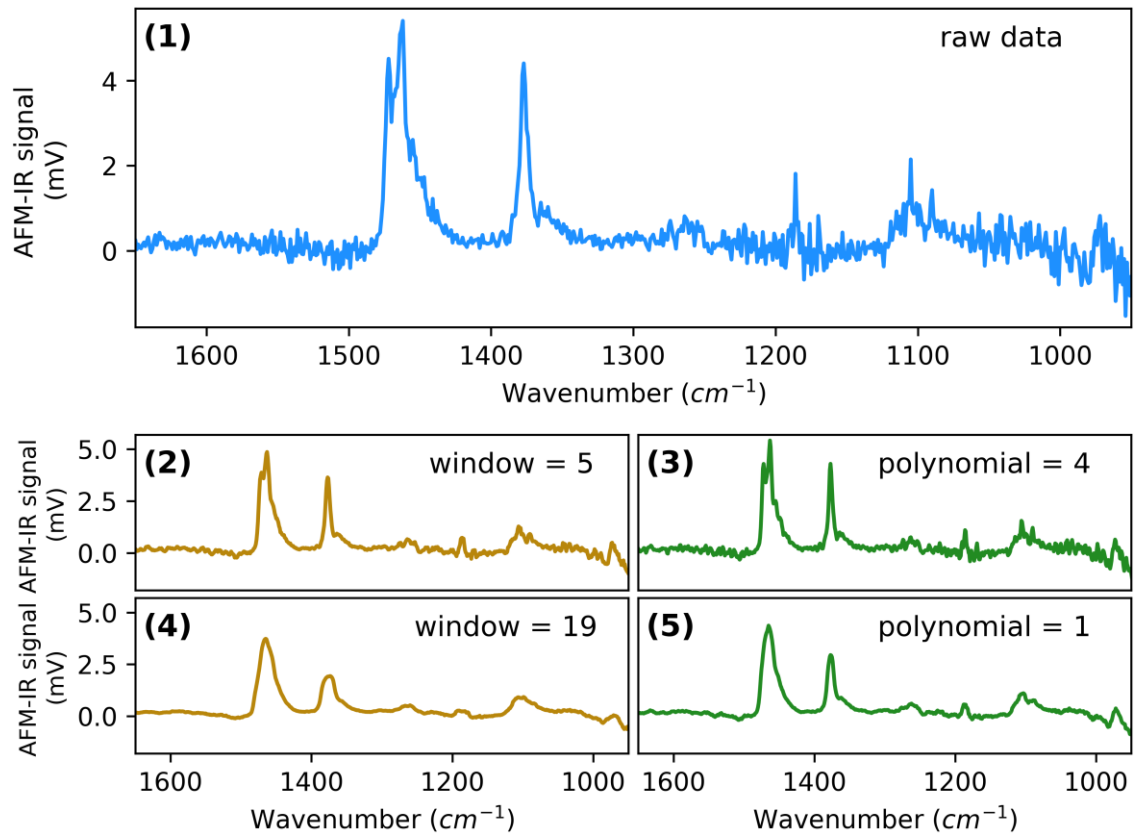


Figure 1.21: Effect of the window and polynomial parameters on the smoothing from a Savitzky-Golay filter. (1) raw AFM-IR spectrum of polypropylene; (2) spectrum (1) after SG filtering with window =5 and polynomial 1; (3) spectrum (1) after SG filtering with window = 9 and polynomial =4; (4) spectrum (1) after SG filtering with window =19 and polynomial =1; (5) spectrum (1) after SG filtering with window = 9 and polynomial =1.

Chapter 2 Results and Introduction to the publications

In this chapter the publications on which this thesis is based are introduced, and their results and conclusions presented. **Section 2.1** introduces publications I and IV in which AFM-IR was applied to the life sciences and a perspective was written on the topic. Publication I deals with the problem of using AFM-IR to map the intracellular location of a specific group of proteins within *Trichoderma reesei*, and is the subject of **section 2.1.1**. **Section 2.2** introduces publications II and III, in which AFM-IR was applied to the field of polymer science. First, a protocol for the tapping mode measurements of polymer samples using AFM-IR is presented (**section 2.2.1**), followed by the analysis of a post-consumer recycled polyolefin sample using tapping mode AFM-IR (**section 2.2.2**).

2.1 AFM-IR in life sciences (Publications I and IV)

In publication IV a concise summary of the working principles and operation modes of AFM-IR, as well as its recent key applications to the life sciences are presented. Additionally, relevant limitations were discussed, as well as potential future areas of research. This perspective was written with the aim of presenting the technique to readers of life science backgrounds, ultimately hoping to foster more interdisciplinary cooperation. Publication I is an example of such cooperation and is introduced and discussed in the following section.

2.1.1 AFM-IR for the localization of intracellular protein distribution (Publication I)

Proteins are biomolecules constituted of amino acid residue chains (>30 residues), which are linked together by amide (peptide) bonds. The structure of a protein is determined by the amino acid sequence that constitutes the peptide chain (Figure 2.1),¹²⁷ and the resulting interactions of the residues' side chains with each other.

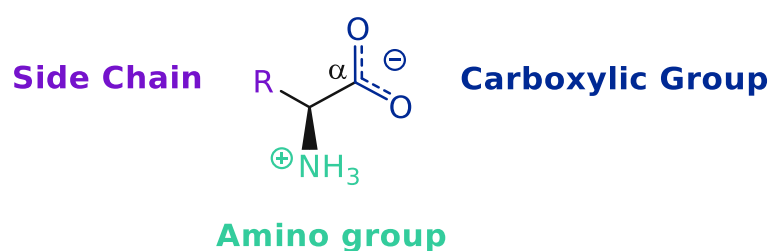


Figure 2.1: General structure of an L- α -amino acid in its zwitterionic form (the form present at physiological pH).

There are several levels of protein structure: primary, secondary, tertiary, and quaternary. Primary structure simply refers to the amino acid chain sequence, bound together by peptide bonds. Secondary structures are the regularly repeating structures that the polypeptide chain forms at a local level, of which there are two main types: α -helix and β -sheet. Whether a polypeptide chain will form one or the other type of structure depends on the side chains of its amino acid sequence and the resulting steric constraints, which results in favorable or unfavorable combinations of the rotational bond angles phi and psi (Figure 2.2).¹²⁷

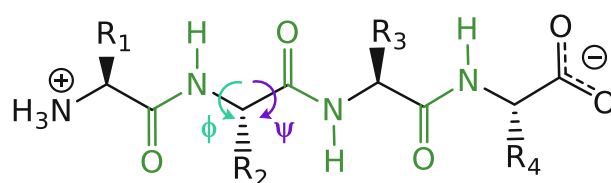


Figure 2.2: A small polypeptide (four residues) with the three peptide bonds highlighted in green. Phi (ϕ) and psi (ψ) are the two major bond angles describing the peptide bond which are determinant of the secondary structure of a chain.

In an α -helix, the residues are arranged in a coil structure, so that the side chains protrude from the helix, and the main chain forms the core of the helix, which is stabilized by hydrogen bonds between the amino group of a residue in position number n and the carbonyl groups of residue $n-4$. β -sheets on the other hand, are composed by two or more β -strands (unfolded chain, with certain degree of freedom of psi and phi) side by side, linked together by hydrogen bonds between the amine and carbonyl groups of the backbone. β -sheets can be parallel, when the β -strands follow the same direction), or anti-parallel, which has an effect on the hydrogen bonding pattern between residues.¹²⁷ β -turns are a common type of secondary structure where there is a reversal in the direction of the chain.¹²⁷

The next level of protein structure is the tertiary structure, which is the overall structure of the protein (one entire polypeptide chain) and the interactions of residues that are distant from each other in the chain. Tertiary structure is highly influenced by the environment (hydrophilic or hydrophobic) in which a protein is found, e. g. a membrane protein will often have its hydrophilic groups either forming a pore on the inside, or in contact with the aqueous environment on either side of the membrane, whereas hydrophobic groups will interact with the hydrophobic tails of membrane lipids.¹²⁸ In aqueous environments (such as the cytoplasm), the hydrophobic effect plays a major role in the tertiary structure.¹²⁷ Other interactions between residues side chains that contribute to the tertiary structure are van der Waals interactions (such as hydrogen bonds), ionic bonds, and disulphide bridges. Finally, quaternary structure refers to the interactions and spatial arrangement of multiple polypeptide chains which come together to perform their function as multimers.¹²⁷

The structure of a protein is intimately related to the function it will perform,¹²⁹ which can range from structural, to metabolic, to signaling, etc. Of particular interest in this work are enzymes, proteins which act as highly specific catalysts to enable countless reactions under the organisms' ambient conditions. Nowadays, enzymes are no longer confined to their roles within biology, and are part of numerous industrial processes such as biofuel¹³⁰ and pharmaceutical production.¹³¹ Thus, it is of great value to be able to monitor a protein's structure and location, as this can give valuable information on cellular processes. Protein location within a cell is generally investigated through the use of imaging techniques, most commonly electron^{132,133} and confocal microscopy,^{134,135} but also the more recently developed super resolution microscopy techniques,

STED, SIM, PALM, and STORM.^{136–139} Despite the great potential of super resolution microscopy, and its numerous important insights provided, these techniques suffer from the extensive sample preparation required, limited availability of fluorophores, long sampling times, required postprocessing of the obtained data and the susceptibility to artifacts.^{140–142}

The structure of a protein is usually determined by either X-ray crystallography, nuclear magnetic resonance (NMR) spectroscopy, or cryo-electron microscopy (cryo-EM). X-ray crystallography is usually the preferred technique, due to its capability to determine the 3D position of the atoms that constitute a protein, thus providing information on the secondary and tertiary structures. This technique however, requires isolation and crystallization of the protein of interest, which is often challenging (and for some complexes, not possible)¹⁴³ and means that the protein will always be observed in isolation from its native environment (e.g. the cell) and conditions (aqueous).¹⁴⁴ NMR spectroscopy, particularly 2D-NMR has also been used to elucidate protein structure, however it is mostly restricted to smaller sized proteins and requires the preparation of concentrated protein solutions.^{144,145} More recently, cryo-EM has emerged a powerful tool for the full structural determination of protein structure, capable of determining protein structure with resolution comparable to X-ray crystallography.¹⁴⁶ Cryo-EM the samples are vitrified, thus preserving their in-solution structures, with the main downside being the labor intensive nature of cryo-EM measurements.¹⁴³ The three previously mentioned techniques are the state of the art for protein structural elucidation, however, when only the secondary structure of a protein is required, other techniques, such as vibrational circular dichroism^{147,148} and infrared spectroscopy,¹⁴⁹ are able to provide this information in a quicker and easier manner.

The mid-IR spectrum of a protein is dominated by two features: the amide I and amide II bands, and to a lower extent, the amide III band (Figure 2.3). The amide I band derives mainly from the stretching vibration of the C=O group in the amide bonds, and from smaller contributions from out of phase C-N vibration, C-C-N deformation, and N-H in-plane bend.¹⁴⁹ This band is usually found centered around 1650 cm^{-1} and ranging from 1600 cm^{-1} to 1700 cm^{-1} , and it is of particular interest due to its sensitivity to protein secondary structure owing to the effect that the varying arrangements of hydrogen bonds, dipole interactions, and geometric constrains (with corresponding bond angles) have on the energy at which the vibrations responsible for the amide I band occur.¹⁵⁰ Thus, α -helical structures have their band center at 1654 cm^{-1} and β -sheets at 1633 cm^{-1} and 1684 cm^{-1} .¹⁴⁹ Amyloid aggregation states, characterized by the increasing presence of intermolecular β -sheets, can also be identified due to their predominant absorption at lower wavenumbers (1620 cm^{-1}).^{149,151}

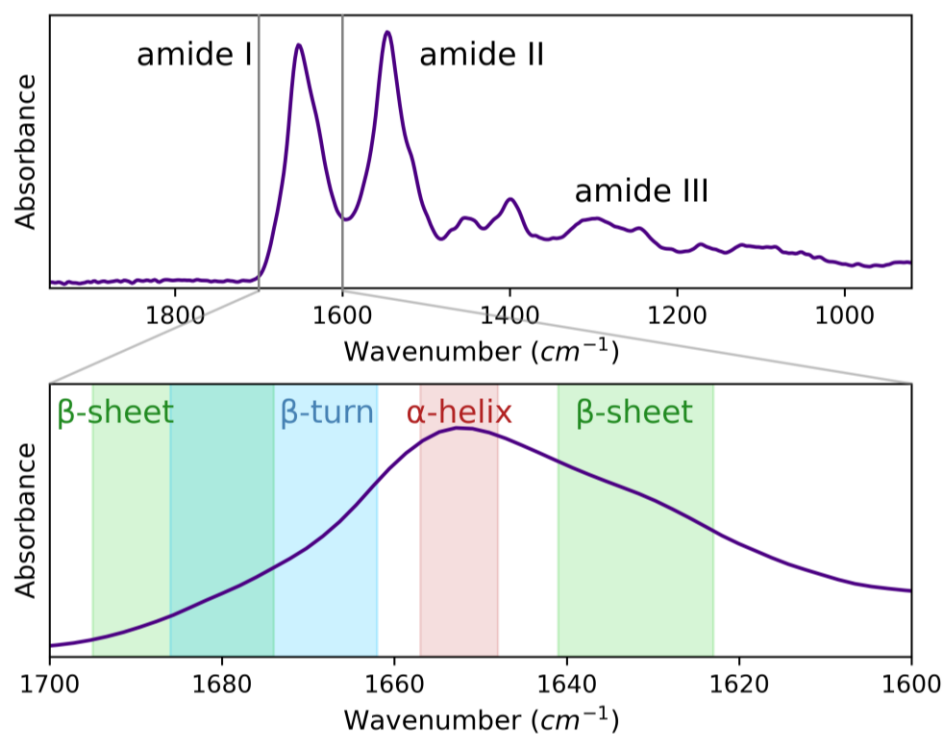


Figure 2.3: FTIR spectrum of bovine serum albumin, highlighting which secondary structure is prominent in the different areas of the amide I band.

The amide II band is centered at around 1550 cm^{-1} and is the result of the in-plane N-H bending and C-N stretching vibrations, with minor contributions from the stretching vibrations of C-C and N-C and the in-plane bend of C-O.¹⁴⁹ This band is also sensitive to protein secondary structure, albeit to a much lesser extent than its amide I counterpart.¹⁵² Lastly, the amide III band is found over a region from 1400 cm^{-1} to 1200 cm^{-1} , and it combines contributions from not only the protein backbone, but also from the residues' side chains, which complicates its interpretation to obtain secondary structure information.¹⁴⁹

FTIR spectroscopy is thus a useful method for the analysis of protein structure and activity in solution, which suffers however, from the fact that water has an absorption band in the same region as the amide I (1645 cm^{-1}). To prevent total absorption due to water shorter pathlengths are used, which in turn require highly concentrated protein samples.¹⁵³ This issue has been recently tackled by the use of QCLs as light sources, which allow high SNRs at concentrations as low as 0.05 mg mL^{-1} .¹⁵³⁻¹⁵⁵ However, when spatial resolution is required, IR microscopy is plagued by the diffraction limit problem described in section 1.1.2, and it is in these situations that AFM-IR can be of use.

There are several examples in literature of AFM-IR applied to the study of intracellular protein structure and location, one of the earlier studies being the work by Baldassare *et al.*,⁷⁸ where the distribution of proteins in both *E. coli* and human HeLa cells was mapped by imaging the amide I band. Another study, this time by Quaroni *et al.*¹⁵⁶ focused on the identification of cytoskeleton filaments in fibroblasts, whereas Perez-Guaita *et al.*¹⁵⁷ made use of unsupervised machine learning methods (cluster analysis) to detect areas with high hemoglobin content within *P. falciparum* infected red blood cells. Furthermore, AFM-IR has been able to locate functional amyloids within bacteria and archaea,¹⁵⁸ and, in another study, Liu *et al.*⁸⁰ investigated the effect of the environment on the proteins expressed by macrophages. The authors were able to differentiate between the two cell groups, and to detect a marked shift in the proteins expressed. Additionally, nanoscale chemical imaging using the tapping mode revealed a heterogeneous distribution of the expressed

proteins according to their secondary structure, allowing for the identification of node-like structures rich in antiparallel β -sheet protein in the extremities of the cells exposed to LPS.

All the studies mentioned above were conducted in a label-free manner, exploiting the fact that no staining is required in order to obtain signals from proteins in the mid-IR region, an advantage in terms of the complexity of sample preparation when compared to other microscopy techniques such as electron microscopy. However, this advantage can also turn into a disadvantage when only a specific protein or group of proteins is the target of a study since in the mid-IR all the proteins will contribute to the obtained signal. In publication I, a novel approach to this problem was pursued through the use of a supervised machine learning method to detect a specific group of proteins within the organism being studied.

To demonstrate this approach the organism chosen was *T. reesei*, a filamentous mesophilic ascomycete which is exceptional at degrading cellulose thanks to its efficient enzymatic secretory system.^{130,159} Several industrial processes in the biofuel,^{130,160} textile,¹⁶¹ pulp,¹⁶² food and animal feed¹⁶³ and recombinants protein production¹⁶⁴ industries take advantage of the high secretion of cellulases and hemicellulases by *T. reesei*, making the fungi a relevant target for protein location studies. The secretory pathway of *T. reesei* has been the object of several studies, often with the ultimate goal of improving protein production yields. *T. reesei*'s genome has been fully sequenced,¹⁶⁵ and several studies were conducted on the regulation of both gene expression^{166–168} and secretory pathways¹⁶⁹ involved in protein production and secretion. Furthermore, electron microscopy^{132,133,170} and confocal microscopy^{171,172} have given important insights into the ultrastructural features and spatial distribution of the secretory pathway components of *T. reesei*. In this work, the goal was to demonstrate the capability of AFM-IR to provide high-resolution information on the intracellular location of the major cellulases and xylanases produced by *T. reesei*. To achieve this goal, a special strain named QM6a SecEYFP was used, in which an expression cassette for the enhanced fluorescent yellow protein (EYFP) has been fused to the N-terminal secretion signal peptide of the main cellobiohydrolase, CBHI¹⁶¹ whose expression is controlled by the *cbh1* promoter. In this strain the expression of EYFP occurs when the expression of other proteins controlled by the *cbh1* promoter also occur, and since the EYFP is fused to the secretion signal peptide it can be expected to be colocalized with the cellulases and xylanases, thus yielding a proportionality between the fluorescence signal and latter's abundance. Thus, by combining fluorescence images with AFM-IR measurements obtained in the same locations, it was possible to obtain a PLS model that connects the fluorescence intensity with the presence of β -sheet-containing proteins in that location.

Sample preparation consisted solely of depositing parts of the mycelium on CaF₂ windows and freeze-drying the sample to quickly remove its water content. The samples were then first analyzed under a fluorescence microscope to search for areas with varying fluorescence intensities where the model might be trained. Once such areas were identified, several images with different magnifications were recorded in both fluorescence and brightfield mode (Figure 2.4), to facilitate the search for the same location in the AFM-IR instrument (equipped with a single 10x objective and the AFM itself). The sample was then transferred to the AFM-IR, and once the measurement spot had been re-located, several AFM-IR spectra were recorded in contact mode. The images and respective spectra locations were aligned using python once the measurements were completed, and the spectra were preprocessed prior to model training (Figure 2.5).

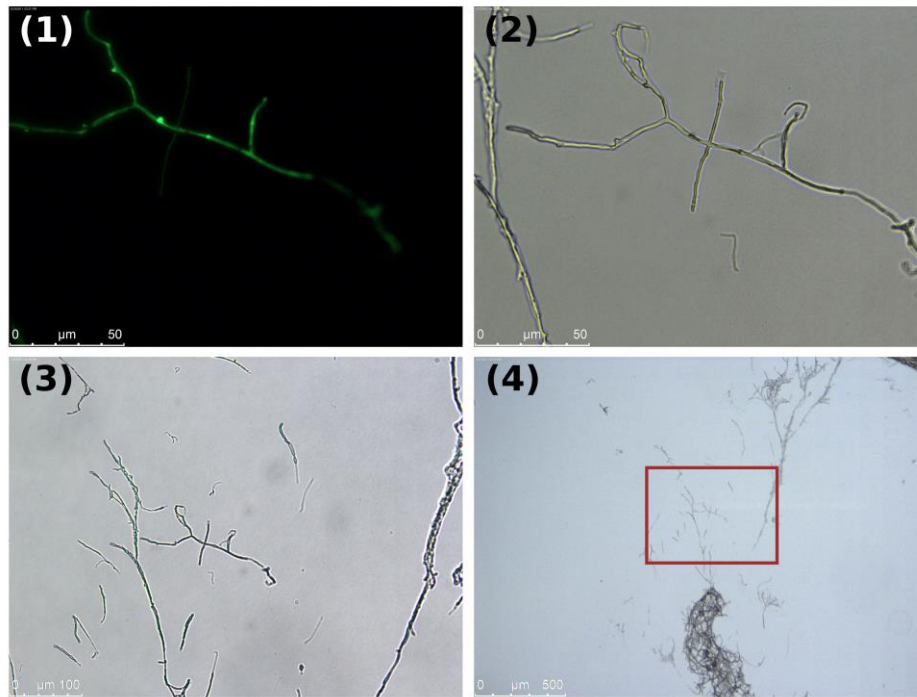


Figure 2.4: (1) Fluorescence image of a hypha of *T. Reesei* of a similar sample to the one used in publication I; (2) Bright field image of the same location and at the same magnification as (1); (3) and (4) are brightfield images of the same location as (1) at lower magnifications.

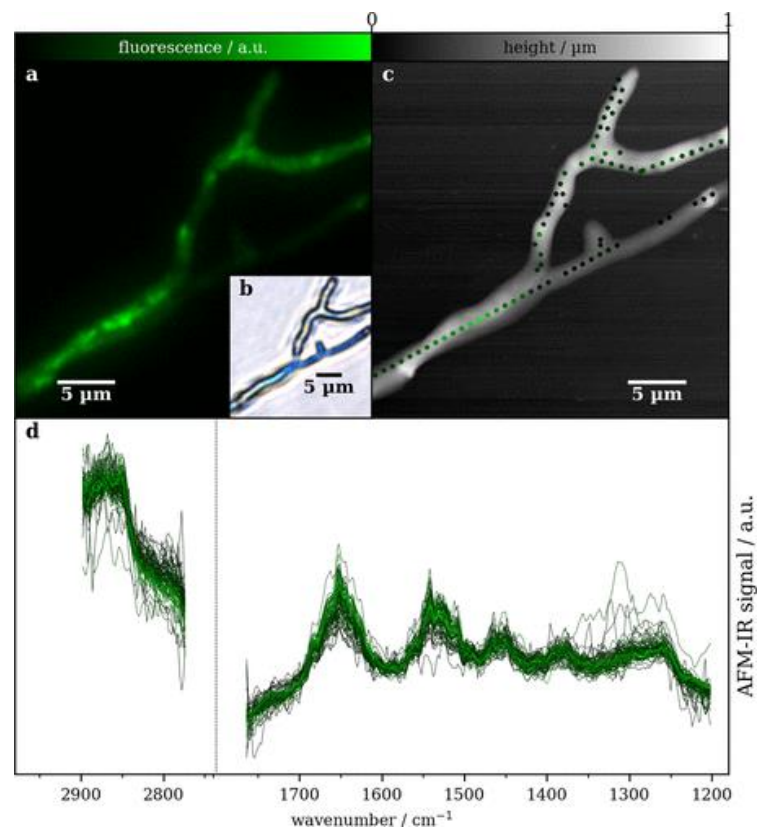


Figure 2.5: Aligned fluorescence (a), brightfield (b), and AFM (c) images a *T. Reesei* hypha. (c) shows the location where AFM-IR spectra were recorded and the corresponding fluorescence intensity at that location; (d) AFM-IR spectra obtained in the locations in (c) and respective fluorescence value as the line colour. Sourced under the terms of CC BY 4.0 license from ref.⁷⁹ (Publication I).

Using the dataset in Figure 2.5, a PLS model was trained using the RMSE as the metric to evaluate the goodness of fit. The optimized model scored an 11% average error of fit for training dataset. Most interestingly, the SR was used to determine which wavenumbers contributed the most to the PLS model at a 90% confidence level (Figure 2.6). The highest contributions come from wavenumbers associated with β -sheet secondary structures, as well as lipids (CH₂ stretching vibrations).

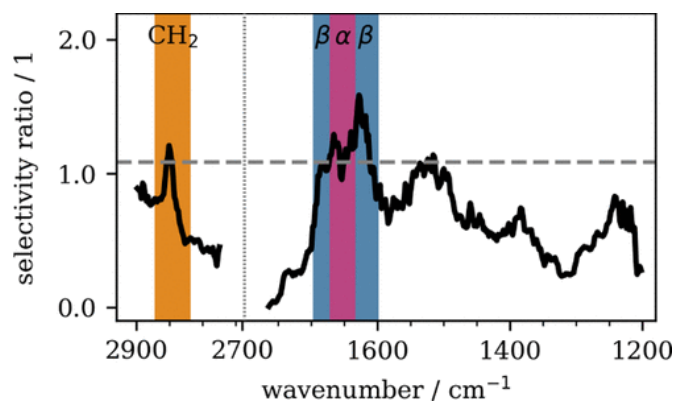


Figure 2.6: Selectivity ratio for each wavenumber used in the model. Wavenumber groups above the 90% confidence level are identified according to the group or secondary protein structure associated with those spectral regions. Sourced under the terms of CC BY 4.0 license from ref.⁷⁹ (Publication I).

Despite the structure of EYFP being mostly composed of β -sheets arranged in a β -barrel configuration, it is unlikely that the fluorescent protein significantly contributes to the IR signal obtained in the areas where it is located. This is supported by existing literature, particularly one study which concluded that the cellulase expressed under the *egl1* gene, EGL1 (which in normal conditions represents only 10% of the total secreted protein) is much more abundant than recombinant proteins expressed under the *cbh1* promoter carrying only the secretion signal peptide (ratios of 0.001 and 0.01 recombinant protein/EGL1, depending on the strain).¹⁷³ Therefore, the IR signal detected largely comes from other more abundant β -sheet containing proteins co-localized with EYFP, namely CBHI, the most abundant cellulase,^{161,174} whose expression is also driven by the *cbh1* promoter and which contains the same secretion signal peptide. Furthermore, EGL1 and the most abundant xylanase, XYNII are also produced under the cultivation conditions used in this study (lactose as the carbon source),¹⁷⁵ and are predominantly composed by β -sheet secondary structure motifs.^{176,177} Finally, the high SR of the 2850 cm⁻¹ absorption band associated with the CH₂ groups of lipids further hints at the sensitivity of the model towards β -sheet containing cellulases and xylanases, which are enveloped in lipid bilayers throughout their whole path inside of the cell due to their final destination being secretion rather than remaining inside the cell.¹⁶⁹

The obtained PLS model was then applied to another dataset which was not used in the training of the model with only a marginal increase in the RMSE (from 10% in the training set to 13%), which indicates that the model has a good generalization capability and is not overfitting the training dataset. Thus, from the AFM-IR spectra it is possible to calculate a fluorescence intensity value, thus having a visual comparison between calculated and actual fluorescence values (Figure 2.7).

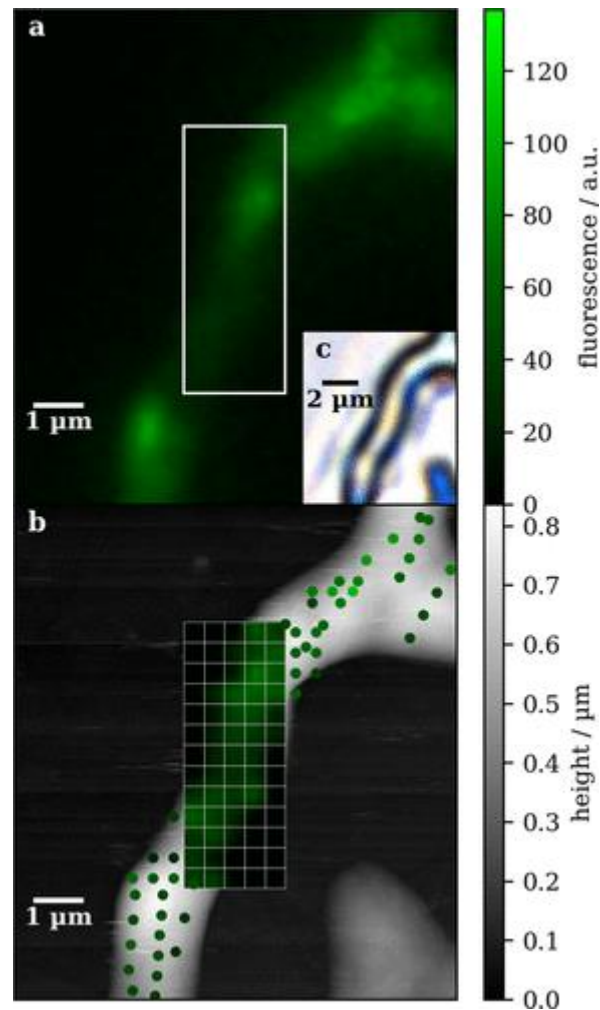


Figure 2.7: Visual comparison between the calculated (b) and actual fluorescence (a) of the training dataset. Collecting AFM-IR spectra in a grid allows for partial reconstruction of the fluorescence image from the AFM-IR data. Sourced under the terms of CC BY 4.0 license from ref.⁷⁹ (Publication I).

The approach presented in Publication I was thus able to circumvent one of the major challenges associated with the analysis of whole cells using AFM-IR, which is the similarity of the spectra obtained, since at nearly every location in the cell there will be proteins and lipids, and often carbohydrates present. Using the fluorescence signal generated by small amounts of EYFP as a starting point for the training of a model avoids the need to chemically label the target analytes (β -sheet containing cellulases and xylanases) by using what can be described as a “digital stain”. This method could be further improved by reducing the gap between the resolutions of the methods used (e.g. by replacing epifluorescence microscopy with confocal microscopy), and through the development of automated software for the alignment of the images obtained from different instruments.

2.2 AFM-IR in polymer science (Publications II and III)

Polymers are one of the most important and widely used class of materials, due to their light weight, low price, versatility and durability. The following sections introduce publications II and III, in which AFM-IR was applied to the nanoscale analysis of polymer samples, specifically polyolefins, which represented 46.2% of the global plastic production and 40.6% of the European plastic production in 2021.¹⁷⁸

Polyolefins are a class of polymers derived from alkene monomers such as ethylene and propylene, which originate the two most produced polyolefins: polyethylene and polypropylene. Polyethylene (PE) can be further subdivided into three different polymer types (Figure 2.8): high density (HDPE), low density (LDPE), and linear low density (LLDPE). In HDPE the polymer chains have nearly no branching, which allows for compact packing and stronger intermolecular interactions between the polymeric chains (higher crystallinity), in turn leading to increased rigidity, stiffness, tensile strength and chemical resistance of the polymer, as well as a higher melting point than the other PEs.^{179,180} LDPE is characterized by a high degree of branching of its polymer chains, which prevents the formation of compact crystalline structures (hence the low density) due to weaker intermolecular interactions.¹⁸⁰ LDPE is thus more suited to applications that require a more flexible material, such as packaging, and plastic bags. Finally, LLDPE is different from the two previous PEs due to its combination of a long linear backbone with short side-chain branching, added to the chain through the introduction of small amounts of other comonomers. This results in improved tear and puncture resistance when compared to LDPE, while maintaining higher flexibility than HDPE.^{180,181}

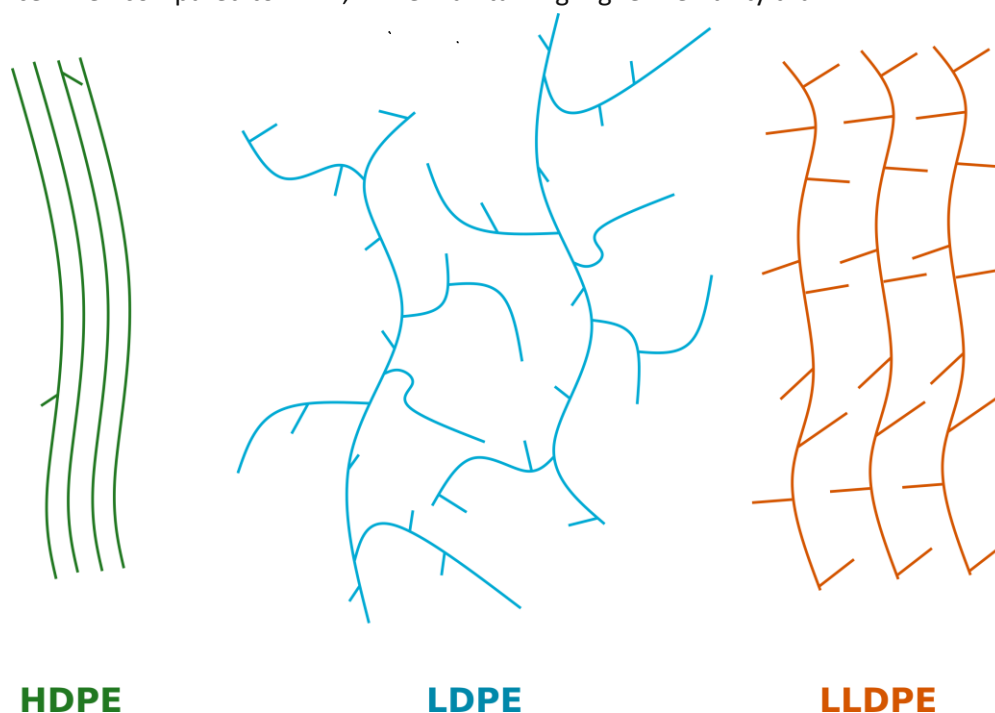


Figure 2.8: Diagram showing the different branching and packing of the polymeric chains of HDPE, LDPE, and LLDPE.

Polypropylene (PP) has a lower density than PE, and depending on the orientation of the side chain it can be divided into isotactic PP (crystalline), and atactic PP (amorphous).¹⁸⁰ In isotactic PP (iPP), all the side chains are positioned on the same side of the main chain, thus allowing for a closer packing of the polymeric chains. iPP is harder, stiffer and more resistant to heat than PE, but unsuitable for applications below 0°C.¹⁸² PP alone represented 19.3% of the global production of plastics in 2021,¹⁷⁸ and is used in many everyday life applications particularly in food packaging, but

also in medical devices, research equipment, and garden furniture.

Information about a polymer's structure at the nano- and micro-scale is usually obtained by either SEM,^{183,184} TEM,^{185,186} X-Ray diffraction,¹⁸⁷ or AFM,^{188,189} and occasionally by fluorescence confocal microscopy.¹⁹⁰ Despite providing valuable information, some of these methods require tedious sample preparation protocols, namely heavy metal staining and chemical etching (in the case of electron microscopy), or the preparation of special polymer samples labeled with fluorescent molecules (confocal microscopy). AFM-IR is thus a useful technique that can add value to the nanoscale characterization of a polymer by providing explicit chemical information at the nanoscale, which can be of great use to further our understanding of the relationship between nanoscale structure, chemical composition, and macroscale properties.

With the exception of publication II and III presented in this thesis, all of the AFM-IR studies of polyolefins published in literature used the contact mode to investigate their samples, mostly focusing on the phase distribution in impact polypropylene copolymer (IPC), an in-reactor alloy in which propylene and ethylene monomers are combined resulting in a core-shell morphology with an iPP matrix and rubber phase composed of ethylene-propylene rubber (EPR), ethylene-propylene block copolymers of varying lengths (EbP) and small amounts of PE.⁸⁴ The 2016 and 2018 works by Tang et al. used contact mode images and spectra to determine that the composition of the rigid core of the rubber particles can be controlled by the polymerization conditions to be either PE or PP.^{84,191} Further studies on IPC using AFM-IR concluded that the addition of a higher amount of PE results in improved interface adhesion and subsequent improvement of mechanical properties,⁸⁵ and that having PP in the rigid core yields better mechanical properties than a PE core.¹⁹² More recently Zhong et al. studied the distribution of antioxidant in a blend of iPP and ethylene-octene copolymer and concluded that it is mostly concentrated in the ethylene-octene phase and not in the iPP matrix.¹⁹³ The above mentioned studies focused on samples whose composition was already known to a reasonable degree before the application of AFM-IR, and furthermore, provide no systematic routine to tackle the analysis of polymers using AFM-IR. Publications II and III represent contributions to both of these questions.

2.2.1 Analysis of polymers using tapping mode AFM-IR (Publication II)

In this work, a protocol for the systematic analysis of polymer samples (particularly those of unknown or uncertain composition) was developed and is summarized in figure 2.9. The protocol was then applied to the analysis of four different commercially available polymer samples, two of which were virgin polymers, and two were recyclates. The two virgin samples were LLDPE and a reactor thermoplastic polyolefin (rTPO), which consists of a hard PP or PE matrix and a soft component, in this case EPR. The two recyclates consisted of PE/PP mixtures with varying PE content (Skyfil 1 had 35% PE whereas Skyfil 2 had only 20%) as well as mineral fillers that were added to improve the recycled blend's properties (CaCO₃ in Skyfil 1 and talc in Skyfil 2).

Step 1 of the protocol consists of collecting bulk ATR spectra in order to obtain information about the general composition of the sample to be analyzed. The obtained spectra are particularly useful during the optimization phase of the AFM-IR measurement, where it is necessary to know at least one absorption band of the sample per chip of the EC-QCL used.

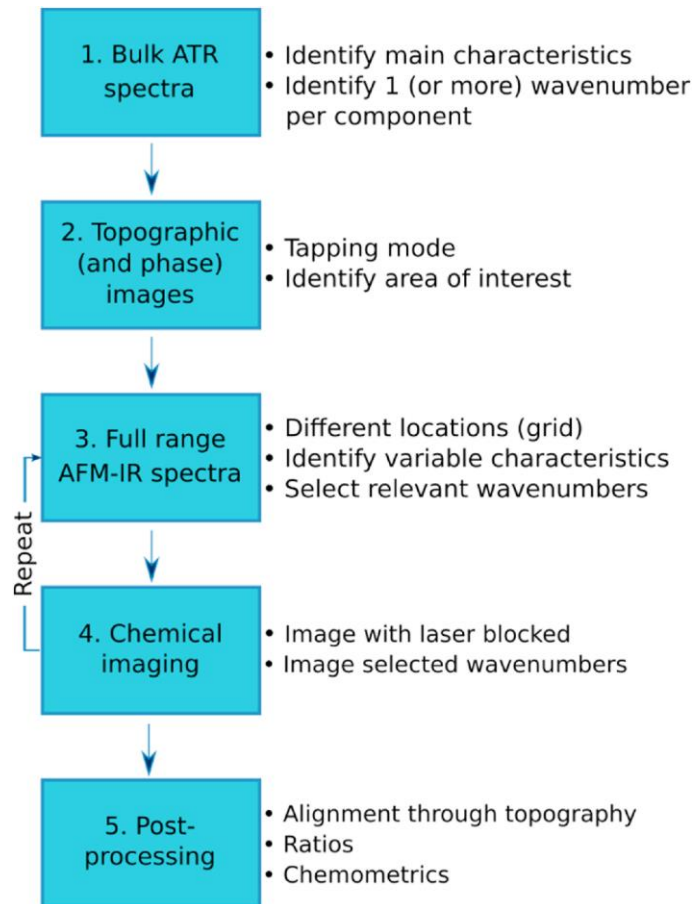


Figure 2.9: Protocol for the analysis of unknown polymer samples using AFM-IR. Sourced under the terms of CC BY 4.0 license from ref.⁶⁴ (Publication II).

Before moving on to the AFM-IR measurements, the sample needs to be prepared so that its surface is flat enough to be measurable by an AFM. Additionally, to prevent signal saturation, mitigate peak shifts, and to help prevent sample overheating and melting, it is advisable to keep sample thickness below the one micrometer threshold.^{63,70} For polymer samples it is absolutely crucial to have the samples cut below their glass transition temperature to prevent smearing (Figure 2.10) that can lead to wrong conclusions about the morphology and nanoscale chemical distribution of the sample in question.

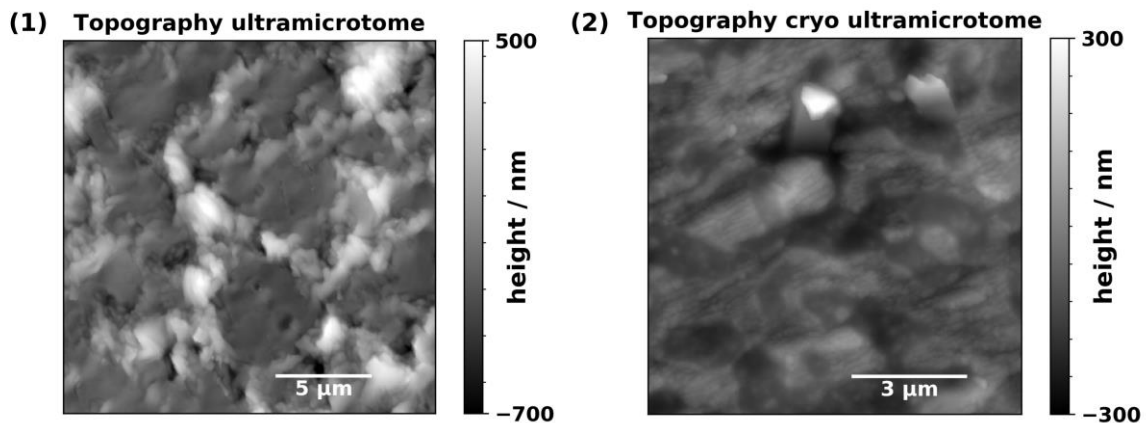


Figure 2.10: Tapping mode topography images of the same material (an rTPO) cut with an ultramicrotome at room temperature (1), and -100°C (2). In (1) the smearing of the softer EPR phase in the direction of the cut is clearly visible.

When starting an AFM-IR measurement a decision has to be made as to whether one will use contact mode (resonance enhanced) or tapping mode. Generally speaking, a first attempt is often carried out using the contact mode, which gives out stronger signals and is usually more stable than tapping mode. However, contact mode is not always suitable, particularly for softer, highly heterogeneous and/or loosely attached samples. An example of resonance-enhanced contact mode being unsuitable for the measurement of polymers is shown in figure 2.11, where the rugged topography of the rTPO being analyzed led to failures of the PLL loop in tracking the changes in the resonant frequency and adjusting the laser repetition rate accordingly. A first indication that the contact mode is not suited for this sample is visible in the topography images where some edges appear to have artifacts. This is further confirmed by the horizontal lines in the contact mode IR map, that indicate where the tracking failed. Tapping mode achieved significantly better imaging quality and was thus the chosen mode for the measurements of the polyolefins (figure 2.11 (2)). This is due to several factors: lateral tip-sample interactions are reduced in tapping mode, viscoelastic samples exhibit increased apparent stiffness due to the vertical tip motion,^{194,195} and importantly, because the cantilever resonance frequencies are less sensitive to changing mechanical properties,^{73,93} which is particularly relevant for AFM-IR imaging. It is important to point out that in extreme cases where there is a large range of stiffnesses in the scanned area (such as in the case of soft polymeric nanoparticles resembling liposomes lying on a hard substrate), it is always beneficial to track the changes in resonance frequency, even in the tapping mode. However, this is not the case for the polymers analyzed here, where the lower sensitivity of the tapping mode to the sample's mechanical properties is enough to obtain artifact-free measurements. Furthermore, measuring in tapping mode allowed for the use of higher scanning speeds than contact mode, which not only allows for more time efficient measurements, but also reduces the effect of stage drift.

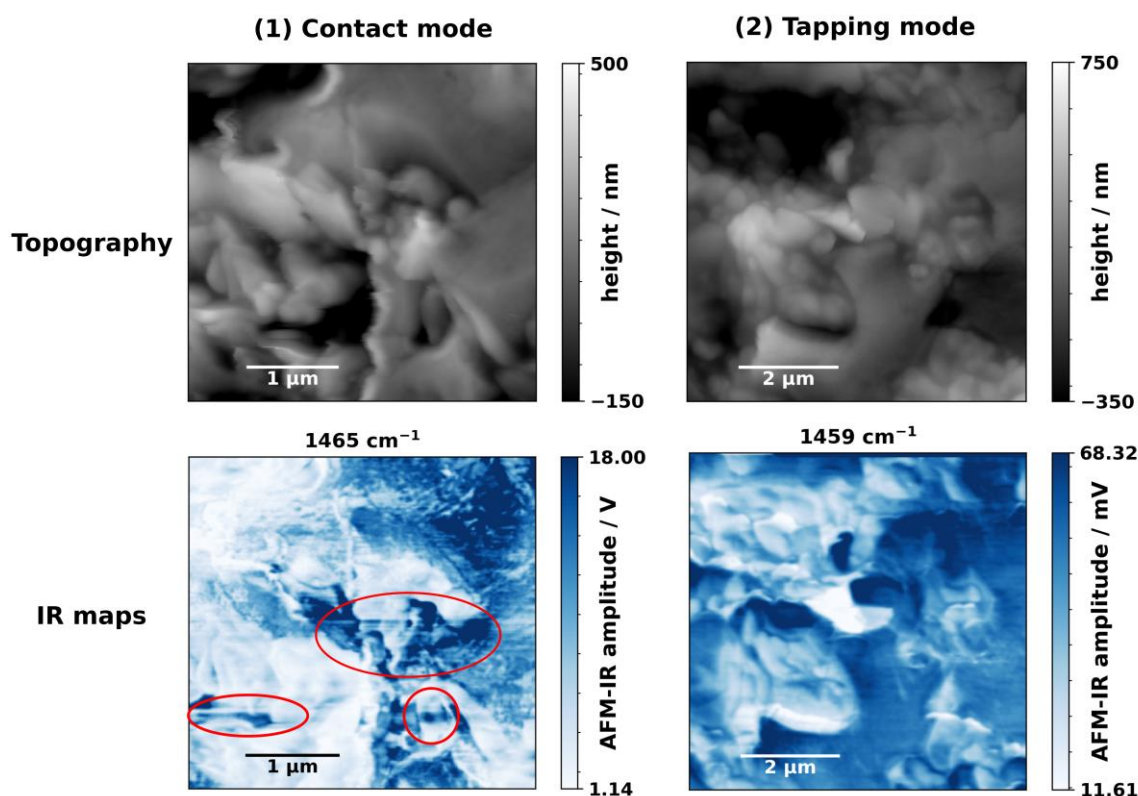


Figure 2.11: Contact mode (1) and tapping mode (2) topography and IR maps of an rTPO. The red circles mark areas where the PLL tracking of the resonance was not correct, causing the horizontal stripes and discontinuities visible on the image.

Step 3 and 4 of the protocol represent the AFM-IR measurement *per se*, and can be repeated iteratively for as long as necessary, until no new features are revealed. Thermal drifting of the AFM stage is a common occurrence in the AFM-IR system used in this study, and can affect the measurement quality, particularly when images of IR band ratios are necessary. Before calculating the band ratio one must ensure that the pixels in the two images correspond to the same location in the sample, otherwise the results obtained will not correspond to reality. In this work this was achieved using the scikit-image python package to determine the shift between the topographic images recorded through time and then use this value to obtain the correct coordinates for all the pixels in relation to a reference topographic image.^{196,197}

The protocol presented in publication II is particularly useful when the contents of a sample are not previously well known, such as in the case of recyclates (figure 2.12, Skyfil 1 and 2), whose composition can vary from batch to batch due to the variability in composition of the post-consumer polymer waste collected. Here it is possible to see that both polymers contain talc and CaCO₃ as mineral fillers, despite only one being added during the manufacturing process to each of the recyclates. However, AFM-IR can provide new information even in more conventional samples such as the rTPO, namely that the mineral filler talc appears to be mostly present at the interface between the PP and EPR phases. This hints at the possibility of talc influencing the miscibility of the rTPO components, something which had previously been described in polyurethane (PU)/PP blends.¹⁹⁸

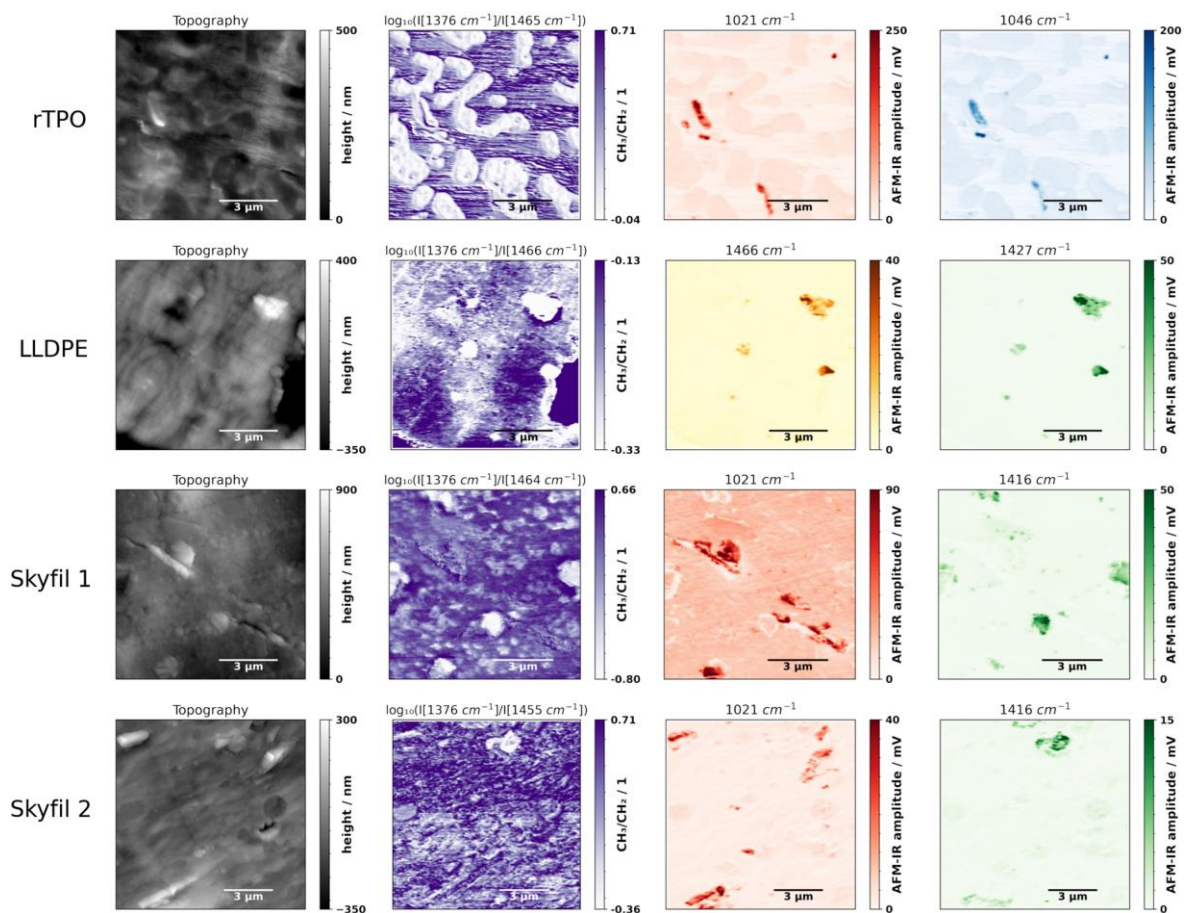


Figure 2.12: IR maps and topography images obtained through the application of the protocol described in this work. Sourced under the terms of CC BY 4.0 license from ref.⁶⁴ (Publication II).

Publication II is a contribution towards the establishment of community-wide standardized

workflows, in this case to analyze the nanostructure and composition of polymer samples, with a particular focus on the tapping mode technique. Despite all of its advantages for the analysis of polymers, tapping mode AFM-IR is still underused in this field. This work serves as a demonstration of its usefulness, as evidenced by the results shown in Figure 2.12 and in publication II. Furthermore, common difficulties faced during AFM-IR measurements were highlighted and solutions were presented to tackle these challenges (cryomicrotomy, image alignment).

2.2.2 Analysis of post-consumer polyolefin recyclates using tapping mode AFM-IR (Publication III)

The abundance of polyolefins in day-to-day life shows how versatile and important these materials are, but it has also led to a correspondingly large amount of polyolefin waste being generated every year. Post-consumer plastic waste generally faces one of three processes: recycling, burning to produce energy, or disposal in landfills (Figure 2.13). In 2020 in the EU27+3 (EU27, Norway, Switzerland, and the United Kingdom) 29.5 Mt of post-consumer plastic waste was generated, of which only 35% was recycled, 42% went to energy recovery, and 23% to landfills. Of these 29.5 Mt, 17.9 Mt were plastics used in packaging, a category where recycling percentages reach 46%, and only 17% of packaging plastics end up in landfills.¹⁷⁸ This latter option is the least desirable of the three due to the long degradation times of most plastics and the soil and groundwater contamination that it can lead to.^{199,200} Recycling allows for the polyolefins to remain in circulation for longer and reduces consumption of the virgin raw materials required to produce them, which are still largely non-renewable, despite the expectable development of green feedstocks in the coming decades.²⁰¹

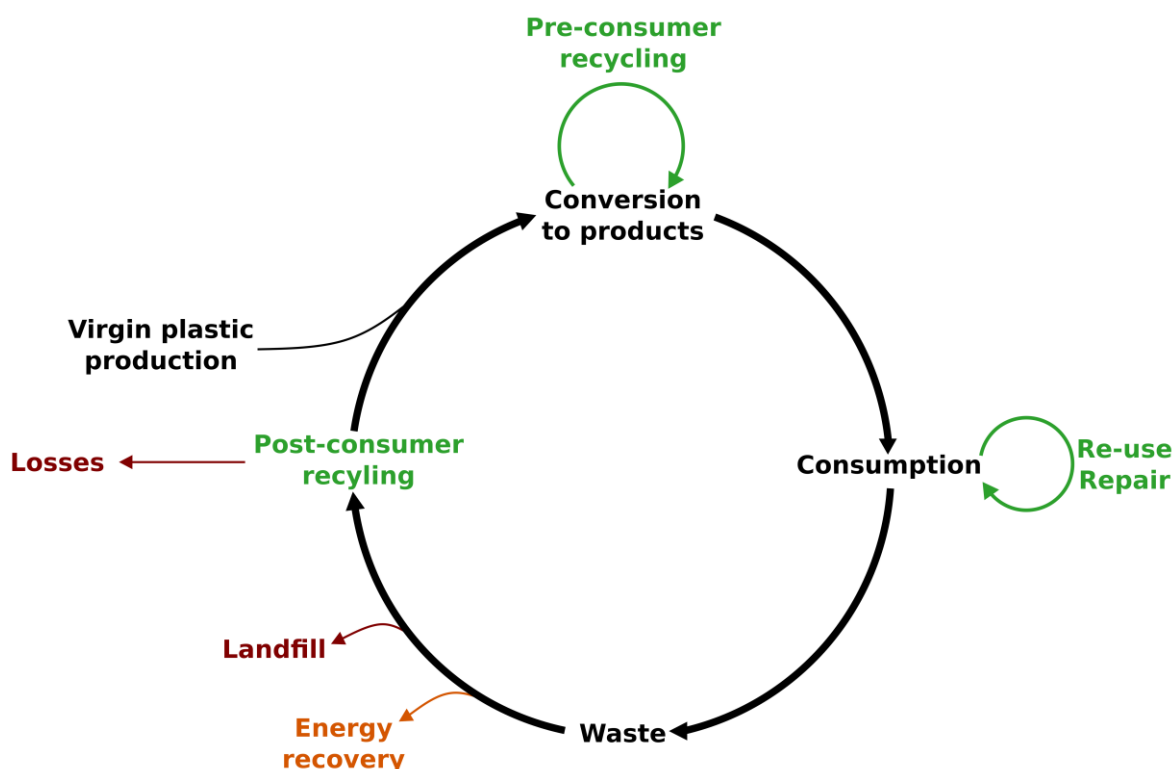


Figure 2.13: Lifecycle of plastics items. Adapted from ref.¹⁷⁸

Post-consumer polyolefin waste goes through several stages from the point of generation until it is recycled, and in each stage there are some material losses (Figure 2.15). One key step is the sorting

of the polymer waste into each different polymer type that takes place at the material recovery facilities. The success of the separation process depends on the waste collected (type, purity, complexity of the materials collected) and on the separation methods available at the material recovery facility.²⁰² Polymer waste can be separated according to density (sink-float separation, air classifier, hydrocycloning), electrostatic charge according to the polarity (electrostatic separation), surface wettability (flotation), presence of ferrous particles (magnetic separation), and chemical composition (through visible and near-infrared spectroscopy, laser-induced breakdown spectroscopy, among others).²⁰³

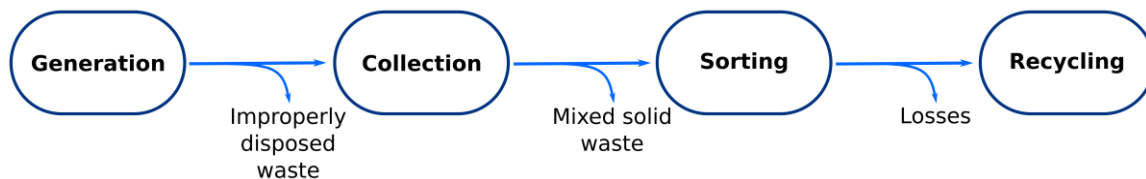


Figure 2.14: Steps from plastic waste generation until recycling and losses that occur at each step. Adapted from ref.²⁰²

The effectiveness of the sorting step can be evaluated by the sorting rate, which compares the total input of a certain polymer to the plant with the output of the same polymer that will move on to the recycling plant:

$$\text{sorting rate} = \frac{\text{bale of target polymer incl. impurities (ww)}}{\text{input of polymer to the plant (ww)}} \% \quad (2.1)$$

Despite all of the above-mentioned methods, the sorting rates of most polymers remain far from a no-loss scenario. The average sorting rate in the EU for PP is 55%, whereas HDPE reaches 76%, which is the one of the highest average of the polymers analyzed in the work by Antonopoulos et al, second only to polyethylene terephthalate (PET).²⁰² Improvements to the sorting rate need to take into account not only the process itself but also its cost, so that recycled plastics can remain competitive with virgin plastics. Balancing these two parameters can be particularly challenging for multilayered packaging.²⁰⁴ In the case of polyolefins, mixed polyolefin waste fractions (MPO) produced with relative ease using flotation sorting techniques,^{203,205} are a common solution to cut the costs associated with the thorough separation of PP and PE from a mixed waste input. These are composed mainly of PP and LDPE residues (HDPE bottles can be sorted out of this fraction),²⁰⁶ and are often sold to energy recovery plants as fuel.²⁰² Mechanical recycling of MPOs, despite its cost-reduction potential, is usually not undertaken since despite their chemical similarities, PE and iPP are immiscible, leading to the resulting recyclates having worse mechanical properties than the virgin materials that generated them. Poor interfacial adhesion between the two phases is responsible for the loss of desirable macroscale mechanical properties, namely, a lower Young's modulus (deform more easily) and lower tensile strength.^{205,207}

Chemical recycling of MPOs through pyrolysis and subsequent recovery of monomers is an alternative, however, a study by Jeswani et al. indicates that this alternative, despite having a 42% lower climate change impact when compared to the production of virgin plastics comes with higher environmental impacts in other categories (acidification and eutrophication) and requires high energy consumptions. Furthermore, when compared to mechanical recycling, chemical recycling had an overall worse environmental performance with a 7% higher climate change impact and significantly higher other environmental impacts (acidification, eutrophication, and generation of

ozone and photochemicals).²⁰⁸

Considering the advantages of mechanical recycling, several approaches are being tested to increase the interfacial adhesion between PE and iPP,^{209,210} of which the use of compatibilizers is of particular interest to this work. Compatibilizers are additives that combine parts compatible with the two phases of the polymer blend in the same molecule. This allows it to be present at the interface of the blend and reduce the interfacial tension, leading to a better phase dispersion and interfacial adhesion (Figure 2.15) and subsequent improvement of mechanical properties, ideally in a cost-efficient manner. By doing so the problem of poor mechanical properties of recycled polymers can be reduced. A comprehensive review on compatibilizers used in recycled PE/PP blends can be found in literature.²⁰⁹

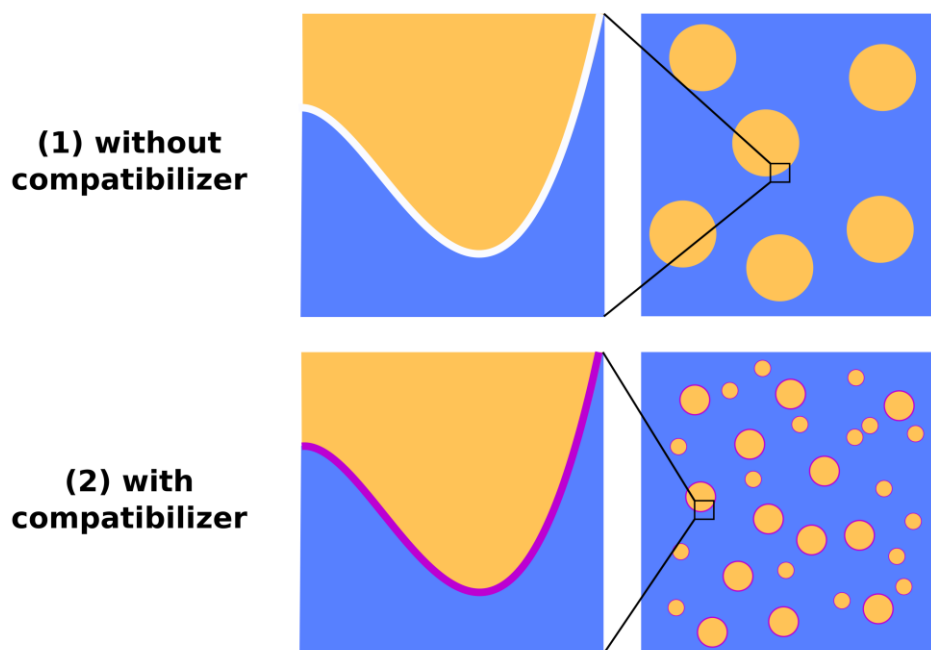


Figure 2.15: Effect of a compatibilizer in a polymer blend consisting of two different phases. The addition of a compatibilizer in blend (2) leads to a finer phase dispersion than that of blend (1) and to more stress resistant morphology.

AFM-IR offers a significant advantage in the analysis of recyclates due to the possibility to record chemical information (through infrared spectra), allowing for the identification of the various components at the nanoscale. This information can only be obtained in a limited way through other techniques such as SEM, TEM, and AFM. Tapping mode was chosen because of the advantages mentioned in section 2.2.1, particularly low lateral forces and lower sensitivity of the cantilever's mechanical resonance to changing mechanical properties.

In this work, a commercial post-consumer recycled polyolefin blend was analyzed at the nanoscale using tapping mode AFM-IR. The sample, derived from an MPO of pre-sorted municipal and household waste, was recycled through mechanical processes and contained no added compatibilizers. Previous analysis of the sample using soluble fraction analysis revealed that the sample contained 8.5% of amorphous content (rubber) with an ethylene content of 46%, and SEM using a RuO₄ showed the presence of an interface between the PE and PP phases. With this in mind, the tapping mode AFM-IR analysis was carried out following the steps described in the previous section.

First a larger area (10 μm x 10 μm) was investigated and after drift correction, the ratio of the

absorptions at 1462 cm^{-1} and 1377 cm^{-1} was calculated. Absorption at 1462 cm^{-1} is associated with the scissor bending vibration of CH_2 groups (present in both PE and PP), whereas the 1377 cm^{-1} absorption corresponds to the symmetric deformation vibration of CH_3 groups, which predominantly exist in the side chains of PP.^{211,212} Thus, by calculating the ratio between the IR absorption at these two wavenumbers it is possible to obtain a map of the distribution of CH_3/CH_2 groups, which corresponds to the two different phases seen in figure 2.16 (b) with purple corresponding to PP and white to PE. This revealed the presence of small ($\approx 500\text{ nm}$ diameter) PP droplets within the PE phase, with so far unknown implications to the mechanical properties.

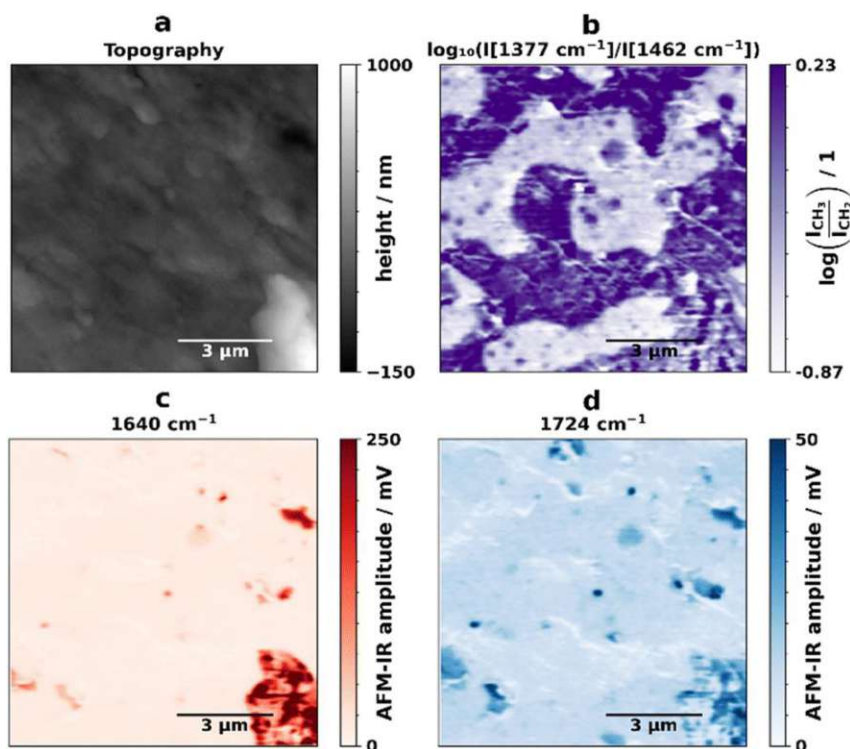


Figure 2.16: IR maps (b,c, d) and topography (a) images over a larger area ($10\text{ }\mu\text{m} \times 10\text{ }\mu\text{m}$) reveal the phase distribution of PE and PP (b) as well as the distribution of PA and PS. Sourced under the terms of CC BY 3.0 license from ref.⁹⁷ (Publication III).

Furthermore, the presence of non-polyolefin polymer contaminants was widely spread in the area analyzed. The contaminant in figure 2.16 (c) was identified as being polyamide (PA), whereas the contaminant in figure 2.16 (d) was initially thought to be polyurethane (PU) due to presence of an absorption band at 1724 cm^{-1} attributed to a carbonyl group, as well as a band at 1602 cm^{-1} attributed to the presence of aromatic double bonds which are often part of the R' group in polyurethane (Figure 2.17).^{213,214}

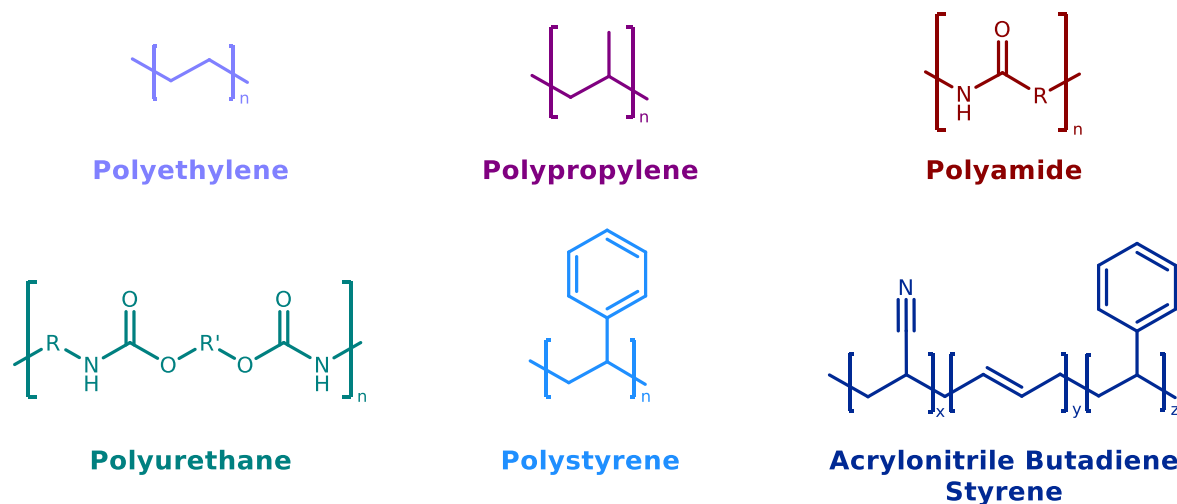


Figure 2.17: Chemical structures of the repeating units of PE, PP, PA, PU, PS and ABS.

However, a later analysis of the spectra obtained in one of the areas with high 1724 cm^{-1} absorption revealed that the initially thought to be PU is in reality either oxidized polystyrene (PS) or oxidized acrylonitrile butadiene styrene (ABS). The AFM-IR spectrum (Figure 2.18) has absorption bands at 1602 cm^{-1} , 1492 cm^{-1} , and 1452 cm^{-1} in addition to the carbonyl band, which are a better match with literature spectra of oxidized PS and ABS.^{215,216} Though the mid-IR spectra of PS and ABS are different, the major differentiator bands (e.g. from the nitrile group) are not present in the recorded range and it is thus not possible to make a final assignment. The small band at 1668 cm^{-1} could be indicative of ABS since *trans*-butadiene groups absorb in this region,²¹⁵ but the widespread presence of PA residues might also explain residual absorption in this region (amide I).

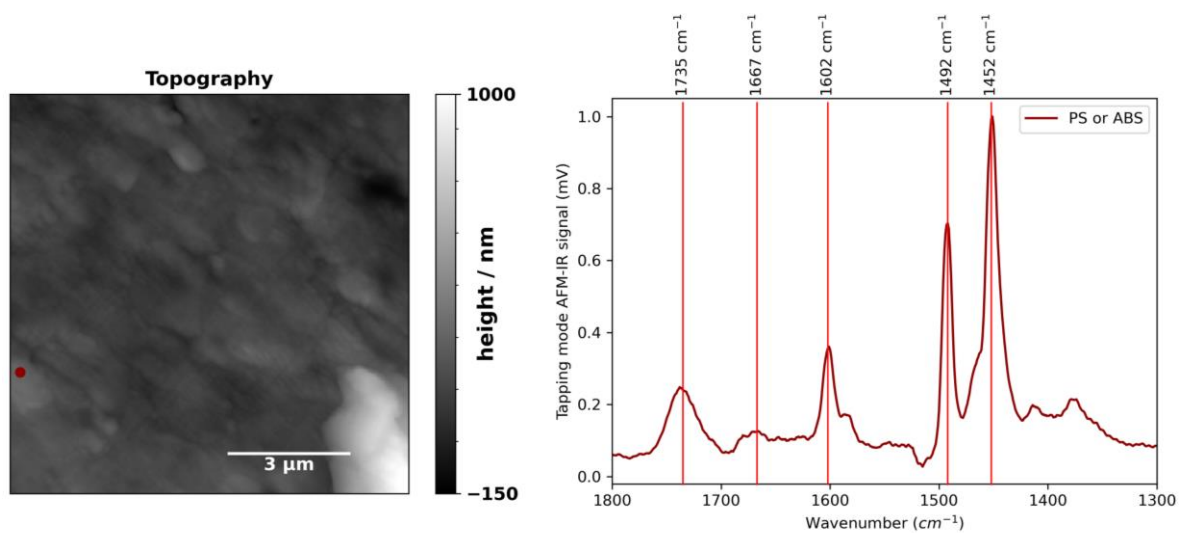


Figure 2.18: AFM-IR spectrum of an area with 1725 cm^{-1} absorption corresponding to PS or ABS.

Besides the identification of non-polyolefin polymer contaminants, AFM-IR was also able to map and identify the compound present at the interface between the PP and PE phases through the combination of AFM-IR imaging with a Gaussian mixture model and of spectra with hierarchical cluster analysis (HCA) (Figure 2.19). By analyzing the average values of the HCA cluster and the Gaussian mixture category corresponding to the interface it was possible to identify it as most likely being ethylene-propylene rubber (EPR), which is known to act as a compatibilizer in PP/PE blends

resulting in finer phase dispersions and improved mechanical properties of the blend.¹⁸⁵

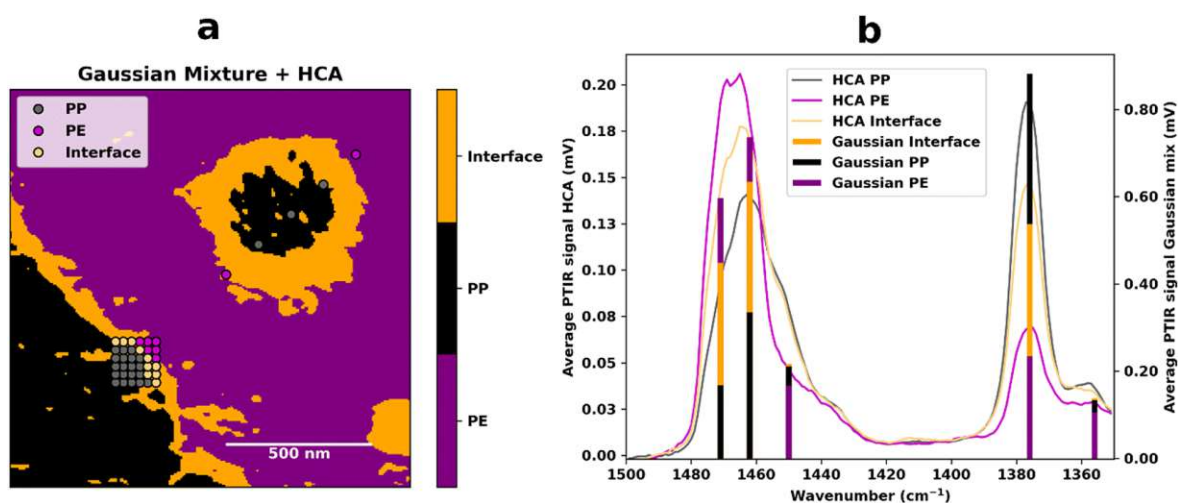


Figure 2.19: (a) Gaussian mixture analysis of AFM-IR maps obtained in a smaller area (1.5 μm x 1.5 μm) and HCA clustering of AFM-IR spectra obtained at the interface; (b) average spectra of each HCA cluster and average value for each Gaussian mixture category (bars for each wavenumber at which an AFM-IR image was recorded). Sourced under the terms of CC BY 3.0 license from ref.⁹⁷ (Publication III).

The presence of EPR at the interface of the PE/PP phases is an interesting result due to its likely role as a cost-free compatibilizer, since it was already present in the initial polyolefin waste fraction. This could mean that sorting MPOs in a way that includes EPR or other known polymer compatibilizers could be a cost-efficient way to improve the mechanical properties of post-consumer polyolefin blends. However, this may prove challenging, as the composition of municipal and post-consumer waste varies with time.

Publication III shows that AFM-IR is a valuable technique for the nanoscale analysis of polymer samples, particularly those with uncertain compositions such as recyclates. The results obtained are in agreement with standard techniques such as SEM and soluble fraction analysis and act as a complement to these techniques by providing chemical information at the nanoscale without the need for cumbersome sample preparation. Furthermore, AFM-IR was able to detect and identify polymer contaminant particles that are below the diffraction limit of conventional FTIR microscopy, as well as the presence of EPR at the interface.

Chapter 3 Conclusion and Outlook

In this thesis, an effort was made to expand the applications of both contact and tapping mode AFM-IR to encompass problems with real-life applications, and to move from proofs of concept and samples created specifically for AFM-IR analysis towards samples originating from every-day situations. This could (and can) only be achieved through cooperation with researchers and companies in other fields that are willing to share and explain their problems, goals and needs, thus allowing for an interdisciplinary approach that aims at providing a more complete view of the samples analyzed and a better understanding of AFM-IR's potential.

In the field of the life sciences, a combination of AFM-IR, fluorescence microscopy and chemometrics allowed for the mapping of β -sheet containing cellulases and xylanases in an industrially-relevant fungi, *T. Reesei*. One of the largest challenges of unstained mid-IR microscopy, its sensitivity to all proteins, was overcome with the help of an external reference that does not significantly interfere with the overall protein composition of the cell. This approach could be extended to other types of organisms as well, such as bacteria, and is not limited to the analysis of soluble proteins, but may also include inclusion bodies. Additionally, a perspective article summarizing the latest applications of AFM-IR to the life sciences and highlighting potential future developments was published.

In the field of polymer sciences, the first step was to establish a protocol that would permit the reliable analysis of such samples. To reach this goal it was necessary to optimize the sample preparation conditions (cutting below the glass transition temperature), without which it is difficult to achieve artifact-free measurements or to reach the full potential that AFM-IR has in this field. The effectiveness of the established workflow was demonstrated in four different samples, all of which are commercially available materials: two virgin plastics and two post-consumer recyclates. Furthermore, this work highlights the benefits of tapping mode AFM-IR in the analysis of soft and heterogeneous polymer samples, due to its lower sensitivity to changing mechanical properties.

A further step was taken in which tapping mode AFM-IR was used to elucidate the nanoscale composition of another commercially available post-consumer polyolefin waste recyclate blend. Here, the interface between the two phases observed in SEM could be identified as being EPR, which appears to act as a compatibilizer, opening the way for more cost-efficient blend recycling approaches. Furthermore, the presence of micro- and nano-scale contaminants was mapped and the contaminants identified. In the future AFM-IR studies might become part of the routine analysis of polymers and feature in polymer science works as one of several characterization techniques, as

is already the case for more established analytical techniques such as SEM, TEM, and AFM. A major advantage of AFM-IR is its non-destructive nature, which allows for the same sample to be analyzed with other techniques once the measurements are concluded.

This thesis shows that AFM-IR has reached a development stage where it is mature enough to be a part of interdisciplinary works in conjunction with other techniques. The recent development of a surface sensitive mode might help simplify the sample preparation protocols for polymer samples, for which in the future a simpler cryo-polishing of the sample's surface (instead of the sectioning described here) might suffice. Nonetheless, some of limitations of AFM-IR remain its low throughput, long measurement times, requirement of specialized operators, and the extreme sensitivity of the instrumentation to the ambient conditions of the room it is located in. However, since the technique is relatively young and new modes are still being developed, instrumental improvements can be expected that will mitigate some of these current disadvantages.

Bibliography

- (1) Larkin, P. J. *IR and Raman Spectroscopy: Principles and Spectral Interpretation*; Elsevier, 2011.
- (2) Griffiths, P. R. Introduction to the Theory and Instrumentation for Vibrational Spectroscopy. In *Handbook of Vibrational Spectroscopy*; John Wiley & Sons, Ltd, 2010. <https://doi.org/10.1002/0470027320.s8935>.
- (3) Thompson, J. M. *Infrared Spectroscopy*; Jenny Stanford Publishing: New York, 2018. <https://doi.org/10.1201/9781351206037>.
- (4) Griffiths, P. R.; De Haseth, J. A. *Fourier Transform Infrared Spectrometry*, 2nd ed.; Chemical analysis; Wiley-Interscience: Hoboken, N.J, 2007.
- (5) IUPAC. *Compendium of Chemical Terminology: The Gold Book*, 2nd ed.; McNaught, A. D., Wilkinson, A., Chalk, S. J., Eds.; Blackwell Scientific Publications: Oxford, 1997. <https://doi.org/10.1351/goldbook>.
- (6) Dabrowska, A.; Lindner, S.; Schwaighofer, A.; Lendl, B. Mid-IR Dispersion Spectroscopy – A New Avenue for Liquid Phase Analysis. *Spectrochimica Acta Part A: Molecular and Biomolecular Spectroscopy* **2022**, 122014. <https://doi.org/10.1016/j.saa.2022.122014>.
- (7) Hermann, D. R.; Ramer, G.; Kitzler-Zeiler, M.; Lendl, B. Quantum Cascade Laser-Based Vibrational Circular Dichroism Augmented by a Balanced Detection Scheme. *Anal. Chem.* **2022**, 94 (29), 10384–10390. <https://doi.org/10.1021/acs.analchem.2c01269>.
- (8) Ricchiuti, G.; Dabrowska, A.; Pinto, D.; Ramer, G.; Lendl, B. Dual-Beam Photothermal Spectroscopy Employing a Mach–Zehnder Interferometer and an External Cavity Quantum Cascade Laser for Detection of Water Traces in Organic Solvents. *Anal. Chem.* **2022**, 94 (47), 16353–16360. <https://doi.org/10.1021/acs.analchem.2c03303>.
- (9) Pinto, D.; Waclawek, J. P.; Lindner, S.; Moser, H.; Ricchiuti, G.; Lendl, B. Wavelength Modulated Diode Probe Laser for an Interferometric Cavity-Assisted Photothermal Spectroscopy Gas Sensor. *Sensors and Actuators B: Chemical* **2023**, 377, 133061. <https://doi.org/10.1016/j.snb.2022.133061>.
- (10) Hayden, J.; Giglio, M.; Sampaolo, A.; Spagnolo, V.; Lendl, B. Mid-Infrared Intracavity Quartz-Enhanced Photoacoustic Spectroscopy with Pptv – Level Sensitivity Using a T-Shaped Custom Tuning Fork. *Photoacoustics* **2022**, 25, 100330. <https://doi.org/10.1016/j.pacs.2022.100330>.
- (11) Gautam, R.; Samuel, A.; Sil, S.; Chaturvedi, D.; Dutta, A.; Ariese, F.; Umopathy, S. Raman and Mid-Infrared Spectroscopic Imaging: Applications and Advancements. *Current Science* **2015**, 108 (3), 341–356.
- (12) Miller, L. M.; Smith, R. J. Synchrotrons versus Globars, Point-Detectors versus Focal Plane Arrays: Selecting the Best Source and Detector for Specific Infrared Microspectroscopy and Imaging Applications. *Vibrational Spectroscopy* **2005**, 38 (1), 237–240. <https://doi.org/10.1016/j.vibspec.2005.03.010>.
- (13) Wagner, C. Application of Microfluidic Devices for Time Resolved FTIR Spectroscopy. Thesis, Technische Universität Wien, Vienna, 2012. <https://repositum.tuwien.at/handle/20.500.12708/12950> (accessed 2022-09-19).
- (14) Schwaighofer, A.; Brandstetter, M.; Lendl, B. Quantum Cascade Lasers (QCLs) in Biomedical Spectroscopy. *Chemical Society Reviews* **2017**, 46 (19), 5903–5924. <https://doi.org/10.1039/C7CS00403F>.
- (15) Sedman, J.; Ghetler, A.; Enfield, A.; Ismail, A. A. Infrared Imaging: Principles and Practices. In *Handbook of Vibrational Spectroscopy*; John Wiley & Sons, Ltd, 2010. <https://doi.org/10.1002/0470027320.s8938>.
- (16) Prati, S.; Joseph, E.; Scitutto, G.; Mazzeo, R. New Advances in the Application of FTIR Microscopy and Spectroscopy for the Characterization of Artistic Materials. *Acc. Chem. Res.* **2010**, 43 (6), 792–801. <https://doi.org/10.1021/ar900274f>.
- (17) Townsend, D.; Miljković, M.; Bird, B.; Lenau, K.; Old, O.; Almond, M.; Kendall, C.; Lloyd, G.; Shepherd, N.; Barr, H.; Stone, N.; Diem, M. Infrared Micro-Spectroscopy for Cyto-Pathological Classification of Esophageal Cells. *Analyst* **2015**, 140 (7), 2215–2223. <https://doi.org/10.1039/C4AN01884B>.

- (18) Peñaranda, F.; Naranjo, V.; Lloyd, G. R.; Kastl, L.; Kemper, B.; Schnekenburger, J.; Nallala, J.; Stone, N. Discrimination of Skin Cancer Cells Using Fourier Transform Infrared Spectroscopy. *Computers in Biology and Medicine* **2018**, *100*, 50–61. <https://doi.org/10.1016/j.compbiomed.2018.06.023>.
- (19) Tint, D.; Stabler, C. T.; Hanifi, A.; Yousefi, F.; Linkov, G.; Hy, K.; Soliman, A. M. S.; Pleshko, N. Spectroscopic Analysis of Human Tracheal Tissue during Decellularization. *Otolaryngol Head Neck Surg* **2019**, *160* (2), 302–309. <https://doi.org/10.1177/0194599818806271>.
- (20) Chrabaszcz, K.; Jasztal, A.; Smęda, M.; Zieliński, B.; Błat, A.; Diem, M.; Chłopicki, S.; Malek, K.; Marzec, K. M. Label-Free FTIR Spectroscopy Detects and Visualizes the Early Stage of Pulmonary Micrometastasis Seeded from Breast Carcinoma. *Biochimica et Biophysica Acta (BBA) - Molecular Basis of Disease* **2018**, *1864* (11), 3574–3584. <https://doi.org/10.1016/j.bbadis.2018.08.022>.
- (21) Wrobel, T. P.; Bhargava, R. Infrared Spectroscopic Imaging Advances as an Analytical Technology for Biomedical Sciences. *Anal. Chem.* **2018**, *90* (3), 1444–1463. <https://doi.org/10.1021/acs.analchem.7b05330>.
- (22) Mukherjee, P.; Ghosh, A.; Spegazzini, N.; Lamborn, M. J.; Monwar, M. M.; DesLauriers, P. J.; Bhargava, R. Relating Post-Yield Mechanical Behavior in Polyethylenes to Spatially Varying Molecular Deformation Using Infrared Spectroscopic Imaging: Homopolymers. *Macromolecules* **2018**, *51* (10), 3836–3844. <https://doi.org/10.1021/acs.macromol.8b00363>.
- (23) Ling, C.; Sommer, A. J. The Advantages of an Attenuated Total Internal Reflection Infrared Microspectroscopic Imaging Technique for the Analysis of Polymer Laminates. *Microscopy and Microanalysis* **2015**, *21* (3), 626–636. <https://doi.org/10.1017/S1431927615000410>.
- (24) Chalmers, J. M.; Everall, N. J.; Schaeberle, M. D.; Levin, I. W.; Neil Lewis, E.; Kidder, L. H.; Wilson, J.; Crocombe, R. FT-IR Imaging of Polymers: An Industrial Appraisal. *Vibrational Spectroscopy* **2002**, *30* (1), 43–52. [https://doi.org/10.1016/S0924-2031\(02\)00037-1](https://doi.org/10.1016/S0924-2031(02)00037-1).
- (25) Liu, G.-L.; Kazarian, S. G. Recent Advances and Applications to Cultural Heritage Using ATR-FTIR Spectroscopy and ATR-FTIR Spectroscopic Imaging. *Analyst* **2022**, *147* (9), 1777–1797. <https://doi.org/10.1039/D2AN00005A>.
- (26) Spring, M.; Ricci, C.; Peggie, D. A.; Kazarian, S. G. ATR-FTIR Imaging for the Analysis of Organic Materials in Paint Cross Sections: Case Studies on Paint Samples from the National Gallery, London. *Anal Bioanal Chem* **2008**, *392* (1), 37–45. <https://doi.org/10.1007/s00216-008-2092-y>.
- (27) Sharaha, U.; Rodriguez-Diaz, E.; Sagi, O.; Riesenberger, K.; Salman, A.; Bigio, I. J.; Huleihel, M. Fast and Reliable Determination of Escherichia Coli Susceptibility to Antibiotics: Infrared Microscopy in Tandem with Machine Learning Algorithms. *Journal of Biophotonics* **2019**, *12* (7), e201800478. <https://doi.org/10.1002/jbio.201800478>.
- (28) Suleiman, M.; Abu-Aqil, G.; Sharaha, U.; Riesenberger, K.; Sagi, O.; Lapidot, I.; Huleihel, M.; Salman, A. Rapid Detection of Klebsiella Pneumoniae Producing Extended Spectrum β Lactamase Enzymes by Infrared Microspectroscopy and Machine Learning Algorithms. *Analyst* **2021**, *146* (4), 1421–1429. <https://doi.org/10.1039/D0AN02182B>.
- (29) Ramer, G.; Lendl, B. Attenuated Total Reflection Fourier Transform Infrared Spectroscopy. In *Encyclopedia of Analytical Chemistry*; John Wiley & Sons, Ltd, 2013. <https://doi.org/10.1002/9780470027318.a9287>.
- (30) Tamburini, F.; Anzolin, G.; Umbriaco, G.; Bianchini, A.; Barbieri, C. Overcoming the Rayleigh Criterion Limit with Optical Vortices. *Phys. Rev. Lett.* **2006**, *97* (16), 163903. <https://doi.org/10.1103/PhysRevLett.97.163903>.
- (31) Eaton, P.; West, P. *Atomic Force Microscopy*; Oxford University Press, 2010.
- (32) Binnig, G.; Quate, C. F.; Gerber, Ch. Atomic Force Microscope. *Phys. Rev. Lett.* **1986**, *56* (9), 930–933. <https://doi.org/10.1103/PhysRevLett.56.930>.
- (33) Sudarsan, V. Chapter 4 - Materials for Hostile Chemical Environments. In *Materials Under Extreme Conditions*; Tyagi, A. K., Banerjee, S., Eds.; Elsevier: Amsterdam, 2017; pp 129–158. <https://doi.org/10.1016/B978-0-12-801300-7.00004-8>.
- (34) Abramovitch, D. Y.; Andersson, S. B.; Pao, L. Y.; Schitter, G. A Tutorial on the Mechanisms,

- Dynamics, and Control of Atomic Force Microscopes. In *2007 American Control Conference*; 2007; pp 3488–3502. <https://doi.org/10.1109/ACC.2007.4282300>.
- (35) Eaton, P.; West, P. AFM Instrumentation. In *Atomic Force Microscopy*; Oxford University Press, 2010.
- (36) Eaton, P.; West, P. AFM Modes. In *Atomic Force Microscopy*; Oxford University Press, 2010.
- (37) Rabe, U.; Janser, K.; Arnold, W. Vibrations of Free and Surface-coupled Atomic Force Microscope Cantilevers: Theory and Experiment. *Review of Scientific Instruments* **1996**, *67* (9), 3281–3293. <https://doi.org/10.1063/1.1147409>.
- (38) Hayek, S. I. Mechanical Vibration and Damping. In *digital Encyclopedia of Applied Physics*; John Wiley & Sons, Ltd, 2003. <https://doi.org/10.1002/3527600434.eap231>.
- (39) Nemes-Incze, P.; Osváth, Z.; Kamarás, K.; Biró, L. P. Anomalies in Thickness Measurements of Graphene and Few Layer Graphite Crystals by Tapping Mode Atomic Force Microscopy. *Carbon* **2008**, *46* (11), 1435–1442. <https://doi.org/10.1016/j.carbon.2008.06.022>.
- (40) Fang, H. H. P.; Chan, K.-Y.; Xu, L.-C. Quantification of Bacterial Adhesion Forces Using Atomic Force Microscopy (AFM). *Journal of Microbiological Methods* **2000**, *40* (1), 89–97. [https://doi.org/10.1016/S0167-7012\(99\)00137-2](https://doi.org/10.1016/S0167-7012(99)00137-2).
- (41) Núñez, M. E.; Martin, M. O.; Chan, P. H.; Duong, L. K.; Sindhurakar, A. R.; Spain, E. M. Atomic Force Microscopy of Bacterial Communities. In *Methods in Enzymology*; Environmental Microbiology; Academic Press, 2005; Vol. 397, pp 256–268. [https://doi.org/10.1016/S0076-6879\(05\)97015-8](https://doi.org/10.1016/S0076-6879(05)97015-8).
- (42) Kaminskyj, S. G. W.; Dahms, T. E. S. High Spatial Resolution Surface Imaging and Analysis of Fungal Cells Using SEM and AFM. *Micron* **2008**, *39* (4), 349–361. <https://doi.org/10.1016/j.micron.2007.10.023>.
- (43) Seo, Y.; Jhe, W. Atomic Force Microscopy and Spectroscopy. *Rep. Prog. Phys.* **2007**, *71* (1), 016101. <https://doi.org/10.1088/0034-4885/71/1/016101>.
- (44) Paulo, Á. S.; García, R. Unifying Theory of Tapping-Mode Atomic-Force Microscopy. *Phys. Rev. B* **2002**, *66* (4), 041406. <https://doi.org/10.1103/PhysRevB.66.041406>.
- (45) García, R.; San Paulo, A. Attractive and Repulsive Tip-Sample Interaction Regimes in Tapping-Mode Atomic Force Microscopy. *Phys. Rev. B* **1999**, *60* (7), 4961–4967. <https://doi.org/10.1103/PhysRevB.60.4961>.
- (46) Schmitz, I.; Schreiner, M.; Friedbacher, G.; Grasserbauer, M. Phase Imaging as an Extension to Tapping Mode AFM for the Identification of Material Properties on Humidity-Sensitive Surfaces. *Applied Surface Science* **1997**, *115* (2), 190–198. [https://doi.org/10.1016/S0169-4332\(97\)80204-8](https://doi.org/10.1016/S0169-4332(97)80204-8).
- (47) Magonov, S. N.; Elings, V.; Whangbo, M.-H. Phase Imaging and Stiffness in Tapping-Mode Atomic Force Microscopy. *Surface Science* **1997**, *375* (2), L385–L391. [https://doi.org/10.1016/S0039-6028\(96\)01591-9](https://doi.org/10.1016/S0039-6028(96)01591-9).
- (48) Berquand, A.; Mazeran, P.-E.; Laval, J.-M. Influence of Volume and Surface Properties on Phase Contrast in Tapping Mode Atomic Force Microscopy. *Surface Science* **2003**, *523* (1), 125–130. [https://doi.org/10.1016/S0039-6028\(02\)02455-X](https://doi.org/10.1016/S0039-6028(02)02455-X).
- (49) Stark, R. W.; Drobek, T.; Heckl, W. M. Tapping-Mode Atomic Force Microscopy and Phase-Imaging in Higher Eigenmodes. *Appl. Phys. Lett.* **1999**, *74* (22), 3296–3298. <https://doi.org/10.1063/1.123323>.
- (50) Margeat, E.; Le Grimellec, C.; Royer, C. A. Visualization of Trp Repressor and Its Complexes with DNA by Atomic Force Microscopy. *Biophysical Journal* **1998**, *75* (6), 2712–2720. [https://doi.org/10.1016/S0006-3495\(98\)77715-X](https://doi.org/10.1016/S0006-3495(98)77715-X).
- (51) Magonov, S. N.; Cleveland, J.; Elings, V.; Denley, D.; Whangbo, M.-H. Tapping-Mode Atomic Force Microscopy Study of the near-Surface Composition of a Styrene-Butadiene-Styrene Triblock Copolymer Film. *Surface Science* **1997**, *389* (1), 201–211. [https://doi.org/10.1016/S0039-6028\(97\)00412-3](https://doi.org/10.1016/S0039-6028(97)00412-3).
- (52) Farias, E. D.; Passeggi, M. C. G.; Brunetti, V. Tuning Properties of Carbon Surfaces Functionalized with Amino-Ended Dendron Layers by Exploring Their Supramolecular Interactions. *Thin Solid Films* **2017**, *642*, 339–344. <https://doi.org/10.1016/j.tsf.2017.10.005>.

- (53) Dazzi, A.; Prazeres, R.; Glotin, F.; Ortega, J. M. Local Infrared Microspectroscopy with Subwavelength Spatial Resolution with an Atomic Force Microscope Tip Used as a Photothermal Sensor. *Opt. Lett.*, **OL** **2005**, *30* (18), 2388–2390. <https://doi.org/10.1364/OL.30.002388>.
- (54) J. Schwartz, J.; S. Jakob, D.; Centrone, A. A Guide to Nanoscale IR Spectroscopy: Resonance Enhanced Transduction in Contact and Tapping Mode AFM-IR. *Chemical Society Reviews* **2022**. <https://doi.org/10.1039/D2CS00095D>.
- (55) Mathurin, J.; Deniset-Besseau, A.; Bazin, D.; Dartois, E.; Wagner, M.; Dazzi, A. Photothermal AFM-IR Spectroscopy and Imaging: Status, Challenges, and Trends. *Journal of Applied Physics* **2022**, *131* (1), 010901. <https://doi.org/10.1063/5.0063902>.
- (56) Ren, T.; Wu, C.; Yu, Y.; Dai, T.; Chen, F.; Pan, Q. Development Progress of 3–5 Mm Mid-Infrared Lasers: OPO, Solid-State and Fiber Laser. *Applied Sciences* **2021**, *11* (23), 11451. <https://doi.org/10.3390/app112311451>.
- (57) Dazzi, A.; Glotin, F.; Carminati, R. Theory of Infrared Nanospectroscopy by Photothermal Induced Resonance. *Journal of Applied Physics* **2010**, *107* (12), 124519. <https://doi.org/10.1063/1.3429214>.
- (58) Dazzi, A.; Prater, C. B.; Hu, Q.; Chase, D. B.; Rabolt, J. F.; Marcott, C. AFM-IR: Combining Atomic Force Microscopy and Infrared Spectroscopy for Nanoscale Chemical Characterization. *Appl Spectrosc* **2012**, *66* (12), 1365–1384. <https://doi.org/10.1366/12-06804>.
- (59) Chae, J.; An, S.; Ramer, G.; Stavila, V.; Holland, G.; Yoon, Y.; Talin, A. A.; Allendorf, M.; Aksyuk, V. A.; Centrone, A. Nanophotonic Atomic Force Microscope Transducers Enable Chemical Composition and Thermal Conductivity Measurements at the Nanoscale. *Nano Lett.* **2017**, *17* (9), 5587–5594. <https://doi.org/10.1021/acs.nanolett.7b02404>.
- (60) Schwartz, J. J.; Pavlidis, G.; Centrone, A. Understanding Cantilever Transduction Efficiency and Spatial Resolution in Nanoscale Infrared Microscopy. *Anal. Chem.* **2022**. <https://doi.org/10.1021/acs.analchem.2c02612>.
- (61) Lu, F.; Jin, M.; Belkin, M. A. Tip-Enhanced Infrared Nanospectroscopy via Molecular Expansion Force Detection. *Nature Photonics* **2014**, *8* (4), 307–312. <https://doi.org/10.1038/nphoton.2013.373>.
- (62) Wieland, K.; Ramer, G.; Weiss, V. U.; Allmaier, G.; Lendl, B.; Centrone, A. Nanoscale Chemical Imaging of Individual Chemotherapeutic Cytarabine-Loaded Liposomal Nanocarriers. *Nano Research* **2019**, *12* (1), 197–203. <https://doi.org/10.1007/s12274-018-2202-x>.
- (63) Ramer, G.; Aksyuk, V. A.; Centrone, A. Quantitative Chemical Analysis at the Nanoscale Using the PTIR Technique. *Analytical Chemistry* **2017**, *89* (24), 13524–13531. <https://doi.org/10.1021/acs.analchem.7b03878>.
- (64) V. D. dos Santos, A. C.; Lendl, B.; Ramer, G. Systematic Analysis and Nanoscale Chemical Imaging of Polymers Using Photothermal-Induced Resonance (AFM-IR) Infrared Spectroscopy. *Polymer Testing* **2022**, *106*, 107443. <https://doi.org/10.1016/j.polymertesting.2021.107443>.
- (65) Barlow, D. E.; Biffinger, J. C.; Cockrell-Zugell, A. L.; Lo, M.; Kjoller, K.; Cook, D.; Lee, W. K.; Pehrsson, P. E.; Crookes-Goodson, W. J.; Hung, C.-S.; Nadeau, L. J.; Russell, J. N. The Importance of Correcting for Variable Probe-Sample Interactions in AFM-IR Spectroscopy: AFM-IR of Dried Bacteria on a Polyurethane Film. *Analyst* **2016**, *141* (16), 4848–4854. <https://doi.org/10.1039/C6AN00940A>.
- (66) Ramer, G.; Ruggeri, F. S.; Levin, A.; Knowles, T. P. J.; Centrone, A. Determination of Polypeptide Conformation with Nanoscale Resolution in Water. *ACS Nano* **2018**, *12* (7), 6612–6619. <https://doi.org/10.1021/acsnano.8b01425>.
- (67) V. D. dos Santos, A. C.; Hondl, N.; Ramos-Garcia, V.; Kuligowski, J.; Lendl, B.; Ramer, G. AFM-IR for Nanoscale Chemical Characterization in Life Sciences: Recent Developments and Future Directions. *ACS Meas. Sci. Au* **2023**. <https://doi.org/10.1021/acsmesuresciau.3c00010>.
- (68) Rizevsky, S.; Zhaliyazka, K.; Dou, T.; Matveyenka, M.; Kurouski, D. Characterization of Substrates and Surface-Enhancement in Atomic Force Microscopy Infrared Analysis of Amyloid Aggregates. *J. Phys. Chem. C* **2022**, *126* (8), 4157–4162.

- <https://doi.org/10.1021/acs.jpcc.1c09643>.
- (69) Wang, C.-T.; Jiang, B.; Zhou, Y.-W.; Jiang, T.-W.; Liu, J.-H.; Zhu, G.-D.; Cai, W.-B. Exploiting the Surface-Enhanced IR Absorption Effect in the Photothermally Induced Resonance AFM-IR Technique toward Nanoscale Chemical Analysis. *Anal. Chem.* **2019**, *91* (16), 10541–10548. <https://doi.org/10.1021/acs.analchem.9b01554>.
- (70) Morsch, S.; Lyon, S. B.; Edmondson, S.; Gibbon, S. R. Reflectance in AFM-IR: Implications for Interpretation and Remote Analysis of the Buried Interface. *Anal. Chem.* **2020**, *92* (12), 8117–8124. <https://doi.org/10.1021/acs.analchem.9b05793>.
- (71) Katzenmeyer, A. M.; Holland, G.; Kjoller, K.; Centrone, A. Absorption Spectroscopy and Imaging from the Visible through Mid-Infrared with 20 Nm Resolution. *Anal. Chem.* **2015**, *87* (6), 3154–3159. <https://doi.org/10.1021/ac504672t>.
- (72) Lahiri, B.; Holland, G.; Centrone, A. Chemical Imaging Beyond the Diffraction Limit: Experimental Validation of the PTIR Technique. *Small* **2013**, *9* (3), 439–445. <https://doi.org/10.1002/smll.201200788>.
- (73) Kurouski, D.; Dazzi, A.; Zenobi, R.; Centrone, A. Infrared and Raman Chemical Imaging and Spectroscopy at the Nanoscale. *Chem. Soc. Rev.* **2020**, *49* (11), 3315–3347. <https://doi.org/10.1039/C8CS00916C>.
- (74) Lu, F.; Belkin, M. A. Infrared Absorption Nano-Spectroscopy Using Sample Photoexpansion Induced by Tunable Quantum Cascade Lasers. *Opt. Express, OE* **2011**, *19* (21), 19942–19947. <https://doi.org/10.1364/OE.19.019942>.
- (75) Quaroni, L. Understanding and Controlling Spatial Resolution, Sensitivity, and Surface Selectivity in Resonant-Mode Photothermal-Induced Resonance Spectroscopy. *Anal. Chem.* **2020**, *92* (5), 3544–3554. <https://doi.org/10.1021/acs.analchem.9b03468>.
- (76) Ramer, G.; Reisenbauer, F.; Steindl, B.; Tomischko, W.; Lendl, B. Implementation of Resonance Tracking for Assuring Reliability in Resonance Enhanced Photothermal Infrared Spectroscopy and Imaging. *Appl Spectrosc* **2017**, *71* (8), 2013–2020. <https://doi.org/10.1177/0003702817695290>.
- (77) Kenkel, S.; Mittal, A.; Mittal, S.; Bhargava, R. Probe–Sample Interaction-Independent Atomic Force Microscopy–Infrared Spectroscopy: Toward Robust Nanoscale Compositional Mapping. *Anal. Chem.* **2018**, *90* (15), 8845–8855. <https://doi.org/10.1021/acs.analchem.8b00823>.
- (78) Baldassarre, L.; Giliberti, V.; Rosa, A.; Ortolani, M.; Bonamore, A.; Baiocco, P.; Kjoller, K.; Calvani, P.; Nucara, A. Mapping the Amide I Absorption in Single Bacteria and Mammalian Cells with Resonant Infrared Nanospectroscopy. *Nanotechnology* **2016**, *27* (7), 075101. <https://doi.org/10.1088/0957-4484/27/7/075101>.
- (79) V. D. dos Santos, A. C.; Heydenreich, R.; Derntl, C.; Mach-Aigner, A. R.; Mach, R. L.; Ramer, G.; Lendl, B. Nanoscale Infrared Spectroscopy and Chemometrics Enable Detection of Intracellular Protein Distribution. *Anal. Chem.* **2020**, *92* (24), 15719–15725. <https://doi.org/10.1021/acs.analchem.0c02228>.
- (80) Liu, Z.; Zeng, H.; Xu, K.; Zhao, K.; Fu Liu, Z.; Yao, J.; You, Y.; Wang, D. AFM-IR Probing the Influence of Polarization on the Expression of Protein within Single Macrophages. *Journal of Materials Chemistry B* **2021**. <https://doi.org/10.1039/D0TB02584D>.
- (81) Giliberti, V.; Badioli, M.; Nucara, A.; Calvani, P.; Ritter, E.; Puskar, L.; Aziz, E. F.; Hegemann, P.; Schade, U.; Ortolani, M.; Baldassarre, L. Heterogeneity of the Transmembrane Protein Conformation in Purple Membranes Identified by Infrared Nanospectroscopy. *Small* **2017**, *13* (44), 1701181. <https://doi.org/10.1002/smll.201701181>.
- (82) Rizevsky, S.; Kurouski, D. Nanoscale Structural Organization of Insulin Fibril Polymorphs Revealed by Atomic Force Microscopy–Infrared Spectroscopy (AFM-IR). *ChemBioChem* **2020**, *21* (4), 481–485. <https://doi.org/10.1002/cbic.201900394>.
- (83) Nguyen-Tri, P.; Ghassemi, P.; Carriere, P.; Nanda, S.; Assadi, A. A.; Nguyen, D. D. Recent Applications of Advanced Atomic Force Microscopy in Polymer Science: A Review. *Polymers* **2020**, *12* (5), 1142. <https://doi.org/10.3390/polym12051142>.
- (84) Tang, F.; Bao, P.; Roy, A.; Wang, Y.; Su, Z. In-Situ Spectroscopic and Thermal Analyses of Phase Domains in High-Impact Polypropylene. *Polymer* **2018**, *142*, 155–163.

- <https://doi.org/10.1016/j.polymer.2018.03.037>.
- (85) Jiang, C.; Jiang, B.; Yang, Y.; Huang, Z.; Liao, Z.; Sun, J.; Wang, J.; Yang, Y. Enhanced Multiphase Interfacial Interaction of Impact Polypropylene Copolymer by In-Situ Introducing Polyethylene. *Polymer* **2021**, *214*, 123373. <https://doi.org/10.1016/j.polymer.2020.123373>.
- (86) Zeng, H.; Li, L.; Liu, F.; Li, M.; Zhang, S.; Zheng, X.; Luo, L.; You, S.; Zhao, Y.; Guo, R.; Gong, Z.; Huang, R.; Li, Z.; Wang, T.; Cui, Y.; Rong, Y.; Li, X. Improved Performance and Stability of Perovskite Solar Modules by Regulating Interfacial Ion Diffusion with Nonionic Cross-Linked 1D Lead-Iodide. *Advanced Energy Materials* **2022**, *12* (1), 2102820. <https://doi.org/10.1002/aenm.202102820>.
- (87) Rao, V. J.; Matthiesen, M.; Goetz, K. P.; Huck, C.; Yim, C.; Siris, R.; Han, J.; Hahn, S.; Bunz, U. H. F.; Dreuw, A.; Duesberg, G. S.; Pucci, A.; Zaumseil, J. AFM-IR and IR-SNOM for the Characterization of Small Molecule Organic Semiconductors. *J. Phys. Chem. C* **2020**, *124* (9), 5331–5344. <https://doi.org/10.1021/acs.jpcc.9b11056>.
- (88) Jubb, A. M.; Birdwell, J. E.; Hackley, P. C.; Hatcherian, J. J.; Qu, J. Nanoscale Molecular Composition of Solid Bitumen from the Eagle Ford Group across a Natural Thermal Maturity Gradient. *Energy Fuels* **2020**, *34* (7), 8167–8177. <https://doi.org/10.1021/acs.energyfuels.0c00963>.
- (89) Jubb, A. M.; Hackley, P. C.; Birdwell, J. E.; Hatcherian, J. J.; Qu, J. Examination of Inertinite within Immature Eagle Ford Shale at the Nanometer-Scale Using Atomic Force Microscopy-Based Infrared Spectroscopy. *International Journal of Coal Geology* **2020**, *231*, 103608. <https://doi.org/10.1016/j.coal.2020.103608>.
- (90) Tuteja, M.; Kang, M.; Leal, C.; Centrone, A. Nanoscale Partitioning of Paclitaxel in Hybrid Lipid–Polymer Membranes. *Analyst* **2018**, *143* (16), 3808–3813. <https://doi.org/10.1039/C8AN00838H>.
- (91) Zurich Instruments. Principles of Lock-in Detection and the State of the Art, 2016. <https://www.zhinst.com/europe/en/resources/principles-of-lock-in-detection>.
- (92) Ma, X.; Beltran, V.; Ramer, G.; Pavlidis, G.; Parkinson, D. Y.; Thoury, M.; Meldrum, T.; Centrone, A.; Berrie, B. H. Revealing the Distribution of Metal Carboxylates in Oil Paint from the Micro- to Nanoscale. *Angewandte Chemie International Edition* **2019**, *58* (34), 11652–11656. <https://doi.org/10.1002/anie.201903553>.
- (93) Mathurin, J.; Deniset-Besseau, A.; Dazzi, A. Advanced Infrared Nanospectroscopy Using Photothermal Induced Resonance Technique, AFMIR: New Approach Using Tapping Mode. *Acta Phys. Pol. A* **2020**, *137* (1), 29–32. <https://doi.org/10.12693/APhysPolA.137.29>.
- (94) Mathurin, J.; Pancani, E.; Deniset-Besseau, A.; Kjoller, K.; B. Prater, C.; Gref, R.; Dazzi, A. How to Unravel the Chemical Structure and Component Localization of Individual Drug-Loaded Polymeric Nanoparticles by Using Tapping AFM-IR. *Analyst* **2018**, *143* (24), 5940–5949. <https://doi.org/10.1039/C8AN01239C>.
- (95) Ma, X.; Pavlidis, G.; Dillon, E.; Beltran, V.; Schwartz, J. J.; Thoury, M.; Borondics, F.; Sandt, C.; Kjoller, K.; Berrie, B. H.; Centrone, A. Micro to Nano: Multiscale IR Analyses Reveal Zinc Soap Heterogeneity in a 19th-Century Painting by Corot. *Anal. Chem.* **2022**, *94* (7), 3103–3110. <https://doi.org/10.1021/acs.analchem.1c04182>.
- (96) Tarpoudi Baheri, F.; Schutzius, T. m.; Poulikakos, D.; Poulikakos, L. d. Bitumen Surface Microstructure Evolution in Subzero Environments. *Journal of Microscopy* **2020**, *279* (1), 3–15. <https://doi.org/10.1111/jmi.12890>.
- (97) V. D. dos Santos, A. C.; Tranchida, D.; Lendl, B.; Ramer, G. Nanoscale Chemical Characterization of a Post-Consumer Recycled Polyolefin Blend Using Tapping Mode AFM-IR. *Analyst* **2022**, *147* (16), 3741–3747. <https://doi.org/10.1039/D2AN00823H>.
- (98) Cremer, C.; Kaufmann, R.; Gunkel, M.; Pres, S.; Weiland, Y.; Müller, P.; Ruckelshausen, T.; Lemmer, P.; Geiger, F.; Degenhard, S.; Wege, C.; Lemmermann, N. A. W.; Holtappels, R.; Strickfaden, H.; Hausmann, M. Superresolution Imaging of Biological Nanostructures by Spectral Precision Distance Microscopy. *Biotechnology Journal* **2011**, *6* (9), 1037–1051. <https://doi.org/10.1002/biot.201100031>.
- (99) Jacquemet, G.; Carisey, A. F.; Hamidi, H.; Henriques, R.; Leterrier, C. The Cell Biologist’s Guide

- to Super-Resolution Microscopy. *Journal of Cell Science* **2020**, *133* (11), jcs240713. <https://doi.org/10.1242/jcs.240713>.
- (100) Lichtman, J. W.; Conchello, J.-A. Fluorescence Microscopy. *Nat Methods* **2005**, *2* (12), 910–919. <https://doi.org/10.1038/nmeth817>.
- (101) Dobrucki, J. W.; Kubitscheck, U. Fluorescence Microscopy. In *Fluorescence Microscopy*; John Wiley & Sons, Ltd, 2017; pp 85–132. <https://doi.org/10.1002/9783527687732.ch3>.
- (102) Chalfie, M.; Tu, Y.; Euskirchen, G.; Ward, W. W.; Prasher, D. C. Green Fluorescent Protein as a Marker for Gene Expression. *Science* **1994**, *263* (5148), 802–805. <https://doi.org/10.1126/science.8303295>.
- (103) Rodriguez, E. A.; Campbell, R. E.; Lin, J. Y.; Lin, M. Z.; Miyawaki, A.; Palmer, A. E.; Shu, X.; Zhang, J.; Tsien, R. Y. The Growing and Glowing Toolbox of Fluorescent and Photoactive Proteins. *Trends in Biochemical Sciences* **2017**, *42* (2), 111–129. <https://doi.org/10.1016/j.tibs.2016.09.010>.
- (104) Cinelli, R. A. G.; Ferrari, A.; Pellegrini, V.; Tyagi, M.; Giacca, M.; Beltram, F. The Enhanced Green Fluorescent Protein as a Tool for the Analysis of Protein Dynamics and Localization: Local Fluorescence Study at the Single-Molecule Level. *Photochemistry and Photobiology* **2000**, *71* (6), 771–776. [https://doi.org/10.1562/0031-8655\(2000\)0710771TEGFA2.0.CO2](https://doi.org/10.1562/0031-8655(2000)0710771TEGFA2.0.CO2).
- (105) Fu, Y.; S. Finney, N. Small-Molecule Fluorescent Probes and Their Design. *RSC Advances* **2018**, *8* (51), 29051–29061. <https://doi.org/10.1039/C8RA02297F>.
- (106) Villamena, F. A. Chapter 4 - Fluorescence Technique. In *Reactive Species Detection in Biology*; Villamena, F. A., Ed.; Elsevier: Boston, 2017; pp 87–162. <https://doi.org/10.1016/B978-0-12-420017-3.00003-7>.
- (107) Masters, B. R. The Development of Fluorescence Microscopy. In *Encyclopedia of Life Sciences (ELS)*; John Wiley & Sons, Ltd, 2010. <https://doi.org/10.1002/9780470015902.a0022093>.
- (108) Webb, D. J.; Brown, C. M. Epi-Fluorescence Microscopy. *Methods Mol Biol* **2013**, *931*, 29–59. https://doi.org/10.1007/978-1-62703-056-4_2.
- (109) Otto, M. Chapter 5 - Pattern Recognition and Classification. In *Chemometrics: Statistics and Computer Application in Analytical Chemistry*; Wiley-VCH Verlag GmbH & Co., 2016; pp 135–211.
- (110) Miller, J. N.; Miller, J. C. Chapter 8 - Multivariate Analysis. In *Statistics and Chemometrics for Analytical Chemistry*; Pearson Education Limited, 2010.
- (111) Otto, M. *Chemometrics: Statistics and Computer Application in Analytical Chemistry*, 3rd ed.; Wiley-VCH Verlag GmbH & Co., 2016.
- (112) Lohninger, H. *Fundamentals of Statistics*; Epina GmbH: Pressbaum, 2012.
- (113) de Amorim, R. C. Feature Relevance in Ward's Hierarchical Clustering Using the LpNorm. *J Classif* **2015**, *32* (1), 46–62. <https://doi.org/10.1007/s00357-015-9167-1>.
- (114) Otto, M. Chapter 6 - Modelling. In *Chemometrics: Statistics and Computer Application in Analytical Chemistry*; Wiley-VCH Verlag GmbH & Co., 2016; pp 213–272.
- (115) Farrés, M.; Platikanov, S.; Tsakovski, S.; Tauler, R. Comparison of the Variable Importance in Projection (VIP) and of the Selectivity Ratio (SR) Methods for Variable Selection and Interpretation. *Journal of Chemometrics* **2015**, *29* (10), 528–536. <https://doi.org/10.1002/cem.2736>.
- (116) Rajalahti, T.; Arneberg, R.; Kroksveen, A. C.; Berle, M.; Myhr, K.-M.; Kvalheim, O. M. Discriminating Variable Test and Selectivity Ratio Plot: Quantitative Tools for Interpretation and Variable (Biomarker) Selection in Complex Spectral or Chromatographic Profiles. *Anal. Chem.* **2009**, *81* (7), 2581–2590. <https://doi.org/10.1021/ac802514y>.
- (117) Chen, T.; Morris, J.; Martin, E. Probability Density Estimation via an Infinite Gaussian Mixture Model: Application to Statistical Process Monitoring. *Journal of the Royal Statistical Society: Series C (Applied Statistics)* **2006**, *55* (5), 699–715. <https://doi.org/10.1111/j.1467-9876.2006.00560.x>.
- (118) Dempster, A. P.; Laird, N. M.; Rubin, D. B. Maximum Likelihood from Incomplete Data Via the EM Algorithm. *Journal of the Royal Statistical Society: Series B (Methodological)* **1977**, *39* (1), 1–22. <https://doi.org/10.1111/j.2517-6161.1977.tb01600.x>.

- (119) Hosseinzadeh, D.; Krishnan, S. Gaussian Mixture Modeling of Keystroke Patterns for Biometric Applications. *IEEE Transactions on Systems, Man, and Cybernetics, Part C (Applications and Reviews)* **2008**, *38* (6), 816–826. <https://doi.org/10.1109/TSMCC.2008.2001696>.
- (120) Goyal, K.; Singhai, J. Review of Background Subtraction Methods Using Gaussian Mixture Model for Video Surveillance Systems. *Artif Intell Rev* **2018**, *50* (2), 241–259. <https://doi.org/10.1007/s10462-017-9542-x>.
- (121) Plataniotis, K. N.; Hatzinakos, D. Gaussian Mixtures and Their Applications to Signal Processing. In *Advanced Signal Processing Handbook*; CRC Press, 2001.
- (122) Moraru, L.; Moldovanu, S.; Dimitrievici, L. T.; Dey, N.; Ashour, A. S.; Shi, F.; Fong, S. J.; Khan, S.; Biswas, A. Gaussian Mixture Model for Texture Characterization with Application to Brain DTI Images. *Journal of Advanced Research* **2019**, *16*, 15–23. <https://doi.org/10.1016/j.jare.2019.01.001>.
- (123) Gupta, C.; Gondhi, N. K.; Lehana, P. K. Analysis and Identification of Dermatological Diseases Using Gaussian Mixture Modeling. *IEEE Access* **2019**, *7*, 99407–99427. <https://doi.org/10.1109/ACCESS.2019.2929857>.
- (124) Prasad, S.; Cui, M.; Li, W.; Fowler, J. E. Segmented Mixture-of-Gaussian Classification for Hyperspectral Image Analysis. *IEEE Geoscience and Remote Sensing Letters* **2014**, *11* (1), 138–142. <https://doi.org/10.1109/LGRS.2013.2250902>.
- (125) Savitzky, Abraham.; Golay, M. J. E. Smoothing and Differentiation of Data by Simplified Least Squares Procedures. *Anal. Chem.* **1964**, *36* (8), 1627–1639. <https://doi.org/10.1021/ac60214a047>.
- (126) Zimmermann, B.; Kohler, A. Optimizing Savitzky–Golay Parameters for Improving Spectral Resolution and Quantification in Infrared Spectroscopy. *Appl Spectrosc* **2013**, *67* (8), 892–902. <https://doi.org/10.1366/12-06723>.
- (127) Berg, J. M.; Tymoczko, J. L.; Gatto, Jr., G. J.; Stryer, L. Chapter 2 - Protein Composition and Structure. In *Biochemistry*; W. H. Freeman and Company, 2015; pp 27–57.
- (128) Alberts, B.; Johnson, A.; Lewis, J.; Raff, M.; Roberts, K.; Walter, P. Membrane Proteins. In *Molecular Biology of the Cell*; Garland Science, 2002.
- (129) Lee, D.; Redfern, O.; Orengo, C. Predicting Protein Function from Sequence and Structure. *Nat Rev Mol Cell Biol* **2007**, *8* (12), 995–1005. <https://doi.org/10.1038/nrm2281>.
- (130) Bischof, R. H.; Ramoni, J.; Seiboth, B. Cellulases and beyond: The First 70 Years of the Enzyme Producer *Trichoderma Reesei*. *Microbial Cell Factories* **2016**, *15* (1), 106. <https://doi.org/10.1186/s12934-016-0507-6>.
- (131) Wells, E.; Robinson, A. S. Cellular Engineering for Therapeutic Protein Production: Product Quality, Host Modification, and Process Improvement. *Biotechnology Journal* **2017**, *12* (1), 1600105. <https://doi.org/10.1002/biot.201600105>.
- (132) Ghosh, A.; Al-Rabaii, S.; Ghosh, B. K.; Trimiño-Vazquez, H.; Eveleigh, D. E.; Montenecourt, B. S. Increased Endoplasmic Reticulum Content of a Mutant of *Trichoderma Reesei* (RUT-C30) in Relation to Cellulase Synthesis. *Enzyme and Microbial Technology* **1982**, *4* (2), 110–113. [https://doi.org/10.1016/0141-0229\(82\)90093-X](https://doi.org/10.1016/0141-0229(82)90093-X).
- (133) Nykänen, M.; Birch, D.; Peterson, R.; Yu, H.; Kautto, L.; Gryshyna, A.; Te’o, J.; Nevalainen, H. Ultrastructural Features of the Early Secretory Pathway in *Trichoderma Reesei*. *Current Genetics* **2016**, *62* (2), 455–465. <https://doi.org/10.1007/s00294-015-0555-1>.
- (134) Lee, Y.-W.; Luther, D. C.; Kretzmann, J. A.; Burden, A.; Jeon, T.; Zhai, S.; Rotello, V. M. Protein Delivery into the Cell Cytosol Using Non-Viral Nanocarriers. *Theranostics* **2019**, *9* (11), 3280–3292. <https://doi.org/10.7150/thno.34412>.
- (135) Patel, S. G.; Sayers, E. J.; He, L.; Narayan, R.; Williams, T. L.; Mills, E. M.; Allemann, R. K.; Luk, L. Y. P.; Jones, A. T.; Tsai, Y.-H. Cell-Penetrating Peptide Sequence and Modification Dependent Uptake and Subcellular Distribution of Green Florescent Protein in Different Cell Lines. *Sci Rep* **2019**, *9* (1), 6298. <https://doi.org/10.1038/s41598-019-42456-8>.
- (136) Huang, B.; Babcock, H.; Zhuang, X. Breaking the Diffraction Barrier: Super-Resolution Imaging of Cells. *Cell* **2010**, *143* (7), 1047–1058. <https://doi.org/10.1016/j.cell.2010.12.002>.
- (137) Schubert, V. Super-Resolution Microscopy – Applications in Plant Cell Research. *Frontiers in*

- Plant Science* **2017**, *8*, 531. <https://doi.org/10.3389/fpls.2017.00531>.
- (138) Bergstrand, J.; Xu, L.; Miao, X.; Li, N.; Öktem, O.; Franzén, B.; Auer, G.; Lomnyska, M.; Widengren, J. Super-Resolution Microscopy Can Identify Specific Protein Distribution Patterns in Platelets Incubated with Cancer Cells. *Nanoscale* **2019**, *11* (20), 10023–10033. <https://doi.org/10.1039/C9NR01967G>.
- (139) Huang, Y.; Ma, T.; Lau, P. K.; Wang, J.; Zhao, T.; Du, S.; Loy, M. M. T.; Guo, Y. Visualization of Protein Sorting at the Trans-Golgi Network and Endosomes Through Super-Resolution Imaging. *Front. Cell Dev. Biol.* **2019**, *7*. <https://doi.org/10.3389/fcell.2019.00181>.
- (140) MacDonald, L.; Baldini, G.; Storrie, B. Does Super-Resolution Fluorescence Microscopy Obsolete Previous Microscopic Approaches to Protein Co-Localization? In *Membrane Trafficking: Second Edition*; Tang, B. L., Ed.; Springer New York: New York, NY, 2015; pp 255–275. https://doi.org/10.1007/978-1-4939-2309-0_19.
- (141) Lambert, T. J.; Waters, J. C. Navigating Challenges in the Application of Superresolution Microscopy. *Journal of Cell Biology* **2016**, *216* (1), 53–63. <https://doi.org/10.1083/jcb.201610011>.
- (142) Samanta, S.; Gong, W.; Li, W.; Sharma, A.; Shim, I.; Zhang, W.; Das, P.; Pan, W.; Liu, L.; Yang, Z.; Qu, J.; Kim, J. S. Organic Fluorescent Probes for Stochastic Optical Reconstruction Microscopy (STORM): Recent Highlights and Future Possibilities. *Coordination Chemistry Reviews* **2019**, *380*, 17–34. <https://doi.org/10.1016/j.ccr.2018.08.006>.
- (143) Egelman, E. H. The Current Revolution in Cryo-EM. *Biophysical Journal* **2016**, *110* (5), 1008–1012. <https://doi.org/10.1016/j.bpj.2016.02.001>.
- (144) Berg, J. M.; Tymoczko, J. L.; Gatto, Jr., G. J.; Stryer, L. Chapter 3 - Exploring Proteins and Proteomes. In *Biochemistry*; W. H. Freeman and Company, 2015; pp 65–104.
- (145) Leelananda, S. P.; Lindert, S. Using NMR Chemical Shifts and Cryo-EM Density Restraints in Iterative Rosetta-MD Protein Structure Refinement. *J. Chem. Inf. Model.* **2020**, *60* (5), 2522–2532. <https://doi.org/10.1021/acs.jcim.9b00932>.
- (146) Yip, K. M.; Fischer, N.; Paknia, E.; Chari, A.; Stark, H. Atomic-Resolution Protein Structure Determination by Cryo-EM. *Nature* **2020**, *587* (7832), 157–161. <https://doi.org/10.1038/s41586-020-2833-4>.
- (147) Ryu, S. R.; Czarnik-Matuszewicz, B.; Dukor, R. K.; Nafie, L. A.; Jung, Y. M. Analysis of the Molten Globule State of Bovine α -Lactalbumin by Using Vibrational Circular Dichroism. *Vibrational Spectroscopy* **2012**, *60*, 68–72. <https://doi.org/10.1016/j.vibspec.2012.02.006>.
- (148) Giugliarelli, A.; Sassi, P.; Paolantoni, M.; Morresi, A.; Dukor, R.; Nafie, L. Vibrational Circular Dichroism Spectra of Lysozyme Solutions: Solvent Effects on Thermal Denaturation Processes. *J. Phys. Chem. B* **2013**, *117* (9), 2645–2652. <https://doi.org/10.1021/jp311268x>.
- (149) Barth, A. Infrared Spectroscopy of Proteins. *Biochimica et Biophysica Acta (BBA) - Bioenergetics* **2007**, *1767* (9), 1073–1101. <https://doi.org/10.1016/j.bbabi.2007.06.004>.
- (150) Singh, B. R. Basic Aspects of the Technique and Applications of Infrared Spectroscopy of Peptides and Proteins. In *Infrared Analysis of Peptides and Proteins*; ACS Symposium Series; American Chemical Society, 1999; Vol. 750, pp 2–37. <https://doi.org/10.1021/bk-2000-0750.ch001>.
- (151) Wilkosz, N.; Czaja, M.; Seweryn, S.; Skirlińska-Nosek, K.; Szymonski, M.; Lipiec, E.; Sofińska, K. Molecular Spectroscopic Markers of Abnormal Protein Aggregation. *Molecules* **2020**, *25* (11), 2498. <https://doi.org/10.3390/molecules25112498>.
- (152) Kong, J.; Yu, S. Fourier Transform Infrared Spectroscopic Analysis of Protein Secondary Structures. *Acta Biochimica et Biophysica Sinica* **2007**, *39* (8), 549–559. <https://doi.org/10.1111/j.1745-7270.2007.00320.x>.
- (153) Schwaighofer, A.; Montemurro, M.; Freitag, S.; Kristament, C.; Culzoni, M. J.; Lendl, B. Beyond Fourier Transform Infrared Spectroscopy: External Cavity Quantum Cascade Laser-Based Mid-Infrared Transmission Spectroscopy of Proteins in the Amide I and Amide II Region. *Anal. Chem.* **2018**, *90* (11), 7072–7079. <https://doi.org/10.1021/acs.analchem.8b01632>.
- (154) Schwaighofer, A.; Akhgar, C. K.; Lendl, B. Broadband Laser-Based Mid-IR Spectroscopy for Analysis of Proteins and Monitoring of Enzyme Activity. *Spectrochimica Acta Part A: Molecular*

- and Biomolecular Spectroscopy* **2021**, *253*, 119563. <https://doi.org/10.1016/j.saa.2021.119563>.
- (155) Akhgar, C. K.; Ramer, G.; Žbik, M.; Trajnerowicz, A.; Pawluczyk, J.; Schwaighofer, A.; Lendl, B. The Next Generation of IR Spectroscopy: EC-QCL-Based Mid-IR Transmission Spectroscopy of Proteins with Balanced Detection. *Anal. Chem.* **2020**, *92* (14), 9901–9907. <https://doi.org/10.1021/acs.analchem.0c01406>.
- (156) Quaroni, L.; Pogoda, K.; Wiltowska-Zuber, J.; Kwiatek, W. M. Mid-Infrared Spectroscopy and Microscopy of Subcellular Structures in Eukaryotic Cells with Atomic Force Microscopy – Infrared Spectroscopy. *RSC Adv.* **2018**, *8* (5), 2786–2794. <https://doi.org/10.1039/C7RA10240B>.
- (157) Perez-Guaita, D.; Kochan, K.; Batty, M.; Doerig, C.; Garcia-Bustos, J.; Espinoza, S.; McNaughton, D.; Heraud, P.; Wood, B. R. Multispectral Atomic Force Microscopy-Infrared Nano-Imaging of Malaria Infected Red Blood Cells. *Anal. Chem.* **2018**, *90* (5), 3140–3148. <https://doi.org/10.1021/acs.analchem.7b04318>.
- (158) Otzen, D. E.; Dueholm, M. S.; Najarzadeh, Z.; Knowles, T. P. J.; Ruggeri, F. S. In Situ Sub-Cellular Identification of Functional Amyloids in Bacteria and Archaea by Infrared Nanospectroscopy. *Small Methods* **2021**, *5* (6), 2001002. <https://doi.org/10.1002/smt.202001002>.
- (159) Druzhinina, I. S.; Kubicek, C. P. Chapter Two - Familiar Stranger: Ecological Genomics of the Model Saprotroph and Industrial Enzyme Producer *Trichoderma Reesei* Breaks the Stereotypes. In *Advances in Applied Microbiology*; Sariaslani, S., Michael Gadd, G., Eds.; Academic Press, 2016; Vol. 95, pp 69–147. <https://doi.org/10.1016/bs.aambs.2016.02.001>.
- (160) Ellilä, S.; Fonseca, L.; Uchima, C.; Cota, J.; Goldman, G. H.; Saloheimo, M.; Sacon, V.; Siika-aho, M. Development of a Low-Cost Cellulase Production Process Using *Trichoderma Reesei* for Brazilian Biorefineries. *Biotechnology for Biofuels* **2017**, *10* (1), 30. <https://doi.org/10.1186/s13068-017-0717-0>.
- (161) Miettinen-Oinonen, A.; Paloheimo, M.; Lantto, R.; Suominen, P. Enhanced Production of Cellobiohydrolases in *Trichoderma Reesei* and Evaluation of the New Preparations in Biofinishing of Cotton. *Journal of Biotechnology* **2005**, *116* (3), 305–317. <https://doi.org/10.1016/j.jbiotec.2004.10.017>.
- (162) Suurnäkki, A.; Tenkanen, M.; Siika-aho, M.; Niku-Paavola, M.-L.; Viikari, L.; Buchert, J. *Trichoderma Reesei* Cellulases and Their Core Domains in the Hydrolysis and Modification of Chemical Pulp. *Cellulose* **2000**, *7* (2), 189–209. <https://doi.org/10.1023/A:1009280109519>.
- (163) Nevalainen, H.; Suominen, P.; Taimisto, K. On the Safety of *Trichoderma Reesei*. *Journal of Biotechnology* **1994**, *37* (3), 193–200. [https://doi.org/10.1016/0168-1656\(94\)90126-0](https://doi.org/10.1016/0168-1656(94)90126-0).
- (164) Fischer, A. J.; Maiyuran, S.; Yaver, D. S. Industrial Relevance of *Trichoderma Reesei* as an Enzyme Producer. In *Trichoderma reesei: Methods and Protocols*; Mach-Aigner, A. R., Martzy, R., Eds.; Methods in Molecular Biology; Springer US: New York, NY, 2021; pp 23–43. https://doi.org/10.1007/978-1-0716-1048-0_2.
- (165) Martinez, D.; Berka, R. M.; Henrissat, B.; Saloheimo, M.; Arvas, M.; Baker, S. E.; Chapman, J.; Chertkov, O.; Coutinho, P. M.; Cullen, D.; Danchin, E. G. J.; Grigoriev, I. V.; Harris, P.; Jackson, M.; Kubicek, C. P.; Han, C. S.; Ho, I.; Larrondo, L. F.; de Leon, A. L.; Magnuson, J. K.; Merino, S.; Misra, M.; Nelson, B.; Putnam, N.; Robbertse, B.; Salamov, A. A.; Schmoll, M.; Terry, A.; Thayer, N.; Westerholm-Parvinen, A.; Schoch, C. L.; Yao, J.; Barabote, R.; Nelson, M. A.; Detter, C.; Bruce, D.; Kuske, C. R.; Xie, G.; Richardson, P.; Rokhsar, D. S.; Lucas, S. M.; Rubin, E. M.; Dunn-Coleman, N.; Ward, M.; Brettin, T. S. Genome Sequencing and Analysis of the Biomass-Degrading Fungus *Trichoderma Reesei* (Syn. *Hypocrea Jecorina*). *Nature Biotechnology* **2008**, *26* (5), 553–560. <https://doi.org/10.1038/nbt1403>.
- (166) Zhang, J.; Chen, Y.; Wu, C.; Liu, P.; Wang, W.; Wei, D. The Transcription Factor ACE3 Controls Cellulase Activities and Lactose Metabolism via Two Additional Regulators in the Fungus *Trichoderma Reesei*. *Journal of Biological Chemistry* **2019**, *294* (48), 18435–18450. <https://doi.org/10.1074/jbc.RA119.008497>.
- (167) Mach-Aigner, A. R.; Pucher, M. E.; Steiger, M. G.; Bauer, G. E.; Preis, S. J.; Mach, R. L. Transcriptional Regulation of Xyr1, Encoding the Main Regulator of the Xylanolytic and

- Cellulolytic Enzyme System in *Hypocrea Jecorina*. *Appl. Environ. Microbiol.* **2008**, *74* (21), 6554. <https://doi.org/10.1128/AEM.01143-08>.
- (168) Saloheimo, A.; Aro, N.; Ilmén, M.; Penttilä, M. Isolation of the Ace1 Gene Encoding a Cys2-His2 Transcription Factor Involved in Regulation of Activity of the Cellulase Promoter Cbh1of *Trichoderma Reesei*. *Journal of Biological Chemistry* **2000**, *275* (8), 5817–5825. <https://doi.org/10.1074/jbc.275.8.5817>.
- (169) Saloheimo, M.; Pakula, T. M. The Cargo and the Transport System: Secreted Proteins and Protein Secretion in *Trichoderma Reesei* (*Hypocrea Jecorina*). *Microbiology*, 2012, *158*, 46–57. <https://doi.org/10.1099/mic.0.053132-0>.
- (170) de Paula, R. G.; Antoniêto, A. C. C.; Nogueira, K. M. V.; Ribeiro, L. F. C.; Rocha, M. C.; Malavazi, I.; Almeida, F.; Silva, R. N. Extracellular Vesicles Carry Cellulases in the Industrial Fungus *Trichoderma Reesei*. *Biotechnology for Biofuels* **2019**, *12* (1), 146. <https://doi.org/10.1186/s13068-019-1487-7>.
- (171) Li, C.; Pang, A.-P.; Yang, H.; Lv, R.; Zhou, Z.; Wu, F.-G.; Lin, F. Tracking Localization and Secretion of Cellulase Spatiotemporally and Directly in Living *Trichoderma Reesei*. *Biotechnology for Biofuels* **2019**, *12* (1), 200. <https://doi.org/10.1186/s13068-019-1538-0>.
- (172) Mustalahti, E.; Saloheimo, M.; Joensuu, J. J. Intracellular Protein Production in *Trichoderma Reesei* (*Hypocrea Jecorina*) with Hydrophobin Fusion Technology. *New Biotechnology* **2013**, *30* (2), 262–268. <https://doi.org/10.1016/j.nbt.2011.09.006>.
- (173) Nyssönen, E.; Keränen, S. Multiple Roles of the Cellulase CBHI in Enhancing Production of Fusion Antibodies by the Filamentous Fungus *Trichoderma Reesei*. *Current Genetics* **1995**, *28* (1), 71–79. <https://doi.org/10.1007/BF00311884>.
- (174) Divne, C.; Stahlberg, J.; Reinikainen, T.; Ruohonen, L.; Pettersson, G.; Knowles, J.; Teeri, T.; Jones, T. The Three-Dimensional Crystal Structure of the Catalytic Core of Cellobiohydrolase I from *Trichoderma Reesei*. *Science* **1994**, *265* (5171), 524. <https://doi.org/10.1126/science.8036495>.
- (175) Stricker, A. R.; Steiger, M. G.; Mach, R. L. Xyr1 Receives the Lactose Induction Signal and Regulates Lactose Metabolism in *Hypocrea Jecorina*. *FEBS Letters* **2007**, *581* (21), 3915–3920. <https://doi.org/10.1016/j.febslet.2007.07.025>.
- (176) Torronen, A.; Rouvinen, J. Structural Comparison of Two Major Endo-1,4-Xylanases from *Trichoderma Reesei*. *Biochemistry* **1995**, *34* (3), 847–856. <https://doi.org/10.1021/bi00003a019>.
- (177) Kleywegt, G. J.; Zou, J.-Y.; Divne, C.; Davies, G. J.; Sinning, I.; Ståhlberg, J.; Reinikainen, T.; Srisodsuk, M.; Teeri, T. T.; Jones, T. A. The Crystal Structure of the Catalytic Core Domain of Endoglucanase I from *Trichoderma Reesei* at 3.6 Å Resolution, and a Comparison with Related Enzymes. Edited by K. Nagai. *Journal of Molecular Biology* **1997**, *272* (3), 383–397. <https://doi.org/10.1006/jmbi.1997.1243>.
- (178) *Plastics - the Facts 2022*; PlasticsEurope. <https://plasticseurope.org/knowledge-hub/plastics-the-facts-2022/> (accessed 2021-11-17).
- (179) Agboola, O.; Sadiku, R.; Mokrani, T.; Amer, I.; Imoru, O. 4 - Polyolefins and the Environment. In *Polyolefin Fibres (Second Edition)*; Ugbohue, S. C. O., Ed.; The Textile Institute Book Series; Woodhead Publishing, 2017; pp 89–133. <https://doi.org/10.1016/B978-0-08-101132-4.00004-7>.
- (180) Posch, W. 3 - Polyolefins. In *Applied Plastics Engineering Handbook*; Kutz, M., Ed.; Plastics Design Library; William Andrew Publishing: Oxford, 2011; pp 23–48. <https://doi.org/10.1016/B978-1-4377-3514-7.10003-0>.
- (181) Selke, S. E.; Hernandez, R. J. Packaging: Polymers in Flexible Packaging. In *Encyclopedia of Materials: Science and Technology*; Buschow, K. H. J., Cahn, R. W., Flemings, M. C., Ilshner, B., Kramer, E. J., Mahajan, S., Veyssi re, P., Eds.; Elsevier: Oxford, 2001; pp 6652–6656. <https://doi.org/10.1016/B0-08-043152-6/01176-1>.
- (182) Maddah, H. A. Polypropylene as a Promising Plastic: A Review. *American Journal of Polymer Science* **2016**, *6* (1), 1–11.
- (183) Louizi, M.; Massardier, V.; Cassagnau, P. Contribution of High-Shear Processing to the

- Compatibilization of (PP/EPR)/PE Ternary Blends. *Macromolecular Materials and Engineering* **2014**, 299 (6), 674–688. <https://doi.org/10.1002/mame.201300268>.
- (184) Ghalia, M. A.; Hassan, A.; Yussuf, A. Mechanical and Thermal Properties of Calcium Carbonate-Filled PP/LLDPE Composite. *Journal of Applied Polymer Science* **2011**, 121 (4), 2413–2421. <https://doi.org/10.1002/app.33570>.
- (185) Radonjič, G.; Gubelj, N. The Use of Ethylene/Propylene Copolymers as Compatibilizers for Recycled Polyolefin Blends. *Macromolecular Materials and Engineering* **2002**, 287 (2), 122–132. [https://doi.org/10.1002/1439-2054\(20020201\)287:2<122::AID-MAME122>3.0.CO;2-A](https://doi.org/10.1002/1439-2054(20020201)287:2<122::AID-MAME122>3.0.CO;2-A).
- (186) Kim, D.; Lee, J. S.; Barry, C. M. F.; Mead, J. L. Microscopic Measurement of the Degree of Mixing for Nanoparticles in Polymer Nanocomposites by TEM Images. *Microscopy Research and Technique* **2007**, 70 (6), 539–546. <https://doi.org/10.1002/jemt.20478>.
- (187) Kory, M. J.; Wörle, M.; Weber, T.; Payamyar, P.; van de Poll, S. W.; Dshemuchadse, J.; Trapp, N.; Schlüter, A. D. Gram-Scale Synthesis of Two-Dimensional Polymer Crystals and Their Structure Analysis by X-Ray Diffraction. *Nature Chem* **2014**, 6 (9), 779–784. <https://doi.org/10.1038/nchem.2007>.
- (188) Xu, J.; Guo, B.-H.; Zhang, Z.-M.; Zhou, J.-J.; Jiang, Y.; Yan, S.; Li, L.; Wu, Q.; Chen, G.-Q.; Schultz, J. M. Direct AFM Observation of Crystal Twisting and Organization in Banded Spherulites of Chiral Poly(3-Hydroxybutyrate-Co-3-Hydroxyhexanoate). *Macromolecules* **2004**, 37 (11), 4118–4123. <https://doi.org/10.1021/ma0499122>.
- (189) Schirmeister, C. G.; Schächtele, S.; Keßler, Y.; Hees, T.; Köhler, R.; Schmitz, K.; Licht, E. H.; Muelhaupt, R. Low Warpage Nanophase-Separated Polypropylene/Olefinic Elastomer Reactor Blend Composites with Digitally Tuned Glass Fiber Orientation by Extrusion-Based Additive Manufacturing. *ACS Appl. Polym. Mater.* **2021**, 3 (4), 2070–2081. <https://doi.org/10.1021/acsapm.1c00119>.
- (190) Li, L.; Chen, L.; Bruin, P.; Winnik, M. A. Morphology Evolution and Location of Ethylene–Propylene Copolymer in Annealed Polyethylene/Polypropylene Blends. *Journal of Polymer Science Part B: Polymer Physics* **1997**, 35 (6), 979–991. [https://doi.org/10.1002/\(SICI\)1099-0488\(19970430\)35:6<979::AID-POLB12>3.0.CO;2-C](https://doi.org/10.1002/(SICI)1099-0488(19970430)35:6<979::AID-POLB12>3.0.CO;2-C).
- (191) Tang, F.; Bao, P.; Su, Z. Analysis of Nanodomain Composition in High-Impact Polypropylene by Atomic Force Microscopy–Infrared. *Anal. Chem.* **2016**, 88 (9), 4926–4930. <https://doi.org/10.1021/acs.analchem.6b00798>.
- (192) Li, C.; Wang, Z.; Liu, W.; Ji, X.; Su, Z. Copolymer Distribution in Core–Shell Rubber Particles in High-Impact Polypropylene Investigated by Atomic Force Microscopy–Infrared. *Macromolecules* **2020**, 53 (7), 2686–2693. <https://doi.org/10.1021/acs.macromol.0c00328>.
- (193) Zhong, Z.; Peng, L.; Su, J.; Luo, Z.; Han, C. C.; Huang, X.; Su, Z. Distribution of an Antioxidant in Polypropylene/Ethylene–Octene Copolymer Blends Studied by Atomic Force Microscopy–Infrared. *Soft Matter* **2022**. <https://doi.org/10.1039/D2SM00765G>.
- (194) Putman, C. A.; van der Werf, K. O.; de Groot, B. G.; van Hulst, N. F.; Greve, J. Viscoelasticity of Living Cells Allows High Resolution Imaging by Tapping Mode Atomic Force Microscopy. *Biophysical Journal* **1994**, 67 (4), 1749–1753. [https://doi.org/10.1016/S0006-3495\(94\)80649-6](https://doi.org/10.1016/S0006-3495(94)80649-6).
- (195) Tsukruk, V. V.; Gorbunov, V. V.; Huang, Z.; Chizhik, S. A. Dynamic Microprobing of Viscoelastic Polymer Properties. *Polymer International* **2000**, 49 (5), 441–444. [https://doi.org/10.1002/\(SICI\)1097-0126\(200005\)49:5<441::AID-PI240>3.0.CO;2-U](https://doi.org/10.1002/(SICI)1097-0126(200005)49:5<441::AID-PI240>3.0.CO;2-U).
- (196) van der Walt, S.; Schönberger, J. L.; Nunez-Iglesias, J.; Boulogne, F.; Warner, J. D.; Yager, N.; Guillard, E.; Yu, T.; contributors, the scikit-image. Scikit-Image: Image Processing in Python. *PeerJ* **2014**, 2, e453. <https://doi.org/10.7717/peerj.453>.
- (197) Guizar-Sicairos, M.; Thurman, S. T.; Fienup, J. R. Efficient Subpixel Image Registration Algorithms. *Opt. Lett.*, *OL* **2008**, 33 (2), 156–158. <https://doi.org/10.1364/OL.33.000156>.
- (198) Govorčin Bajsić, E.; Rek, V.; Čosić, I. Preparation and Characterization of Talc Filled Thermoplastic Polyurethane/Polypropylene Blends. *Journal of Polymers* **2014**, 2014, e289283. <https://doi.org/10.1155/2014/289283>.
- (199) Irvanian, A.; Ravari, S. O. Types of Contamination in Landfills and Effects on The Environment:

- A Review Study. *IOP Conf. Ser.: Earth Environ. Sci.* **2020**, 614 (1), 012083. <https://doi.org/10.1088/1755-1315/614/1/012083>.
- (200) Mortula, M. M.; Atabay, S.; Fattah, K. P.; Madbully, A. Leachability of Microplastic from Different Plastic Materials. *Journal of Environmental Management* **2021**, 294, 112995. <https://doi.org/10.1016/j.jenvman.2021.112995>.
- (201) Reznichenko, A.; Harlin, A. Next Generation of Polyolefin Plastics: Improving Sustainability with Existing and Novel Feedstock Base. *SN Appl. Sci.* **2022**, 4 (4), 108. <https://doi.org/10.1007/s42452-022-04991-4>.
- (202) Antonopoulos, I.; Faraca, G.; Tonini, D. Recycling of Post-Consumer Plastic Packaging Waste in the EU: Recovery Rates, Material Flows, and Barriers. *Waste Management* **2021**, 126, 694–705. <https://doi.org/10.1016/j.wasman.2021.04.002>.
- (203) Serranti, S.; Bonifazi, G. 2 - Techniques for Separation of Plastic Wastes. In *Use of Recycled Plastics in Eco-efficient Concrete*; Pacheco-Torgal, F., Khatib, J., Colangelo, F., Tuladhar, R., Eds.; Woodhead Publishing Series in Civil and Structural Engineering; Woodhead Publishing, 2019; pp 9–37. <https://doi.org/10.1016/B978-0-08-102676-2.00002-5>.
- (204) Kaiser, K.; Schmid, M.; Schlummer, M. Recycling of Polymer-Based Multilayer Packaging: A Review. *Recycling* **2018**, 3 (1), 1. <https://doi.org/10.3390/recycling3010001>.
- (205) Schyns, Z. O. G.; Shaver, M. P. Mechanical Recycling of Packaging Plastics: A Review. *Macromolecular Rapid Communications* **2021**, 42 (3), 2000415. <https://doi.org/10.1002/marc.202000415>.
- (206) Larrain, M.; Van Passel, S.; Thomassen, G.; Kresovic, U.; Alderweireldt, N.; Moerman, E.; Billen, P. Economic Performance of Pyrolysis of Mixed Plastic Waste: Open-Loop versus Closed-Loop Recycling. *Journal of Cleaner Production* **2020**, 270, 122442. <https://doi.org/10.1016/j.jclepro.2020.122442>.
- (207) Chaffin, K. A.; Bates, F. S.; Brant, P.; Brown, G. M. Semicrystalline Blends of Polyethylene and Isotactic Polypropylene: Improving Mechanical Performance by Enhancing the Interfacial Structure. *Journal of Polymer Science Part B: Polymer Physics* **2000**, 38 (1), 108–121. [https://doi.org/10.1002/\(SICI\)1099-0488\(20000101\)38:1<108::AID-POLB14>3.0.CO;2-9](https://doi.org/10.1002/(SICI)1099-0488(20000101)38:1<108::AID-POLB14>3.0.CO;2-9).
- (208) Jeswani, H.; Krüger, C.; Russ, M.; Horlacher, M.; Antony, F.; Hann, S.; Azapagic, A. Life Cycle Environmental Impacts of Chemical Recycling via Pyrolysis of Mixed Plastic Waste in Comparison with Mechanical Recycling and Energy Recovery. *Science of The Total Environment* **2021**, 769, 144483. <https://doi.org/10.1016/j.scitotenv.2020.144483>.
- (209) Ghosh, A. Performance Modifying Techniques for Recycled Thermoplastics. *Resources, Conservation and Recycling* **2021**, 175, 105887. <https://doi.org/10.1016/j.resconrec.2021.105887>.
- (210) Jordan, A. M.; Kim, K.; Soetrisno, D.; Hannah, J.; Bates, F. S.; Jaffer, S. A.; Lhost, O.; Macosko, C. W. Role of Crystallization on Polyolefin Interfaces: An Improved Outlook for Polyolefin Blends. *Macromolecules* **2018**, 51 (7), 2506–2516. <https://doi.org/10.1021/acs.macromol.8b00206>.
- (211) Olayo, M. G.; Colín, E.; Cruz, G. J.; Morales, J.; Olayo, R. Accelerated Nitridation and Oxidation by Plasma on Polyethylene. *Eur. Phys. J. Appl. Phys.* **2009**, 48 (3), 30501. <https://doi.org/10.1051/epjap/2009166>.
- (212) Prabowo, I.; Pratama, J. N.; Chalid, M. The Effect of Modified Ijuk Fibers to Crystallinity of Polypropylene Composite. *IOP Conf. Ser.: Mater. Sci. Eng.* **2017**, 223, 012020. <https://doi.org/10.1088/1757-899X/223/1/012020>.
- (213) Farias-Aguilar, J. C.; Ramírez-Moreno, M. J.; Téllez-Jurado, L.; Balmori-Ramírez, H. Low Pressure and Low Temperature Synthesis of Polyamide-6 (PA6) Using NaO as Catalyst. *Materials Letters* **2014**, 136, 388–392. <https://doi.org/10.1016/j.matlet.2014.08.071>.
- (214) McCarthy, S. J.; Meijs, G. F.; Mitchell, N.; Gunatillake, P. A.; Heath, G.; Brandwood, A.; Schindhelm, K. In-Vivo Degradation of Polyurethanes: Transmission-FTIR Microscopic Characterization of Polyurethanes Sectioned by Cryomicrotomy. *Biomaterials* **1997**, 18 (21), 1387–1409. [https://doi.org/10.1016/S0142-9612\(97\)00083-5](https://doi.org/10.1016/S0142-9612(97)00083-5).
- (215) Saviello, D.; Pouyet, E.; Toniolo, L.; Cotte, M.; Nevin, A. Synchrotron-Based FTIR

- Microspectroscopy for the Mapping of Photo-Oxidation and Additives in Acrylonitrile–Butadiene–Styrene Model Samples and Historical Objects. *Analytica Chimica Acta* **2014**, *843*, 59–72. <https://doi.org/10.1016/j.aca.2014.07.021>.
- (216) Motta, O.; Proto, A.; De Carlo, F.; De Caro, F.; Santoro, E.; Brunetti, L.; Capunzo, M. Utilization of Chemically Oxidized Polystyrene as Co-Substrate by Filamentous Fungi. *International Journal of Hygiene and Environmental Health* **2009**, *212* (1), 61–66. <https://doi.org/10.1016/j.ijheh.2007.09.014>.

Appendix

A. Scientific publications

A list of contributions to the individual scientific publications presented in this cumulative thesis divided into little (x), medium (xx) and high (xxx) is shown in the table below.

	Publication			
	I	II	III	IV
Data acquisition	xxx	xxx	xxx	(Not required)
Data analysis	xx	xxx	xxx	(Not required)
Interpretation	xxx	xxx	xxx	xxx
Manuscript writing	xxx	xxx	xxx	xxx

Publication I

Nanoscale Infrared Spectroscopy and Chemometrics Enable Detection of Intracellular Protein Distribution

A. Catarina V. D. dos Santos, Rosa Heydenreich, Christian Derntl, Astrid R. Mach-Aigner, Robert L. Mach, Georg Ramer, and Bernhard Lendl*
Analytical Chemistry, **2020**, 92, 15719-15725

Nanoscale Infrared Spectroscopy and Chemometrics Enable Detection of Intracellular Protein Distribution

A. Catarina V. D. dos Santos, Rosa Heydenreich, Christian Derntl, Astrid R. Mach-Aigner, Robert L. Mach, Georg Ramer,* and Bernhard Lendl



Cite This: *Anal. Chem.* 2020, 92, 15719–15725



Read Online

ACCESS |



Metrics & More

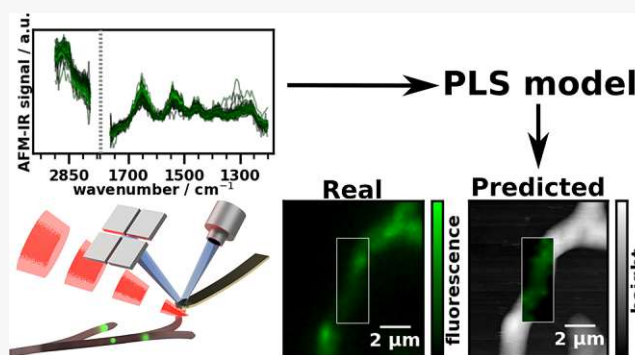


Article Recommendations



Supporting Information

ABSTRACT: Determination of the intracellular location of proteins is one of the fundamental tasks of microbiology. Conventionally, label-based microscopy and super-resolution techniques are employed. In this work, we demonstrate a new technique that can determine intracellular protein distribution at nanometer spatial resolution. This method combines nanoscale spatial resolution chemical imaging using the photothermal-induced resonance (PTIR) technique with multivariate modeling to reveal the intracellular distribution of cell components. Here, we demonstrate its viability by imaging the distribution of major cellulases and xylanases in *Trichoderma reesei* using the colocalization of a fluorescent label (enhanced yellow fluorescence protein, EYFP) with the target enzymes to calibrate the chemometric model. The obtained partial least squares model successfully shows the distribution of these proteins inside the cell and opens the door for further studies on protein secretion mechanisms using PTIR.



From transcription to secretion, proteins have a central role in life: a cell will invest up to 75% of its energy in translation alone.¹ Proteins are impressive in many ways. As catalysts, they are present in almost all metabolic pathways, catalyzing reactions that would otherwise not take place in an organism's lifetime² and doing so under mild conditions and with a selectivity that is hard to rival with.³ However, not all proteins are enzymes, others serve a structural function or participate in cell signaling and signal transduction. This means that failures and errors that occur in such an important system are the cause of a number of pathologies.⁴ Furthermore, proteins are present in several high-value industrial processes such as the production of pharmaceuticals,⁵ biofuels,⁶ and macromolecules.³ Therefore, it is of great interest to have a detailed knowledge about the intracellular synthesis and trafficking of proteins and their regulation. Gene expression,⁷ protein quality control mechanisms,¹ and protein secretion⁸ have been studied for decades in a continuous multi-disciplinary effort. Imaging techniques such as electron microscopy^{9–11} and visible microscopy techniques that are capable of resolution below the diffraction limit (STED, SIM, PALM, and STORM)^{12–15} are typical of this kind of research and have given important insights into the ultrastructural features, processes, and metabolic pathways of cells. However, these super resolution microscopy techniques are often limited by the choice of fluorophore (which needs to meet a series of tight criteria), tedious sample preparation, long sampling time, extensive postprocessing, and propensity for artifacts.^{16–18}

the distribution of these proteins inside the cell and opens the

In this work, a new approach to localization and detection of proteins and groups of proteins inside of cells at a nanoscale lateral resolution is introduced. This novel method is able to provide spatial resolution rivaling that of the above-mentioned super-resolution techniques while also being able to provide label-free information about protein distribution at ambient conditions. It is based on nanometer spatial resolution mid-infrared molecular spectroscopy coupled with chemometric data evaluation. While in general spatial resolution in mid-IR microscopy is diffraction-limited in the micrometer range,¹⁹ techniques based on near field are not limited by diffraction.²⁰

Here, we use the photothermal-induced resonance technique (PTIR, also known as AFM-IR)^{21,22} to perform near-field IR spectroscopy. PTIR is a combination of atomic force microscopy (AFM) and infrared spectroscopy. In this technique, a pulsed wavelength-tunable IR laser is aimed at the sample area under the AFM tip, causing it to rapidly heat up and expand. The thermal expansion is detected through changes in the deflection signal of the AFM cantilever, which oscillates with an amplitude proportional to the absorbed

Received: May 25, 2020

Accepted: November 16, 2020

Published: December 1, 2020



energy.²⁰ The signal detection occurs in the near-field region, allowing lateral spatial resolutions below the diffraction limit and down to 20 nm.²⁰ Vertically, PTIR can detect signals buried at over 1 μm in a sample.²³ The signal obtained in both PTIR and FTIR is proportional to the wavelength-dependent absorption coefficient of the sample.²⁰ Thus, PTIR spectral bands can be assigned to the localized vibrations of functional groups using well-established spectra–structure correlations. In the same way as FTIR spectroscopy, PTIR also provides access to the fingerprint range of the infrared spectrum, where absorption bands are present that result from vibrations involving a higher number of atoms than localized vibrations. General spectral ranges can be assigned to biologically relevant functional groups that are characteristic building blocks of, for example, DNA/RNA, carbohydrates, lipids, and proteins. For evaluation beyond the quantitation of these major compounds, multivariate methods or machine learning approaches are typically used in FTIR.²⁴ PTIR has found applications in material science,^{25–31} art conservation,^{32,33} environmental analysis,³⁴ nano-optics,³⁵ geology,^{36,37} and in the life sciences. In the latter case, PTIR has been applied to the imaging of whole cells^{38–41} and successfully identified and characterized lipid droplets,⁴² poly(hydroxybutyrate) vesicles,⁴³ extracellular vesicles,⁴⁴ liposomal drug nanocarriers,⁴⁵ and photosynthetic complexes.⁴⁶ Protein and polypeptide secondary structure has been extensively studied by PTIR,^{47,48} including in aqueous medium⁴⁹ and in human tissue.⁵⁰ Studies on the intracellular distribution of proteins with varying degrees of complexity have been reported.^{38,40,51} In 2016, Baldassarre et al.⁴⁰ imaged *E. coli* and human (HeLa) cells and reported inhomogeneous protein density in the latter. In 2018, Quaroni et al.⁵¹ identified filaments visible in topographical images as belonging to the cytoskeleton of fibroblasts. In these studies, the linear correlation between the PTIR signal and the concentration is used to determine the distribution of chemicals. Perez-Guaita et al.³⁸ located areas with relatively high hemoglobin content within red blood cells infected with *P. falciparum* using (unsupervised) cluster analysis. We take a different approach by using supervised machine learning to detect one predetermined group of analytes. We demonstrate the versatility of our method by analyzing the distribution of cellulases and enhanced yellow fluorescent protein (EYFP) in *Trichoderma reesei*. The filamentous mesophilic ascomycete *T. reesei* was found a little over 75 years ago on the Solomon Islands and soon caught the attention of researchers because of its exceptional cellulose-degrading capabilities.⁶ In the wild, *T. reesei* is a saprobe, and the secretion of cellulases and hemicellulases in high amounts is essential for its survival.⁵² *T. reesei*'s efficient enzymatic secretory system has since been exploited in industrial-scale enzyme production. The cellulases and hemicellulases find application in numerous industries such as the pulp,⁵³ food and animal feed,⁵⁴ and textile industry⁵⁵ and are used for the production of second-generation biofuels.^{6,56} The strain used, QM6a SecEYFP, derived from QM6a Δtmus53 , bears an expression cassette for EYFP fused to the N-terminal secretion signal peptide of the main cellobiohydrolase CBHI⁵⁵ under the control of the *cbh1* promoter. Hence, the fluorescence brightness can be considered proportional to the cellulase abundance.

In this work, fluorescence images from an EYFP secreting *T. reesei* strain were obtained and combined with AFM topographic images measured in the same locations. Using this information, a fluorescence value could then be attributed to

each PTIR spectrum location and used to create a chemometric model using partial least squares regression (PLS). This PLS model relates the fluorescence intensity to the presence of β -sheet-containing proteins, such as cellulases and xylanases, and could then successfully be applied to a validation data set.

EXPERIMENTAL SECTION

Fungal Strains. The *T. reesei* strains QM6a Δtmus53 ⁵⁷ and QM6a SecEYFP used in this study were maintained on malt extract agar (MEX) at 30 °C. Hygromycin B was added when applicable to a final concentration of 113 U/mL.

Plasmid Construction. Polymerase chain reactions (PCRs) for cloning purposes were performed with Q5 high-fidelity DNA polymerase (New England Biolabs, Ipswich, MA, USA) according to the manufacturer's instructions. All used primers are listed in Table 1. First, the *cbh1* promoter and the

Table 1. Primers Used in This Study

primer name	primer sequence (5'-3')
Yfp-fwd-XbaI	AGTGTCTAGAATGGTGAGCAAGGGC GAG
Yfp-rev-NotI-NsiI	AGTGATGCATGCGGCCGCTTACTTG TACAGCTCGTCCATGCC
Pcbh1_fwd_XhoI	CTCGAGATGGCGCTATATTGGCTGT TTC
Pcbh1_Q18r_NheI	GCTAGCCTGAGCACGAGCTGTGGC

sequence encoding for the first 18 amino acids of *cbh1* were amplified with the primers Pcbh1_fwd_XhoI and Pcbh1_Q18r_NheI using chromosomal DNA of QM6a Δtmus53 as the template and inserted into an EcoRV-digested pJET1.2 (Thermo Scientific, part of Thermo Fisher Scientific Inc., Waltham, MA, USA) yielding pJET-Pcbh1+18. Next, a codon-optimized eyfp was amplified with the primers Yfp-fwd-XbaI and Yfp-rev-NotI-NsiI using pCD-EYFP⁵⁸ as the template and then inserted into pRLM_{ex}30⁵⁹ via digestion with Xba and NsiI. The eyfp:Tcbh2 fragment was released by digestion with XbaI and HindIII and inserted into an accordingly digested pJET1.2 (Thermo Scientific). This plasmid was digested with BspEI and XbaI and the *cbh1* promoter fragment was inserted after the release from pJET-Pcbh1+18 via digestion with BspEI and NheI, yielding pCD-SecYFP.

Fungal Transformation. The protoplast transformation of *T. reesei* was performed as described by Gruber et al.⁶⁰ Approximately 10⁷ protoplasts of the strain QM6a Δtmus53 were co-transformed with 5 μg of pCD-SecYFP and 1 μg of pAN7-1,⁶¹ yielding the strain QM6a SecEYFP. The transformation reaction was added to the 40 mL melted, 50 °C warm MEX agar containing 1.2 M sorbitol. Equal parts of this mixture were poured into four sterile Petri dishes and incubated at 30 °C for 5 h after solidification. Subsequently, 10 mL melted, 50 °C warm MEX agar containing 1.2 M sorbitol and double concentration of hygromycin B were poured on top of each protoplast-containing layer. Plates were incubated at 30 °C for 2–5 days until colonies were visible. Resulting candidates were subjected to homokaryon purification by streaking conidia on selection plates.

Fungal Sample Preparation. Conidiospores of QM6a SecEYFP were harvested from a MEX plate, suspended in 0.8% NaCl/0.05% Tween 80 and diluted to approximately 10²–10³ spores/mL. 100 μL of this spore suspension was spread on a

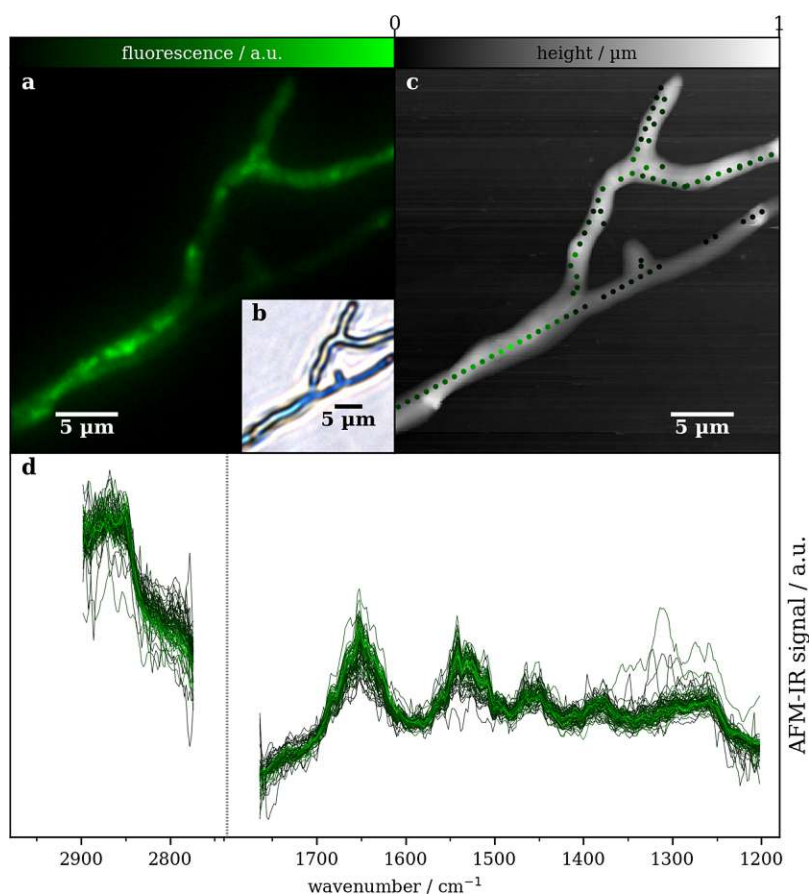


Figure 1. Images of hypha and PTIR spectra: the fluorescence intensity corresponding to each spectrum was determined by aligning the fluorescence image (a) and the AFM topography image (c). (b) Bright-field image of the hypha. PTIR spectra (d), here shown after pretreatment as described in the text, were recorded along the center of the hypha. The color of the spectra in (d) denotes the corresponding fluorescence brightness from black (no fluorescence detected) to light green (maximum fluorescence).

cellophane foil on Mandels–Andreotti medium⁶² plates containing 1% lactose. Plates were incubated for 96 h at 30 °C in darkness. To harvest and wash the mycelium, the cellophane foil was transferred into ice-cold deionized water using sterile tweezers. Floating mycelium was then transferred onto a CaF₂ disk (12 mm diameter × 2 mm thickness from Crystran) and dried using a freeze-drier (FreeZone 2.5 L benchtop freeze-drier from Labconco) at –50 °C and 0.160 mbar for 30 min.

Fluorescence Measurements. All fluorescence images were recorded using a Leica DMI8 inverted microscope equipped with an HC PL FLUOTAR L 63×/0.70 DRY objective (numerical aperture 0.70), a Leica GFP cube (excitation filter 470–440 nm, emission filter 525–550 nm), and a SOLA SM 5 light engine (Lumencor) with 3.5–4.0 mW nominal output power as the light source. The exposure time was 220 ms. The bright-field images were obtained using the same microscope using an HC PL FLUOTAR L 40×/0.60 DRY (numerical aperture 0.60) objective.

PTIR Measurements. All PTIR measurements were carried out using a Bruker nano-IR 3 s coupled to a MIRcat external cavity quantum cascade laser array from Daylight Solutions. Spectra covering the range from 1200 to 1758 cm⁻¹ (QCL transition at 1360.5 cm⁻¹) and from 2770 to 2900 cm⁻¹ were obtained using resonance-enhanced PTIR⁶³ in contact mode by tuning the repetition rate of the laser to match the second contact resonance frequency of the cantilever (roughly

190 to 220 kHz) and the sample. The cantilevers used were gold-coated with nominal first free resonance frequencies of 13 ± 4 kHz and spring constants between 0.07 and 0.4 N/m (PR-EX-nIR2 from Anasys Instruments/Bruker). The laser source operated at 3% duty cycle (corresponding to 160 to 140 ns pulse length) and 14.75% power (before beam splitter), and for each location, five spectra were recorded at 2 cm⁻¹ spectral resolution. The instrument and all beam paths were purged with dry air generated by an adsorptive dry air generator.

Data Preprocessing. Recorded spectra in which no bands were above the noise level were rejected, and the remaining spectra were averaged by location. The spectra were then normalized using vector normalization in the range between 1200 and 2900 cm⁻¹ (excluding the wavenumbers where no laser emitted from calculations) and smoothed using a Savitzky–Golay filter (three points, first-order, treating both contiguous spectral ranges separately).

To align the fluorescence images to the AFM coordinate system, each fluorescence image was rotated, scaled, and shifted to match it to its AFM topography counterpart. Fluorescence intensity was determined from the green channel of the fluorescence image because of the GFP filter used. Finally, for each location at which PTIR spectra were recorded, the fluorescence intensity was determined by performing a linear interpolation of the neighboring fluorescence image pixels.

Chemometric Modeling of Fluorescence. A PLS regression was performed to fit the fluorescence using PTIR spectra. The optimum number of components was determined using 5-fold cross validation with the root mean square error (RMSE) as metric. Modeling was performed using the scikit-learn⁶⁴ (v0.22.2) machine learning library for Python 3.

To diagnose which spectral features were most important for the regression, the selectivity ratio (SR)⁶⁵ of the PLS was calculated. In brief, the SR determines the fraction of the variance of a variable that is explained by the model. High SR at a specific wavenumber means that a large part of it is correlated to the target variable. The SR was calculated as outlined by Farrés et al.⁶⁵

RESULTS AND DISCUSSION

QM6a SecEYFP was grown on Mandels–Andreotti medium containing lactose because this carbon source induces cellulase production in *T. reesei*.⁶⁶ In the strain QM6a SecEYFP, the cellulase production is accompanied by EYFP production. Furthermore, the EYFP carries the same signal peptide as the main cellulase, hence the fluorescence intensity correlates with the presence of cellulase. After deposition on the sample carrier, first, a bright-field (see Figure 1b) and fluorescence image (see Figure 1a) were collected before transferring the sample into the AFM instrument. AFM topography images (see Figure 1c) and PTIR spectra (Figure 1d) were recorded in the same area. After overlaying the fluorescence image and AFM topography image, each PTIR spectrum could be assigned a fluorescence brightness (denoted by the color of PTIR spectra and location markers in Figure 1d,c, respectively), as described in the Experimental Section.

To establish a regression from PTIR spectra to fluorescence intensities in the training set, a PLS model was constructed. The metric used here for the quality of the fit, RMSE, was 11% of the maximum fluorescence measured, indicating that the average error of the fit was 11% of the maximum fluorescence.

A cutoff between statistically significant and not statistically significant variables according to the SR is given by the F-test.⁶⁵ Here, we use the critical value at a 90% confidence level (the horizontal line in Figure 2). It should be noted that a low

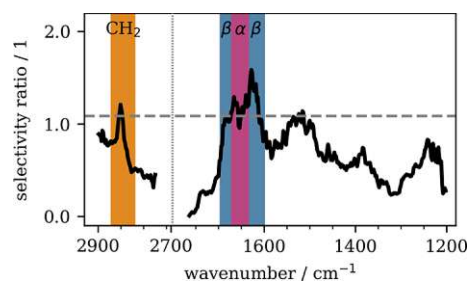


Figure 2. SR of the PLS model. The gray line corresponds to a 90% significance level of the SR. Important spectral regions are from 1600 to 1700 and around 2850 cm^{-1} .

SR in a part of the spectrum could be caused by low signal to noise, high variance in the spectra uncorrelated to the target variable, or the absence of biologically relevant spectral information.

Wavenumbers between 1618 and 1634 cm^{-1} have the highest SR with the maximum occurring at 1628 cm^{-1} . This area of the spectrum is part of the amide I band (1600 to 1700 cm^{-1}) which is sensitive to the protein concentration and

protein secondary structure. The central part of this range (here marked with α) contains spectral signatures of α -helix secondary structure amide backbones, as well as contributions from turns and disordered proteins. The bands between ~ 1600 and 1634 cm^{-1} (maximum at 1628 cm^{-1}) and between 1670 and 1700 cm^{-1} (maximum at 1685 cm^{-1}) correspond to proteins with a β -sheet secondary structure.^{67–71} EYFP, the protein used for the calibration of this model, has a β -barrel structure;⁷² however, because the expression of EYFP is driven by the *cbh1* promoter and EYFP is fused to the secretion signal peptide, it should follow the same path and be colocalized with CBHI, the most abundant cellulase,⁵⁵ whose structure also contains β -sheets.⁷³ Furthermore, the presence of lactose causes not only the expression of CBHI and EYFP but also of other cellulases such as CBHII, EGLI, and EGLII and the expression of some xylanases.^{66,74} Of these, EGLI and the major xylanase XYNII have structures which are mostly composed of β -sheets.^{75,76} Because PTIR would pick up a signal from all the β -sheet containing proteins, this means that proteins with this type of structure whose distribution coincides with that of EYFP contribute to the model and are in turn detected by it. Furthermore, as the literature suggests that these cellulases and xylanases are significantly more abundant than EYFP,⁷⁷ we posit that our model is mainly sensitive to these proteins, while EYFP only serves as a necessary crutch to establish the regression.

The absorption band at 2850 cm^{-1} also has a high SR. The cellulases, xylanases, and the accompanying EYFP are the proteins tagged for secretion with a signal sequence. During translation or post-translation, the proteins carrying this peptide sequence are translocated into the ER lumen where they are modified (e.g., glycosylation) and folded to their correct conformation with the help of chaperones. Correctly folded proteins are then transported in vesicles to the Golgi complex where they undergo further modifications and are then placed in vesicles once again, this time bound for the plasma membrane and, ultimately, the outside of the cell.⁷⁸ Thus, these proteins are surrounded at every step by lipid membranes, either from the vesicles or from the ER or the Golgi apparatus. This collocation of the enzymes with lipids likely explains the high SR of CH_2 stretch vibrations at 2850 cm^{-1} . Having thus established, that there are indeed local differences in the protein concentration across the hypha and that these are used to model the fluorescence intensity rather than a spurious correlation with an unrelated latent variable or even noise, the model was applied to a sample outside the training set.

A second PTIR data set (testing set) was collected and pretreated in the same way as the training set before applying the model. The model yielded a slightly worse RMSE of 13% of the maximum value for the testing set than was achieved for the training set with a comparable distribution of residuals (Figure 3). Because the RMSE did not have a large increase from the training to the testing set, we can assume that the model applies well to data which was not part of its training set and that it is not overfitting. Hence, the model can be applied to PTIR spectra outside its training set.

Using the testing set also allows to demonstrate one important property of using PTIR to determine the local fluorescence brightness: by collecting PTIR spectra in a grid, a fluorescence image can be calculated using the PLS model that closely matches the original fluorescence image (see Figure 4). However, as PTIR has a significantly higher spatial resolution

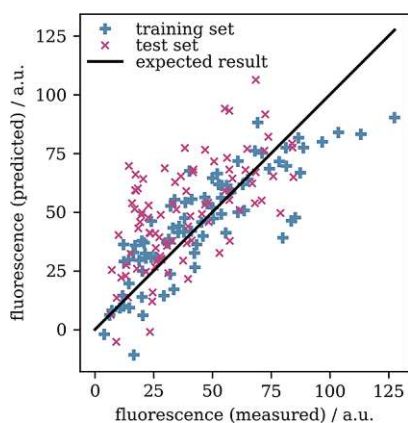


Figure 3. Deviation of PLS regression from ground truth value. In the optimum case, all points should lie on the diagonal line. Points above or below the line correspond to over and underestimation of the fluorescence by the PLS regression, respectively.

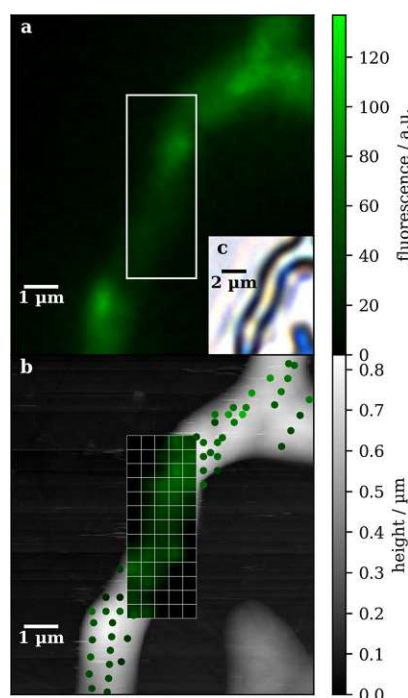


Figure 4. Testing set: comparison of truth and model output. (a) Fluorescence image of fungal hypha used for this data set and (b) model output displayed over an AFM topography image. Fluorescence values derived from single point PTIR spectra are depicted as circles, and the hyperspectral PTIR image-derived fluorescence image is depicted as grid of pixels. The grid lines show the spacing of measurements, not the spatial resolution of PTIR. (c) Bright-field image of the hypha.

(approximately 20 nm) than fluorescence microscopy, the PTIR image here is significantly under sampled. This likely explains some of the lack of fit in Figure 3 and part of the RMSE, as small local differences in protein concentration are picked up by the PTIR but not by fluorescence microscopy. However, a PLS model with an appropriately chosen number of components will still fit the general trend in the data set, disregarding small deviations in a few measurement locations.

CONCLUSIONS AND OUTLOOK

In this work, we demonstrated that PTIR spectroscopy and multivariate modeling enabled spatially resolved determination of the presence of proteins. The model was applied here to determine the distribution of cellulases and xylanases that contain β -sheets in a technologically relevant fungus, *T. reesei*. Because of the well-established properties of mid-IR spectroscopy,²⁴ the procedure should translate well to other microorganisms and types of cells as well as to other properties beyond distribution of proteins such as the presence of inclusion bodies or metabolic imbalances in cells. The only requirement for applying this technique is an external reference that can be used to establish the chemometric model. The calibration procedure could be improved through the use of confocal fluorescence microscopy in future studies. It should be noted, that while in this study, the label was expressed by the microorganism together with the molecule of interest, this is not strictly required.²⁴ Therefore, label-free applications of this method can be conceived. Furthermore, as recent works have demonstrated PTIR measurements in aqueous media,⁴⁹ PTIR-based imaging of living microorganisms would appear to be a promising endeavor.

ASSOCIATED CONTENT

Supporting Information

The Supporting Information is available free of charge at <https://pubs.acs.org/doi/10.1021/acs.analchem.0c02228>.

Raw data and script files to perform the data analysis as described in the manuscript (zip archive) (ZIP)

PTIR spectra of the *T. reesei* strain used in this work, a wild type, and a super producer strain (PDF)

AUTHOR INFORMATION

Corresponding Author

Georg Ramer – Institute of Chemical Technologies and Analytics, TU Wien, Vienna 1060, Austria; orcid.org/0000-0001-8307-5435; Email: georg.ramer@tuwien.ac.at

Authors

A. Catarina V. D. dos Santos – Institute of Chemical Technologies and Analytics, TU Wien, Vienna 1060, Austria; orcid.org/0000-0001-6342-2823

Rosa Heydenreich – Institute of Chemical, Environmental and Bioscience Engineering, TU Wien, Vienna 1060, Austria

Christian Derntl – Institute of Chemical, Environmental and Bioscience Engineering, TU Wien, Vienna 1060, Austria

Astrid R. Mach-Aigner – Institute of Chemical, Environmental and Bioscience Engineering, TU Wien, Vienna 1060, Austria

Robert L. Mach – Institute of Chemical, Environmental and Bioscience Engineering, TU Wien, Vienna 1060, Austria

Bernhard Lendl – Institute of Chemical Technologies and Analytics, TU Wien, Vienna 1060, Austria; orcid.org/0000-0003-3838-5842

Complete contact information is available at:

<https://pubs.acs.org/10.1021/acs.analchem.0c02228>

Author Contributions

The experiment was devised jointly by all authors. R.H., C.D., A.R.M.A., and R.M. developed the fungal strain and prepared the samples. C.S. and R.H. performed fluorescence microscopy, C.S. and G.R. performed PTIR measurements and data

evaluation. The manuscript was written through contributions of all authors. All authors have given approval to the final version of the manuscript.

Notes

The authors declare no competing financial interest.

ACKNOWLEDGMENTS

This work is part of the COMET Centre CHASE. The COMET Centre CHASE is funded within the framework of the COMET-Competence Centers for Excellent Technologies by BMVIT, BMDW, and the Federal Provinces of Upper Austria and Vienna. The COMET program is run by the Austrian Research Promotion Agency (FFG). This study was also supported by a grant from the Austrian Science Fund (FWF): P26733-B22 given to A.R.M.A.

REFERENCES

- Wolff, S.; Weissman, J. S.; Dillin, A. *Cell* **2014**, *157*, 52–64.
- Wolfenden, R.; Snider, M. J. *Acc. Chem. Res.* **2001**, *34*, 938–945.
- Shoda, S.-i.; Uyama, H.; Kadokawa, J.-i.; Kimura, S.; Kobayashi, S. *Chem. Rev.* **2016**, *116*, 2307–2413.
- Hartl, F. U. *Annu. Rev. Biochem.* **2017**, *86*, 21–26.
- Wells, E.; Robinson, A. S. *Biotechnol. J.* **2017**, *12*, 1600105.
- Bischof, R. H.; Ramoni, J.; Seiboth, B. *Microb. Cell Fact.* **2016**, *15*, 106.
- Lelli, K. M.; Slattery, M.; Mann, R. S. *Annu. Rev. Genet.* **2012**, *46*, 43–68.
- Cavalli, G.; Cenci, S. *J. Mol. Biol.* **2020**, *432*, 2525–2545.
- Ghosh, A.; Al-Rabaii, S.; Ghosh, B. K.; Trimiño-Vazquez, H.; Eveleigh, D. E.; Montencourt, B. S. *Enzyme Microb. Technol.* **1982**, *4*, 110–113.
- Nykänen, M.; Birch, D.; Peterson, R.; Yu, H.; Kautto, L.; Gryshyna, A.; Te'o, J.; Nevalainen, H. *Curr. Genet.* **2016**, *62*, 455–465.
- de Paula, R. G.; Antoniêto, A. C. C.; Nogueira, K. M. V.; Ribeiro, L. F. C.; Rocha, M. C.; Malavazi, I.; Almeida, F.; Silva, R. N. *Biotechnol. Biofuels* **2019**, *12*, 146.
- Huang, B.; Babcock, H.; Zhuang, X. *Cell* **2010**, *143*, 1047–1058.
- Schubert, V. *Front. Plant Sci.* **2017**, *8*, 531.
- Bergstrand, J.; Xu, L.; Miao, X.; Li, N.; Öktem, O.; Franzén, B.; Auer, G.; Lomnytska, M.; Widengren, J. *Nanoscale* **2019**, *11*, 10023–10033.
- Huang, Y.; Ma, T.; Lau, P. K.; Wang, J.; Zhao, T.; Du, S.; Loy, M. M. T.; Guo, Y. *Front. Cell Dev. Biol.* **2019**, *7*, 181.
- MacDonald, L.; Baldini, G.; Storrie, B. Does Super-Resolution Fluorescence Microscopy Obsolete Previous Microscopic Approaches to Protein Co-Localization? In *Membrane Trafficking*; 2nd Edition; Tang, B. L., Ed.; Springer New York: New York, NY, 2015; pp 255–275.
- Lambert, T. J.; Waters, J. C. *J. Cell Biol.* **2016**, *216*, 53–63.
- Samanta, S.; Gong, W.; Li, W.; Sharma, A.; Shim, I.; Zhang, W.; Das, P.; Pan, W.; Liu, L.; Yang, Z.; Qu, J.; Kim, J. S. *Coord. Chem. Rev.* **2019**, *380*, 17–34.
- Lasch, P.; Naumann, D. *Biochim. Biophys. Acta* **2006**, *1758*, 814–829.
- Dazzi, A.; Glotin, F.; Carminati, R. *J. Appl. Phys.* **2010**, *107*, 124519.
- Dazzi, A.; Prater, C. B. *Chem. Rev.* **2017**, *117*, 5146–5173.
- Dazzi, A. PhotoThermal Induced Resonance. Application to Infrared Spectromicroscopy. In *Topics in Applied Physics: Thermal Nanosystems and Nanomaterials*; Volz, S., Ed.; Springer, 2009; Vol. 118.
- Lahiri, B.; Holland, G.; Centrone, A. *Small* **2013**, *9*, 439–445.
- Baker, M. J.; Trevisan, J.; Bassan, P.; Bhargava, R.; Butler, H. J.; Dorling, K. M.; Fielden, P. R.; Fogarty, S. W.; Fullwood, N. J.; Heys, K. A.; Hughes, C.; Lasch, P.; Martin-Hirsch, P. L.; Obinaju, B.; Sockalingum, G. D.; Sulé-Suso, J.; Strong, R. J.; Walsh, M. J.; Wood, B. R.; Gardner, P.; Martin, F. L. *Nat. Protoc.* **2014**, *9*, 1771–1791.
- Katzenmeyer, A. M.; Canivet, J.; Holland, G.; Farrusseng, D.; Centrone, A. *Angew. Chem., Int. Ed.* **2014**, *53*, 2852–2856.
- Ma, X.; Zhou, X.; Yu, A.; Zhao, W.; Zhang, W.; Zhang, S.; Wei, L.; Cook, D. J.; Roy, A. *J. Chromatogr. A* **2018**, *1537*, 1–9.
- Morsch, S.; Emad, S.; Farren, L. A.; Goodall, M. D.; Lyon, S. B.; Gibbon, S. R. *Sci. Rep.* **2018**, *8*, 17450.
- Yu, H. M.; Oh, H. M.; Park, D. Y.; Jeong, M. S. *J. Phys. Chem. C* **2020**, *124*, 3915–3922.
- Liu, Y.; Collins, L.; Proksch, R.; Kim, S.; Watson, B. R.; Doughty, B.; Calhoun, T. R.; Ahmadi, M.; Ievlev, A. V.; Jesse, S.; Retterer, S. T.; Belianinov, A.; Xiao, K.; Huang, J.; Sumpter, B. G.; Kalinin, S. V.; Hu, B.; Ovchinnikova, O. S. *Nat. Mater.* **2018**, *17*, 1013–1019.
- Li, C.; Wang, Z.; Liu, W.; Ji, X.; Su, Z. *Macromolecules* **2020**, *53*, 2686–2693.
- Nguyen-Tri, P.; Prud'homme, R. E. *J. Photochem. Photobiol. Chem.* **2019**, *371*, 196–204.
- Morsch, S.; van Driel, B. A.; van den Berg, K. J.; Dik, J. *ACS Appl. Mater. Interfaces* **2017**, *9*, 10169–10179.
- Ma, X.; Beltran, V.; Ramer, G.; Pavlidis, G.; Parkinson, D. Y.; Thoury, M.; Meldrum, T.; Centrone, A.; Berrie, B. H. *Angew. Chem., Int. Ed.* **2019**, *58*, 11652–11656.
- Bondy, A. L.; Kirpes, R. M.; Merzel, R. L.; Pratt, K. A.; Banaszak Holl, M. M.; Ault, A. P. *Anal. Chem.* **2017**, *89*, 8594–8598.
- Kurouski, D.; Dazzi, A.; Zenobi, R.; Centrone, A. *Chem. Soc. Rev.* **2020**, *49*, 3315.
- Abarghani, A.; Gentzis, T.; Liu, B.; Hohlbauch, S.; Griffin, D.; Bubach, B.; Shokouhimehr, M.; Ostadhassan, M. *Int. J. Coal Geol.* **2020**, *223*, 103465.
- Kebukawa, Y.; Kobayashi, H.; Urayama, N.; Baden, N.; Kondo, M.; Zolensky, M. E.; Kobayashi, K. *Proc. Natl. Acad. Sci. U.S.A.* **2019**, *116*, 753.
- Perez-Guaita, D.; Kochan, K.; Batty, M.; Doerig, C.; Garcia-Bustos, J.; Espinoza, S.; McNaughton, D.; Heraud, P.; Wood, B. R. *Anal. Chem.* **2018**, *90*, 3140–3148.
- Quaroni, L. *Molecules* **2019**, *24*, 4504.
- Baldassarre, L.; Giliberti, V.; Rosa, A.; Ortolani, M.; Bonamore, A.; Baiocco, P.; Kjoller, K.; Calvani, P.; Nucara, A. *Nanotechnology* **2016**, *27*, 075101.
- Chan, K. L. A.; Lekkas, I.; Frogley, M. D.; Cinque, G.; Altharawi, A.; Bello, G.; Dailey, L. A. *Anal. Chem.* **2020**, *92*, 8097.
- Deniset-Besseau, A.; Prater, C. B.; Viroille, M.-J.; Dazzi, A. *J. Phys. Chem. Lett.* **2014**, *5*, 654–658.
- Rebois, R.; Onidas, D.; Marcott, C.; Noda, I.; Dazzi, A. *Anal. Bioanal. Chem.* **2017**, *409*, 2353–2361.
- Kim, S. Y.; Khanal, D.; Tharkar, P.; Kalionis, B.; Chrzanowski, W. *Nanoscale Horiz.* **2018**, *3*, 430–438.
- Wieland, K.; Ramer, G.; Weiss, V. U.; Allmaier, G.; Lendl, B.; Centrone, A. *Nano Res.* **2019**, *12*, 197–203.
- Zhou, J.; Sekatskii, S.; Welc, R.; Dietler, G.; Gruszecki, W. I. *Biochim. Biophys. Acta Bioenerg.* **2020**, *1861*, 148117.
- Ramer, G.; Balbekova, A.; Schwaighofer, A.; Lendl, B. *Anal. Chem.* **2015**, *87*, 4415–4420.
- Rizevsky, S.; Kurouski, D. *ChemBioChem* **2020**, *21*, 481–485.
- Ramer, G.; Ruggeri, F. S.; Levin, A.; Knowles, T. P. J.; Centrone, A. *ACS Nano* **2018**, *12*, 6612–6619.
- Paluszkiwicz, C.; Piergies, N.; Chaniecki, P.; Rękas, M.; Miszczyk, J.; Kwiatek, W. M. *J. Pharm. Biomed. Anal.* **2017**, *139*, 125–132.
- Quaroni, L.; Pogoda, K.; Wiltowska-Zuber, J.; Kwiatek, W. M. *RSC Adv.* **2018**, *8*, 2786–2794.
- Druzhinina, I. S.; Kubicek, C. P. Familiar Stranger: Ecological Genomics of the Model Saprotroph and Industrial Enzyme Producer *Trichoderma Reesei* Breaks the Stereotypes. In *Advances in Applied Microbiology*; Sariaslani, S., Michael Gadd, G., Eds.; Academic Press, 2016; Vol. 95, Chapter 2, pp 69–147. DOI: 10.1016/bs.aambs.2016.02.001

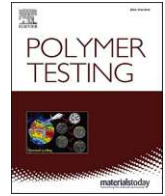
- (53) Suurnäkki, A.; Tenkanen, M.; Siika-aho, M.; Niku-Paavola, M.-L.; Viikari, L.; Buchert, J. *Cellulose* **2000**, *7*, 189–209.
- (54) Nevalainen, H.; Suominen, P.; Taimisto, K. J. *Biotechnol.* **1994**, *37*, 193–200.
- (55) Miettinen-Oinonen, A.; Paloheimo, M.; Lantto, R.; Suominen, P. J. *Biotechnol.* **2005**, *116*, 305–317.
- (56) Ellilä, S.; Fonseca, L.; Uchima, C.; Cota, J.; Goldman, G. H.; Saloheimo, M.; Sacon, V.; Siika-Aho, M. *Biotechnol. Biofuels* **2017**, *10*, 30.
- (57) Steiger, M. G.; Vitikainen, M.; Uskonen, P.; Brunner, K.; Adam, G.; Pakula, T.; Penttilä, M.; Saloheimo, M.; Mach, R. L.; Mach-Aigner, A. R. *Appl. Environ. Microbiol.* **2011**, *77*, 114.
- (58) Derntl, C.; Kiesenhofer, D. P.; Mach, R. L.; Mach-Aigner, A. R. *Appl. Environ. Microbiol.* **2015**, *81*, 6314.
- (59) Mach, R. L.; Schindler, M.; Kubicek, C. P. *Curr. Genet.* **1994**, *25*, 567–570.
- (60) Gruber, F.; Visser, J.; Kubicek, C. P.; de Graaff, L. H. *Curr. Genet.* **1990**, *18*, 71–76.
- (61) Punt, P. J.; Oliver, R. P.; Dingemanse, M. A.; Pouwels, P. H.; van den Hondel, C. A. M. J. *J. Gene* **1987**, *56*, 117–124.
- (62) Mandels, M. *Biochem. Soc. Trans.* **1985**, *13*, 414–416.
- (63) Lu, F.; Jin, M.; Belkin, M. A. *Nat. Photonics* **2014**, *8*, 307–312.
- (64) Pedregosa, F.; Varoquaux, G.; Gramfort, A.; Michel, V.; Thirion, B.; Grisel, O.; Blondel, M.; Prettenhofer, P.; Weiss, R.; Dubourg, V.; Vanderplas, J.; Passos, A.; Cournapeau, D.; Brucher, M.; Perrot, M.; Duchesnay, E. *J. Mach. Learn. Res.* **2011**, *12*, 2825–2830.
- (65) Farrés, M.; Platikanov, S.; Tsakovski, S.; Tauler, R. *J. Chemom.* **2015**, *29*, 528–536.
- (66) Stricker, A. R.; Steiger, M. G.; Mach, R. L. *FEBS Lett.* **2007**, *581*, 3915–3920.
- (67) Miyazawa, T.; Blout, E. R. *J. Am. Chem. Soc.* **1961**, *83*, 712–719.
- (68) Goormaghtigh, E.; Ruysschaert, J.-M.; Raussens, V. *Biophys. J.* **2006**, *90*, 2946–2957.
- (69) Barth, A. *Biochim. Biophys. Acta Bioenerg.* **2007**, *1767*, 1073–1101.
- (70) Kong, J.; Yu, S. *Acta Biochim. Biophys. Sin.* **2007**, *39*, 549–559.
- (71) Wilkosz, N.; Czaja, M.; Seweryn, S.; Skirlińska-Nosek, K.; Szymanski, M.; Lipiec, E.; Sofińska, K. *Molecules* **2020**, *25*, 2498.
- (72) De Meulenaere, E.; Nguyen Bich, N.; de Wergifosse, M.; Van Hecke, K.; Van Meervelt, L.; Vanderleyden, J.; Champagne, B.; Clays, K. *J. Am. Chem. Soc.* **2013**, *135*, 4061–4069.
- (73) Divne, C.; Stahlberg, J.; Reinikainen, T.; Ruohonen, L.; Pettersson, G.; Knowles, J.; Teeri, T.; Jones, T. *Science* **1994**, *265*, 524.
- (74) Zhang, J.; Chen, Y.; Wu, C.; Liu, P.; Wang, W.; Wei, D. *J. Biol. Chem.* **2019**, *294*, 18435–18450.
- (75) Kleywegt, G. J.; Zou, J.-Y.; Divne, C.; Davies, G. J.; Sinning, I.; Ståhlberg, J.; Reinikainen, T.; Srisodsuk, M.; Teeri, T. T.; Jones, T. A. *J. Mol. Biol.* **1997**, *272*, 383–397.
- (76) Torronen, A.; Rouvinen, J. *Biochemistry* **1995**, *34*, 847–856.
- (77) Nyssönen, E.; Keränen, S. *Curr. Genet.* **1995**, *28*, 71–79.
- (78) Saloheimo, M.; Pakula, T. M. *Microbiology* **2012**, *158*, 46–57.

Publication II

Systematic Analysis and Nanoscale Chemical Imaging of Polymers Using Photothermal-Induced Resonance (AFM-IR) Infrared Spectroscopy

*A. Catarina V. D. dos Santos, Bernhard Lendl, and Georg Ramer**

Polymer Testing, 2022, 106, 107443



Systematic analysis and nanoscale chemical imaging of polymers using photothermal-induced resonance (AFM-IR) infrared spectroscopy

A. Catarina V.D. dos Santos, Bernhard Lendl **, Georg Ramer *

Institute of Chemical Technologies and Analytics, TU Wien, 1060, Vienna, Austria

ARTICLE INFO

Keywords:

AFM-IR
Chemical characterization
Polymer analysis
Nanoscale infrared spectroscopy

ABSTRACT

In this work, a reliable and time-saving protocol for the measurement of polymers using photothermal-induced resonance (AFM-IR) at the nanoscale was developed and applied to 4 industrially relevant polymers: a polypropylene-based reactor thermoplastic polyolefin (rTPO), linear low density polyethylene (LLDPE) for molding and two recycled post-consumer polypropylene/polyethylene blends. In addition to the morphology obtained through AFM, we were able to identify and image the major components of each polymer, including the mineral fillers (talc and calcium carbonate) present in each blend using nanoscale spatial resolution infrared imaging. The protocol developed allows the quick analysis and identification at the nanoscale of the major components of a blend without having previous knowledge of the sample composition, a major advantage when compared to other traditionally used imaging techniques such as TEM and SEM.

1. Introduction

Synthetic polymers are a success story: in a little over a century and a half they have gone from a curiosity in the chemistry labs to being omnipresent in day-to-day life [1]. This takeover was driven by the advantages these materials have over traditional ones, such as their lower price, lighter weight, versatility, and durability. Nowadays, in addition to improving performance of polymer materials, polymer recycling and recyclability have gained in importance. For example, the European Union (EU) considers polymer recycling as an important piece of the circular economy action plan, a key element for the success of the European green deal [2] as a way to both reduce the production of new polymers and the percentage of already existing polymers that become waste. In contrast to recycling of inorganic materials polymer recycling poses some additional challenges: there is a limit to the amount of recycling cycles a polymer can go through before it becomes waste, and the presence of contaminants can lead to undesirable blends [3,4].

The nano- and microscale structure and chemical composition of a polymer has great influence on its macroscale properties [5]. It is therefore of great importance, to have methods that allow us to probe into this nano realm and obtain as much information as possible. This information could provide valuable insights into the improvement of recycling and manufacturing processes. The structure of polymers can

be analyzed by a variety of methods including mass spectrometry (often hyphenated with chromatographic techniques) [6–8], X-ray diffraction [9,10], transmission electron microscopy (TEM) [11,12], scanning electron microscopy (SEM) [13–15], atomic force microscopy (AFM) [16–18], Raman spectroscopy [19,20], and FTIR [21–23]. Although these techniques provide a great deal of information, they cannot provide explicit chemical analysis at the nanoscale.

AFM-IR, also called PTIR, is a recent technique that allows for infrared spectroscopy to be performed at the nanometer spatial resolution scale [24], a huge advantage when compared to the diffraction-limited mid-IR microscopy which only achieves micrometer spatial resolution [25]. AFM-IR uses the thermal expansion of the sample area underneath the AFM tip caused by the absorption of radiation from a pulsed wavelength-tunable IR laser to achieve spatial resolution significantly below the limit of diffraction.

For the chemical spectroscopist one of the most attractive features of AFM-IR is that it provides spectra that compare well to conventional FTIR absorption spectra, because both the FTIR and AFM-IR signals are proportional to the wavelength dependent absorption coefficient of the sample [26]. The thermal expansion is proportional to the absorbed energy and causes changes in the deflection signal of the AFM cantilever. The signal is thus detected in the near-field, which permits lateral resolutions of up to 20 nm in contact mode and ≈ 10 nm in tapping mode

* Corresponding author.

** Corresponding author.

E-mail addresses: bernhard.lendl@tuwien.ac.at (B. Lendl), georg.ramer@tuwien.ac.at (G. Ramer).

<https://doi.org/10.1016/j.polymertesting.2021.107443>

Received 3 November 2021; Accepted 26 November 2021

Available online 27 November 2021

0142-9418/© 2021 The Authors. Published by Elsevier Ltd. This is an open access article under the CC BY license (<http://creativecommons.org/licenses/by/4.0/>).

[26,27]. The recent invention of tapping mode AFM-IR makes the method more attractive for polymer analysis [28], as tapping mode AFM-IR is better suited for the analysis of soft and heterogeneous samples (such as polymers), due to the cantilever resonance frequencies being less susceptible to changes in the mechanical properties of the sample when compared to resonance-enhanced contact-mode AFM-IR [29]. This has enabled the application of AFM-IR to various types of samples such as aerosol particles [30,31], semiconductors [32], drug nanocarriers [27,33], metal organic frameworks (MOFs) [34], oil paints [35], viruses [36,37], and cells and intracellular proteins [38–40]. Studies on polymers and their properties have also been reported, namely on polymer structure [41–43], degradation [44–46], and polymer-metal interfaces [47,48], among others.

AFM-IR has also been applied previously to polymers by Tang et al. [49] in their first analysis of the nanodomains present in impact polypropylene copolymer (IPC) in 2016. In 2018, the researchers complemented this analysis by concluding that the composition of the core in the core-shell rubber particle morphology typical of this polymer is dependent on the polymerization conditions, and can be PE or PP [50]. Despite all of these studies, which are typically focused on answering highly specialized research questions there is still no established protocol for routine reproducible AFM-IR measurements of polymers, a knowledge gap that this work intends to fill. We compiled a five step protocol that include guidelines from sample preparation to interpretation of results. This protocol is then applied to a range of common commercial polymers of the most produced polymer group in Europe in 2019, polyolefins [51]. These include a reactor thermoplastic polyolefin (rTPO), LLDPE, and two recycled PP/PE blends.

Reactor thermoplastic polyolefins (rTPOs), also known as impact copolymers or heterophasic copolymers, consist of a hard semi-crystalline PP or PE matrix and a soft component such as ethylene-propylene rubber (EPR) [52]. rTPOs are produced by co-polymerization of different monomers in several reactors, resulting in a polymer alloy with smaller size of evenly distributed rubber crystals and improved impact strength when compared to those produced by melt compounding [53,54]. It is important to find balance between improving the impact strength and other potentially desirable properties such as stiffness, heat deflection temperature and toughness. One way to achieve this is through the addition of mineral fillers, which can be further fine-tuned by adjusting the concentration and particle size [55]. rTPOs are commonly used in the automotive industry as bumpers and battery cases [56].

Linear low density polyethylene (LLDPE) has a long linear backbone and randomly distributed short side chain branches [52]. LLDPE has higher tensile strength, impact strength, tear resistance, and puncture resistance than low-density polyethylene (LDPE) and has found widespread use in injection molding and blow molding, as well as in films, packaging, cable insulation, and tubing, among others [57–59].

In this work, we take a systematic approach to the analysis of polymers using AFM-IR and present a protocol that leads from an unknown polymer sample to knowledge of its general nanoscale characteristics in one measurement. Care is taken to ensure that the chemical images obtained are not affected by topographic cross-talk. We demonstrate the validity of our protocol by applying it to four commercially available samples and obtaining the chemical distribution of not only its phase domains (when present) but also of the distribution of the mineral fillers and other components. In the recycled post-consumer polymers analyzed it was possible to characterize in detail various phases present.

2. Experimental

2.1. Materials

Hifax CA 7442A from LyondellBasell, a commercially available polypropylene rTPO, and LL 6101 from ExxonMobil, a commercially available LLDPE were provided by Omya. Furthermore, two

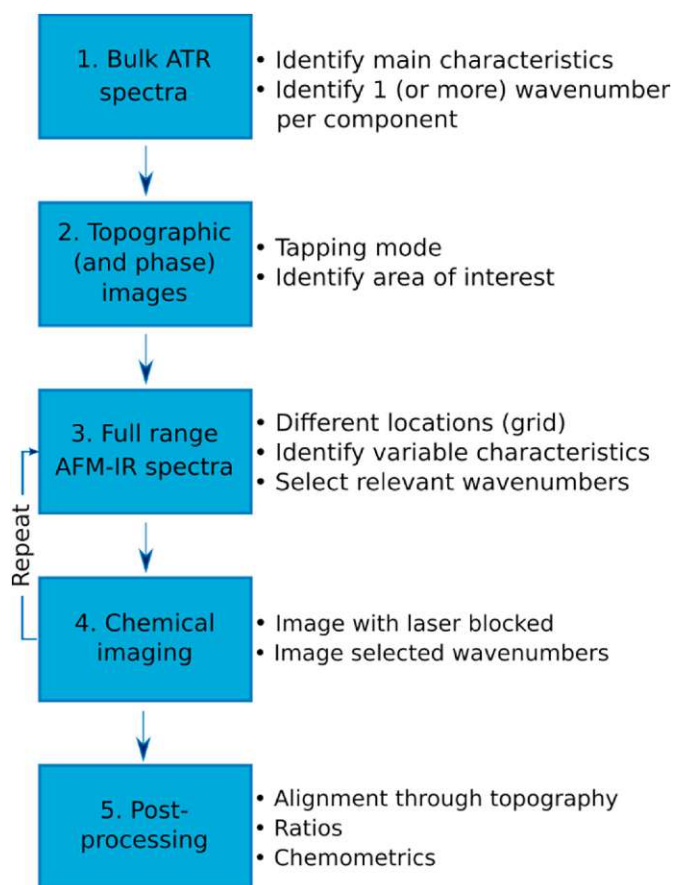


Fig. 1. Protocol for AFM-IR measurements of unknown polymer samples. Steps 3. and 4. can be repeated, if necessary, to obtain optimal chemical imaging.

commercially available recycled PP/PE copolymers containing different mineral fillers from the Skyfil product line were provided by PreZero Polymers: Skyfil 1 (06MT05C15) and Skyfil 2 (06HH06T10).

2.2. ATR-FTIR measurements

ATR FTIR measurements were performed on a Bruker Tensor 37 equipped with a Platinum ATR accessory. The spectra were collected by averaging 8 spectra with 2 cm^{-1} resolution.

2.3. Sample preparation

The samples were ultra-cryomicrotomed at $-100\text{ }^{\circ}\text{C}$ on a Leica EM-UC7 equipped with a Leica EM FC7 cryochamber or on a PowerTome PC with CR-X cryosectioning system (Boeckeler Instruments), and the resulting sections were placed on ZnS substrates (13 mm diameter \times 1 mm thickness from Crystran).

2.4. AFM-IR measurements

All AFM-IR measurements were carried out using a Bruker nano-IR 3s coupled to a MIRcat-QT external cavity quantum cascade laser array (EC-QCL) from Daylight Solutions. Spectra covering the range from 910 cm^{-1} to 1650 cm^{-1} were obtained using AFM-IR in tapping mode with a heterodyne detection scheme. The measurements were obtained while driving the cantilever at its second resonance frequency ($f_2 \approx 1500\text{ kHz}$) and demodulating the AFM-IR signal at the first resonance frequency ($f_1 \approx 250\text{ kHz}$) using a digital lock-in amplifier (MFLI from Zurich Instruments). The laser repetition rate was set to $f_L = f_2 - f_1 \approx 1300\text{ kHz}$. The cantilevers used were gold coated with nominal first

free resonance frequencies of 300 ± 100 kHz and spring constants between 20 and 75 N/m (Tap300GB-G from BudgetSensors). The laser source operated at 10% duty cycle and 14.8% power (before beam splitter). For each location, 3 spectra were recorded at 1 cm^{-1} spectral resolution. The instrument and all beam paths were purged with dry air generated by an adsorptive dry air generator.

2.5. Data processing

Recorded AFM-IR spectra were averaged by location, normalized to the maximum value in the range between 1400 cm^{-1} and 1500 cm^{-1} and smoothed using a Savitzky-Golay filter (9 points, first order).

The shift between chemical images was corrected using sub pixel registration via phase cross correlation based on their simultaneously recorded topography counterparts as reference. Calculations were performed using the phase cross correlation implementation in the scikit-image package for Python 3 [60].

3. Results and discussion

Key to reproducible and routine AFM-IR polymer characterization is a protocol that can be applied to a wide range of polymer samples. The protocol developed in this study is presented in Fig. 1.

3.1. Bulk ATR spectra (step 1)

The first step of this protocol entails gaining a general mid-IR spectroscopic understanding of the sample. In this study, we chose to take single bulk ATR spectrum to get an overview of the bands present in each material. However, if there are other established sources of information (prior experience, band assignment tables, reference spectra) they can be used instead. Taking a new spectrum of each material is thus optional but recommended. The information obtained will also prove useful in the final optimization steps necessary to start an AFM-IR measurement when using an EC-QCL array, where knowledge of absorption bands in different regions of the spectrum (one for each EC-QCL chip used) is necessary for the final alignment of the mid-IR laser source. Due to the vastly different spatial resolutions achieved in far field IR and AFM-IR, we have found no advantage in taking care to image the same sample area using a far field IR microscope.

3.2. Topography (and phase) images (step 2)

Sample preparation is a critical step to ensure a successful measurement. The polymer samples should be cut with an ultra-(cryo) microtome below their glass-transition temperature (to avoid smearing) into sections with a submicron thickness, as in thicker sections signal saturation may occur [61]. Furthermore, the choice of a reflective substrate (e.g., gold) will have a wavelength-dependent influence on the spectra obtained [61], therefore, we recommend the use of non-reflective IR transparent substrates, such as CaF_2 or ZnSe . These substrates are available commercially as optical windows. The initial part of an AFM-IR measurement is a topographic AFM measurement. For polymer samples tapping mode is preferred over contact mode, since it reduces the possibility of sample damage due to weaker tip-sample interactions [62].

3.3. Full range AFM-IR spectra (step 3)

Once a region of interest is chosen and an AFM image is obtained, the next step is to obtain several AFM-IR spectra in a grid. In this work we have used 4×4 grids covering the $10 \mu\text{m} \times 10 \mu\text{m}$ areas imaged, an example of which can be found in Appendix A. This allows us to quickly estimate whether certain bands are present everywhere or only in certain locations. If there are further points of interest visible in the topography, additional spectra can be obtained before selecting which

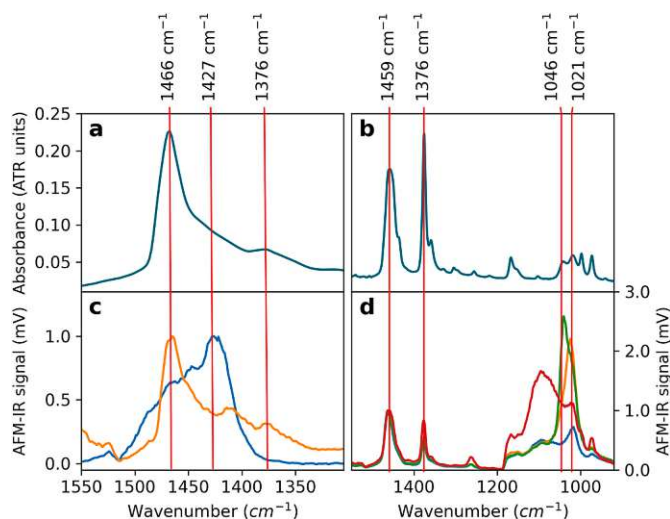


Fig. 2. Comparison of bulk ATR spectra (top row) and AFM-IR spectra (bottom row) obtained in different locations for LLDPE (a,c) and rTPO (b,d). The AFM-IR spectra are normalized to the 1459 cm^{-1} band intensity.

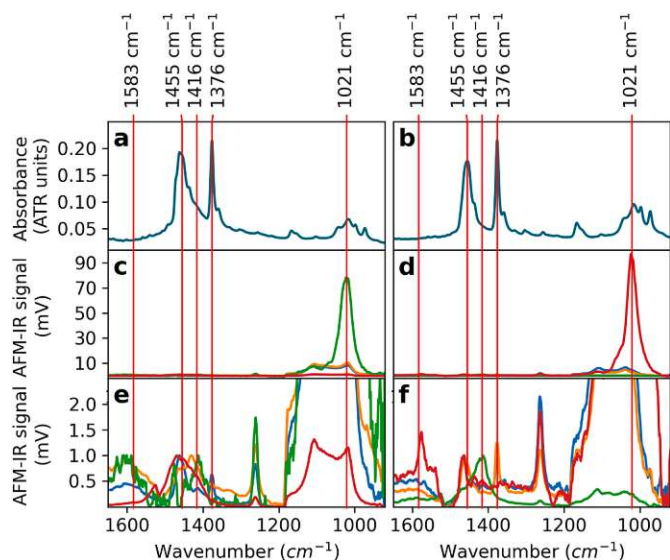


Fig. 3. Comparison of bulk ATR spectra and AFM-IR spectra obtained in different locations for (a), (c), (e) Skyfil 1 and (b), (d), (f) Skyfil 2. (c) and (e), and (d) and (f) correspond to the same spectra but with different scales. The AFM-IR spectra are normalized to the 1459 cm^{-1} band intensity. (*) The peak at 1263 cm^{-1} is present in all the samples analyzed and has been attributed to silicone oil contamination of commercial AFM cantilever tips [66].

wavenumbers to image. The wavelength selection process can vary depending on prior knowledge and sample complexity. For simpler samples (with only a few major components) the identification of the wavenumbers of interest is straightforward. Fig. 2 and Fig. 3 are examples of such selections. However, more complex samples may require chemometric analysis such as clustering or PCA to facilitate the identification of the main features. Examples of the application of chemometrics to the analysis of polymer samples using FTIR are abundant and demonstrate the versatility and usefulness of such approach [63–65]. Figs. 2 and 3 illustrate how the selection of relevant wavenumbers can be performed. In the case of LLDPE (Fig. 2, (a) and (c)) the advantage of AFM-IR over bulk FTIR is clearly visible, as from spectra obtained in two distinct locations it is possible to separately identify the polymer itself (orange), and CaCO_3 (blue) with a peak at 1427 cm^{-1} , the filler. Also, for the rTPO (Fig. 2, (b) and (d)) it is possible to separate locations with

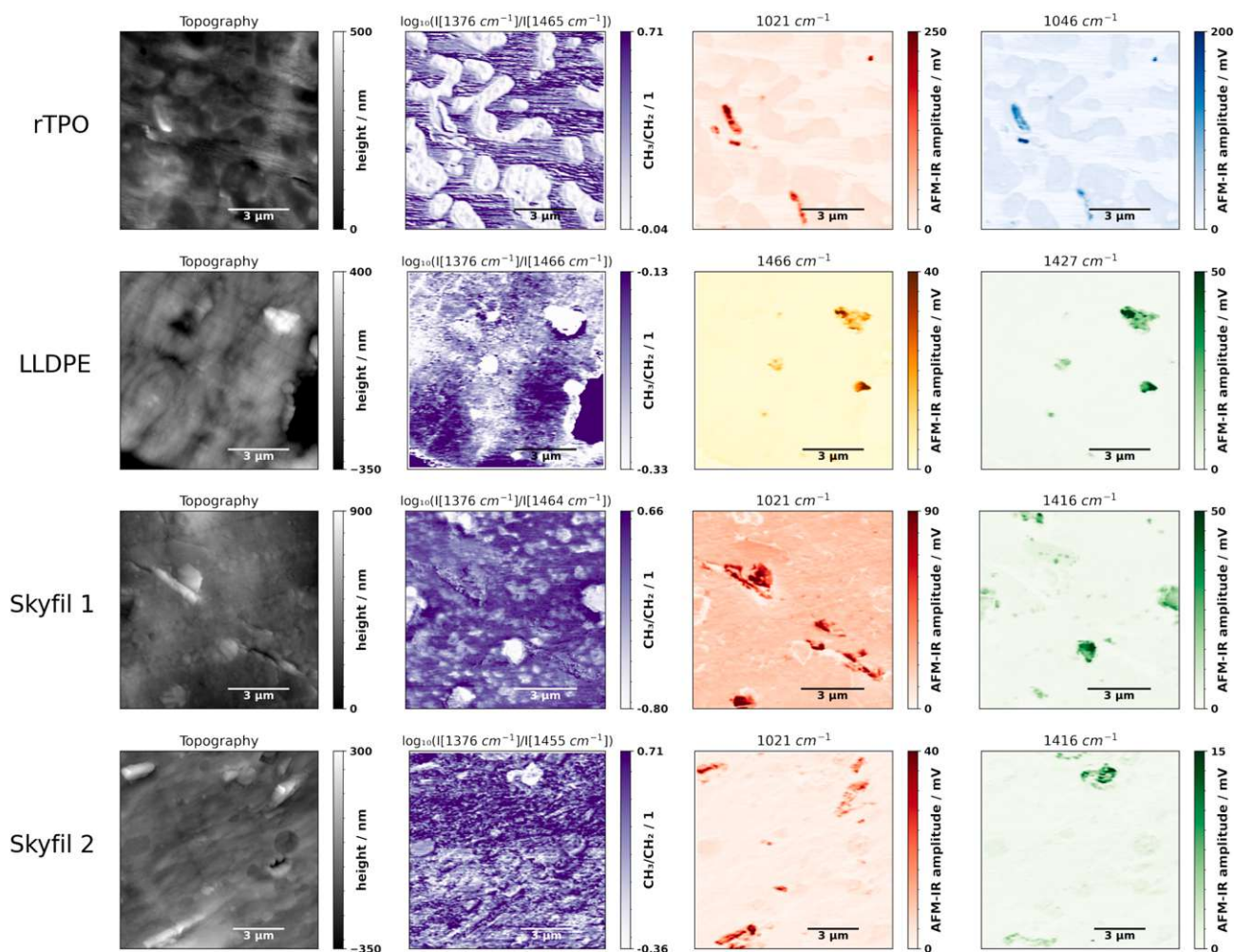


Fig. 4. Topography and chemical maps of the analyzed samples for selected wavenumbers for each of the analyzed samples. Purple corresponds to the ratio of the bands corresponding to deformation vibrations of CH_2 and symmetric deformation of CH_3 groups; Red and blue correspond to the presence of talc; Yellow to CH_2 deformation vibrations; Green indicates the presence of CaCO_3 . (For interpretation of the references to color in this figure legend, the reader is referred to the Web version of this article.)

higher and lower PE content by comparison of the relative heights of the 1459 cm^{-1} (corresponding to the scissor vibration of $-\text{CH}_2$ groups with contributions from asymmetric deformation vibrations of $-\text{CH}_3$ groups) and 1376 cm^{-1} peaks (corresponding exclusively to the CH_3 group symmetric vibration band). Moreover, it is also possible to single out locations where talc is present (absorption at 1021 cm^{-1} and 1046 cm^{-1}).

In the case of the recyclates, Skyfil 1 and Skyfil 2 (Fig. 3), the spectra are, as expected, more complex. These recyclates are mixtures of post-consumer and post-industrial materials and contain no virgin material. Both contain talc (1021 cm^{-1}) and CaCO_3 (1416 cm^{-1}). As with rTPO it is possible to see differences in PE content for both. An additional band at 1583 cm^{-1} was found in one location which is hardly visible in the bulk FTIR.

3.4. Chemical imaging (step 4)

Once a list of wavenumbers of interest has been compiled, images are taken at each of them (Fig. 1, step 4). Since the AFM-IR signal is transduced as AFM cantilever oscillations that can also be induced or modulated by processes independent of the infrared absorption and laser intensity, it is important to ensure that the AFM-IR amplitude is significantly above the level of such artifacts. A facile way to ensure this is to collect a “mock” AFM-IR image with the laser beam blocked. An

example of this can be found in Appendix A. Any features that appear in these mock images that have a magnitude similar those found in actual images point towards issues in the experimental setting (e.g. insufficient tracking of the surface). The image and image ratios obtained from the samples analyzed in this work are presented in Fig. 4. Steps 3 (wavelength selection) and 4 (imaging) may be repeated if some new characteristic is revealed during the imaging that justifies a return to step 3.

3.5. Post-processing (step 5)

The final step involves the interpretation of the acquired data. For single wavelength images, direct interpretation without preprocessing is possible if the signal amplitude for a given wavelength is close to zero everywhere except for a few spots with high absorption. If, however, the imaged wavelength is absorbed in large parts of the image, then evaluation should only be performed via band ratios or multivariate chemometric methods [38,40,67]. Otherwise, the contrast in the image might be dominated by changes in the contact stiffness or the local thermal and mechanical properties rather than absorption. Band ratios are calculated by dividing the pixel values in a chemical image taken at one wavenumber by those measured for another wavenumber. The result is an image that shows the relative changes of the absorption at both signals. The ratio should be unaffected by wavelength independent sample properties, as these are independent of the wavelength.

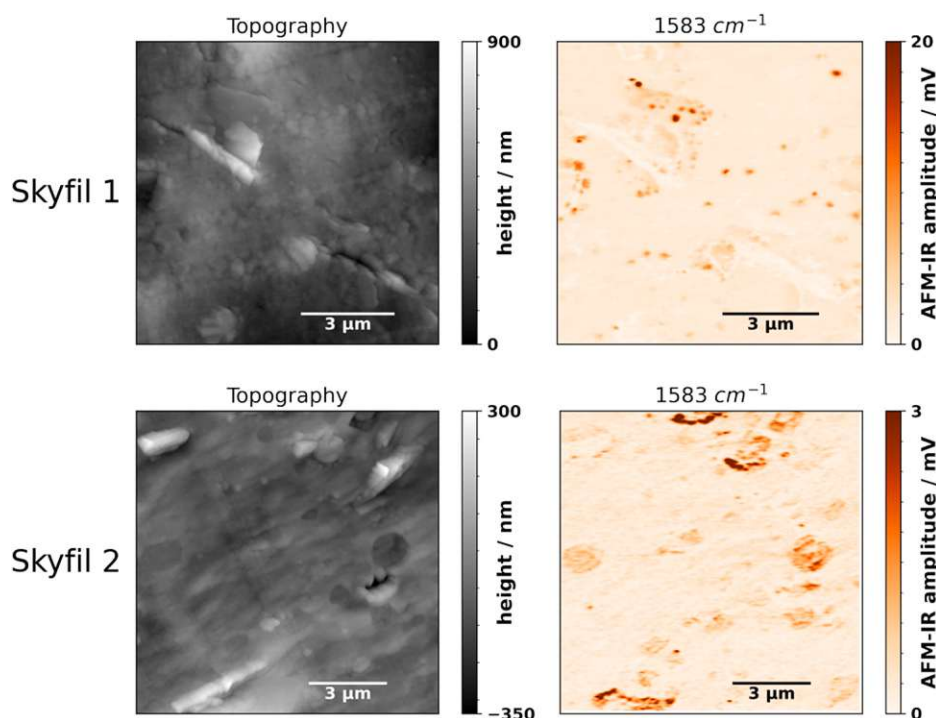


Fig. 5. Topography and chemical maps for further selected wavenumbers for the two recycled samples.

Multivariate methods combine information from a large number of wavelengths via algorithms to either find common trends (e.g., phases) in the data set or to perform quantitation in complex mixtures. A large number of such methods have successfully been applied to mid-IR imaging data, however, the choice of method for a given problem as well as the required preprocessing of data and tuning of hyperparameters is beyond the scope of this article. In this article band ratios (Fig. 4, purple) will be used to aid interpretation.

Independent of whether band ratios or multivariate methods are used some pre-processing is necessary. As the AFM is subject to thermal drift and measurement times for multiple images typically are several hours, images obtained in succession without intentionally moving the sample position show lateral shifts of the sample position. This can be problematic when multiple single wavelength images are combined. For example, band ratios offsets can result in artificially high or low values at the interfaces between phases. Since AFM-IR always acquires an AFM topography image concurrently with the chemical image, the sample topography can be used for correcting sample drifts. The images in Fig. 4 were corrected/registered by using cross correlation in the Fourier domain to determine the shift [68] via the scikit-image python package [60].

After alignment, we calculate the logarithm of the ratio of CH_3 (1376 cm^{-1}) and CH_2 (1466 cm^{-1} or 1455 cm^{-1}) groups intensity and the reveal the distribution of PP and PE in each sample (taking the logarithm ensures that doubling of the intensity in the numerator will lead to an equal but opposite change of the value as a doubling of the intensity of the denominator).

3.6. Interpretation

Below we apply our protocol to several commercial polymers to demonstrate the level of information it can provide.

TPO. For rTPO the CH_3/CH_2 ratio (Fig. 4, purple) allows for a clear visualization of the EPR component (white) inside of the propylene matrix (purple). The core-shell morphology of the rubber particles previously described in literature is well visible with the rigid PP cores inside the rubber particles appearing as purple dots inside the white

rubber [50]. Most interestingly, the distribution of the filler, talc (1021 cm^{-1} and 1046 cm^{-1}) is revealed which is not immediately apparent from the topography image: the larger filler particles in this area are present at or close to the interface between PP and EPR (an overlay image for clearer visualization is presented in Appendix A). This could mean that in addition to the nucleating effect and improved impact strength, talc also plays a role in improving the miscibility of PP/EPR blends. Such an effect has been previously observed for talc filled thermoplastic polyurethane/PP blends [69].

LLDPE. In the topography image of the LLDPE sample there are two main features: banded spherulites and a larger particle which IR analysis identifies as CaCO_3 . Unsurprisingly for a homopolymer, the 1376 cm^{-1} to 1466 cm^{-1} ratio shows no large variations (note that the color bar for the log ratio only covers a delta of 0.2 whereas for the other samples it is three to four times as large) and no particular structures, with the exception of the CaCO_3 particles which appear in white. This is due to the CaCO_3 band being broad and thus contributing to the 1466 cm^{-1} band and not due to the presence of a different polymer as is the case for rTPO. This effect is identifiable by comparison of the AFM-IR spectra taken in these locations, as well as by comparison of the 1466 cm^{-1} and 1427 cm^{-1} absorption maps, the latter being exclusively due to the presence of CaCO_3 . CaCO_3 is a common filler for LLDPE to reduce melt processing instabilities and increase the tensile yield stress [70,71].

Recyclates. The main distinction between Skyfil 1 and Skyfil 2 is the amount of PE present (approximately 35% PE for Skyfil 1 and 20% for Skyfil 2 according to data provided by PreZero) which is visible when comparing the ratio images for the two recyclates (Fig. 4). As with the LLDPE, care needs to be taken when interpreting the whitest areas of the ratio images. These correspond to CaCO_3 particles (as seen in the 1416 cm^{-1} images) and not to PE rich areas. Nonetheless it is possible to see phase separation between the PE and PP components in Skyfil 1. Both polymers contain talc, as well as CaCO_3 , even though according to information provided by PreZero Polymers, only CaCO_3 was intentionally added to Skyfil 1 and talc to Skyfil 2 during the manufacturing process. The amount of filler in recycled samples is thus dependent on the waste material used and may vary, potentially affecting the properties of the final product. For the recyclates an additional band detected in the AFM-

IR spectra was imaged: 1583 cm⁻¹ (Fig. 5). Although the band was barely detectable in the bulk FTIR spectra it is widely distributed in both recyclates. In Skyfil 1 it is present as small spots whereas in Skyfil 2 it appears to have a smoother distribution. Since these materials derive from post-consumer plastics they may contain numerous constituents both from the original material (antioxidants, plasticizers, etc.) as well as contaminants picked up during their “former lives” making the identification of what causes this band a challenge. Nonetheless the 1583 band most likely arises from C=C stretching vibration, indicating the presence of unsaturated compounds.

4. Conclusion

A protocol for the fast and reliable identification of the nanostructure and chemical composition of unknown polymer samples is described. Four different commercially polymer samples (two made from virgin materials and two recyclates) were analyzed using the developed protocol. This allowed for the mapping of the distribution of the core-shell rubber particles in the rTPO and the filler distribution in LLDPE. For the two recyclates it was found that both contain talc and CaCO₃ as fillers, owing to their previous presence in the waste material. Furthermore, the presence of unsaturated compounds was detected and mapped in both of them.

CRedit author statement

A. Catarina V.D. dos Santos: Conceptualization, Investigation, Visualization, Writing – Original Draft; **Georg Ramer:** Conceptualization, Software, Supervision, Writing – Review & Editing; **Bernhard Lendl:** Resources, Supervision, Funding acquisition, Writing – Review & Editing.

Data availability statement

The raw data required to reproduce these findings are available to download from <https://dx.doi.org/10.5281/zenodo.5607039>.

Declaration of competing interest

The authors declare that they have no known competing financial interests or personal relationships that could have appeared to influence the work reported in this paper.

Acknowledgements

The authors gratefully acknowledge Omya International AG, Omya GmbH and PreZero Polymers for providing the samples used in this study.

The microtome cuts were partially carried out by Martin Binder and Karin Whitmore using facilities at the University Service Centre for Transmission Electron Microscopy (USTEM), TU Wien, Austria.

The authors would also like to thank Walter Schaffer from Borealis for sharing his expertise in microtome cutting of polymer samples.

This work is part of the COMET Centre CHASE. The COMET Centre CHASE is funded within the framework of COMET-Competence Centers for Excellent Technologies by BMVIT, BMDW, the Federal Provinces of Upper Austria and Vienna. The COMET program is run by the Austrian Research Promotion Agency (FFG).

Appendix A. Supplementary data

Supplementary data to this article can be found online at <https://doi.org/10.1016/j.polymertesting.2021.107443>.

References

- [1] S.C. Rasmussen, Revisiting the early history of synthetic polymers: critiques and new insights, *Ambix* 65 (2018) 356–372, <https://doi.org/10.1080/00026980.2018.1512775>.
- [2] European Commission, COMMUNICATION FROM THE COMMISSION TO THE EUROPEAN PARLIAMENT, THE COUNCIL, 2020. THE EUROPEAN ECONOMIC AND SOCIAL COMMITTEE AND THE COMMITTEE OF THE REGIONS A new Circular Economy Action Plan For a cleaner and more competitive Europe, <https://eur-lex.europa.eu/legal-content/EN/TXT/?uri=COM%3A2020%3A98%3AFIN>. (Accessed 24 August 2021).
- [3] N. Singh, D. Hui, R. Singh, I.P.S. Ahuja, L. Feo, F. Fraternali, Recycling of plastic solid waste: a state of art review and future applications, *Compos. B Eng.* 115 (2017) 409–422, <https://doi.org/10.1016/j.compositesb.2016.09.013>.
- [4] J.N. Hahladakis, E. Iacovidou, Closing the loop on plastic packaging materials: what is quality and how does it affect their circularity? *Sci. Total Environ.* 630 (2018) 1394–1400, <https://doi.org/10.1016/j.scitotenv.2018.02.330>.
- [5] L. Mandelkern, The relation between structure and properties of crystalline polymers, *Polym. J.* 17 (1985) 337–350, <https://doi.org/10.1295/polymj.17.337>.
- [6] S. Crotty, S. Gerişlioglu, K.J. Endres, C. Wesdemiotis, U.S. Schubert, Polymer architectures via mass spectrometry and hyphenated techniques: a review, *Anal. Chim. Acta* 932 (2016) 1–21, <https://doi.org/10.1016/j.aca.2016.05.024>.
- [7] S.D. Hanton, Mass spectrometry of polymers and polymer surfaces, *Chem. Rev.* 101 (2001) 527–570, <https://doi.org/10.1021/cr9901081>.
- [8] C. Wesdemiotis, Multidimensional mass spectrometry of synthetic polymers and advanced materials, *Angew. Chem. Int. Ed.* 56 (2017) 1452–1464, <https://doi.org/10.1002/anie.201607003>.
- [9] N.S. Murthy, H. Minor, General procedure for evaluating amorphous scattering and crystallinity from X-ray diffraction scans of semicrystalline polymers, *Polymer* 31 (1990) 996–1002, [https://doi.org/10.1016/0032-3861\(90\)90243-R](https://doi.org/10.1016/0032-3861(90)90243-R).
- [10] M.J. Kory, M. Wörle, T. Weber, P. Payamyar, S.W. van de Poll, J. Dshemuchadse, N. Trapp, A.D. Schlüter, Gram-scale synthesis of two-dimensional polymer crystals and their structure analysis by X-ray diffraction, *Nat. Chem.* 6 (2014) 779–784, <https://doi.org/10.1038/nchem.2007>.
- [11] D. Kim, J.S. Lee, C.M.F. Barry, J.L. Mead, Microscopic measurement of the degree of mixing for nanoparticles in polymer nanocomposites by TEM images, *Microsc. Res. Tech.* 70 (2007) 539–546, <https://doi.org/10.1002/jemt.20478>.
- [12] F.M. Mirabella, N. Diod, C.G. Zimba, Theoretical analysis and experimental characterization of the TPO/adhesion promoter/paint interface of painted thermoplastic polyolefins (TPO), *Polym. Eng. Sci.* 40 (2000) 2000–2006, <https://doi.org/10.1002/pen.11332>.
- [13] M.A. Ghalia, A. Hassan, A. Yussuf, Mechanical and thermal properties of calcium carbonate-filled PP/LLDPE composite, *J. Appl. Polym. Sci.* 121 (2011) 2413–2421, <https://doi.org/10.1002/app.33570>.
- [14] J.P. Da Costa, A.R. Nunes, P.S.M. Santos, A.V. Girão, A.C. Duarte, T. Rocha-Santos, Degradation of polyethylene microplastics in seawater: insights into the environmental degradation of polymers, *Journal of Environmental Science and Health, Part A.* 53 (2018) 866–875, <https://doi.org/10.1080/10934529.2018.1455381>.
- [15] V.I. Raman, G.R. Palmese, Nanoporous thermosetting polymers, *Langmuir* 21 (2005) 1539–1546, <https://doi.org/10.1021/la048393t>.
- [16] C.G. Schirmeister, S. Schächtele, Y. Keßler, T. Hees, R. Köhler, K. Schmitz, E. H. Licht, R. Muelhaupt, Low warpage nanophase-separated polypropylene/olefinic elastomer reactor blend composites with digitally tuned glass fiber orientation by extrusion-based additive manufacturing, *ACS Appl. Polym. Mater.* 3 (2021) 2070–2081, <https://doi.org/10.1021/acsapm.1c00119>.
- [17] P. Enrique-Jimenez, J.F. Vega, J. Martínez-Salazar, F. Ania, A. Flores, Mapping the mechanical properties of Poly(3-hydroxybutyrate-co-3-hydroxyvalerate) banded spherulites by nanoindentation, *Polymers* 8 (2016) 358, <https://doi.org/10.3390/polym8100358>.
- [18] J. Xu, B.-H. Guo, Z.-M. Zhang, J.-J. Zhou, Y. Jiang, S. Yan, L. Li, Q. Wu, G.-Q. Chen, J.M. Schultz, Direct AFM observation of crystal twisting and organization in banded spherulites of chiral Poly(3-hydroxybutyrate-co-3-hydroxyhexanoate), *Macromolecules* 37 (2004) 4118–4123, <https://doi.org/10.1021/ma0499122>.
- [19] E. Karavas, M. Georarakis, A. Docoslis, D. Bikiaris, Combining SEM, TEM, and micro-Raman techniques to differentiate between the amorphous molecular level dispersions and nanodispersions of a poorly water-soluble drug within a polymer matrix, *Int. J. Pharm.* 340 (2007) 76–83, <https://doi.org/10.1016/j.ijpharm.2007.03.037>.
- [20] J. Hu, J. Wang, M. Wang, Y. Ozaki, H. Sato, J. Zhang, Investigation of crystallization behavior of asymmetric PLLA/PDLA blend using Raman Imaging measurement, *Polymer* 172 (2019) 1–6, <https://doi.org/10.1016/j.polymer.2019.03.049>.
- [21] J. Cheng, X. Yang, L. Dong, Z. Yuan, W. Wang, S. Wu, S. Chen, G. Zheng, W. Zhang, D. Zhang, H. Wang, Effective nondestructive evaluations on UHMWPE/Recycled-PA6 blends using FTIR imaging and dynamic mechanical analysis, *Polym. Test.* 59 (2017) 371–376, <https://doi.org/10.1016/j.polymertesting.2017.02.021>.
- [22] T. Mukherjee, M.J. Tobin, L. Puskar, M.-A. Sani, N. Kao, R.K. Gupta, M. Pannirselvam, N. Quazi, S. Bhattacharya, Chemically imaging the interaction of acetylated nanocrystalline cellulose (NCC) with a polylactic acid (PLA) polymer matrix, *Cellulose* 24 (2017) 1717–1729, <https://doi.org/10.1007/s10570-017-1217-x>.
- [23] R. Xie, B. Qu, Expandable graphite systems for halogen-free flame-retarding of polyolefins. II. Structures of intumescent char and flame-retardant mechanism, *J. Appl. Polym. Sci.* 80 (2001) 1190–1197, <https://doi.org/10.1002/app.1203>.

- [24] A. Dazzi, PhotoThermal induced resonance. Application to infrared spectromicroscopy, in: S. Volz (Ed.), *Thermal Nanosystems and Nanomaterials*, Springer, Berlin, Heidelberg, 2009, pp. 469–503, https://doi.org/10.1007/978-3-642-04258-4_16.
- [25] P. Lasch, D. Naumann, Spatial resolution in infrared microspectroscopic imaging of tissues, *Biochim. Biophys. Acta Biomembr.* 1758 (2006) 814–829, <https://doi.org/10.1016/j.bbmem.2006.06.008>.
- [26] A. Dazzi, F. Glotin, R. Carminati, Theory of infrared nanospectroscopy by photothermal induced resonance, *J. Appl. Phys.* 107 (2010) 124519, <https://doi.org/10.1063/1.3429214>.
- [27] K. Wieland, G. Ramer, V.U. Weiss, G. Allmaier, B. Lendl, A. Centrone, Nanoscale chemical imaging of individual chemotherapeutic cytarabine-loaded liposomal nanocarriers, *Nano Research* 12 (2019) 197–203, <https://doi.org/10.1007/s12274-018-2202-x>.
- [28] G.J. Verbiest, M.J. Rost, Beating beats mixing in heterodyne detection schemes, *Nat. Commun.* 6 (2015) 6444, <https://doi.org/10.1038/ncomms7444>.
- [29] D. Kurouski, A. Dazzi, R. Zenobi, A. Centrone, Infrared and Raman chemical imaging and spectroscopy at the nanoscale, *Chem. Soc. Rev.* 49 (2020) 3315–3347, <https://doi.org/10.1039/C8CS00916C>.
- [30] V.W. Or, A.D. Estillore, A.V. Tivanski, V.H. Grassian, Lab on a tip: atomic force microscopy – photothermal infrared spectroscopy of atmospherically relevant organic/inorganic aerosol particles in the nanometer to micrometer size range, *Analyst* 143 (2018) 2765–2774, <https://doi.org/10.1039/C8AN00171E>.
- [31] D. Khanal, J. Zhang, W.-R. Ke, M.M. Banaszak Holl, H.-K. Chan, Bulk to nanometer-scale infrared spectroscopy of Pharmaceutical dry Powder aerosols, *Anal. Chem.* 92 (2020) 8323–8332, <https://doi.org/10.1021/acs.analchem.0c00729>.
- [32] V.J. Rao, M. Matthiesen, K.P. Goetz, C. Huck, C. Yim, R. Siris, J. Han, S. Hahn, U.H. F. Bunz, A. Dreuw, G.S. Duesberg, A. Pucci, J. Zausseil, AFM-IR and IR-SNOM for the characterization of small molecule organic semiconductors, *J. Phys. Chem. C* 124 (2020) 5331–5344, <https://doi.org/10.1021/acs.jpcc.9b11056>.
- [33] J. Mathurin, E. Pancani, A. Deniset-Besseau, K. Kjoller, C.B. Prater, R. Gref, A. Dazzi, How to unravel the chemical structure and component localization of individual drug-loaded polymeric nanoparticles by using tapping AFM-IR, *Analyst* 143 (2018) 5940–5949, <https://doi.org/10.1039/C8AN01239C>.
- [34] A.M. Katzenmeyer, J. Canivet, G. Holland, D. Farrusseng, A. Centrone, Assessing chemical heterogeneity at the nanoscale in mixed-ligand metal–organic frameworks with the FTIR technique, *Angew. Chem. Int. Ed.* 53 (2014) 2852–2856, <https://doi.org/10.1002/anie.201309295>.
- [35] X. Ma, V. Beltran, G. Ramer, G. Pavlidis, D.Y. Parkinson, M. Thoury, T. Meldrum, A. Centrone, B.H. Berrie, Revealing the distribution of metal carboxylates in oil paint from the micro- to nanoscale, *Angew. Chem. Int. Ed.* 58 (2019) 11652–11656, <https://doi.org/10.1002/anie.201903553>.
- [36] T. Dou, Z. Li, J. Zhang, A. Evilevitch, D. Kurouski, Nanoscale structural characterization of individual viral particles using atomic force microscopy infrared spectroscopy (AFM-IR) and tip-enhanced Raman spectroscopy (TERS), *Anal. Chem.* 92 (2020) 11297–11304, <https://doi.org/10.1021/acs.analchem.0c01971>.
- [37] D. Khanal, R.Y.K. Chang, S. Morales, H.-K. Chan, W. Chrzanowski, High resolution nanoscale probing of bacteriophages in an inhalable dry Powder formulation for Pulmonary infections, *Anal. Chem.* 91 (2019) 12760–12767, <https://doi.org/10.1021/acs.analchem.9b02282>.
- [38] D. Perez-Guaita, K. Kochan, M. Batty, C. Doerig, J. Garcia-Bustos, S. Espinoza, D. McNaughton, P. Heraud, B.R. Wood, Multispectral atomic force microscopy-infrared nano-imaging of malaria infected red blood cells, *Anal. Chem.* 90 (2018) 3140–3148, <https://doi.org/10.1021/acs.analchem.7b04318>.
- [39] L. Baldassarre, V. Giliberti, A. Rosa, M. Ortolani, A. Bonamore, P. Baiocco, K. Kjoller, P. Calvani, A. Nucara, Mapping the amide I absorption in single bacteria and mammalian cells with resonant infrared nanospectroscopy, *Nanotechnology* 27 (2016), 075101, <https://doi.org/10.1088/0957-4484/27/7/075101>.
- [40] A.C.V.D. dos Santos, R. Heydenreich, C. Derrntl, A.R. Mach-Aigner, R.L. Mach, G. Ramer, B. Lendl, Nanoscale infrared spectroscopy and chemometrics enable detection of intracellular protein distribution, *Anal. Chem.* 92 (2020) 15719–15725, <https://doi.org/10.1021/acs.analchem.0c02228>.
- [41] P.N. Tri, R.E. Prud'homme, Nanoscale lamellar assembly and segregation mechanism of Poly(3-hydroxybutyrate)/Poly(ethylene glycol) blends, *Macromolecules* 51 (2018) 181–188, <https://doi.org/10.1021/acs.macromol.7b02019>.
- [42] P. Nguyen Tri, R.E. Prud'homme, Crystallization and segregation behavior at the submicrometer scale of PCL/PEG blends, *Macromolecules* 51 (2018) 7266–7273, <https://doi.org/10.1021/acs.macromol.8b01503>.
- [43] M.A. Rickard, G.F. Meyers, B.M. Habersberger, C.W. Reinhardt, J.J. Stanley, Nanoscale chemical imaging of a deuterium-labeled polyolefin copolymer in a polyolefin blend by atomic force microscopy-infrared spectroscopy, *Polymer* 129 (2017) 247–251, <https://doi.org/10.1016/j.polymer.2017.09.045>.
- [44] P. Nguyen-Tri, R.E. Prud'homme, Nanoscale analysis of the photodegradation of polyester fibers by AFM-IR, *J. Photochem. Photobiol. Chem.* 371 (2019) 196–204, <https://doi.org/10.1016/j.jphotochem.2018.11.017>.
- [45] H. Luo, Y. Xiang, Y. Li, Y. Zhao, X. Pan, Photocatalytic aging process of Nano-TiO₂ coated polypropylene microplastics: combining atomic force microscopy and infrared spectroscopy (AFM-IR) for nanoscale chemical characterization, *J. Hazard Mater.* 404 (2021) 124159, <https://doi.org/10.1016/j.jhazmat.2020.124159>.
- [46] H. McDonald, S. Morsch, S.M. Rowland, Chemical analysis of tree growth in epoxy resin using AFM-IR spectroscopy, *IEEE Trans. Dielectr. Electr. Insul.* 27 (2020) 773–781, <https://doi.org/10.1109/TDEL.2019.008573>.
- [47] F. Cavezza, S. Pletinckx, R.I. Revilla, J. Weaytens, M. Boehm, H. Terryn, T. Hauffman, Probing the metal oxide/polymer molecular hybrid interfaces with nanoscale resolution using AFM-IR, *J. Phys. Chem. C* 123 (2019) 26178–26184, <https://doi.org/10.1021/acs.jpcc.9b04522>.
- [48] N. Baden, Novel method for high-spatial-resolution chemical analysis of buried polymer-metal interface: atomic force microscopy-infrared (AFM-IR) spectroscopy with low-angle microtomy, *Appl. Spectrosc.* 75 (2021) 901–910, <https://doi.org/10.1177/00037028211007187>.
- [49] F. Tang, P. Bao, Z. Su, Analysis of nanodomain composition in high-impact polypropylene by atomic force microscopy-infrared, *Anal. Chem.* 88 (2016) 4926–4930, <https://doi.org/10.1021/acs.analchem.6b00798>.
- [50] F. Tang, P. Bao, A. Roy, Y. Wang, Z. Su, In-situ spectroscopic and thermal analyses of phase domains in high-impact polypropylene, *Polymer* 142 (2018) 155–163, <https://doi.org/10.1016/j.polymer.2018.03.037>.
- [51] Plastics - the facts 2020, *PlasticsEurope*, n.d., <https://www.plasticseurope.org/en/resources/publications/4312-plastics-facts-2020>. (Accessed 9 August 2021).
- [52] W. Posch, 3 - polyolefins, in: M. Kutz (Ed.), *Applied Plastics Engineering Handbook*, William Andrew Publishing, Oxford, 2011, pp. 23–48, <https://doi.org/10.1016/B978-1-4377-3514-7.10003-0>.
- [53] L.K. Massey, Chapter 70 - olefinic thermoplastic elastomers (TPO), in: L.K. Massey (Ed.), *Permeability Properties of Plastics and Elastomers*, second ed., William Andrew Publishing, Norwich, NY, 2003, pp. 421–425, <https://doi.org/10.1016/B978-188420797-6.50072-3>.
- [54] P. Galli, The reactor granule technology: a revolutionary approach to polymer blends and alloys, *Macromol. Symp.* 78 (1994) 269–284, <https://doi.org/10.1002/masy.19940780123>.
- [55] A. Ghanbari, E. Behzadfar, M. Arjmand, Properties of talc filled reactor-made thermoplastic polyolefin composites, *J. Polym. Res.* 26 (2019) 241, <https://doi.org/10.1007/s10965-019-1902-6>.
- [56] R. Sadiku, D. Ibrahim, O. Agboola, S.J. Owonubi, V.O. Fasiku, W.K. Kupilati, T. Jamiru, A.A. Eze, O.S. Adekomaya, K. Varaprasad, S.C. Agwuncha, A.B. Reddy, B. Manjula, B. Oboirien, C. Nkuna, M. Dluđu, A. Adeyeye, T.S. Osholana, G. Phiri, O. Durowoju, P.A. Olubambi, F. Biotidara, M. Ramakokovhu, B. Shongwe, V. Ojijo, 15 - automotive components composed of polyolefins, in: S.C.O. Ugholue (Ed.), *Polyolefin Fibres*, second ed., Woodhead Publishing, 2017, pp. 449–496, <https://doi.org/10.1016/B978-0-08-101132-4.00015-1>.
- [57] D.M. Simpson, G.A. Vaughan, Ethylene polymers, LLDPE, in: *Encyclopedia of Polymer Science and Technology*, American Cancer Society, 2001, <https://doi.org/10.1002/0471440264.pst122>.
- [58] T.K. Goswami, S. Mangaraj, 8 - advances in polymeric materials for modified atmosphere packaging (MAP), in: J.-M. Lagarón (Ed.), *Multifunctional and Nanoreinforced Polymers for Food Packaging*, Woodhead Publishing, 2011, pp. 163–242, <https://doi.org/10.1533/9780857092786.1.163>.
- [59] S.E. Selke, R.J. Hernandez, Packaging: polymers in flexible packaging, in: K.H. J. Buschow, R.W. Cahn, M.C. Flemings, B. Iltschner, E.J. Kramer, S. Mahajan, P. Veyssière (Eds.), *Encyclopedia of Materials: Science and Technology*, Elsevier, Oxford, 2001, pp. 6652–6656, <https://doi.org/10.1016/B0-08-043152-6/01176-1>.
- [60] S. van der Walt, J.L. Schönberger, J. Nunez-Iglesias, F. Boulogne, J.D. Warner, N. Yager, E. Goullart, T. Yu, The scikit-image contributors, scikit-image: image processing in Python, *PeerJ* 2 (2014) e453, <https://doi.org/10.7717/peerj.453>.
- [61] S. Morsch, S.B. Lyon, S. Edmondson, S.R. Gibbon, Reflectance in AFM-IR: implications for interpretation and remote analysis of the buried interface, *Anal. Chem.* (2020), <https://doi.org/10.1021/acs.analchem.9b05793>.
- [62] S.N. Magonov, D.H. Reneker, Characterization of polymer surfaces with atomic force microscopy, *Annu. Rev. Mater. Sci.* 27 (1997) 175–222, <https://doi.org/10.1146/annurev.matsci.27.1.175>.
- [63] J.M. Chalmers, N.J. Everall, Polymer analysis and characterization by FTIR, FTIR-microscopy, Raman spectroscopy and chemometrics, *Int. J. Polym. Anal. Char.* 5 (1999) 223–245, <https://doi.org/10.1080/10236669908009739>.
- [64] I. Pumure, S. Ford, J. Shannon, C. Kohen, A. Mulcahy, K. Frank, S. Sisco, N. Chaukura, Analysis of ATR-FTIR absorption-reflection data from 13 polymeric fabric materials using chemometrics, *Am. J. Anal. Chem.* (2015) 305, <https://doi.org/10.4236/ajac.2015.64029>, 06.
- [65] J. McGann, M. Willans, G. Sauzier, M.J. Hackett, S.W. Lewis, J. McGinn, T. Trubshoe, W. van Bronswijk, Investigating diversity in polymer-based identity cards using ATR-FTIR spectroscopy and chemometrics, *Forensic Sci. Int.: Report 2* (2020) 100149, <https://doi.org/10.1016/j.fisir.2020.100149>.
- [66] Y.-S. Lo, N.D. Huefner, W.S. Chan, P. Dryden, B. Hagenhoff, T.P. Beebe, Organic and inorganic contamination on commercial AFM cantilevers, *Langmuir* 15 (1999) 6522–6526, <https://doi.org/10.1021/la990371x>.
- [67] G. Ramer, V.A. Aksyuk, A. Centrone, Quantitative chemical analysis at the nanoscale using the FTIR technique, *Anal. Chem.* 89 (2017) 13524–13531, <https://doi.org/10.1021/acs.analchem.7b03878>.
- [68] M. Guizar-Sicairos, S.T. Thurman, J.R. Fienup, Efficient subpixel image registration algorithms, *Opt. Lett.*, OL 33 (2008) 156–158, <https://doi.org/10.1364/OL.33.000156>.
- [69] E. Govorčin Bajsić, V. Rek, I. Čosić, Preparation and characterization of talc filled thermoplastic polyurethane/polypropylene blends, *Journal of Polymers* (2014), e289283, <https://doi.org/10.1155/2014/289283>, 2014.
- [70] M. Barczewski, K. Lewandowski, M. Schmidt, M. Szostak, Melt fracture and rheology of linear low density polyethylene - calcium carbonate composites, *Polym. Eng. Sci.* 57 (2017) 998–1004, <https://doi.org/10.1002/pen.24477>.
- [71] J. Móczó, B. Pukánszky, Polymer micro and nanocomposites: structure, interactions, properties, *J. Ind. Eng. Chem.* 14 (2008) 535–563, <https://doi.org/10.1016/j.jiec.2008.06.011>.

Publication III

Nanoscale Chemical Characterization of a Post-Consumer Recycled Polyolefin Blend Using Tapping Mode AFM-IR

*A. Catarina V. D. dos Santos, Davide Tranchida, Bernhard Lendl, and Georg Ramer**

Analyst, **2022**, 147 (16), 3741–3747



Cite this: *Analyst*, 2022, **147**, 3741

Nanoscale chemical characterization of a post-consumer recycled polyolefin blend using tapping mode AFM-IR†

A. Catarina V. D. dos Santos,^a Davide Tranchida,^b Bernhard Lendl^{ib}*^a and Georg Ramer^{ib}*^a

The routine analysis of polymer blends at the nanoscale is usually carried out using electron microscopy techniques such as scanning electron microscopy (SEM) and transmission electron microscopy (TEM), which often require several sample preparation steps including staining with heavy metals and/or etching. Atomic force microscopy (AFM) is also commonly used, but provides no direct chemical information about the samples analyzed. AFM-IR, a recent technique which combines the AFM's nanoscale resolution with the chemical information provided by IR spectroscopy, is a valuable complement to the already established techniques. Resonance enhanced AFM-IR (contact mode) is the most commonly used measurement mode, due to its signal enhancement and relative ease of use. However, it has severe drawbacks when used in highly heterogeneous samples with changing mechanical properties, such as polymer recyclates. In this work, we use the recently developed tapping mode AFM-IR to chemically image the distribution of rubber in a real-world commercially available polyethylene/polypropylene (PE/PP) recycled blend derived from municipal and household waste. Furthermore, the outstanding IR resolution of AFM-IR allowed for the detection of small PP droplets inside the PE phase. The presence of micro and nanoscale particles of other polymers in the blend was also established, and the polymers identified.

Received 16th May 2022

Accepted 11th July 2022

DOI: 10.1039/d2an00823h

rsc.li/analyst

Introduction

Plastic waste and its improper disposal are environmental hazards whose consequences are visible, but not yet fully understood (ex. effect of microplastic contamination).^{1–5} As the production of polymer materials is increasing, and both long term storage in landfills and incineration are wasteful and hazardous to the environment, only plastic production from polymer waste (recycling) can reduce plastic waste.^{6,7} However, waste plastics can contain contaminants or additives from their “previous lives” that can hinder the recycling process and lead to lower quality products when compared to virgin plastics.^{8–10} For example, the presence of other polymer types in the final blend can lead to a degradation of the mechanical properties, especially when these are immiscible.¹¹ This can be particularly challenging when managing originally heterogeneous feedstock, made of different polymers.

Furthermore, the better the sorting of shredded plastics, the higher the cost of recycling, and this approach may be inefficient in cases like multilayer packaging¹² or even in the case of homogeneous plastic waste which is mixed together during waste collection.^{13,14} Therefore, heterogeneous recyclates that retain desirable mechanical properties may have a cost advantage over other single-polyolefin recyclates in similar applications due to the minimal sorting required.¹⁵

Polyethylene (PE) and isotactic polypropylene (PP) are two polyolefins that are immiscible with each other despite their structural similarity, and whose blend morphology varies with the blend composition.¹⁶ PE/PP blends generally suffer from low interfacial adhesion and the resulting mechanical properties make them unsuitable for higher value applications.^{17,18} Several compatibilizers have been tested to improve the miscibility of PE and PP, and a comprehensive review can be found in literature.¹⁹ These include ethylene propylene rubber (EPR), ethylene propylene diene monomer rubber (EPDM), and styrene-*b*-(ethylene-*co*-butylene)-*b*-styrene (SEBS).^{20–22} Common methods employed to analyse a polymer's micro- and nano-scale morphologies are scanning electron microscopy (SEM), transmission electron microscopy (TEM), and fluorescence confocal microscopy.^{13,20,23} These methods have some disadvantages such as extra sample prepara-

^aInstitute of Chemical Technologies and Analytics, TU Wien, 1060 Vienna, Austria.

E-mail: georg.ramer@tuwien.ac.at, bernhard.lendl@tuwien.ac.at

^bBorealis Polyolefine GmbH, 4021 Linz, Austria

† Electronic supplementary information (ESI) available: AM-FM AFM images, AFM-IR spectra, dendrogram and raw data. See DOI: <https://doi.org/10.1039/d2an00823h>



ration steps (chemical etching, staining with heavy metals) in the case of electron microscopy or the need to label with fluorescent molecules in the case of confocal fluorescence microscopy.^{13,20,23} Furthermore, all of the previously mentioned studies used either virgin polymer blends prepared specifically for the study, or blends where only the PE and PP components came from a waste stream, thus reducing the uncertainty of composition associated with fully recycled blends.

However, when the composition of recyclates is uncertain, established staining protocols might not be enough to fully understand the phase composition at the nanoscale. Here, AFM-IR (also known as photothermal infrared spectroscopy (PTIR)) provides an alternative approach towards the morphology characterization of recycled polymer blends. AFM-IR is a near-field technique that provides chemical identification *via* IR spectroscopy at lateral resolutions as small as ≈ 10 nm in tapping mode.²⁴ This resolution is achieved because the signal detection occurs in the near-field, and is thus not diffraction limited. In AFM-IR, the thermal expansion of the sample caused by the absorption of radiation from a pulsed wavelength-tunable IR laser is detected by the AFM tip, and it is proportional to the absorbed energy.²⁵ As is the case in bulk infrared spectroscopy, the AFM-IR signal is proportional to the wavelength-dependent absorption coefficient,²⁵ meaning that AFM-IR benefits from the long established spectra-structure correlations known to infrared spectroscopy. AFM-IR has found applications in geology,^{26,27} environmental analysis,^{28,29} material,^{30,31} and life sciences.^{32–35}

Previous AFM-IR studies on the morphology of virgin high-impact PP and virgin PP/PE/EPR blends were carried out using contact-mode AFM-IR.^{36–39} In contact mode AFM-IR – specifically the more sensitive “resonance enhanced” implementation – the laser repetition rate is set to match a mechanical contact resonance of the cantilever, which leads to an enhancement of the signal when compared to the older ring-down mode.⁴⁰ In this reliance on contact resonances lies also one of the down-sides of resonance enhanced measurements, particularly during imaging: local changes in the sample’s mechanical properties lead to changes in the resonance frequency, which in turn leads to changes in the signal amplitude. To circumvent this problem, the measurement is either conducted off resonance (forgoing the resonant enhancement),⁴¹ by chirping the laser repetition within a likely range of the resonance (*i.e.* trading some sensitivity for accurate tracking of the resonance),⁴² or with the help of a phase locked loop (PLL) that tracks the changes in resonance frequency and adjusts the driving frequency/laser repetition rate accordingly.⁴²

It has long been recognized that tapping mode AFM, *i.e.* a mode where the AFM tip is driven to oscillation and the tip oscillation amplitude is used as feedback for the cantilever sample distance, is more adept than contact mode AFM for the analysis of soft materials (such as polymers).^{43–45} Tapping mode AFM eliminates lateral tip-sample forces which can damage or deform the sample and the high vertical speed of

the tapping tip leads to an increased apparent stiffness of viscoelastic samples.^{46,47}

Like resonance enhanced AFM-IR, the recently introduced tapping mode AFM-IR,⁴⁸ also relies on mechanical resonance for signal enhancement, but in tapping mode the resonance frequency of the cantilever is less sensitive to changes in the sample’s mechanical properties.^{49,50} This means there is no need to track the resonance frequency, thus reducing the complexity of the experiment. Additionally, tapping mode has a better resolution than contact mode (10 nm *vs.* 20 nm), due to the reduced interaction time between the tip and the sample.⁵⁰ For these reasons, tapping mode AFM-IR is better suited for the analysis of heterogeneous polymer samples with unpredictable changes in mechanical properties. Since this technique is still relatively recent, there are, to the best of our knowledge, no published tapping mode AFM-IR studies on polymers, with the exception of a protocol recently developed by our group.⁵¹ In this work, we go beyond the straightforward application of tapping mode AFM-IR to a polyolefin material by using tapping mode AFM-IR to study the phase distribution and the interphase between PE/PP in a commercially available PE/PP recyclate blend. The analysed sample derives from a post-consumer waste stream containing PE, PP, and a rubber component. Thus, in contrast to previous investigations of polymer interfaces using AFM-IR, we are not studying a tightly controlled material made specifically for AFM-IR analysis but a real-world sample that contains variations in composition as well as an unknown amount of contaminants and fillers. Using tapping mode AFM-IR for recording spectra and images, and chemometric models for data analysis, we are able to locate the rubber component at the interface of the PE and PP and to detect the presence of other polymer contaminants. The AFM-IR data obtained through spectra and chemical images are in agreement with each other, and with data obtained from conventional methods (SEM and soluble fraction analysis), thus demonstrating that AFM-IR is a valuable tool for the nanoscale analysis of recycled polymer blends.

Experimental

Materials

The material studied in this work is a polyolefin mix recyclate, originating from pre-sorted municipal and household waste, and mechanically recycled. Given the origin of the feedstock used to produce this material, market average content of additional components (*e.g.* EPR rubber, fillers, additives) is to be expected.

SEM measurements

Samples were imaged with a ThermoFischer Apreo 2 SEM after RuO₄ staining. The specimen was first cut under cryo-conditions (-100 °C) using an ultra-cryo-microtome Leica EM-UC7. RuO₄ was produced during the staining procedure by mixing RuCl₃ with an aqueous solution of NaIO₄. A staining time of 6 hours at room temperature was used. To remove

over-stained material, a second microtome cutting was performed.

Soluble fraction analysis

The crystalline (CF) and soluble fractions (SF) as well as the comonomer content of the respective fractions were measured by Crystex (crystallisation extraction) method on a Polymer Char Crystex 42 instrument as described in literature.⁵²

Sample preparation for AFM-IR

The samples were ultra-cryomicrotomed at $-100\text{ }^{\circ}\text{C}$ on a Leica EM-UC7 equipped with a Leica EM FC7 cryochamber and the resulting sections were placed on ZnS substrates (13 mm diameter \times 1 mm thickness from Crystran).

AFM-IR measurements

All AFM-IR measurements were carried out using a Bruker nano-IR 3s coupled to a MIRcat-QT external cavity quantum cascade laser array (EC-QCL) from Daylight Solutions. Spectra covering the range from 910 cm^{-1} to 1950 cm^{-1} were obtained using AFM-IR in tapping mode with a heterodyne detection scheme. The measurements were obtained while driving the cantilever at its second resonance frequency ($f_2 \approx 1500\text{ kHz}$) and demodulating the AFM-IR signal at the first resonance frequency ($f_1 \approx 250\text{ kHz}$) using a digital lock-in amplifier (MFLI, Zurich Instruments). The laser repetition rate was set to $f_L = f_2 - f_1 \approx 1300\text{ kHz}$. The cantilevers used were gold coated with nominal first free resonance frequencies of $300 \pm 100\text{ kHz}$ and a nominal spring constant between 20 and 75 N m^{-1} (Tap300GB-G from BudgetSensors). The laser source operated at 10% duty cycle and emitted laser pulses of up to 500 mW peak pulse power. Using metal mesh attenuators, the laser power was adjusted to between 39.66% and 49.6% of the original power (before beam splitter, nominal splitting ratio 1 : 1). For each location, 3 spectra were recorded at 1 cm^{-1} spectral resolution. The instrument and all beam paths were purged with dry air generated by an adsorptive dry air generator.

Data pre-processing

Recorded AFM-IR spectra were averaged by location, normalized individually to the unit norm in the range between 1400 cm^{-1} and 1500 cm^{-1} and smoothed using a Savitzky-Golay filter (9 points, first order).

The shift between chemical images was corrected using sub pixel registration *via* phase cross correlation based on their simultaneously recorded topography counterparts as reference. Calculations were performed using the phase cross correlation implementation in the scikit-image package (v0.18.1) for Python 3.⁵³

Chemometric analysis

Modelling was performed using the scikit-learn (v0.24.2) machine learning library for Python 3.⁵⁴

The averaged and smoothed spectra were clustered using an agglomerative clustering model with 3 clusters.

The analysis of the chemical images was performed using a Gaussian mixture model with 3 components and 5 iterations.

Results & discussion

The post-consumer polyolefin mix recyclate derived from municipal waste investigated in this study was analyzed using soluble fraction analysis, AFM-IR, SEM, and AM-FM AFM.

Bulk characterization of the material was carried out by soluble fraction analysis (results shown in Table 1). The soluble fraction analysis used in this study allows for the determination of the amorphous content and for the analysis of the ethylene content in each of the obtained fractions.⁵² The soluble fraction (Table 1) corresponds mostly to the rubber content present in the sample (amorphous content), which has a total ethylene (C2) content of 46.6%. This fraction could correspond to the rubber compatibilizers EPR, EPDM, or SEBS which are expected to be present at the interface between the PE and PP phases, but further analysis is required to determine which one of them is present in our recyclate.

The first AFM-IR measurements were collected from a $10\text{ }\mu\text{m} \times 10\text{ }\mu\text{m}$ area of a sample section obtained through cryo-microtomy. After an analysis of full AFM-IR spectra obtained, images using tapping mode AFM-IR were recorded at 1377 cm^{-1} , 1462 cm^{-1} , 1640 cm^{-1} , and 1724 cm^{-1} . The spectrum of PE in the region from 950 cm^{-1} to 1950 cm^{-1} is dominated by the strong band at around 1468 cm^{-1} corresponding primarily to the scissor bending of the CH_2 groups.⁵⁵ In the case of PP, in addition to the CH_2 scissor band at 1458 cm^{-1} with contributions from the CH_3 asymmetric deformation vibration, a strong band at 1378 cm^{-1} that originates from the symmetric deformation of CH_3 groups is also present.⁵⁶ The images obtained were drift-corrected as described in literature,⁵¹ and the logarithm of the ratio of CH_3 (1377 cm^{-1}) and CH_2 (1462 cm^{-1}) was calculated and is shown in Fig. 1(b). The ratio of CH_3/CH_2 allows us to visualize the distribution of PE (white) and PP (purple) in the sample and reveals the presence of droplets inside the larger PE domains that are similar to the outer PP phase. This morphology is peculiar because, in a system with roughly 50%/50% content of PP and PE (Table 1), one would expect a co-continuous phase morphology, made of two distinct PE and PP phases. Instead, probably during the extrusion part of the mechanical recycling process, the two materials are made to mix very intimately and small domains of PP are present in the PE phase. This is a new finding, since the size of these domains is not accessible to conventional Fourier transform infrared spectroscopy (FTIR) microscopes.

Table 1 Soluble fraction analysis of the material used in this study

SF (%wt) ^a	C2 total (%wt) ^b	C2 in SF (%wt) ^c	C2 in CF (%wt) ^d
8.5	47.6	46.6	48.4

^a Soluble fraction. ^b Total ethylene content. ^c Ethylene content in the soluble fraction. ^d Ethylene content in the insoluble fraction.

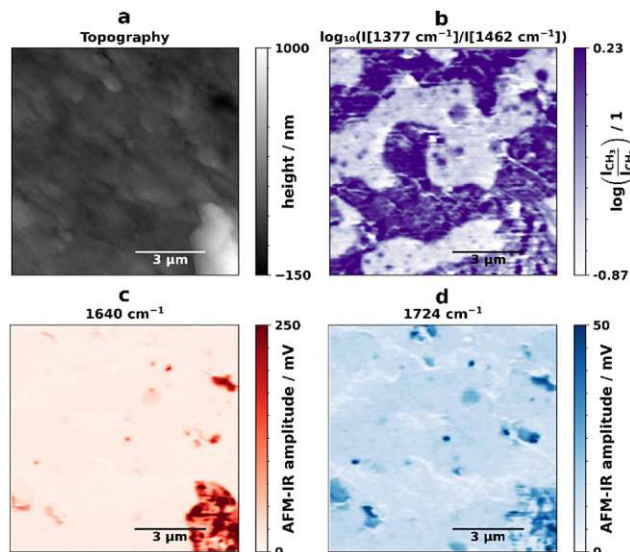


Fig. 1 Topography (a) and chemical maps (10 × 10 μm). (b) Ratio of the bands corresponding to deformation vibrations of CH₂ (1462 cm⁻¹) and symmetric deformation of CH₃ groups (1377 cm⁻¹). (c) Chemical map obtained at 1640 cm⁻¹, corresponding to the distribution of polyamide. (d) Chemical map obtained at 1725 cm⁻¹, corresponding to the distribution of polyurethane.

The existence of patches with different properties can be observed in standard AFM images, however it is not possible to link this observation to chemical information.

Droplets of small size crystallize in a different fashion compared to the bulk material,⁵⁷ and therefore it is not yet known, what are the properties of these very small PP inclusions into the PE phase, or the implications they may have on *e.g.* mechanical properties. A previous study by Tang *et al.* had described the crystallization of PP-rich-sequences of EPR in the core-shell morphology of the rubber.³⁶ These findings differ from ours because not only was the material used different (commercially available recycled polyolefin mix *vs.* special grade high-impact poly-propylene), but also our results indicate that the small particles are PP and not just PP-rich sequences of EPR. This is supported by amplitude modulation-frequency modulation AM-FM AFM measurements (Fig. S1†) which reveal that the inclusions in the PE phase have the same Young's modulus as the PP matrix. If these particles were composed of PP-rich EPR sequences, then the Young's modulus should be lower, since these sequences would not crystallize as well as isotactic PP.⁵⁷

The images obtained at 1640 cm⁻¹ (Fig. 1(c), red) reveal the presence of several polyamide (PA) particles. The obtained full-length spectrum in an area with predominantly only 1640 cm⁻¹ (Fig. S2,† orange spectrum) is in accordance with FTIR spectra of PA found in literature.⁵⁸ The image at 1724 cm⁻¹ likely shows the presence of polyurethane (PU), since AFM-IR spectra obtained in an area with 1724 cm⁻¹ absorption but no 1640 cm⁻¹ absorption (see Fig. S2,† blue spectrum) show a band at 1602 cm⁻¹, as described in litera-

ture.⁵⁹ In some locations there is absorption at both 1640 cm⁻¹ and 1724 cm⁻¹. In this case it is not entirely clear whether this is due to the presence of polyurethane or degraded PA,⁶⁰ because the higher signal produced by the PA may be covering up the polyurethane 1602 cm⁻¹ signal, as indicated by the spectra in Fig. S2.† The PA and PU particles have sizes ranging from several microns to 200 nm (Fig. S3†). Information on the nature and size of contamination in recycles is relevant, because the presence of other polymers that were not fully separated during the sorting process in the blend can be detrimental to the overall mechanical properties.⁶¹ Furthermore, it showcases the advantages of AFM-IR analysis as a technique that allows for the chemical identification of nano-scale impurities and their distribution in the analyzed samples without prior knowledge of said impurities.

To localize and identify the amorphous fraction detected in the soluble fraction analysis (Table 1), further AFM-IR images were collected in a smaller area of the same location (1.5 μm × 1.5 μm), which can be seen in Fig. 2, as well as full spectra in a grid format close to the interface and in a line over the PP inclusion (Fig. 3(a)). The CH₃/CH₂ ratio image (Fig. 2(b)) shows an intermediate color at the PP/PE interface, which hints at the presence of a component with intermediate ratio values, *i.e.* the rubber.

However, to see the rubber interface, we need to combine information from more than just two wavelengths. To facilitate this task given the amount of data collected, two multivariate chemometric methods, hierarchical cluster analysis (HCA) and Gaussian mixture, were applied to the spectra and to the IR images respectively. For the analysis of the IR images, a Gaussian mixture model was chosen, since HCA is not optimal for the handling of large datasets due to its $\mathcal{O}(n^3)$ complexity (n is the number of samples). Fig. 3 shows the superposition of the Gaussian mixture image and the position of the spectral HCA clusters, as well as a combined plot of the average HCA cluster spectra and the average values of each Gaussian mixture subpopulation. The dendrogram obtained for the HCA is shown in Fig. S4.† The two different methods and ways of obtaining AFM-IR data are in agreement and support the hypothesis that the rubber is present at the interface. In the spectra, HCA clearly identifies the PP and PE components, as well as a third component (Fig. 3(a), yellow dots). This com-

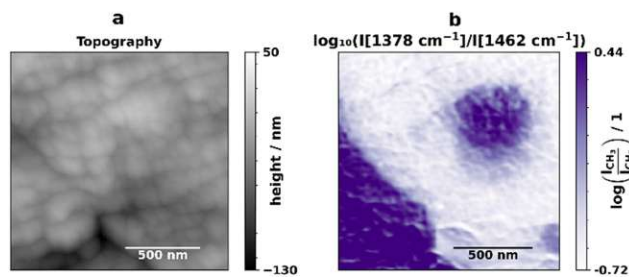


Fig. 2 Topography (a) and band ratio (b) of the bands corresponding to deformation vibrations of CH₂ and symmetric deformation of CH₃ groups (1.5 μm × 1.5 μm).

lysts.⁶⁴ Thus, it is not expected that a polyolefin recyclate that originates from household waste contains such special polymer grades.

Conclusions

This work constitutes the first use of tapping mode AFM-IR to perform a thorough study of the chemical composition and phase distribution of a real-world polyolefin recyclate at the nanoscale. This municipal waste derived (post-consumer) material is shown to contain the typical PP, PE phases and a rubber component. AFM-IR revealed the distribution of the rubber component at the interface of the PE and PP phases using its spectral signature without the need to staining of the sample. This result matches references measurements using SEM after staining with RuO₄ that rely on staining. The presence of small PP particles inside the larger PE phase that had previously been described for freshly prepared materials was also seen in the tapping mode AFM-IR analysis of this recycled polymer. However, in contrast to fresh polymers, in the studied recycled polymer the presence of non-polyolefine polymer inclusions was found. Here, the high sensitivity and spatial resolution of tapping mode AFM-IR is beneficial as it can detect particles orders of magnitude below the diffraction limit of conventional FTIR microscopy. All phases and contaminants were chemically identified using nanoscale spatial resolution mid-IR absorption spectra collected using the AFM-IR instrument. This constitutes a major advantage over established methods which indirectly identify phases *via* physical properties, or *via* staining or etching protocols. Hence, we expect a more widespread adoption of tapping mode AFM-IR in polymer nanoscale analysis in the near future.

Author contributions

A. Catarina V. D. dos Santos: conceptualization, investigation, formal analysis, visualization, writing – original draft; Davide Tranchida: conceptualization, resources, writing – review & editing; Bernhard Lendl: funding acquisition, resources, supervision, writing – review & editing; Georg Ramer: conceptualization, software, supervision, writing – review & editing.

Conflicts of interest

There are no conflicts to declare.

Acknowledgements

The authors would like to thank Walter Schaffer, Ljiljana Jeremic, Gottfried Kandioller, and Helmut Rinnerthaler from Borealis for sharing their expertise in polyolefin characterization.

The authors acknowledge financial support through the COMET Centre CHASE, funded within the COMET – Competence Centres for Excellent Technologies programme by the BMK, the BMDW and the Federal Provinces of Upper Austria and Vienna. The COMET programme is managed by the Austrian Research Promotion Agency (FFG). The authors acknowledge TU Wien Bibliothek for financial support through its Open Access Funding Programme.

Notes and references

- 1 L. Lebreton and A. Andrady, *Palgrave Commun.*, 2019, **5**, 1–11.
- 2 Q. Chen, J. Reisser, S. Cunsolo, C. Kwadijk, M. Kotterman, M. Proietti, B. Slat, F. F. Ferrari, A. Schwarz, A. Levivier, D. Yin, H. Hollert and A. A. Koelmans, *Environ. Sci. Technol.*, 2018, **52**, 446–456.
- 3 D. Santillo, K. Miller and P. Johnston, *Integr. Environ. Assess. Manage.*, 2017, **13**, 516–521.
- 4 E. Danopoulos, M. Twiddy and J. M. Rotchell, *PLoS One*, 2020, **15**(7), e0236838.
- 5 E. Danopoulos, L. C. Jenner, M. Twiddy and J. M. Rotchell, *Environ. Health Perspect.*, 2020, **128**, 126002.
- 6 R. Geyer, J. R. Jambeck and K. L. Law, *Sci. Adv.*, 2017, **3**(7), e1700782.
- 7 M. Okan, H. M. Aydin and M. Barsbay, *J. Chem. Technol. Biotechnol.*, 2019, **94**, 8–21.
- 8 V. S. Cecon, P. F. Da Silva, G. W. Curtzwiler and K. L. Vorst, *Resour., Conserv. Recycl.*, 2021, **167**, 105422.
- 9 B. D. Vogt, K. K. Stokes and S. K. Kumar, *ACS Appl. Polym. Mater.*, 2021, **3**, 4325–4346.
- 10 M. K. Eriksen, K. Pivnenko, M. E. Olsson and T. F. Astrup, *Waste Manage.*, 2018, **79**, 595–606.
- 11 B. Hu, S. Serranti, N. Fraunholz, F. Di Maio and G. Bonifazi, *Waste Manage.*, 2013, **33**, 574–584.
- 12 K. Kaiser, M. Schmid and M. Schlummer, *Recycling*, 2018, **3**, 1.
- 13 M. Louizi, V. Massardier and P. Cassagnau, *Macromol. Mater. Eng.*, 2014, **299**, 674–688.
- 14 D. Wang, Y. Li, X.-M. Xie and B.-H. Guo, *Polymer*, 2011, **52**, 191–200.
- 15 S. Billiet and S. R. Trenor, *ACS Macro Lett.*, 2020, **9**, 1376–1390.
- 16 I. Charfeddine, J. C. Majesté, C. Carrot and O. Lhost, *Polymer*, 2020, **193**, 122334.
- 17 K. A. Chaffin, F. S. Bates, P. Brant and G. M. Brown, *J. Polym. Sci., Part B: Polym. Phys.*, 2000, **38**, 108–121.
- 18 B. C. Poon, S. P. Chum, A. Hiltner and E. Baer, *Polymer*, 2004, **45**, 893–903.
- 19 A. Ghosh, *Resour., Conserv. Recycl.*, 2021, **175**, 105887.
- 20 G. Radonjič and N. Gubelj, *Macromol. Mater. Eng.*, 2002, **287**, 122–132.
- 21 T. Kajiyama, T. Yasuda, T. Yamanaka, K. Shimizu, T. Shimizu, E. Takahashi, A. Ujiie, K. Yamamoto, T. Koike and Y. Nishitani, *Int. Polym. Process.*, 2018, **33**, 564–573.
- 22 N. V. Penava, V. Rek and I. F. Houra, *J. Elastomers Plastics*, 2013, **45**, 391–403.

- 23 L. Li, L. Chen, P. Bruin and M. A. Winnik, *J. Polym. Sci., Part B: Polym. Phys.*, 1997, **35**, 979–991.
- 24 K. Wieland, G. Ramer, V. U. Weiss, G. Allmaier, B. Lendl and A. Centrone, *Nano Res.*, 2019, **12**, 197–203.
- 25 A. Dazzi, F. Glotin and R. Carminati, *J. Appl. Phys.*, 2010, **107**, 124519.
- 26 Y. Kebukawa, H. Kobayashi, N. Urayama, N. Baden, M. Kondo, M. E. Zolensky and K. Kobayashi, *Proc. Natl. Acad. Sci. U. S. A.*, 2019, **116**, 753.
- 27 K. Wang, L. Ma and K. G. Taylor, *Fuel*, 2022, **310**, 122278.
- 28 V. W. Or, A. D. Estillore, A. V. Tivanski and V. H. Grassian, *Analyst*, 2018, **143**, 2765–2774.
- 29 A. L. Bondy, R. M. Kirpes, R. L. Merzel, K. A. Pratt, M. M. Banaszak Holl and A. P. Ault, *Anal. Chem.*, 2017, **89**, 8594–8598.
- 30 T. Kong, H. Xie, Y. Zhang, J. Song, Y. Li, E. L. Lim, A. Hagfeldt and D. Bi, *Adv. Energy Mater.*, 2021, **11**, 2101018.
- 31 Y. Liu, L. Collins, R. Proksch, S. Kim, B. R. Watson, B. Doughty, T. R. Calhoun, M. Ahmadi, A. V. Ievlev, S. Jesse, S. T. Retterer, A. Belianinov, K. Xiao, J. Huang, B. G. Sumpter, S. V. Kalinin, B. Hu and O. S. Ovchinnikova, *Nat. Mater.*, 2018, **17**, 1013–1019.
- 32 R. Rebois, D. Onidas, C. Marcott, I. Noda and A. Dazzi, *Anal. Bioanal. Chem.*, 2017, **409**, 2353–2361.
- 33 D. Perez-Guaita, K. Kochan, M. Batty, C. Doerig, J. Garcia-Bustos, S. Espinoza, D. McNaughton, P. Heraud and B. R. Wood, *Anal. Chem.*, 2018, **90**, 3140–3148.
- 34 A. C. V. D. dos Santos, R. Heydenreich, C. Derntl, A. R. Mach-Aigner, R. L. Mach, G. Ramer and B. Lendl, *Anal. Chem.*, 2020, **92**, 15719–15725.
- 35 A. Deniset-Besseau, C. B. Prater, M.-J. Virolle and A. Dazzi, *J. Phys. Chem. Lett.*, 2014, **5**, 654–658.
- 36 F. Tang, P. Bao, A. Roy, Y. Wang and Z. Su, *Polymer*, 2018, **142**, 155–163.
- 37 F. Tang, P. Bao and Z. Su, *Anal. Chem.*, 2016, **88**, 4926–4930.
- 38 C. Jiang, B. Jiang, Y. Yang, Z. Huang, Z. Liao, J. Sun, J. Wang and Y. Yang, *Polymer*, 2021, **214**, 123373.
- 39 C. Li, Z. Wang, W. Liu, X. Ji and Z. Su, *Macromolecules*, 2020, **53**, 2686–2693.
- 40 F. Lu and M. A. Belkin, *Opt. Express*, 2011, **19**, 19942–19947.
- 41 S. Kenkel, A. Mittal, S. Mittal and R. Bhargava, *Anal. Chem.*, 2018, **90**, 8845–8855.
- 42 G. Ramer, F. Reisenbauer, B. Steindl, W. Tomischko and B. Lendl, *Appl. Spectrosc.*, 2017, **71**, 2013–2020.
- 43 S. N. Magonov and D. H. Reneker, *Annu. Rev. Mater. Sci.*, 1997, **27**, 175–222.
- 44 M. A. S. R. Saadi, B. Uluutku, C. H. Parvini and S. D. Solares, *Surf. Topogr.: Metrol. Prop.*, 2020, **8**, 045004.
- 45 G.-L. Liu and S. G. Kazarian, *Analyst*, 2022, **147**, 1777–1797.
- 46 C. A. Putman, K. O. van der Werf, B. G. de Grooth, N. F. van Hulst and J. Greve, *Biophys. J.*, 1994, **67**, 1749–1753.
- 47 V. V. Tsukruk, V. V. Gorbunov, Z. Huang and S. A. Chizhik, *Polym. Int.*, 2000, **49**, 441–444.
- 48 M. Tuteja, M. Kang, C. Leal and A. Centrone, *Analyst*, 2018, **143**, 3808–3813.
- 49 J. Mathurin, A. Deniset-Besseau and A. Dazzi, *Acta Phys. Pol., A*, 2020, **137**, 29–32.
- 50 D. Kurouski, A. Dazzi, R. Zenobi and A. Centrone, *Chem. Soc. Rev.*, 2020, **49**, 3315–3347.
- 51 A. C. V. D. dos Santos, B. Lendl and G. Ramer, *Polym. Test.*, 2022, **106**, 107443.
- 52 L. Jeremic, A. Albrecht, M. Sandholzer and M. Gahleitner, *Int. J. Polym. Anal. Charact.*, 2020, **25**, 581–596.
- 53 S. van der Walt, J. L. Schönberger, J. Nunez-Iglesias, F. Boulogne, J. D. Warner, N. Yager, E. Gouillart, T. Yu and the scikit-image contributors, *PeerJ*, 2014, **2**, e453.
- 54 F. Pedregosa, G. Varoquaux, A. Gramfort, V. Michel, B. Thirion, O. Grisel, M. Blondel, P. Prettenhofer, R. Weiss, V. Dubourg, J. Vanderplas, A. Passos, D. Cournapeau, M. Brucher, M. Perrot and É. Duchesnay, *J. Mach. Learn. Res.*, 2011, **12**, 2825–2830.
- 55 M. G. Olayo, E. Colín, G. J. Cruz, J. Morales and R. Olayo, *Eur. Phys. J.: Appl. Phys.*, 2009, **48**, 30501.
- 56 I. Prabowo, J. N. Pratama and M. Chalid, *IOP Conf. Ser.: Mater. Sci. Eng.*, 2017, **223**, 012020.
- 57 R. M. Michell, I. Blaszczyk-Lezak, C. Mijangos and A. J. Müller, *Polymer*, 2013, **54**, 4059–4077.
- 58 J. C. Farias-Aguilar, M. J. Ramírez-Moreno, L. Téllez-Jurado and H. Balmori-Ramírez, *Mater. Lett.*, 2014, **136**, 388–392.
- 59 S. J. McCarthy, G. F. Meijis, N. Mitchell, P. A. Gunatillake, G. Heath, A. Brandwood and K. Schindhelm, *Biomaterials*, 1997, **18**, 1387–1409.
- 60 E. S. Gonçalves, L. Poulsen and P. R. Ogilby, *Polym. Degrad. Stab.*, 2007, **92**, 1977–1985.
- 61 A. Schweighuber, M. Gall, J. Fischer, Y. Liu, H. Braun and W. Buchberger, *Anal. Bioanal. Chem.*, 2021, **413**, 1091–1098.
- 62 M. A. Vargas, N. N. López, M. J. Cruz, F. Calderas and O. Manero, *Rubber Chem. Technol.*, 2009, **82**, 244–270.
- 63 H. Sano, T. Usami and H. Nakagawa, *Polymer*, 1986, **27**, 1497–1504.
- 64 J. M. Eagan, J. Xu, R. Di Girolamo, C. M. Thurber, C. W. Macosko, A. M. LaPointe, F. S. Bates and G. W. Coates, *Science*, 2017, **355**, 814–816.

Publication IV

AFM-IR for Nanoscale Chemical Characterization in Life Sciences: Recent Developments and Future Directions

*A. Catarina V. D. dos Santos, Nikolaus Hondl, Victoria Ramos-Garcia, Julia Kuligowski, Bernhard Lendl, and Georg Ramer**

ACS Measurement Science, 2023

AFM-IR for Nanoscale Chemical Characterization in Life Sciences: Recent Developments and Future Directions

A. Catarina V. D. dos Santos, Nikolaus Hondl, Victoria Ramos-Garcia, Julia Kuligowski, Bernhard Lendl, and Georg Ramer*

Cite This: <https://doi.org/10.1021/acsmeasuresciau.3c00010>

Read Online

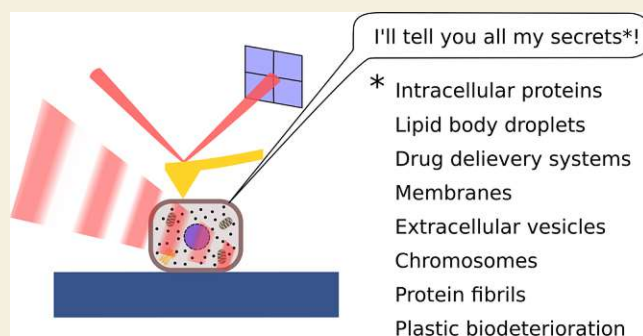
ACCESS |

Metrics & More

Article Recommendations

ABSTRACT: Despite the ubiquitous absorption of mid-infrared (IR) radiation by virtually all molecules that belong to the major biomolecules groups (proteins, lipids, carbohydrates, nucleic acids), the application of conventional IR microscopy to the life sciences remained somewhat limited, due to the restrictions on spatial resolution imposed by the diffraction limit (in the order of several micrometers). This issue is addressed by AFM-IR, a scanning probe-based technique that allows for chemical analysis at the nanoscale with resolutions down to 10 nm and thus has the potential to contribute to the investigation of nano and microscale biological processes. In this perspective, in addition to a concise description of the working principles and operating modes of AFM-IR, we present and evaluate the latest key applications of AFM-IR to the life sciences, summarizing what the technique has to offer to this field. Furthermore, we discuss the most relevant current limitations and point out potential future developments and areas for further application for fruitful interdisciplinary collaboration.

KEYWORDS: AFM-IR, chemical imaging, biospectroscopy, single cell imaging, mid-infrared spectroscopy



Atomic force microscopy-infrared spectroscopy (AFM-IR), named in some publications as photothermal-induced resonance (PTIR), is a scanning probe technique where a pulsed, tunable, IR laser is added to an AFM instrument, resulting in nanoscale IR molecular chemical information. Lateral and vertical spatial resolutions that can be achieved with AFM-IR depend on the measurement mode used (further discussed below), with tapping mode AFM-IR providing the best lateral resolution of the technique at 10 nm.¹ This technique is still relatively recent and has been the subject of improvements in measurement speeds, types, resolution, and sensitivity since it was first published in 2005.² The technical evolution of AFM-IR has been the subject of several reviews, in which the interested reader can find a detailed description of this subject.^{3–5} In this perspective, only a brief description of the main characteristics and working modes of AFM-IR will be given, with the intention of allowing readers with life sciences backgrounds to better understand the potential of this technique and its potential applications to their research.

A typical AFM-IR setup is depicted in Figure 1 in its two possible illumination geometries, bottom illumination (a) and top illumination (b), referring to the positioning of the IR laser relative to the sample and AFM cantilever. In bottom illumination, the IR radiation hits the sample from below in an attenuated total reflection (ATR) configuration which

restricts sample thicknesses to <500 nm due to an otherwise loss of signal linearity.⁶ The prism is composed of an IR-transparent material, most commonly ZnSe, which may place restrictions on sample and sample preparation protocols due to its chemical incompatibility with acids. However, bottom illumination also has advantages, namely the possibility of carrying out measurements in liquid, and the use of cantilevers made from IR absorbing materials such as silicon and silicon nitride, whose use is restricted in top-illumination configurations.⁷ In top illumination geometries there is more freedom in the choice of substrate, which may include silicon wafers and gold-coated substrates, in addition to mid-IR-transparent materials (CaF₂, ZnS, ZnSe, etc.),⁸ which opens the way for a higher variety of sample preparation protocols. The positioning of the IR laser path directly hits the cantilever in this configuration, which therefore needs to be metal-coated to prevent undesired contributions to the signal by IR absorption of the cantilever itself. When gold-coated canti-

Received: March 16, 2023

Revised: May 30, 2023

Accepted: May 30, 2023

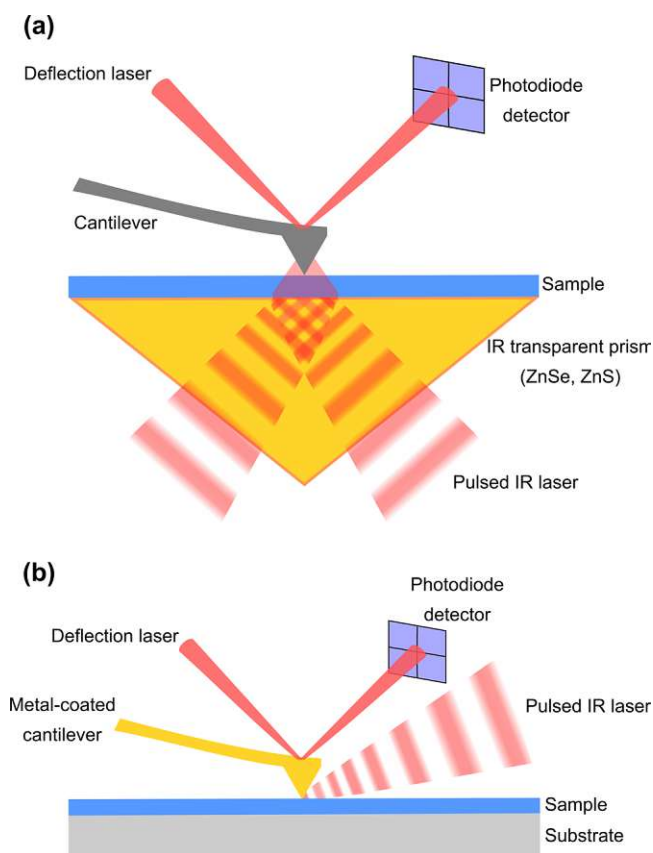


Figure 1. Schematic representation of the two possible AFM-IR illumination geometries: (a) bottom illumination and (b) top illumination.

levers and substrates are used either alone or in combination, an enhancement of the AFM-IR signal up to 8-fold can be obtained;^{9,10} however, care must be taken when interpreting the resulting AFM-IR spectra due to the wavelength-dependence of this phenomenon.¹¹

The basic working principle of AFM-IR is the thermal expansion of the sample area below the AFM tip upon absorption of the IR laser radiation which is focused at this location. During the on phase of the laser cycle, the sample absorbs IR photons and the molecules convert to an excited vibrational state. When returning to the ground vibrational state some of the energy is lost in the form of heat through the lattice, which in turn is dissipated through mechanical expansion.^{5,12} This quick expansion “hits” the cantilever resulting in an oscillation motion which is picked up through the cantilever deflection signal and is proportional to the wavelength-dependent absorption coefficient, as is the case for classical IR transmission spectroscopy.¹² This means that when interpreting an AFM-IR spectrum, one can make use of the many spectra-structure correlations that have been established over the years for Fourier-transform IR spectroscopy (FTIR), a critical advantage. AFM-IR is able to circumvent the diffraction limit and reach spatial resolutions within tens of nanometers due to the signal detection occurring only on the portion of the sample directly below the tip and not on the whole area of the sample illuminated by the IR laser spot.⁹ In AFM-IR there are two possible ways to record data, one being taking a full-length spectrum by sweeping the wavelength range of the laser used

and the other collecting an absorption map at a chosen wavenumber.

It should be noted that AFM-IR is not the only technique capable of delivering vibrational spectroscopy beyond the resolution limit: O-PTIR (optical-photothermal infrared spectroscopy), TERS (tip-enhanced Raman spectroscopy), and s-SNOM (scattering scanning near-field optical microscopy)¹³ are examples of such techniques. In O-PTIR the signal is generated in a similar fashion to AFM-IR: a pulsed, tunable IR laser aimed at the sample causes thermal expansion upon radiation absorption. The main difference between these two techniques is the detection of the expansion, which is carried out using a visible laser in the case of O-PTIR, meaning that it is not a scanning probe technique and has a higher potential throughput.¹⁴ Furthermore, the presence of the visible laser allows for the simultaneous collection of Raman spectra, thus providing extra information.¹⁵ The resolution limit of O-PTIR is determined by diffraction limit of the visible laser and can reach 400–500 nm,¹⁶ which is lower than that of AFM-IR. TERS on the other hand, is a scanning probe technique that takes advantage of metal-coated AFM tips or etched conductive scanning tunneling microscopy (STM) wire tips to enhance the electromagnetic field in the vicinity of the tip, leading to stronger Raman signals with subnanometer resolutions and sampled depths of a few nanometers.⁴ The spatial resolution of TERS depends on the experimental conditions (air or vacuum, room temperature or lower temperatures), with typical values ranging from 3 nm to 5 nm⁴ and sub nanometer resolutions (1.5 Å) have also been reported.^{17,18} Thus, AFM-IR and TERS can be used in a complementary manner since their typical resolutions and probed depths do not overlap. For a more detailed description of TERS, as well as a review of some of its applications to biological samples, a review by Kurouski et al.⁴ is recommended. In s-SNOM, (infrared) light scattered from a metalized AFM tip is collected and analyzed.¹³ This allows access to information on the sample’s optical properties (e.g., its complex refractive index) in the near-field around the tip with lateral spatial resolutions of 5 to 170 nm, depending on the sharpness of the tip used.^{19,20} s-SNOM is not limited to the mid-IR range,¹⁹ but its application using mid-IR to biological samples has been recently reviewed by Wang et al.²¹

AFM-IR can be operated in three main modes, distinguished by the type of AFM mode of operation and by the way the AFM-IR signal is modulated: ring-down contact mode, resonance-enhanced contact mode, or in tapping mode. Additionally, two recently developed modes are peak-force tapping IR (PFIR)²² and surface sensitive AFM-IR.²³ The first mode to be developed was the ring-down contact mode, in which upon IR absorption and thermal expansion of the sample the cantilever (which is always in contact with the sample) is struck into a slowly decaying oscillation (slow in comparison to the time scale of the thermal expansion), thus producing a ring-down pattern. In this mode, several of the cantilever’s mechanical modes are excited, and the AFM-IR signal is obtained either from the amplitude of a specific mode or from the peak-to-peak of the cantilever’s oscillation, both of which are directly proportional to the wavelength-dependent absorption coefficient of the sample.¹² Measurements using this mode are usually carried out with optical parametric oscillators as the pulsed IR source which have high power output and short pulse lengths (<10 ns).²⁴ Ringdown measurements have lower sensitivity than resonance-enhanced

contact mode measurements (see below)²³ but yield similar spatial resolutions (lateral resolution of both modes ≈ 20 nm,^{9,25} probe depth of >1 μm).^{3,26}

The second option when measuring in contact mode is the resonance-enhanced contact mode, in which the pulse rate of the IR laser is set to match one of the mechanical contact resonance frequencies of the cantilever, leading to an amplification of the deflection amplitude and, consequently, of the signal obtained.²³ For typical AFM contact mode cantilevers, contact resonance frequencies lie in the range of several tens to several hundreds of kilohertz and depend on cantilever properties as well as local sample mechanical properties and measurement settings. Hence, this mode requires the use of a laser source capable of reaching and rapidly adjusting high pulse repetition rates in the range of hundreds of kilohertz, usually a quantum cascade laser (QCL). Furthermore, since the enhancement is dependent on the laser repetition rate matching the contact resonance frequency of the cantilever, some sort of resonance tracking is required to ensure that this condition is met, even when the AFM tip scans through materials with different mechanical properties. When measuring spectra this is usually achieved by quickly scanning a set range of frequencies around the original resonance position and adjusting the repetition rate accordingly (chirp) once before each spectrum;²⁶ however, when recording images a phase-locked loop (PLL) is used instead, which relies on phase angle rather than amplitude to more quickly monitor and react to changes in the peak position. Resonance tracking during AFM-IR imaging is not always able to properly compensate for the shifts observed when measuring samples with large disparities in mechanical properties such as polymer blends,²⁷ or soft liposomes deposited on a hard substrate. An alternative approach to this problem using a closed-loop piezo controller allowing for off-resonance measurements has also been described.²⁸ When combined with gold coated cantilevers and substrates, resonance-enhanced contact mode AFM-IR can reach monolayer sensitivity due to “lightning-rod” enhancement.⁹

Tapping mode AFM-IR was first published in 2018, making it the most recent of the three main AFM-IR modes.²⁹ In this mode, the cantilever is oscillated at one of its resonance frequencies (e.g., f_1) and the signal detection occurs at another resonance frequency (e.g., f_2) in a heterodyne detection scheme. To achieve this, the laser repetition rate f_L is set to $f_2 - f_1$, which usually requires the use of a QCL, as the f_L for commonly used cantilevers will usually have values within the range between 250 and 1500 kHz.^{1,27} Measurements where the tapping frequency used is the second resonance of the cantilever and signal detection occurs at the first resonance frequency are also possible and can result in a higher signal³⁰ but are also more prone to signal instability. In tapping mode AFM-IR, the cantilever is only intermittently in contact with the sample, resulting in reduced tip–sample interactions, particularly lateral forces,³¹ which make this mode well-suited for the analysis of soft, easily damaged and/or loosely adhered (to the substrate) samples. However, tapping mode AFM-IR yields lower intensity signals, which may lead to the use of higher laser power that requires care not to damage the sample. An important advantage of tapping mode AFM-IR is the lower sensitivity of the resonance frequency to changes in a sample’s mechanical properties,³² which can be of relevance, for instance, in polymer samples.²⁷ This does, however, have its limits, and in extreme cases the use of a PLL to track and

adjust the laser frequency (similarly to the resonance-enhanced contact mode) is advisable.²³ The best lateral resolution reported for this mode is ≈ 10 nm,¹ and it has been reported to achieve a probe depth of 50 nm,²³ allowing one to monitor only the top layer of the sample.

Finally, in PFIR the tip is in intermittent contact with the sample, but unlike the tapping mode, this oscillation happens at frequencies lower than the resonance frequency.²² During the part of the cycle where the tip is in contact with the sample, the IR laser is triggered and, similarly to the ring-down mode, the ensuing photothermal expansion is detected by the cantilever through the deflection signal in addition to information on the sample’s mechanical properties given by conventional peak force imaging.²² Similarly to the tapping mode, PFIR exerts lower lateral tip–sample forces, but the IR signal acquisition is closer to that of ring-down contact mode AFM-IR,²³ albeit with higher lateral resolutions of down to 6 nm in air³³ and 10 nm in liquid.³⁴ PFIR has been applied in the context of the life sciences. We recommend to the interested reader the following studies on cell wall particles,³³ lignocellulosic fibers,³⁵ macrophage immune regulation,³⁶ and protein fibrils in liquid.³⁴

Even though there is a large number of available AFM-IR modes, most studies appear to use contact mode AFM-IR. We suspect that the choice between resonance-enhanced and ring-down AFM-IR is made due to available infrastructure (older AFM-IR systems used a low repetition rate laser incapable of resonant excitation) rather than due to experimental considerations. When the contact mode is not possible due to sample properties, the tapping mode AFM-IR is used. Surface sensitive AFM-IR is not yet in widespread use, but we expect that, like tapping mode AFM-IR, it will be chosen when ordinary resonance enhanced AFM-IR is insufficient. PFIR is, at the time of writing, not available commercially and therefore not used by many groups.

AFM-IR’s chemical imaging is based on the use of mid-infrared radiation (mid-IR), which is usually defined as having wavenumbers between 400 cm^{-1} and 4000 cm^{-1} . Due to these long wavelengths, mid-IR is nondestructive. Spectral features in the mid-IR correspond to the excitation of molecular vibrations, and their frequency depends on both the bond strength and the mass of the atoms involved, hence, in first approximation, mid-IR bands can be assigned to specific functional groups.³⁷ Each molecule has unique energy levels of its vibrational modes, which translate into a unique IR spectrum (“fingerprint”).³⁸ Furthermore, intermolecular interactions such as hydrogen bonds can have an influence on the bond strengths of the molecules they are formed from, and thus, their presence is detectable through mid-IR spectroscopy.^{39,40} Mid-IR spectroscopy is of particular interest to the life sciences because it can provide information in a non-destructive, label-free manner: all of the major groups of biomolecules (proteins, nucleic acids, lipids, and polysaccharides) are active in the mid-IR region. However, this advantage can also become a disadvantage when analyzing complex biological samples in which all above-mentioned biomolecule groups are present: the IR spectrum will be a mixture of all, and small variations can be difficult to detect and disentangle from the spectrum without recurring to chemometric modeling or the use of IR-tags. Conventional mid-IR microscopy is diffraction limited and can only reach resolutions in the order of several micrometers (from $2.5\text{ }\mu\text{m}$ to up to $25\text{ }\mu\text{m}$ as the wavelength increases).⁴¹ The use of attenuated total reflection

(ATR) configurations can improve the resolution to the range of 2–4 μm ,⁴² which nonetheless hampers its widespread application, since many intracellular components have smaller dimensions, hence the usefulness of a technique like AFM-IR. It is however important to highlight that the spectral range of AFM-IR is in practice limited by the type of laser used, potentially meaning that not all of the mid-IR spectral features of a target analyte will be visible in the AFM-IR spectra using a specific light source. For example, the widely used multichip QCL systems that are currently commercially available typically cover $\approx 1000\text{ cm}^{-1}$ by combining several individual external cavity-QCLs in one housing. In the following paragraphs, a brief overview over the most prominent mid-IR spectroscopic features of each biomolecule group is provided (Figure 2), for deeper insights into the applications of conventional mid-IR spectroscopy methods to the life sciences, the following reviews are suggested.^{43–47}

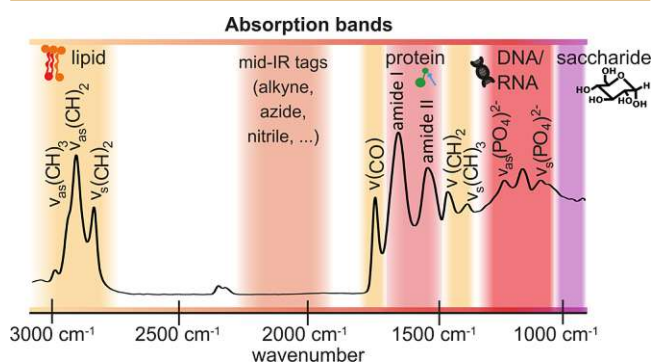


Figure 2. Absorption bands of biomolecules and mid-IR tags in the mid-infrared region.

Proteins have five dominant bands in the mid-IR spectra: the amide I (1600 cm^{-1} to 1700 cm^{-1} , usually centered around 1650 cm^{-1}), amide II (centered around 1550 cm^{-1}), amide III (from 1400 cm^{-1} to 1200 cm^{-1}), amide A (centered around 3500 cm^{-1}), and amide B (centered around 3100 cm^{-1}). The amide I band, caused mainly by the stretching vibration of the C=O group, is especially useful for its well-established sensitivity to a protein's secondary structure, of which a thorough description can be found in the review by Barth.⁴⁸ In short, β -sheet-containing proteins absorb predominantly at 1633 cm^{-1} and 1684 cm^{-1} , whereas α -helix structures result in absorption around 1654 cm^{-1} .⁴⁸ In intermolecular β -sheets, the major component of amyloid aggregations produces a distinct absorption band at 1620 cm^{-1} , thus allowing for the detection and characterization of protein aggregation states such as amyloid fibrils.⁴⁹

Mid-IR spectra of lipids are generally composed of bands from the hydrocarbon chain ($-\text{CH}_2$ groups) and from the polar head groups (phosphate, PO_4^{2-} , and ester groups). From the hydrocarbon chain there are two groups of bands: the stretching vibrations in the region of 2950 cm^{-1} to 2800 cm^{-1} and bending vibrations at $\approx 1460\text{ cm}^{-1}$.⁵⁰ CH_3 groups produce bands at $\approx 2955\text{ cm}^{-1}$ and 1377 cm^{-1} and alkenes at 3010 cm^{-1} and $\approx 1660\text{ cm}^{-1}$.^{50,51} Analysis of these bands, particularly of those in the higher wavenumber region (from 2850 cm^{-1} to 3050 cm^{-1}) provides information on chain length, chain unsaturation, phase transitions, and lipid orientation (when using polarized light).⁵⁰ Furthermore, membrane phospholipids have a strong absorption band at $\approx 1735\text{ cm}^{-1}$

corresponding to the C=O vibration of ester groups, as well as bands at 1240 cm^{-1} and 1090 cm^{-1} from the phosphate groups present in the polar head.⁵⁰

Nucleic acids, similarly to lipids, absorb at 1240 cm^{-1} and $\approx 1085\text{ cm}^{-1}$ due to the presence of phosphate groups in the backbone of both DNA and RNA.⁵² Additionally, nucleic acids also absorb around 1700 cm^{-1} to 1717 cm^{-1} (due to C=O stretching vibrations)⁵³ and in the spectral range between 1520 cm^{-1} and 1663 cm^{-1} in characteristic patterns that can be attributed to specific bases and base pairings.⁵⁴ This spectral area partially overlaps with the amide I and II bands of proteins and thus requires a careful interpretation.

Saccharides have numerous absorption bands in the mid-IR region: $-\text{OH}$ groups absorb from 3000 cm^{-1} to 3600 cm^{-1} (stretching vibration), and CH and CH_2 absorb both at $2800\text{--}2950\text{ cm}^{-1}$ and at $\approx 1460\text{ cm}^{-1}$ (as described in the lipids paragraph).⁵⁵ However, it is the “fingerprint” region between 800 cm^{-1} and 1200 cm^{-1} that offers information on a polysaccharide's glycosylic linkages (between 1140 cm^{-1} and 1175 cm^{-1} corresponding to a C–O–C stretching vibration) and their conformation (between 920 cm^{-1} and 1000 cm^{-1} region),⁵⁶ as well as on the conformation of the anomeric carbon (between 800 cm^{-1} and 900 cm^{-1} region).^{55,57}

Thus, combining the described wealth of chemical information provided by AFM-IR with its ability for subcellular spatial resolution at ambient conditions, it is easy to see why there has been a great interest in applying AFM-IR in the life sciences. In fact, first AFM-IR images of cells were published shortly after the technique's invention.² Due to the constant improvement and development of novel measurement modes, the types of samples that this technique can be applied to have increased tremendously in recent years, thus, without reduction of generality we focus here on the most relevant recent works (published less than five years ago) on AFM-IR in the life sciences and highlight potential directions for future research. Furthermore, we highlight key areas of future improvements, such as liquid measurements, surface sensitive mode, labeling of target molecules, and the current status of image and data treatment in the AFM-IR field and discuss advantages and applications that these can bring.

RECENT APPLICATIONS TO THE LIFE SCIENCES

Analysis of Whole Cells

The analysis of whole cells using AFM-IR with the goal of identifying the intracellular distribution of its components often runs into the aforementioned blessing and curse of “everything” being IR active. With some exceptions in which the target analytes have particular IR signatures,⁵⁸ most studies rely to some extent on the use of chemometric models to circumvent this and extract relevant information from the AFM-IR data.^{59–61} In 2020, our group published an approach to this problem which combined fluorescence microscopy and supervised machine learning with resonance-enhanced contact mode AFM-IR, with the goal of mapping the distribution of the major cellulases and xylanases within *T. Reesei*.⁶¹ This fungus is notorious for its well-developed enzyme secretion system essential to its survival in the wild as a saprobe⁶² and which has been leveraged in numerous industrial processes including recombinant protein production.⁶³ The strain used in this study, QM6a SecEYFP, has been modified to express yellow fluorescent protein (EYFP) under the same conditions of the main cellobiohydrolase, CBHI, and to follow the same

intracellular path. Therefore, in this strain the EYFP and its respective fluorescence signal are colocalized with the cellulases and xylanases, allowing for a correlation between fluorescence intensity and the presence of proteins containing β -sheet secondary structures in the same location. This was the basis for the training of a partial least-squares (PLS) model to predict cellobiohydrolase abundance from AFM-IR spectra. This model could achieve a root mean squared error (RMSE) of 13% when applied to a data set which had not been used for model training. Interestingly, the selectivity ratio (SR) showed the highest contributions to the model coming from the amide I band wavenumbers related to β -sheet secondary structures and CH_2 stretching vibrations (lipids). This is in line with the main secondary structure motifs of several of the most abundant cellulases and xylanases, as well as with the expected intracellular path of these proteins leading up to secretion in which they are enveloped in the lipid bilayers of several organelles and later inside vesicles. Thus, it was possible to obtain a PLS model capable of mapping the intracellular distribution of the main cellulases and xylanases in *T. Reesei* (Figure 3).

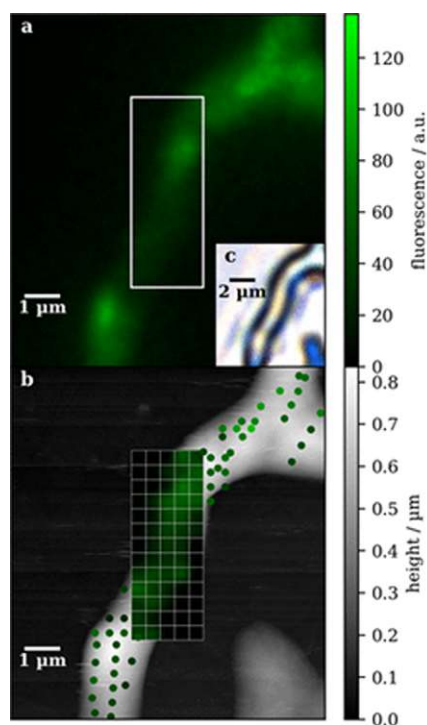


Figure 3. Fluorescence image (a), topography map (b), and brightfield image (c) of a *T. Reesei* hypha. Fluorescence values calculated from AFM-IR spectra [points and grid in panel (c)] using a PLS model calibrated to the presence of β -sheet-containing proteins can be compared with those measured using the fluorescence microscope (a). Reproduced from ref 61. Copyright 2020 American Chemical Society.

Another approach was carried out by Liu et al. in 2021 for the analysis and comparison of protein expression in macrophages using AFM-IR (resonance-enhanced contact mode for single-point spectra and tapping mode for imaging) and a chemometric model to identify the subcellular differences between two *a priori* known groups of macrophages.⁶⁰ Depending on the stimulus present in an environment, macrophages express different phenotypes, allowing

them to adapt and take over different functions as necessary. These phenotypes can be divided into two broad categories: M1 macrophages that participate in pro-inflammatory responses, and M2 macrophages which participate in anti-inflammatory responses. In this study, macrophages were polarized *in vitro* and their protein expression at the subcellular scale was studied using resonance-enhanced contact mode AFM-IR for single spectra and tapping mode AFM-IR for chemical imaging. After collecting spectra at several locations in the central portions of macrophages belonging to group M1, M2, and M0 (nondifferentiated control group), the data was analyzed using principal component analysis (PCA). The three different macrophage groups clustered separately, with major differences between groups appearing in the amide I spectral region. M1 macrophages had β -sheet as the most common secondary structure motif (35% antiparallel and 5.6% parallel), whereas in M2, α -helix was the most common (38.8%). The different secondary structure detected by the AFM-IR spectra is in agreement with previous studies on protein expression of polarized macrophages. Chemical images obtained at selected amide I wavenumbers showed different patterns of protein distribution in the two groups, with the highlight being the detection of antiparallel β -sheet rich nodes in the extremities of M1 macrophages corresponding to $\text{TNF-}\alpha$, a pro-inflammatory factor.

An example of whole cell imaging without resorting to chemometric models to detect the target analyte is the study by Deniset-Besseau et al.⁶⁴ of lipid body droplet formation in *P. kesslerii*, a microalgae used in biofuel production. This organism produces large quantities of triacylglycerol (TAG)-containing lipid bodies, which due to their unique spectral signature can be located and imaged without the use of labels or chemometric approaches. Furthermore, a correlative approach was used combining ring-down contact mode AFM-IR in bottom illumination with fluorescence microscopy, which permitted the mapping of TAG lipid droplets (through AFM-IR) and their relationship to chloroplast location (mapped with fluorescence microscopy). As the cells begin producing lipid droplets, these accumulate in the center of the cell, pushing the chloroplasts to the edges.

Another study by Pancani et al.⁶⁵ focused on the imaging with nanoscale resolution of the location of polymeric nanoparticles typically used for drug-delivery inside macrophages (Figure 4). This study was conducted using resonance-enhanced contact mode AFM-IR with no additional labeling of the nanoparticles (NPs), taking advantage of the fact that the main absorption peak of the NPs studied (1730 cm^{-1}) does not overlap with major absorption peaks of the cells analyzed. When these conditions are met, AFM-IR has a critical advantage over other high-resolution imaging methods such as fluorescence microscopy techniques, which always require the presence of a fluorophore to label the analyte of interest.

Beyond the studies summarized here, AFM-IR has also been applied to red blood cells (including pathological states)^{59,66–68} and cancer cells,^{69–71} as well as on isolated viruses.^{72,73}

We would like to emphasize that whole cell analysis using AFM-IR would benefit significantly from more robust liquid measurement AFM-IR mode. Current work on liquid AFM-IR does not change the medium composition or enable long-term measurements of live cells. Thus, microfluidic integration, which allows for the monitoring of cells in a controlled environment and the ability to add nutrients and reagents in a

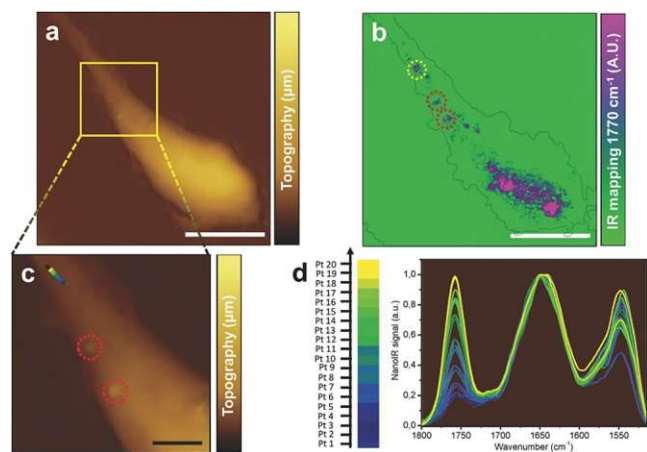


Figure 4. Label-free AFM-IR imaging of NPs inside a macrophage. (a) and (c) AFM topography maps with some polymeric NPs visible in panel (c). (b) AFM-IR absorption map taken at 1770 cm^{-1} , a marker band for the NPs. (d) AFM-IR point spectra taken in the points marked in panel (b). Reproduced with permission under a Creative Commons Attribution 4.0 International License from ref 65. Copyright 2018 Wiley-VCH.

controlled way would enable a wealth of new studies on cell response to stimuli. Furthermore, whole cell AFM-IR analysis yields complex data sets that often require resorting to multivariate models. The lack of community-accepted best practices with regard to multivariate evaluation makes it hard to compare different studies, and the lack of community-accepted software packages for data processing is a barrier for newcomers.

Analysis of Tissues

In the histological context, AFM-IR has been employed in the characterization of different tissues, providing chemical information at the nanoscale complementary to other traditional tissue analysis methods. Bone tissue has been studied by Imbert et al.⁷⁴ using ring-down contact mode AFM-IR, and by Ahn et al.⁷⁵ using both ring-down and resonance-enhanced contact mode. Despite using bone tissue from two different mammals (sheep and mouse), both studies observed an increase in mineralization with bone tissue age and were able to map this distribution using AFM-IR (Figure 5). Furthermore, an alternating pattern with $2\text{--}8\ \mu\text{m}$ periodicity consisting of higher and lower mineral-to-matrix ratios was identified as being the lamellae, a key structural element in mammalian bone.⁷⁴ Qian et al.⁷⁶ performed a study comparing the nanoscale properties of bones affected by osteoporosis with healthy controls using resonance-enhanced contact mode AFM-IR. Bone sections from osteoporosis patients were found to have a less mature mineral matrix than that of the control group, which can be associated with reduced stability.⁷⁶ Further related studies include AFM-IR analysis of bone-like nodules formed by stem cells,⁷⁷ of bone composite xenografts,⁷⁸ and of human dentin.⁷⁹

We would also like to highlight recent studies focusing on characterizing human hair samples at the nanoscale using AFM-IR.^{80–83} This includes the hair medulla,⁸¹ cuticle,⁸⁰ and cortex.⁸² Other tissues analyzed include the anterior cruciate ligament,⁸⁴ stratum corneum⁸⁵ (as well as drug penetration on the skin),⁸⁶ and breast cancer,⁸⁷ which further expand the application of this technique to the histological context.

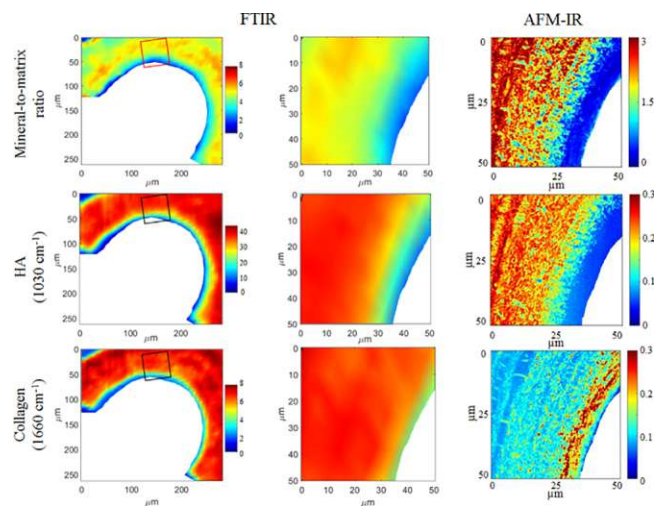


Figure 5. FTIR (left and middle column) and AFM-IR absorption ratios of sheep cancellous bone (right column). Here the superior resolution of AFM-IR allows for a much more detailed analysis of the distribution of the mineral-to-matrix ratio (first row), hydroxyapatite content, HA (second row), and collagen distribution (third row). AFM-IR enables the identification of a collagen-rich, nonmineralized area (osteoid). Reproduced with permission under a Creative Commons Attribution 4.0 International License from ref 74. Copyright 2018 Public Library of Science.

Biodeterioration Studies

AFM-IR has been applied to study the biodeterioration of polyurethane films by the yeast *P. laurentii* in a 2020 study by Barlow et al.⁸⁸ The yeast was incubated for 30 days on two ZnSe substrates spin coated with two different types of polyurethane films and then measured using a ring-down contact mode in a bottom-illumination configuration. The yeast cells formed monolayer aggregates over the urethane and deteriorated the polymer through both ester hydrolysis and bulk loss. The authors had to deal with cell translocation and microplastic erosion due to the incubation conditions of up to 95% relative humidity and further influenced by biofilm production, which caused water condensation on the sample surface. Through the acquisition of chemical image ratios, the authors showed that this biodegradation is most pronounced at the edges of cells or cell clusters and results in a depression in the urethane coating where extracellular polymeric substance (EPS) residues typical of biofilms are left. Several components of EPS could be detected in the spectra, including polysaccharide and protein residues in addition to urethane-rich secondary microplastics. The edge degradation pattern observed in the study is attributed to the high affinity between the hydrolases secreted by *P. laurentii* and the polymer substrate (particularly the ester moieties) which “traps” them in the polymer directly near the cell. The degradation of the coated film and subsequent viability tests show that at least some of the cells were able to remain alive and degrade the coating for a time. However, in the absence of nitrogen sources other than dead cells, most cells eventually died or became metabolically inactive. This raises the question of whether longer term observations of deterioration processes might occur under more favorable conditions for cellular growth, e.g., in the presence of liquid growth medium. The cells tested for viability in this study were, however, not the same cells that underwent AFM-IR measurements and were placed on glass and not ZnSe substrates.⁸⁸ It would be important to establish

whether it is possible for cells to survive (a) on commonly used AFM-IR substrates and (b) AFM-IR measurements, and under which conditions (laser power, air vs liquid medium, and under which ambient conditions). A 2018 study by Kochan et al.⁸⁹ claims that the majority of the bacteria present on the substrate survives AFM-IR measurement conditions; however, it is not clear that the single bacteria subject to AFM-IR measurements did, and thus, this remains an open question.

Lipid Membrane Studies

AFM is a common technique for the study of biological lipid membranes as it provides high-resolution imaging of the different components, of lipid phase separation, and of the organization of membrane proteins.⁹⁰ Using AFM-IR, it is possible to combine this information with infrared spectroscopy, allowing for the chemical identification of the membrane components in addition to their spatial distribution. This has been demonstrated in a 2019 study by Lipiec et al., which studied the distribution of components in an artificial membrane system composed of two lipids, sphingomyelin (SM) and cholesterol (Chol), and one peptide, cyclosporin A (CsA), using resonance-enhanced contact mode AFM-IR.⁵¹ First, by acquiring spectra using the *p* and *s* polarizations of the infrared laser, the authors were able to detect the orientation of some functional groups. The hydrocarbon chains (CH₂) orient perpendicular to the surface of the substrate, whereas the amide and unsaturated groups in SM appear to be oriented parallel to the substrate. The studied membrane system phase separates into circular domains containing higher surface densities of SM surrounded by a Chol phase. As the percentage of Chol in the system increased, the peptide component, CsA, moves from a homogeneous distribution to a preferential location in the Chol domains where it forms complexes with SM and Chol molecules akin to those present in lipid rafts.

The study by Lipiec et al.⁵¹ opens the way for more biomembrane studies using AFM-IR, perhaps focusing on membrane proteins and making use of the several established protocols for membrane sample preparation used in AFM.⁹¹ Indeed there is literature published on light-induced conformational changes of membrane proteins in purple membranes detected using resonance-enhanced contact mode AFM-IR.^{92,93} Although purple membranes are known for being particularly good subjects for AFM analysis due to their 2D crystal structure,⁹⁴ these results are nonetheless encouraging and AFM-IR analysis of biomembranes is a promising field.

Extracellular Vesicle Characterization

Extracellular vesicles (EVs) are membrane-bound vesicles secreted by both prokaryotic and eukaryotic cells that can transport proteins, lipids, as well as nucleic acids, thus serving as important intercellular messengers.^{95–97} Exosomes are EVs with sizes from 20 to 150 nm diameter and are commonly found in bodily fluids such as milk, tears, and blood.⁹⁷ Larger EVs with diameters between 100 nm and 1 μm are classified as microvesicles.⁹⁷ EVs can trigger a number of responses in the target cells including apoptosis, immune-responses (by acting as antigen-presenting vesicles), and overall tissue regeneration.⁹⁷ Furthermore, under pathological conditions EVs also play a role, e.g., in the spread of cancer metastases and in neurodegenerative disorders through the spread of toxic protein aggregates.⁹⁷ Due to their minute size, the analysis of individual EVs is challenging and inaccessible to most conventional methods which focus instead on bulk measure-

ments or provide no direct label-free chemical information on individual EVs.^{95,99,100}

In 2018, Kim et al.⁹⁶ reported the first analysis of EVs with AFM-IR using a bottom illumination configuration and contact mode ring-down measurements. In this study, the authors were able to obtain AFM-IR spectra of isolated EVs and their content, identifying the presence of proteins and nucleic acids and the variations of these between two EV populations and also within different EVs of the same population.⁹⁶ The sample preparation in this study was simple, consisting of depositing a droplet of water containing isolated EVs on a ZnSe prism. Depositing particles on a substrate as done in this study can lead to the accumulation of particles on a ring-shape once the liquid evaporates called the coffee ring effect. This can be detrimental to the analysis by limiting the number of EVs that can effectively be individually studied, as particles in the ring tend to overlap. To tackle this problem, our group has recently developed a protocol that allows for the immobilization of EVs onto a silicone surface using microcontact printed anti-CD9 antibodies (Figure 6). In comparison to Kim et al.,⁹⁶ where the

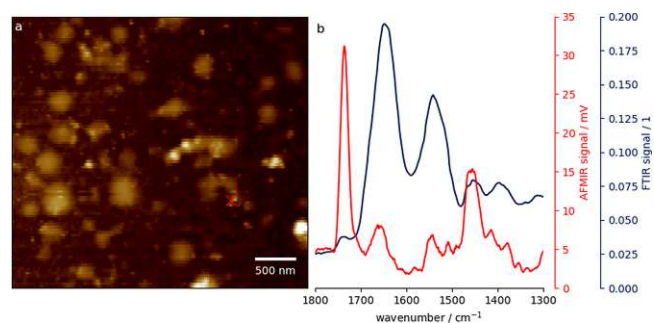


Figure 6. Baseline-corrected tapping mode AFM topography map (a) and AFM-IR (in red) and bulk FTIR (in blue) spectra (b) of a human milk EVs showing protein and lipid spectral signatures. EVs were immobilized on the surface of a silicon wafer using microcontact printed anti-CD9 antibodies and measured using tapping mode AFM-IR with $f_2 = 1500$ kHz, $f_{\text{laser}} \approx 1250$ kHz, and detection at $f_1 = 250$ kHz (measured on a Bruker nano-IR 3s; IR laser source: MIRcat-QT from Daylight Solutions; cantilever: Tap300GB-G from Budget-Sensors; laser power: 49.6%; laser duty cycle: 16%). Spectrum b is an average of three spectra taken at the same location [marked with a cross in panel (a)] and smoothed using a Savitzky-Golay filter (20 points, second order).⁹⁸

EVs are placed and dried on a zinc selenide prism, here they are placed on a functionalized silicone surface, a more chemically resistant and versatile substrate. By using the anti-CD9 antibodies, the coffee ring effect can be prevented, which permits the access to more EVs. Furthermore, as only EVs are immobilized by anti-CD9, the selectivity is increased significantly, as residues from the purification steps can be washed away before tapping mode AFM-IR measurements are performed. This protocol has been applied with promising results to human milk EVs (Figure 6), which play an important role in early life immunity and intestinal development.⁹⁵ AFM-IR spectra obtained from immobilized EVs display marker bands (Figure 6, b) in agreement with those obtained from bulk FTIR studies,¹⁰¹ thus showing the suitability of this approach for the label-free tapping mode AFM-IR analysis of human milk EVs. As demonstrated in these two approaches, AFM-IR can be applied to the nanoscale label-free chemical

analysis of individual EVs and thus provide a valuable contribution to EV research.

Chromosome and DNA Studies

AFM-IR can also give valuable information about DNA methylation as well as anticancer binding locations in chromosomes with characteristically high spatial resolution.⁵² Chromosomes contain two types of chromatin (i.e., DNA–protein complex), euchromatin and heterochromatin, distinguishable by the methylation of the cytosine bases and how packed the structure is. Heterochromatin is characterized by denser chromatin structures containing methylated cytosine bases, which in turn means that it is not active for transcription. Euchromatin, on the other hand, is loosely packed, and its genes are available for transcription. Using ring-down contact mode AFM-IR, Lipiec et al.⁵² mapped DNA methylation in metaphase chromosomes, arriving at the characteristic banding pattern known from immunofluorescence techniques but without the use of labeling agents. Furthermore, by applying PCA to the different areas of the AFM-IR spectra collected, the authors were able to confirm the distinction between heterochromatin and euchromatin areas. The study goes on to demonstrate the capability of AFM-IR to distinguish between active and inactive chromosomes, as well as the preferential binding site of a platinum anticancer drug (the inactive heterochromatin) through the use of a PCA to analyze spectral data. Despite the experimental complexity of this study,⁵² the results are very promising, particularly the ability to identify drug-binding sites in chromosomes, which can provide important mechanistic information on how anticancer drugs affect cells without the use of staining agents.

Recently, Custovic et al.⁵⁴ published a methodological approach to analyze DNA networks and single molecules using resonance-enhanced contact mode AFM-IR. Leveraging previously available methodological approaches for DNA deposition on mica surfaces, the authors demonstrated the applicability of these methods to the AFM-IR technique and were able to acquire AFM-IR spectra and maps of DNA networks and single molecules (Figure 7). This study is an important first step in what can be the future application of AFM-IR to study DNA molecules and DNA–protein complexes.

Studies of Protein Fibrils and Aggregates

Protein fibrils are involved in numerous neurodegenerative diseases in humans¹⁰² and are thus an important target of studies aiming at a better understanding of their structure, properties, and aggregation mechanisms. AFM-IR is a promising technique in this field, since it can provide information on a protein's secondary structure at the nanoscale in a label-free manner. Rizevsky and Kurouski¹⁰³ studied the structural features of insulin fibril aggregates using contact mode AFM-IR without recourse to labels and identified two structural polymorphs: one composed of a β -sheet core and an outer, unordered, α -helix-containing surrounding layer and another polymorph composed of a mixed β -sheet and α -helix/unordered core surrounded by an outer β -sheet structure layer.¹⁰³ The secondary structure of the outermost layer of the fibril's surface varies between the two polymorphs, presumably due to distinct lateral growth mechanisms.¹⁰³ Further AFM-IR studies of protein aggregation state's structure have been conducted on A β 42 (present in Alzheimer's disease),^{104–107} cell-penetrating peptides,¹⁰⁸ functional amyloids,¹⁰⁹ and α -synuclein (present in Parkinson's disease),¹¹⁰ whereas other

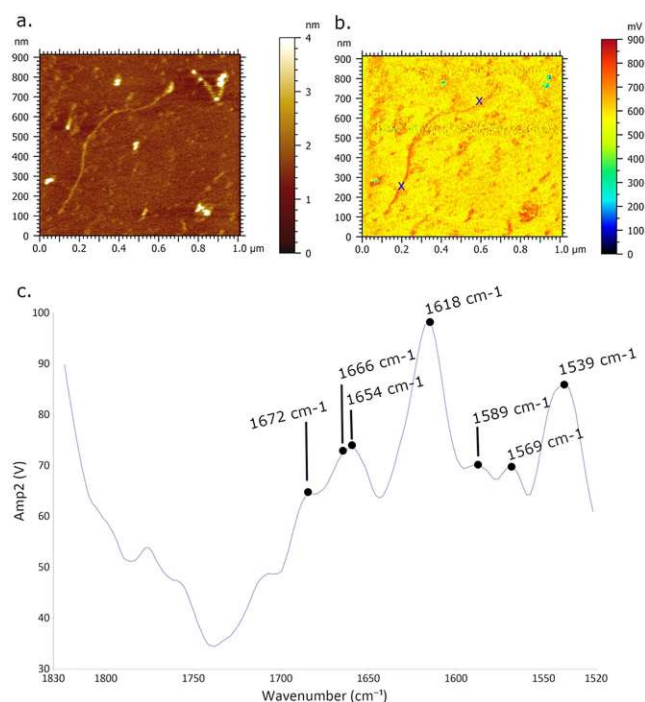


Figure 7. Topography map (a) and AFM-IR absorption map at 1633 cm^{-1} (b) of single DNA molecules deposited on a Ni^+ -functionalized mica surface. Average AFM-IR spectrum (c) collected at the locations marked in panel (b) show the characteristic mid-IR absorption bands of nucleic acid bases. Reproduced with permission under a Creative Commons Attribution 4.0 International License from ref 54. Copyright 2022 Nature Portfolio.

studies have focused on the effect of lipids on protein aggregation^{111–113} or the formation of amyloid microcrystals.¹¹⁴

A further step in AFM-IR studies of protein aggregation states is to investigate the interaction of these with potential drugs and drug candidate molecules. Ruggeri et al.¹¹⁵ studied the interaction between different A β 42 aggregation species and bexarotene, a drug which delays protein aggregation. The study mainly used AFM-IR and combined it with chemometric models to allow for more effective data interpretation. This study made use of the lighting-rod signal enhancement by using gold-coated substrates and tips and was measured using short laser pulses and off-resonance to minimize sample damage and limit the contribution of the substrate to the signal obtained, which otherwise hinders the measurement of objects smaller than the diameter of the tip.^{115,116} The authors were able to distinguish between the spectral signatures of oligomers (composed of proteins in random coil conformation as well as in antiparallel intermolecular β -sheet conformation) and fibrils (composed overwhelmingly of parallel intermolecular β -sheet structures).¹¹⁵ However, the most interesting result was the observation that bexarotene molecules form hydrogen bonds linking their carboxyl groups to the A β 42 aggregates which hinders the progression to further aggregation states such as fibrils. This study showcases the potential of AFM-IR to contribute to a better understanding of drug–target interactions.

When analyzing amyloid fibrils using AFM-IR particular care is required when the obtained spectra will be greatly affected by the experimental setup used.¹¹⁷ For highly oriented samples with less than 10 nm thickness (as can be the case when

measuring amyloid fibers and other types of protein aggregation states, depending on sample preparation), a recent study by Waeytens et al. recommends using bottom illumination, Si cantilevers, and s-polarized light to obtain closer results to those expected from classical ATR-FTIR spectroscopy.¹¹⁷ These are important considerations when setting up a study, particularly as the use of gold tips is frequent due to the signal enhancement they provide. This enhancement, however, comes at the expense of spectral reliability for structural analysis.¹¹⁷

■ FUTURE DIRECTIONS AND PROMISING NEW APPROACHES

Liquid Measurements

The AFM-IR study of biological samples in water, their native environment, is a technique that has so far remained elusive and seldomly used.^{7,118,119} AFM-IR measurements in liquid are particularly challenging due to the extra cantilever oscillation dampening leading to lower signal-to-noise ratios, as well as the intense background absorption of water.⁷ To tackle the background absorption challenge, deuterated water can be used instead of water and measurements are carried out in bottom illumination to limit the exposure of the medium to the IR laser beam, and thus its contribution to the signal.³ Furthermore, the use of bottom illumination schemes requiring IR-transparent prisms typically restricts the list of potential substrates to materials such as ZnSe and CaF₂, which are chemically incompatible with a variety of sampling protocols, e.g., those requiring the use of acidic substances, are harder to manipulate due to their brittleness, and are costly. All of these factors have contributed to the small number of recent studies employing this methodology: excluding studies carried out using peak-force infrared microscopy, an emerging subtype of AFM-IR, only two papers have been published in the past five years using AFM-IR in liquid mode.^{7,23}

Nonetheless, the perspective of measurements in liquid is attractive, provided technical improvements to the technique are undertaken. These might include the development of cheaper and more easily manipulable substrates, improvements in the instrument's measurement stability, and a better understanding of the behavior of cantilevers during an AFM-IR measurement in liquid. Recent results show that measuring in liquid using the tapping mode might be the key to solvent signal suppression, since tapping mode measurements are inherently insensitive to the acoustic waves that result from the absorption of IR radiation by the surrounding medium (water).²³ Future interesting avenues of research for liquid AFM-IR studies include polymer biodeterioration focusing on the longer-term survival of the cell in liquid media, protein aggregation processes and how they are affected by medium components in real-time, as well as the imaging of biological processes, to name a few. A further step could be the integration of microfluidic setups with AFM-IR, as is already the case for AFM.¹²⁰ Such addition would enable the AFM-IR of individual cells while they are exposed to different nutrients or media components or to detect the capture and analyze the properties of vesicles captured by membrane proteins.

Surface Sensitive Mode

Recently a "surface sensitive" mode has been developed, which is a type of contact mode leveraging a heterodyne detection scheme that allows for the probing of only the upper 10–30 nm of the sample.²³ In this mode, the cantilever is oscillated at

a high frequency, f_1 , and the laser set to a high off-resonance frequency, f_{laser} such that the sum or difference of these two frequencies coincides with one of the cantilever contact resonances (ideally with a high Q factor).²³ Through nonlinear interactions, the AFM-IR signal could be detected at the resonance frequency and corresponds only to the uppermost layers of the sample.²³ Despite not requiring hardware changes to instruments already capable of tapping mode experiments, this mode is so recent (less than two years old) that, to date, there are no published studies on its application to biological samples. This mode could allow for studies targeting cell membranes (4–5 nm thick)¹²¹ and immediate surroundings such as cell walls without the need to isolate them from the rest of the cell. Indeed, by combining surface sensitive measurements with previously existing modes that have no probing depth sensitivity, the deeper parts of the cell can be probed in the same experiment.

Labeling of Target Molecules

Although one of the strong suits of AFM-IR is the possibility of high-resolution label-free studies, this is not feasible in all cases, particularly when the target analytes are not chemically distinct from their surrounding environment. A glimpse into such a possibility is offered in the work by Clède et al.,¹²² in which a rhenium tricarbonyl complex (mid-IR tag) coupled to a luminescent probe allowed for the multimodal imaging of the intracellular distribution of an estrogen derivative within breast cancer cells. The multimodal probe was linked to the target molecule via "click" chemistry. More recently, the same class of rhenium tags was used to show the intracellular targets of ferrocifens, which are potential anticancer drugs.¹²³ Rhenium tricarbonyls absorb strongly at around 1950 cm⁻¹, an area in which biological samples tend to have little to no absorption.¹²² Besides rhenium carbonyl tags, alkynes are another class of compounds that have an application potential as mid-IR tags in AFM-IR studies. Alkynes are widely used as Raman tags due to their absorption band in the region of 2100 cm⁻¹ to 2200 cm⁻¹, isolated from typical biomolecule bands (Figure 2).¹²⁴ Tagging target analytes with alkyne-containing molecules represents another potential field of investigation, albeit with one possible downside: the QCLs commonly used in AFM-IR setups often do not cover this "remote" area of the mid-IR spectrum.

Finally, isotope labeling of compounds to study processes within the cell, or even interactions between cells, is another potential avenue of study for AFM-IR. This kind of approach has been demonstrated on bacteria using O-PTIR.¹²⁵ The similar signal generation of the two techniques hints at the possibility of such studies also being feasible using AFM-IR.

Image Processing and Data Analysis

Thermal drift is a known and common problem affecting AFM-IR measurements, particularly when these are conducted over longer periods of time, resulting in unintentional position changes. Especially when calculating ratios of two AFM-IR maps acquired at different wavenumbers, image alignment is crucial to avoid artifacts at the edges of features. Thermal drift correction is carried out by phase cross-correlation using the topography maps, which are recorded at the same time as the AFM-IR maps. However, the absence of a community-wide consensus on how to implement this drift-correction approach has led to widely different software implementations being employed, including Ansys Studio,⁷⁵ SPIP,^{52,116} Python,¹²⁶ and Matlab.⁵⁹ Furthermore, beyond this simple step of data

(pre-) processing, little discussion is happening within the community regarding data evaluation, i.e., how multivariate methods like PLSs should be applied to AFM-IR data sets, which types of normalization, smoothing and “bad pixel” removal are acceptable in AFM-IR data sets to retrieve reproducible spectra and images, and so forth. We expect that as the number of groups working on AFM-IR increases, especially those with a focus on the life sciences that most require multivariate methods for evaluation, this aspect will move toward the center of attention.

CONCLUSION

In the last five years, AFM-IR has been applied to increasingly complex biological samples, from single DNA molecules⁵⁴ and proteins¹¹⁶ to breast cancer tissue sections.⁸⁷ The technique is increasingly moving from proof-of-concept studies toward application to practical problems where its potentially nondestructive nature allows for integration with other established microscopy techniques to obtain complementary information. We have summarized some of the recent applications of AFM-IR to the life sciences, identifying potential future directions of research, as well as relevant current limitations. AFM-IR's high lateral resolution allows for an unprecedented access to chemical information on whole cells, cell components, and biodeterioration of materials. We hope that this perspective encourages more interdisciplinary collaboration between the life sciences and the growing field of AFM-IR by highlighting its potential contributions to challenges relevant to the life sciences.

ASSOCIATED CONTENT

Data Availability Statement

Experimental details of the data in Figure 4 are available upon reasonable request to the corresponding author.

AUTHOR INFORMATION

Corresponding Author

Georg Ramer – Institute of Chemical Technologies and Analytics, TU Wien, 1060 Vienna, Austria; orcid.org/0000-0001-8307-5435; Email: georg.ramer@tuwien.ac.at

Authors

- A. Catarina V. D. dos Santos** – Institute of Chemical Technologies and Analytics, TU Wien, 1060 Vienna, Austria; orcid.org/0000-0001-6342-2823
- Nikolaus Hondl** – Institute of Chemical Technologies and Analytics, TU Wien, 1060 Vienna, Austria; orcid.org/0009-0001-9282-4474
- Victoria Ramos-Garcia** – Health Research Institute La Fe, 46026 Valencia, Spain; orcid.org/0000-0001-8306-199X
- Julia Kuligowski** – Health Research Institute La Fe, 46026 Valencia, Spain; orcid.org/0000-0001-6979-2235
- Bernhard Lendl** – Institute of Chemical Technologies and Analytics, TU Wien, 1060 Vienna, Austria; orcid.org/0000-0003-3838-5842

Complete contact information is available at: <https://pubs.acs.org/10.1021/acsmeasuresciau.3c00010>

Author Contributions

All authors have given approval to the final version of the manuscript. CRediT: **A. Catarina V. D. dos Santos** conceptualization (equal), validation (lead), writing-original draft (lead); **Nikolaus Hondl** investigation (equal), visualization (equal); **Victoria Ramos-Garcia** investigation (equal), writing-review & editing (equal); **Julia Kuligowski** funding acquisition (equal), writing-review & editing (equal); **Bernhard Lendl** funding acquisition (equal), supervision (supporting), writing-review & editing (equal); **Georg Ramer** conceptualization (equal), supervision (equal), writing-review & editing (equal).

Notes

The authors declare no competing financial interest.

ACKNOWLEDGMENTS

The authors acknowledge financial support through the COMET Centre CHASE, funded within the COMET, Competence Centers for Excellent Technologies, programme by the BMK, the BMDW, and the Federal Provinces of Upper Austria and Vienna. The COMET programme is managed by the Austrian Research Promotion Agency (FFG). G.R. and N.H. acknowledge funding from the European Union's Horizon 2020 research and innovation programme under Grant no. 953234. G.R. acknowledges funding from the European Union's Horizon 2020 research and innovation programme under Grant no. 8619858. J.K. and V.R.G. acknowledge financial support by the Carlos III Health Institute and cofunded by the European Union [Grant CPII21/00003]. The authors acknowledge TU Wien Bibliothek for financial support through its Open Access Funding Programme.

REFERENCES

- Wieland, K.; Ramer, G.; Weiss, V. U.; Allmaier, G.; Lendl, B.; Centrone, A. Nanoscale Chemical Imaging of Individual Chemotherapeutic Cytarabine-Loaded Liposomal Nanocarriers. *Nano Research* **2019**, *12* (1), 197–203.
- Dazzi, A.; Prazeres, R.; Glotin, F.; Ortega, J. M. Local Infrared Microspectroscopy with Subwavelength Spatial Resolution with an Atomic Force Microscope Tip Used as a Photothermal Sensor. *Opt. Lett.*, *OL* **2005**, *30* (18), 2388–2390.
- Schwartz, J. J.; Jakob, D. S.; Centrone, A. A Guide to Nanoscale IR Spectroscopy: Resonance Enhanced Transduction in Contact and Tapping Mode AFM-IR. *Chem. Soc. Rev.* **2022**, *51* (13), 5248–5267.
- Kurouski, D.; Dazzi, A.; Zenobi, R.; Centrone, A. Infrared and Raman Chemical Imaging and Spectroscopy at the Nanoscale. *Chem. Soc. Rev.* **2020**, *49* (11), 3315–3347.
- Dazzi, A.; Prater, C. B.; Hu, Q.; Chase, D. B.; Rabolt, J. F.; Marcott, C. AFM-IR: Combining Atomic Force Microscopy and Infrared Spectroscopy for Nanoscale Chemical Characterization. *Appl. Spectrosc.* **2012**, *66* (12), 1365–1384.
- Ramer, G.; Aksyuk, V. A.; Centrone, A. Quantitative Chemical Analysis at the Nanoscale Using the PTIR Technique. *Anal. Chem.* **2017**, *89* (24), 13524–13531.
- Ramer, G.; Ruggeri, F. S.; Levin, A.; Knowles, T. P. J.; Centrone, A. Determination of Polypeptide Conformation with Nanoscale Resolution in Water. *ACS Nano* **2018**, *12* (7), 6612–6619.
- Rizevsky, S.; Zhaliyazka, K.; Dou, T.; Matveyenka, M.; Kurouski, D. Characterization of Substrates and Surface-Enhancement in Atomic Force Microscopy Infrared Analysis of Amyloid Aggregates. *J. Phys. Chem. C* **2022**, *126* (8), 4157–4162.
- Lu, F.; Jin, M.; Belkin, M. A. Tip-Enhanced Infrared Nanospectroscopy via Molecular Expansion Force Detection. *Nat. Photonics* **2014**, *8* (4), 307–312.

- (10) Wang, C.-T.; Jiang, B.; Zhou, Y.-W.; Jiang, T.-W.; Liu, J.-H.; Zhu, G.-D.; Cai, W.-B. Exploiting the Surface-Enhanced IR Absorption Effect in the Photothermally Induced Resonance AFM-IR Technique toward Nanoscale Chemical Analysis. *Anal. Chem.* **2019**, *91* (16), 10541–10548.
- (11) Morsch, S.; Lyon, S. B.; Edmondson, S.; Gibbon, S. R. Reflectance in AFM-IR: Implications for Interpretation and Remote Analysis of the Buried Interface. *Anal. Chem.* **2020**, *92* (12), 8117–8124.
- (12) Dazzi, A.; Glotin, F.; Carminati, R. Theory of Infrared Nanospectroscopy by Photothermal Induced Resonance. *J. Appl. Phys.* **2010**, *107* (12), 124519.
- (13) Vincent, T. Scanning Near-Field Infrared Microscopy. *Nat. Rev. Phys.* **2021**, *3* (8), 537–537.
- (14) Marchetti, A.; Beltran, V.; Nuyts, G.; Borondics, F.; De Meyer, S.; Van Bos, M.; Jaroszewicz, J.; Otten, E.; Debulpaep, M.; De Wael, K. Novel Optical Photothermal Infrared (O-PTIR) Spectroscopy for the Noninvasive Characterization of Heritage Glass-Metal Objects. *Science Advances* **2022**, *8* (9), No. eabl6769.
- (15) Lima, C.; Muhamadali, H.; Goodacre, R. Simultaneous Raman and Infrared Spectroscopy of Stable Isotope Labeled *Escherichia Coli*. *Sensors* **2022**, *22* (10), 3928.
- (16) Klementieva, O.; Sandt, C.; Martinsson, I.; Kansiz, M.; Gouras, G. K.; Borondics, F. Super-Resolution Infrared Imaging of Polymorphic Amyloid Aggregates Directly in Neurons. *Advanced Science* **2020**, *7* (6), 1903004.
- (17) Zhang, Y.; Yang, B.; Ghafoor, A.; Zhang, Y.; Zhang, Y.-F.; Wang, R.-P.; Yang, J.-L.; Luo, Y.; Dong, Z.-C.; Hou, J. G. Visually Constructing the Chemical Structure of a Single Molecule by Scanning Raman Picoscopy. *National Science Review* **2019**, *6* (6), 1169–1175.
- (18) Lee, J.; Crampton, K. T.; Tallarida, N.; Apkarian, V. A. Visualizing Vibrational Normal Modes of a Single Molecule with Atomically Confined Light. *Nature* **2019**, *568* (7750), 78–82.
- (19) Maissen, C.; Chen, S.; Nikulina, E.; Govyadinov, A.; Hillenbrand, R. Probes for Ultrasensitive THz Nanoscopy. *ACS Photonics* **2019**, *6* (5), 1279–1288.
- (20) Mastel, S.; Govyadinov, A. A.; Maissen, C.; Chuvilin, A.; Berger, A.; Hillenbrand, R. Understanding the Image Contrast of Material Boundaries in IR Nanoscopy Reaching 5 Nm Spatial Resolution. *ACS Photonics* **2018**, *5* (8), 3372–3378.
- (21) Wang, H.; Xie, Q.; Xu, X. G. Super-Resolution Mid-Infrared Spectro-Microscopy of Biological Applications through Tapping Mode and Peak Force Tapping Mode Atomic Force Microscope. *Adv. Drug Delivery Rev.* **2022**, *180*, 114080.
- (22) Wang, L.; Wang, H.; Xu, X. G. Principle and Applications of Peak Force Infrared Microscopy. *Chem. Soc. Rev.* **2022**, *51* (13), 5268–5286.
- (23) Mathurin, J.; Deniset-Besseau, A.; Bazin, D.; Dartois, E.; Wagner, M.; Dazzi, A. Photothermal AFM-IR Spectroscopy and Imaging: Status, Challenges, and Trends. *J. Appl. Phys.* **2022**, *131* (1), 010901.
- (24) Schwartz, J. J.; Jakob, D. S.; Centrone, A. A Guide to Nanoscale IR Spectroscopy: Resonance Enhanced Transduction in Contact and Tapping Mode AFM-IR. *Chem. Soc. Rev.* **2022**, *51*, 5248.
- (25) Katzenmeyer, A. M.; Holland, G.; Kjoller, K.; Centrone, A. Absorption Spectroscopy and Imaging from the Visible through Mid-Infrared with 20 Nm Resolution. *Anal. Chem.* **2015**, *87* (6), 3154–3159.
- (26) Ramer, G.; Reisenbauer, F.; Steindl, B.; Tomischko, W.; Lendl, B. Implementation of Resonance Tracking for Assuring Reliability in Resonance Enhanced Photothermal Infrared Spectroscopy and Imaging. *Appl. Spectrosc.* **2017**, *71* (8), 2013–2020.
- (27) dos Santos, A. C. V. D.; Tranchida, D.; Lendl, B.; Ramer, G. Nanoscale Chemical Characterization of a Post-Consumer Recycled Polyolefin Blend Using Tapping Mode AFM-IR. *Analyst* **2022**, *147* (16), 3741–3747.
- (28) Kenkel, S.; Mittal, S.; Bhargava, R. Closed-Loop Atomic Force Microscopy-Infrared Spectroscopic Imaging for Nanoscale Molecular Characterization. *Nat. Commun.* **2020**, *11* (1), 3225.
- (29) Tuteja, M.; Kang, M.; Leal, C.; Centrone, A. Nanoscale Partitioning of Paclitaxel in Hybrid Lipid-Polymer Membranes. *Analyst* **2018**, *143* (16), 3808–3813.
- (30) Ma, X.; Beltran, V.; Ramer, G.; Pavlidis, G.; Parkinson, D. Y.; Thoury, M.; Meldrum, T.; Centrone, A.; Berrie, B. H. Revealing the Distribution of Metal Carboxylates in Oil Paint from the Micro- to Nanoscale. *Angew. Chem., Int. Ed.* **2019**, *58* (34), 11652–11656.
- (31) Saadi, M. A. S. R.; Uluotku, B.; Parvini, C. H.; Solares, S. D. Soft Sample Deformation, Damage and Induced Electromechanical Property Changes in Contact- and Tapping-Mode Atomic Force Microscopy. *Surf. Topogr.: Metrol. Prop.* **2020**, *8* (4), 045004.
- (32) Mathurin, J.; Deniset-Besseau, A.; Dazzi, A. Advanced Infrared Nanospectroscopy Using Photothermal Induced Resonance Technique, AFMIR: New Approach Using Tapping Mode. *Acta Phys. Polym., A* **2020**, *137* (1), 29–32.
- (33) Li, W.; Wang, H.; Xu, X. G.; Yu, Y. Simultaneous Nanoscale Imaging of Chemical and Architectural Heterogeneity on Yeast Cell Wall Particles. *Langmuir* **2020**, *36* (22), 6169–6177.
- (34) Wang, H.; González-Fialkowski, J. M.; Li, W.; Xie, Q.; Yu, Y.; Xu, X. G. Liquid-Phase Peak Force Infrared Microscopy for Chemical Nanoimaging and Spectroscopy. *Anal. Chem.* **2021**, *93* (7), 3567–3575.
- (35) Gusenbauer, C.; Nypelö, T.; Jakob, D. S.; Xu, X. G.; Vezenov, D. V.; Asaadi, S.; Sixta, H.; Konnerth, J. Differences in Surface Chemistry of Regenerated Lignocellulose Fibers Determined by Chemically Sensitive Scanning Probe Microscopy. *Int. J. Biol. Macromol.* **2020**, *165*, 2520–2527.
- (36) Li, M.; Wang, H.; Li, W.; Xu, X. G.; Yu, Y. Macrophage Activation on “Phagocytic Synapse” Arrays: Spacing of Nanoclustered Ligands Directs TLR1/2 Signaling with an Intrinsic Limit. *Science Advances* **2020**, *6* (49), No. eabc8482.
- (37) Larkin, P. J. Basic Principles. In *IR and Raman Spectroscopy: Principles and Spectral Interpretation*; Elsevier, 2011; Chapter 2, pp 7–25.
- (38) Larkin, P. J. Introduction: Infrared and Raman Spectroscopy. In *IR and Raman Spectroscopy: Principles and Spectral Interpretation*; Elsevier, 2011; Chapter 1, pp 1–6.
- (39) Baumgartner, B.; Hayden, J.; Loizillon, J.; Steinbacher, S.; Grosso, D.; Lendl, B. Pore Size-Dependent Structure of Confined Water in Mesoporous Silica Films from Water Adsorption/Desorption Using ATR-FTIR Spectroscopy. *Langmuir* **2019**, *35* (37), 11986–11994.
- (40) Baiz, C. R.; Blasiak, B.; Bredenbeck, J.; Cho, M.; Choi, J.-H.; Corcelli, S. A.; Dijkstra, A. G.; Feng, C.-J.; Garrett-Roe, S.; Ge, N.-H.; Hanson-Heine, M. W. D.; Hirst, J. D.; Jansen, T. L. C.; Kwac, K.; Kubarych, K. J.; Londergan, C. H.; Maekawa, H.; Reppert, M.; Saito, S.; Roy, S.; Skinner, J. L.; Stock, G.; Straub, J. E.; Thielges, M. C.; Tominaga, K.; Tokmakoff, A.; Torii, H.; Wang, L.; Webb, L. J.; Zanni, M. T. Vibrational Spectroscopic Map, Vibrational Spectroscopy, and Intermolecular Interaction. *Chem. Rev.* **2020**, *120* (15), 7152–7218.
- (41) Griffiths, P. R.; de Haseth, J. A. Microspectroscopy and Imaging. In *Fourier Transform Infrared Spectroscopy*; Chemical Analysis: a Series of Monographs on Analytical Chemistry and Its Applications; John Wiley & Sons, Inc, 2007; Chapter 14, pp 303–320.
- (42) Ramer, G.; Lendl, B. Attenuated Total Reflection Fourier Transform Infrared Spectroscopy. In *Encyclopedia of Analytical Chemistry*; John Wiley & Sons, Ltd: Chichester, UK, 2013, DOI: 10.1002/9780470027318.a9287.
- (43) Chan, K. L. A.; Kazarian, S. G. Attenuated Total Reflection Fourier-Transform Infrared (ATR-FTIR) Imaging of Tissues and Live Cells. *Chem. Soc. Rev.* **2016**, *45* (7), 1850–1864.
- (44) Talari, A. C. S.; Martinez, M. A. G.; Movasaghi, Z.; Rehman, S.; Rehman, I. U. Advances in Fourier Transform Infrared (FTIR) Spectroscopy of Biological Tissues. *Appl. Spectrosc. Rev.* **2017**, *52* (5), 456–506.

- (45) Baker, M. J.; Trevisan, J.; Bassan, P.; Bhargava, R.; Butler, H. J.; Dorling, K. M.; Fielden, P. R.; Fogarty, S. W.; Fullwood, N. J.; Heys, K. A.; Hughes, C.; Lasch, P. L.; Martin-Hirsch, P. L.; Obinaju, B.; Sockalingum, G. D.; Sulé-Suso, J.; Strong, R. J.; Walsh, M. J.; Wood, B. R.; Gardner, P.; Martin, F. L. Using Fourier Transform IR Spectroscopy to Analyze Biological Materials. *Nat. Protoc.* **2014**, *9* (8), 1771–1791.
- (46) Faelelbom, K. M.; Saleh, A.; Al-Tabakha, M. M. A.; Ashames, A. A. Recent Applications of Quantitative Analytical FTIR Spectroscopy in Pharmaceutical, Biomedical, and Clinical Fields: A Brief Review. *Reviews in Analytical Chemistry* **2022**, *41* (1), 21–33.
- (47) Fadllemoula, A.; Pinho, D.; Carvalho, V. H.; Catarino, S. O.; Minas, G. Fourier Transform Infrared (FTIR) Spectroscopy to Analyse Human Blood over the Last 20 Years: A Review towards Lab-on-a-Chip Devices. *Micromachines* **2022**, *13* (2), 187.
- (48) Barth, A. Infrared Spectroscopy of Proteins. *Biochimica et Biophysica Acta (BBA) - Bioenergetics* **2007**, *1767* (9), 1073–1101.
- (49) Wilkosz, N.; Czaja, M.; Seweryn, S.; Skirlińska-Nosek, K.; Szymonski, M.; Lipiec, E.; Sofińska, K. Molecular Spectroscopic Markers of Abnormal Protein Aggregation. *Molecules* **2020**, *25* (11), 2498.
- (50) Derenne, A.; Claessens, T.; Conus, C.; Goormaghtigh, E. Infrared Spectroscopy of Membrane Lipids. In *Encyclopedia of Biophysics*; Roberts, G. C. K., Ed.; Springer: Berlin, 2013; pp 1074–1081, DOI: 10.1007/978-3-642-16712-6_558.
- (51) Lipiec, E.; Wnętrzak, A.; Chachaj-Brekiesz, A.; Kwiatek, W.; Dynarowicz-Latka, P. High-Resolution Label-Free Studies of Molecular Distribution and Orientation in Ultrathin, Multicomponent Model Membranes with Infrared Nano-Spectroscopy AFM-IR. *J. Colloid Interface Sci.* **2019**, *542*, 347–354.
- (52) Lipiec, E.; Ruggeri, F. S.; Benadiba, C.; Borkowska, A. M.; Kobierski, J. D.; Miszczyk, J.; Wood, B. R.; Deacon, G. B.; Kulik, A.; Dietler, G.; Kwiatek, W. M. Infrared Nanospectroscopic Mapping of a Single Metaphase Chromosome. *Nucleic Acids Res.* **2019**, *47* (18), No. e108.
- (53) Movasaghi, Z.; Rehman, S.; ur Rehman, Dr. I. Fourier Transform Infrared (FTIR) Spectroscopy of Biological Tissues. *Appl. Spectrosc. Rev.* **2008**, *43* (2), 134–179.
- (54) Custovic, I.; Pocholle, N.; Bourillot, E.; Lesniewska, E.; Piétrement, O. Infrared Nanospectroscopic Imaging of DNA Molecules on Mica Surface. *Sci. Rep.* **2022**, *12* (1), 18972.
- (55) Hong, T.; Yin, J.-Y.; Nie, S.-P.; Xie, M.-Y. Applications of Infrared Spectroscopy in Polysaccharide Structural Analysis: Progress, Challenge and Perspective. *Food Chemistry: X* **2021**, *12*, 100168.
- (56) Nikonenko, N. A.; Buslov, D. K.; Sushko, N. I.; Zhbakov, R. G. Spectroscopic Manifestation of Stretching Vibrations of Glycosidic Linkage in Polysaccharides. *J. Mol. Struct.* **2005**, *752* (1), 20–24.
- (57) Wang, Y.-X.; Xin, Y.; Yin, J.-Y.; Huang, X.-J.; Wang, J.-Q.; Hu, J.-L.; Geng, F.; Nie, S.-P. Revealing the Architecture and Solution Properties of Polysaccharide Fractions from *Macrolepiota Albuminosa* (Berk.) Pegler. *Food Chem.* **2022**, *368*, 130772.
- (58) Quaroni, L.; Pogoda, K.; Wiltowska-Zuber, J.; Kwiatek, W. M. Mid-Infrared Spectroscopy and Microscopy of Subcellular Structures in Eukaryotic Cells with Atomic Force Microscopy - Infrared Spectroscopy. *RSC Adv.* **2018**, *8* (5), 2786–2794.
- (59) Perez-Guaita, D.; Kochan, K.; Batty, M.; Doerig, C.; Garcia-Bustos, J.; Espinoza, S.; McNaughton, D.; Heraud, P.; Wood, B. R. Multispectral Atomic Force Microscopy-Infrared Nano-Imaging of Malaria Infected Red Blood Cells. *Anal. Chem.* **2018**, *90* (5), 3140–3148.
- (60) Liu, Z.; Zeng, H.; Xu, K.; Zhao, K.; Liu, Z.; Yao, J.; You, Y.; Wang, D. AFM-IR Probing the Influence of Polarization on the Expression of Proteins within Single Macrophages. *J. Mater. Chem. B* **2021**, *9* (12), 2909–2917.
- (61) dos Santos, A. C. V. D.; Heydenreich, R.; Derntl, C.; Mach-Aigner, A. R.; Mach, R. L.; Ramer, G.; Lendl, B. Nanoscale Infrared Spectroscopy and Chemometrics Enable Detection of Intracellular Protein Distribution. *Anal. Chem.* **2020**, *92* (24), 15719–15725.
- (62) Druzhinina, I. S.; Kubicek, C. P. Familiar Stranger: Ecological Genomics of the Model Saprotroph and Industrial Enzyme Producer *Trichoderma Reesei* Breaks the Stereotypes. In *Advances in Applied Microbiology*; Sariaslani, S., Michael Gadd, G., Eds.; Academic Press, 2016; Chapter 2, Vol. 95, pp 69–147, DOI: 10.1016/bs.aambs.2016.02.001.
- (63) Fischer, A. J.; Maiyuran, S.; Yaver, D. S. Industrial Relevance of *Trichoderma Reesei* as an Enzyme Producer. In *Trichoderma reesei: Methods and Protocols*; Mach-Aigner, A. R.; Martzy, R., Eds.; Methods in Molecular Biology; Springer US: New York, NY, 2021; pp 23–43, DOI: 10.1007/978-1-0716-1048-0_2.
- (64) Deniset-Besseau, A.; Coat, R.; Moutel, B.; Rebois, R.; Mathurin, J.; Grizeau, D.; Dazzi, A.; Gonçalves, O. Revealing Lipid Body Formation and Its Subcellular Reorganization in Oleaginous Microalgae Using Correlative Optical Microscopy and Infrared Nanospectroscopy. *Appl. Spectrosc.* **2021**, *75* (12), 1538–1547.
- (65) Pancani, E.; Mathurin, J.; Bilent, S.; Bernet-Camard, M.-F.; Dazzi, A.; Deniset-Besseau, A.; Gref, R. High-Resolution Label-Free Detection of Biocompatible Polymeric Nanoparticles in Cells. *Particle & Particle Systems Characterization* **2018**, *35* (3), 1700457.
- (66) Banas, A. M.; Banas, K.; Chu, T. T. T.; Naidu, R.; Hutchinson, P. E.; Agrawal, R.; Lo, M. K. F.; Kansiz, M.; Roy, A.; Chandramohanadas, R.; Breese, M. B. H. Comparing Infrared Spectroscopic Methods for the Characterization of Plasmodium Falciparum-Infected Human Erythrocytes. *Commun. Chem.* **2021**, *4* (1), 1–12.
- (67) Ruggeri, F. S.; Marcott, C.; Dinarelli, S.; Longo, G.; Girasole, M.; Dietler, G.; Knowles, T. P. J. Identification of Oxidative Stress in Red Blood Cells with Nanoscale Chemical Resolution by Infrared Nanospectroscopy. *International Journal of Molecular Sciences* **2018**, *19* (9), 2582.
- (68) Fellows, A. P.; Casford, M. T. L.; Davies, P. B.; Gibson, J. S.; Brewin, J. N.; Rees, D. C. Nanoscale Adhesion Profiling and Membrane Characterisation in Sickle Cell Disease Using Hybrid Atomic Force Microscopy-IR Spectroscopy. *Colloids Surf., B* **2021**, *197*, 111383.
- (69) Roman, M.; Wrobel, T. P.; Panek, A.; Paluszkiwicz, C.; Kwiatek, W. M. Nanoscale AFM-IR Spectroscopic Imaging of Lipid Heterogeneity and Effect of Irradiation in Prostate Cancer Cells. *Nanotechnology* **2019**, *30* (42), 425502.
- (70) Roman, M.; Wrobel, T. P.; Paluszkiwicz, C.; Kwiatek, W. M. Comparison between High Definition FT-IR, Raman and AFM-IR for Subcellular Chemical Imaging of Cholesteryl Esters in Prostate Cancer Cells. *Journal of Biophotonics* **2020**, *13* (5), No. e201960094.
- (71) Pięta, E. Nanoscale Insight into Biochemical Changes in Cervical Cancer Cells Exposed to Adaptogenic Drug. *Micron* **2023**, *170*, 103462.
- (72) Dou, T.; Li, Z.; Zhang, J.; Evilevitch, A.; Kurouski, D. Nanoscale Structural Characterization of Individual Viral Particles Using Atomic Force Microscopy Infrared Spectroscopy (AFM-IR) and Tip-Enhanced Raman Spectroscopy (TERS). *Anal. Chem.* **2020**, *92* (16), 11297–11304.
- (73) Khanal, D.; Chang, R. Y. K.; Morales, S.; Chan, H.-K.; Chranowski, W. High Resolution Nanoscale Probing of Bacteriophages in an Inhalable Dry Powder Formulation for Pulmonary Infections. *Anal. Chem.* **2019**, *91* (20), 12760–12767.
- (74) Imbert, L.; Gourion-Arsiquaud, S.; Villarreal-Ramirez, E.; Spevak, L.; Taleb, H.; van der Meulen, M. C. H.; Mendelsohn, R.; Boskey, A. L. Dynamic Structure and Composition of Bone Investigated by Nanoscale Infrared Spectroscopy. *PLoS One* **2018**, *13* (9), No. e0202833.
- (75) Ahn, T.; Jueckstock, M.; Mandair, G. S.; Henderson, J.; Sinder, B. P.; Kozloff, K. M.; Banaszak Holl, M. M. Matrix/Mineral Ratio and Domain Size Variation with Bone Tissue Age: A Photothermal Infrared Study. *J. Struct. Biol.* **2022**, *214* (3), 107878.
- (76) Qian, W.; Schmidt, R.; Turner, J. A.; Bare, S. P.; Lappe, J. M.; Recker, R. R.; Akhter, M. P. A Pilot Study on the Nanoscale Properties of Bone Tissue near Lacunae in Fracturing Women. *Bone Reports* **2022**, *17*, 101604.

- (77) Rammal, H.; Dubus, M.; Bercu, N. B.; Mathieu, E.; Terryn, C.; Molinari, M.; Gangloff, S. C.; Nassif, N.; Mauprivez, C.; Quilès, F.; Kerdjoudj, H. Mechanobiologically Induced Bone-like Nodules: Matrix Characterization from Micro to Nanoscale. *Nanomedicine: Nanotechnology, Biology and Medicine* **2020**, *29*, 102256.
- (78) Rahmati, M.; Stötzel, S.; El Khassawna, T.; Mao, C.; Ali, A.; Vaughan, J. C.; Iskhahova, K.; Florian Wieland, D. C.; Cantalapedra, A. G.; Perale, G.; Betge, F.; Dillon, E. P.; Lyngstadaas, S. P.; Haugen, H. J. Intrinsically Disordered Peptides Enhance Regenerative Capacities of Bone Composite Xenografts. *Mater. Today* **2022**, *S2*, 63–79.
- (79) Huang, L.; Zhang, X.; Shao, J.; Zhou, Z.; Chen, Y.; Hu, X. Nanoscale Chemical and Mechanical Heterogeneity of Human Dentin Characterized by AFM-IR and Bimodal AFM. *Journal of Advanced Research* **2020**, *22*, 163–171.
- (80) Fellows, A. P.; Casford, M. T. L.; Davies, P. B. Nanoscale Molecular Characterization of Hair Cuticle Cells Using Integrated Atomic Force Microscopy-Infrared Laser Spectroscopy. *Appl. Spectrosc.* **2020**, *74* (12), 1540–1550.
- (81) Fellows, A. P.; Casford, M. T. L.; Davies, P. B. Using Hybrid Atomic Force Microscopy and Infrared Spectroscopy (AFM-IR) to Identify Chemical Components of the Hair Medulla on the Nanoscale. *J. Microsc.* **2021**, *284* (3), 189–202.
- (82) Fellows, A. P.; Casford, M. T. L.; Davies, P. B. Chemically Characterizing the Cortical Cell Nano-Structure of Human Hair Using Atomic Force Microscopy Integrated with Infrared Spectroscopy (AFM-IR). *International Journal of Cosmetic Science* **2022**, *44* (1), 42–55.
- (83) Bildstein, L.; Deniset-Besseau, A.; Pasini, I.; Mazilier, C.; Keoung, Y. W.; Dazzi, A.; Baghdadli, N. Discrete Nanoscale Distribution of Hair Lipids Fails to Provide Humidity Resistance. *Anal. Chem.* **2020**, *92* (17), 11498–11504.
- (84) Chen, J.; Kim, J.; Shao, W.; Schlecht, S. H.; Baek, S. Y.; Jones, A. K.; Ahn, T.; Ashton-Miller, J. A.; Banaszak Holl, M. M.; Wojtys, E. M. An Anterior Cruciate Ligament Failure Mechanism. *Am. J. Sports Med.* **2019**, *47* (9), 2067–2076.
- (85) Paz Ramos, A.; Gooris, G.; Bouwstra, J.; Molinari, M.; Lafleur, M. Raman and AFM-IR Chemical Imaging of Stratum Corneum Model Membranes. *Can. J. Chem.* **2020**, *98* (9), 495–501.
- (86) Kemel, K.; Deniset-Besseau, A.; Baillet-Guffroy, A.; Faivre, V.; Dazzi, A.; Laugel, C. Nanoscale Investigation of Human Skin and Study of Skin Penetration of Janus Nanoparticles. *Int. J. Pharm.* **2020**, *579*, 119193.
- (87) Peta, M.; Cherfan, M.; Boudierlique, E.; Reguer, S.; Mathurin, J.; Dazzi, A.; L'Heronde, M.; Daudon, M.; Letavernier, E.; Deniset-Besseau, A.; Bazin, D. Multiscale Approach to Provide a Better Physicochemical Description of Women Breast Microcalcifications. *Comptes Rendus. Chimie* **2022**, *25* (S1), 553–576.
- (88) Barlow, D. E.; Biffinger, J. C.; Estrella, L.; Lu, Q.; Hung, C.-S.; Nadeau, L. J.; Crouch, A. L.; Russell, J. N.; Crookes-Goodson, W. J. Edge-Localized Biodeterioration and Secondary Microplastic Formation by *Papiliotrema Laurentii* Unsaturated Biofilm Cells on Polyurethane Films. *Langmuir* **2020**, *36* (6), 1596–1607.
- (89) Kochan, K.; Perez-Guaita, D.; Pissang, J.; Jiang, J.-H.; Peleg, A. Y.; McNaughton, D.; Heraud, P.; Wood, B. R. In Vivo Atomic Force Microscopy-Infrared Spectroscopy of Bacteria. *Journal of The Royal Society Interface* **2018**, *15* (140), 20180115.
- (90) Frederix, P. L. T. M.; Bosshart, P. D.; Engel, A. Atomic Force Microscopy of Biological Membranes. *Biophys. J.* **2009**, *96* (2), 329–338.
- (91) Cai, M.; Wang, H. Atomic Force Microscopy for Cell Membrane Investigation. In *Pharmaceutical Nanotechnology: Basic Protocols*; Weissig, V.; Elbayoumi, T., Eds.; Methods in Molecular Biology; Springer: New York, NY, 2019; pp 361–372, DOI: 10.1007/978-1-4939-9516-5_22.
- (92) Giliberti, V.; Polito, R.; Ritter, E.; Broser, M.; Hegemann, P.; Puskar, L.; Schade, U.; Zanetti-Polzi, L.; Daidone, I.; Corni, S.; Rusconi, F.; Biagioni, P.; Baldassarre, L.; Ortolani, M. Tip-Enhanced Infrared Difference-Nanospectroscopy of the Proton Pump Activity of Bacteriorhodopsin in Single Purple Membrane Patches. *Nano Lett.* **2019**, *19* (5), 3104–3114.
- (93) Polito, R.; Temperini, M. E.; Ritter, E.; Puskar, L.; Schade, U.; Broser, M.; Hegemann, P.; Baldassarre, L.; Ortolani, M.; Giliberti, V. Conformational Changes of a Membrane Protein Determined by Infrared Difference Spectroscopy beyond the Diffraction Limit. *Phys. Rev. Applied* **2021**, *16* (1), 014048.
- (94) Engel, A. Atomic Force Microscopy and Electron Microscopy of Membrane Proteins. In *Comprehensive Biophysics*; Egelman, E. H., Ed.; Elsevier: Amsterdam, 2012; pp 92–119, DOI: 10.1016/B978-0-12-374920-8.00511-7.
- (95) Ramos-Garcia, V.; Ten-Doménech, I.; Albiach-Delgado, A.; Gómez-Ferrer, M.; Sepúlveda, P.; Parra-Llorca, A.; Campos-Berga, L.; Moreno-Giménez, A.; Quintás, G.; Kuligowski, J. Isolation and Lipidomic Screening of Human Milk Extracellular Vesicles. In *Mass Spectrometry for Metabolomics*; González-Domínguez, R., Ed.; Methods in Molecular Biology; Springer US: New York, NY, 2023; pp 177–188, DOI: 10.1007/978-1-0716-2699-3_18.
- (96) Kim, S. Y.; Khanal, D.; Tharkar, P.; Kalionis, B.; Chrzanowski, W. None of Us Is the Same as All of Us: Resolving the Heterogeneity of Extracellular Vesicles Using Single-Vesicle, Nanoscale Characterization with Resonance Enhanced Atomic Force Microscope Infrared Spectroscopy (AFM-IR). *Nanoscale Horiz.* **2018**, *3* (4), 430–438.
- (97) Doyle, L. M.; Wang, M. Z. Overview of Extracellular Vesicles, Their Origin, Composition, Purpose, and Methods for Exosome Isolation and Analysis. *Cells* **2019**, *8* (7), 727.
- (98) Hondl, N. Chemical Spectroscopy of Individual Human Milk Extracellular Vesicles. *Diplomathesis*; TU Wien: Wien, 2022, DOI: 10.34726/hss.2022.105687.
- (99) Tiwari, S.; Kumar, V.; Randhawa, S.; Verma, S. K. Preparation and Characterization of Extracellular Vesicles. *American Journal of Reproductive Immunology* **2021**, *85* (2), No. e13367.
- (100) Shao, H.; Im, H.; Castro, C. M.; Breakefield, X.; Weissleder, R.; Lee, H. New Technologies for Analysis of Extracellular Vesicles. *Chem. Rev.* **2018**, *118* (4), 1917–1950.
- (101) Ramos-Garcia, V.; Ten-Doménech, I.; Moreno-Giménez, A.; Gormaz, M.; Parra-Llorca, A.; Shephard, A. P.; Sepúlveda, P.; Pérez-Guaita, D.; Vento, M.; Lendl, B.; Quintás, G.; Kuligowski, J. ATR-FTIR Spectroscopy for the Routine Quality Control of Exosome Isolations. *Chemometrics and Intelligent Laboratory Systems* **2021**, *217*, 104401.
- (102) Housmans, J. A. J.; Wu, G.; Schymkowitz, J.; Rousseau, F. A Guide to Studying Protein Aggregation. *FEBS Journal* **2023**, *290* (3), 554–583.
- (103) Rizevsky, S.; Kurouski, D. Nanoscale Structural Organization of Insulin Fibril Polymorphs Revealed by Atomic Force Microscopy-Infrared Spectroscopy (AFM-IR). *ChemBioChem.* **2020**, *21* (4), 481–485.
- (104) Zhaliyazka, K.; Kurouski, D. Nanoscale Characterization of Parallel and Antiparallel β -Sheet Amyloid Beta 1–42 Aggregates. *ACS Chem. Neurosci.* **2022**, *13* (19), 2813–2820.
- (105) Herzberg, M.; Szunyogh, D.; Thulstrup, P. W.; Hassenkam, T.; Hemmingsen, L. Probing the Secondary Structure of Individual A β 40 Amorphous Aggregates and Fibrils by AFM-IR Spectroscopy. *ChemBioChem.* **2020**, *21* (24), 3521–3524.
- (106) Waeytens, J.; Van Hemelryck, V.; Deniset-Besseau, A.; Ruyschaert, J.-M.; Dazzi, A.; Raussens, V. Characterization by Nano-Infrared Spectroscopy of Individual Aggregated Species of Amyloid Proteins. *Molecules* **2020**, *25* (12), 2899.
- (107) Banerjee, S.; Holcombe, B.; Ringold, S.; Foes, A.; Naik, T.; Baghel, D.; Ghosh, A. Nanoscale Infrared Spectroscopy Identifies Structural Heterogeneity in Individual Amyloid Fibrils and Prefibrillar Aggregates. *J. Phys. Chem. B* **2022**, *126* (31), S832–S841.
- (108) de Mello, L. R.; Porosk, L.; Lourenço, T. C.; Garcia, B. B. M.; Costa, C. A. R.; Han, S. W.; de Souza, J. S.; Langel, Ü.; da Silva, E. R. Amyloid-like Self-Assembly of a Hydrophobic Cell-Penetrating Peptide and Its Use as a Carrier for Nucleic Acids. *ACS Appl. Bio Mater.* **2021**, *4* (8), 6404–6416.

(109) Otzen, D. E.; Dueholm, M. S.; Najarzadeh, Z.; Knowles, T. P. J.; Ruggeri, F. S. In Situ Sub-Cellular Identification of Functional Amyloids in Bacteria and Archaea by Infrared Nanospectroscopy. *Small Methods* **2021**, *5* (6), 2001002.

(110) Zhou, L.; Kurouski, D. Structural Characterization of Individual α -Synuclein Oligomers Formed at Different Stages of Protein Aggregation by Atomic Force Microscopy-Infrared Spectroscopy. *Anal. Chem.* **2020**, *92* (10), 6806–6810.

(111) Dou, T.; Kurouski, D. Phosphatidylcholine and Phosphatidylserine Uniquely Modify the Secondary Structure of α -Synuclein Oligomers Formed in Their Presence at the Early Stages of Protein Aggregation. *ACS Chem. Neurosci.* **2022**, *13* (16), 2380–2385.

(112) Rizevsky, S.; Matveyenka, M.; Kurouski, D. Nanoscale Structural Analysis of a Lipid-Driven Aggregation of Insulin. *J. Phys. Chem. Lett.* **2022**, *13* (10), 2467–2473.

(113) Matveyenka, M.; Rizevsky, S.; Kurouski, D. The Degree of Unsaturation of Fatty Acids in Phosphatidylserine Alters the Rate of Insulin Aggregation and the Structure and Toxicity of Amyloid Aggregates. *FEBS Lett.* **2022**, *596* (11), 1424–1433.

(114) Adamcik, J.; Ruggeri, F. S.; Berryman, J. T.; Zhang, A.; Knowles, T. P. J.; Mezzenga, R. Evolution of Conformation, Nanomechanics, and Infrared Nanospectroscopy of Single Amyloid Fibrils Converting into Microcrystals. *Advanced Science* **2021**, *8* (2), 2002182.

(115) Ruggeri, F. S.; Habchi, J.; Chia, S.; Horne, R. I.; Vendruscolo, M.; Knowles, T. P. J. Infrared Nanospectroscopy Reveals the Molecular Interaction Fingerprint of an Aggregation Inhibitor with Single A β 42 Oligomers. *Nat. Commun.* **2021**, *12* (1), 688.

(116) Ruggeri, F. S.; Mannini, B.; Schmid, R.; Vendruscolo, M.; Knowles, T. P. J. Single Molecule Secondary Structure Determination of Proteins through Infrared Absorption Nanospectroscopy. *Nat. Commun.* **2020**, *11* (1), 2945.

(117) Waeytens, J.; Mathurin, J.; Deniset-Besseau, A.; Arluison, V.; Bousset, L.; Rezaei, H.; Raussens, V.; Dazzi, A. Probing Amyloid Fibril Secondary Structures by Infrared Nanospectroscopy: Experimental and Theoretical Considerations. *Analyst* **2021**, *146* (1), 132–145.

(118) Jin, M.; Lu, F.; Belkin, M. A. High-Sensitivity Infrared Vibrational Nanospectroscopy in Water. *Light: Science & Applications* **2017**, *6* (7), No. e17096.

(119) Mayet, C.; Dazzi, A.; Prazeres, R.; Allot, F.; Glotin, F.; Ortega, J. M. Sub-100 Nm IR Spectromicroscopy of Living Cells. *Optics Letters* **2008**, *33* (14), 1611–1613.

(120) Deliorman, M.; Janahi, F. K.; Sukumar, P.; Glia, A.; Alnemari, R.; Fadl, S.; Chen, W.; Qasaimeh, M. A. AFM-Compatible Microfluidic Platform for Affinity-Based Capture and Nanomechanical Characterization of Circulating Tumor Cells. *Microsyst Nanoeng* **2020**, *6* (1), 1–15.

(121) Popescu, G.; Ikeda, T.; Goda, K.; Best-Popescu, C. A.; Laposata, M.; Manley, S.; Dasari, R. R.; Badizadegan, K.; Feld, M. S. Optical Measurement of Cell Membrane Tension. *Phys. Rev. Lett.* **2006**, *97* (21), 218101.

(122) Clède, S.; Lambert, F.; Sandt, C.; Kascakova, S.; Unger, M.; Harté, E.; Plamont, M.-A.; Saint-Fort, R.; Deniset-Besseau, A.; Gueroui, Z.; Hirschmugl, C.; Lecomte, S.; Dazzi, A.; Vessièrès, A.; Policar, C. Detection of an Estrogen Derivative in Two Breast Cancer Cell Lines Using a Single Core Multimodal Probe for Imaging (SCoMPI) Imaged by a Panel of Luminescent and Vibrational Techniques. *Analyst* **2013**, *138* (19), 5627–5638.

(123) Wang, Y.; Heinemann, F.; Top, S.; Dazzi, A.; Policar, C.; Henry, L.; Lambert, F.; Jaouen, G.; Salmain, M.; Vessièrès, A. Ferrocifens Labelled with an Infrared Rhenium Tricarbonyl Tag: Synthesis, Antiproliferative Activity, Quantification and Nano IR Mapping in Cancer Cells. *Dalton Transactions* **2018**, *47* (29), 9824–9833.

(124) Yamakoshi, H.; Dodo, K.; Palonpon, A.; Ando, J.; Fujita, K.; Kawata, S.; Sodeoka, M. Alkyne-Tag Raman Imaging for Visualization of Mobile Small Molecules in Live Cells. *J. Am. Chem. Soc.* **2012**, *134* (51), 20681–20689.

(125) Lima, C.; Muhamadali, H.; Xu, Y.; Kansiz, M.; Goodacre, R. Imaging Isotopically Labeled Bacteria at the Single-Cell Level Using High-Resolution Optical Infrared Photothermal Spectroscopy. *Anal. Chem.* **2021**, *93* (6), 3082–3088.

(126) dos Santos, A. C. V. D.; Lendl, B.; Ramer, G. Systematic Analysis and Nanoscale Chemical Imaging of Polymers Using Photothermal-Induced Resonance (AFM-IR) Infrared Spectroscopy. *Polym. Test.* **2022**, *106*, 107443.

Recommended by ACS

Characterization of Functional Materials Using Coherence Scanning Interferometry and Environmental Chambers

Paul C. Montgomery, Rémi Barillon, *et al.*

MARCH 14, 2023
ACS OMEGA

READ 

Understanding Cantilever Transduction Efficiency and Spatial Resolution in Nanoscale Infrared Microscopy

Jeffrey J. Schwartz, Andrea Centrone, *et al.*

SEPTEMBER 13, 2022
ANALYTICAL CHEMISTRY

READ 

Time-Domain Photothermal AFM Spectroscopy via Femtosecond Pulse Shaping

Miriam Bohlmann Kunz, Martin T. Zanni, *et al.*

AUGUST 30, 2022
ANALYTICAL CHEMISTRY

READ 

Simultaneous Spatiotemporal Measurement of Structural Evolution in Dynamic Complex Media

Ruitao Wu and Aristide Dogariu

MAY 24, 2022
ACS OMEGA

READ 

Get More Suggestions >

B. Curriculum Vitae

Ana Catarina Vieira Dias dos Santos

Education

09 2021- 09 2023	MA in Executive Management, FH Wien der WKW Master Thesis: <i>Waste Management in the Textile Manufacturing Industry: a Dynamic Capabilities perspective</i>
09 2019- 07 2023	PhD Candidate at Institute of Chemical Technologies and Analytics, TU Wien Topic: <i>Applications of Nanoscale Chemical Imaging in the Life and Polymer Sciences</i> . Supervisor: Dr. Georg Ramer and Prof. Bernhard Lendl.
05 2019- 07 2019	Research internship at TU Wien Topic: AFM-IR of biological samples. Supervisor: Dr. Georg Ramer.
08 2017- 03 2019	MSc in Organic Chemistry, Stockholms Universitet Master Thesis: <i>Synthesis of Ketones from Carboxylic Acids or CO₂ using Grignard Reagents and turbo-Hauser Bases</i> .
09 2014- 07 2017	BSc in Biochemistry, Universidade do Porto Bachelor Thesis: <i>Synthesis and Biological Evaluation of GPE Conjugates with Potential Neuroprotective Activity</i> .
09 2011- 08 2014	Secondary school, Colégio Internato dos Carvalhos, with specialization in Biotechnology

Work Experience

09 2019- 12 2022	Project assistant at the Institute of Chemical Technologies and Analytics, TU Wien
04 2019- 06 2019	Internship at the TU Wien, working with AFM-IR
02 2016- 07 2016	Extra-curricular internship at the U. Porto, synthesis of vitamin D analogues

Awards and Fellowships

07 2022	Early career researcher grant to attend EuChem 2022 held in Lisbon, Portugal
10 2022	FemChem travel grant to attend SciX 2022 held in Covington, KY, U.S.A
12 2022	Merit scholarship for outstanding academic performance in the academic year 2021/2022 at the FH Wien der WKW

Peer-Reviewed Publications

ORCID: 0000-0001-6342-2823

- Colas, K.; V. D. dos Santos, A. C.; Mendoza, A. I-Pr₂NMgCl·LiCl Enables the Synthesis of Ketones by Direct Addition of Grignard Reagents to Carboxylate Anions. *Org. Lett.* **2019**, *21* (19), 7908–7913. <https://doi.org/10.1021/acs.orglett.9b02899>.
- Silva-Reis, S. C.; V. D. dos Santos, A. C.; García-Mera, X.; Rodríguez-Borges, J. E.; Sampaio-Dias, I. E. Bioinspired Design for the Assembly of Glypromate® Neuropeptide Conjugates with Active Pharmaceutical Ingredients. *New J. Chem.* **2020**, *44* (48), 21049–21063.

- <https://doi.org/10.1039/D0NJ04851H>.
- V. D. dos Santos, A. C.; Heydenreich, R.; Derntl, C.; Mach-Aigner, A. R.; Mach, R. L.; Ramer, G.; Lendl, B. Nanoscale Infrared Spectroscopy and Chemometrics Enable Detection of Intracellular Protein Distribution. *Anal. Chem.* **2020**, *92* (24), 15719–15725. <https://doi.org/10.1021/acs.analchem.0c02228>.
 - Kumar, D.; Sauer, M.; Kroeckert Ching, K.; Kalss, G.; V. D. dos Santos, A. C.; Ramer, G.; Foelske, A.; Lendl, B.; Liedl, G.; Otto, A. Wettability Transition of Femtosecond Laser Patterned Nodular Cast Iron (NCI) Substrate. *Applied Surface Science* **2021**, *559*, 149897. <https://doi.org/10.1016/j.apsusc.2021.149897>.
 - V. D. dos Santos, A. C.; Lendl, B.; Ramer, G. Systematic Analysis and Nanoscale Chemical Imaging of Polymers Using Photothermal-Induced Resonance (AFM-IR) Infrared Spectroscopy. *Polymer Testing* **2022**, *106*, 107443. <https://doi.org/10.1016/j.polymertesting.2021.107443>.
 - Colas, K.; V. D. dos Santos, A. C.; Kohlhepp, S. V.; Mendoza, A. Direct Addition of Grignard Reagents to Aliphatic Carboxylic Acids Enabled by Bulky Turbo-Organomagnesium Anilides. *Chemistry – A European Journal* **2022**, *28* (9), e202104053. <https://doi.org/10.1002/chem.202104053>.
 - V. D. dos Santos, A. C.; Tranchida, D.; Lendl, B.; Ramer, G. Nanoscale Chemical Characterization of a Post-Consumer Recycled Polyolefin Blend Using Tapping Mode AFM-IR. *Analyst* **2022**, *147* (16), 3741–3747. <https://doi.org/10.1039/D2AN00823H>.
 - V. D. dos Santos, A. C.; Hondl, N.; Ramos-Garcia, V.; Kuligowski, J.; Lendl, B.; Ramer, G. AFM-IR for Nanoscale Chemical Characterization in Life Sciences: Recent Developments and Future Directions. *ACS Measurement Science Au* **2023**. <https://doi.org/10.1021/acsmearsciau.3c00010>.

Conference proceedings

- Ramer, G.; V. D. dos Santos, A. C.; Zhang, Y.; Yilmaz, U.; Lendl, B. Image processing as basis for chemometrics in photothermal atomic force microscopy infrared imaging. *Proc. SPIE 12392, Advanced Chemical Microscopy for Life Sciences and Translational Medicine* **2023**, 1239209. <https://doi.org/10.1117/12.2651424>.

Conference Contributions

As presenting author

- A. Catarina V. D. dos Santos, Georg Ramer, Bernhard Lendl: “AFM-IR-based nanoscale chemical imaging”; Poster: 2nd FemChem Scientific Workshop, Vienna, Austria; 04.10.2019.
- A. Catarina V. D. dos Santos, Georg Ramer, Bernhard Lendl: “AFM-IR-based nanoscale chemical imaging”; Poster: 21st European Symposium on Polymer Spectroscopy, Linz, Austria; 13.01.2020 – 15.01.2020.
- A. Catarina V. D. dos Santos, Georg Ramer, Bernhard Lendl: “Polymer Analysis and Nanoscale IR: a New Chapter in a Decade-Long Story”; Poster: 11th International Conference on Advanced Vibrational Spectroscopy (ICAVS), online conference; 23.08.2021 – 26.08.2021.
- A. Catarina V. D. dos Santos, Davide Tranchida, Bernhard Lendl, Georg Ramer: “Nanoscale chemical imaging of rubber/PE/PP recycled blends using tapping-mode AFM-IR”; Talk: Spring SciX 2022, Liverpool, United Kingdom; 11.04.2022 – 13.04.2022.

5. A. Catarina V. D. dos Santos, Davide Tranchida, Bernhard Lendl, Georg Ramer: *“Nanoscale chemical imaging of rubber/PE/PP post-consumer recycled blends using tapping-mode AFM-IR”*; Poster: 2nd CHASE Expert Day, Vienna, Austria; 14.06.2022.
6. A. Catarina V. D. dos Santos, Davide Tranchida, Bernhard Lendl, Georg Ramer: *“Nanoscale Chemical Characterization and Imaging of a Recycled Post-Consumer Waste Polyolefin Blend using AFM-IR”*; Talk: 8th EuChemS Chemistry Congress, Lisbon, Portugal; 28.08.2022 – 01.09.2022.
7. A. Catarina V. D. dos Santos, Davide Tranchida, Bernhard Lendl, Georg Ramer: *“Application of tapping-mode AFM-IR to a post-consumer waste Polyolefin recyclate”*; Talk: 5th European Forum on Nanoscale IR Spectroscopy (EFNS), Vienna, Austria; 06.09.2022 – 08.09.2022.
8. A. Catarina V. D. dos Santos, Davide Tranchida, Bernhard Lendl, Georg Ramer: *“A closer look at a post-consumer recycled polyolefin blend: chemical characterization at the nanoscale using tapping-mode AFM-IR”*; Talk: SciX 2022, Covington, United States of America; 02.10.2022 – 07.10.2022.